AD-A056 513   AIR FORCE INST OF TECH WRIGHT-PATTERSON AFB OHIO SCH--ETC   F/G 20/4
A NUMERICAL SOLUTION OF SUPERSONIC AND HYPERSONIC VISCOUS FLOW --ETC(U)
JUN 78   G S BLUFORD
UNCLASSIFIED   AFIT/DS/AA/78S-1   NL

1 OF 3
AD
A056 513

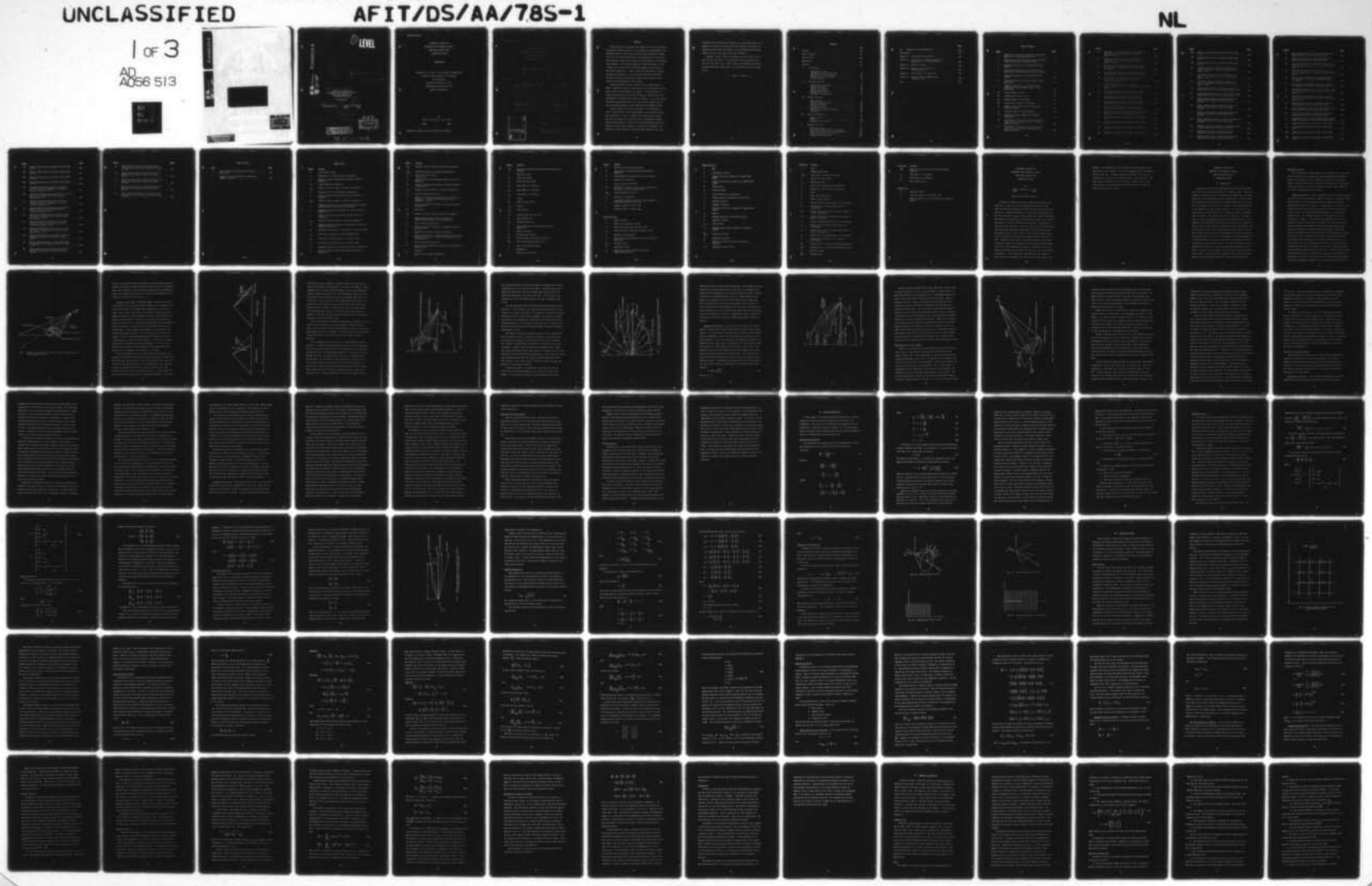

① LEVEL II

AD A056513

AD No.
DDC FILE COPY

⑯ 2404

⑲ 10

⑨ Doctoral thesis

⑥

A NUMERICAL SOLUTION OF SUPERSONIC AND HYPERSONIC VISCOUS FLOW FIELDS AROUND THIN PLANAR DELTA WINGS.

DISSERTATION

⑭ AFIT/DS/AA/78S-1

⑩ Guion S. Stewart Bluford Jr.
Major USAF

⑪ Jun 78

⑫ 239p.

DDC
RECEIVED
JUL 21 1978
B

DISTRIBUTION STATEMENT A
Approved for public release;
Distribution Unlimited

78 07 07 018

412 225

AFIT/DS/AA/78S-1

A NUMERICAL SOLUTION OF SUPERSONIC AND HYPERSONIC VISCOUS FLOW FIELDS AROUND THIN PLANAR DELTA WINGS

DISSERTATION

Presented to the Faculty of the School of Engineering
of the Air Force Institute of Technology
Air University
in Partial Fulfillment of the
Requirements for the Degree of
Doctor of Philosophy

by

Guion S. Bluford, Jr., B.S., M.S.

Major USAF

Approved for public release; distribution unlimited

AFIT/DS/AA/78S-1

A NUMERICAL SOLUTION OF SUPERSONIC AND HYPERSONIC VISCOUS FLOW FIELDS AROUND THIN PLANAR DELTA WINGS

by

Guion S. Bluford, Jr., B.S., M.S.

Major USAF

Approved:

Roger A. Crawford 23 June 1978
Chairman

26 Jun 1978

John R. Shea III 26 Jun 1978

Andrew J. Shine 26 Jun 1978

David A. Lee 26 June 1978

Milton E. Franke 27 June 1978

Accepted:

J. Przemieniecki 27 Jun 1978
Dean, School of Engineering

ACCESSION for
NTIS White Section ☑
DDC B.ff Section ☐
UNANNOUNCED ☐
JUSTIFICATION
BY
DISTRIBUTION/AVAILABILITY CODES
Dist. AVAIL. and/or SPECIAL
A

Preface

This dissertation represents the culmination of over three years of research carried out while I was assigned to the Aerodynamics and Airframe Branch of the Air Force Flight Dynamics Laboratory (AFFDL). It is the first major project that I was assigned to do as an aerospace engineer, and thus it serves as my introduction to the engineering profession. This research required a large investment in time, thought, and effort as well as the kind support and assistance of many other individuals. I wish to take this opportunity to express my sincere appreciation to all those people who have assisted me through the doctoral program, the conduct of this research, and finally in the preparation of this report.

This project was initially conceived by Dr. Wilbur Hankey of AFFDL. During the course of this research, he often provided me with helpful advice, encouragement, and support. His enthusiastic interest and constructive criticism, through good times and bad, were instrumental in bringing this effort to fruition. It has been a great pleasure and rewarding experience to work with Dr. Hankey and with the outstanding engineers in his Computational Aerodynamics Group.

A special thanks must also be extended to the "supporting cast." These include: Major John Kitowski, who provided the necessary environment in order to conduct this in-depth investigation; Major Roger Crawford, who provided me with encouragement, support and the "experimentalist" point of view on this problem; Major Scott McRae, who taught me the rudiments of numerical aerodynamics; the personnel of the Aeronautical Systems Division Computer Center, who provided me with assistance and support on the CDC 6600 computer; the members of my doctoral committee for their guidance and patient consideration; and finally the people of the Aerodynamics and Airframe Branch for their kind support and ready assistance.

Finally, I wish to express my thanks to my wife, Linda, and my sons Stewart and Trevor, for tolerating my highly irregular hours over the last three years. Their patience, encouragement, and understanding contributed immeasurably to the completion of this research effort.

Guion S. Bluford, Jr.

Contents

Page

Preface iii

List of Figures vii

List of Tables xiii

Nomenclature xiv

Abstract xxi

I. Introduction 1

- Description of Flow 2
- Experimental Flow Field Studies 12
- Theoretical Flow Field Studies 16
- Numerical Flow Field Studies 22
- Present Approach 23

II. Governing Equations 25

- Navier-Stokes Equations 25
- Conservative Form 29
- Conical Coordinates 31
- Conical Approximation 33
- Nondimensionalization 36
- Coordinate Transformation 39

III. Numerical Methods 42

- Basic Concepts 42
- Finite-Difference Scheme 46
- Boundary Conditions 53
- Initial Conditions 59
- Stability Analysis 60
- Consistency and Order of Accuracy 64
- Convergence 66

IV. Numerical Computation 68

- Computer Codes 68
- DELTA 68
- Sequence of Calculations 70

V. Numerical Results 76

- Cone Flow Analysis 76
- Delta Wing Expansion Side Flow Analysis 84
- Delta Wing Compression Side Flow Analysis 121
- Total Delta Wing Flow Analysis 125
- Computational Statistics 167

Page

VI. Conclusions and Recommendations 169

Bibliography 174

Appendix A: Transformation Derivatives 186

Appendix B: Convergence of Iterative Methods and Determination of Iteration Errors 188

Appendix C: Stability Analysis 190

Appendix D: Elements of the Linearized Matrix Equations 200

Appendix E: Subroutines of the DELTA Code 204

Appendix F: Conical Velocity Components and Streamline Plots 208

Vita 212

List of Figures

Figure		Page
1	Subsonic Flow Field Over Leeside of Planar Delta Wing with a Leading Edge Separation	3
2	General Delta Wing Flow Features Above and Below a Thin Delta Wing at Supersonic Speeds.	5
3	Qualitative Sketch of the Inviscid Cross-flow Pattern	7
4	Inviscid Streamline Pattern in Conical Cross-flow Plane of a Delta Wing at Supersonic Speeds . . .	9
5	Qualitative Sketch of the Viscous Cross-flow Pattern	11
6	Viscous Hypersonic Flow Field Around a Planar Delta Wing.	13
7	Physical Implications of the Conical Flow Assumptions on the Boundary Layer of a Flat Delta Wing.	35
8a	Physical Domain of Cone	40
8b	Computational Domain of Cone.	40
9a	Physical Domain of Delta Wing	41
9b	Computational Domain of Delta Wing.	41
10	System of Nodal Points Used in the Finite - Difference Method	44
11	Schematic Diagram of DELTA Program.	74
12	Schematic Diagram of PREDICT and CORRECT Subroutines	75
13	Comparison of Static Pressure vs. θ Above the Cone Surface for Different Grid Sizes with McRae's Solution.	78
14	Comparison of Total Velocity vs. θ Above the Cone Surface for Different Grid Sizes with McRae's Solution.	80

Figure		Page
15	Comparison of Static Temperature vs. θ Above the Cone Surface for Different Grid Sizes with McRae's Solution.	81
16	Comparison of Pitot Pressure vs. θ Above the Cone Surface for Different Grid Sizes with McRae's Solution.	83
17	Pitot Pressure Distribution in Spanwise Direction for Supersonic Flow Above a Planar Delta Wing, $\xi = 0.0718$.	89
18	Pitot Pressure Distribution in Spanwise Direction for Supersonic Flow Above a Planar Delta Wing	90
19	Cross-flow Velocity Vector Plot as Projected on ξ-η Plane for Supersonic Flow Above a Planar Delta Wing, $\alpha = 12^o$.	92
20	Cross-flow Streamline Plot as Projected on ξ-η Plane for Supersonic Flow Above a Planar Delta Wing, $\alpha = 12^o$	93
21	Location of Shock Wave and Conical Sonic Line for Supersonic Flow Above a Planar Delta Wing	94
22	Static Pressure Contour in Cross-flow Plane for Supersonic Flow Above a Planar Delta Wing	96
23	Static Temperature Contour in Cross-flow Plane for Supersonic Flow Above a Planar Delta Wing	97
24	Static Density Contour in Cross-flow Plane for Supersonic Flow Above a Planar Delta Wing	99
25	Hypersonic Viscous Layer Development Above a Delta Wing as Determined by Impact Pressure Survey.	101
26	Impact Pressure Survey on Leeside of Delta Wing, $\alpha = 0^o$.	103
27a	Impact Pressure Survey on Leeside of Delta Wing, $\alpha = 5^o$.	104
27b	Impact Pressure Survey on Leeside of Delta Wing, $\alpha = 5^o$.	105
28a	Impact Pressure Survey on Leeside of Delta Wing, $\alpha = 9^o$.	107

Figure Page

28b Impact Pressure Survey on Leeside of Delta Wing, $\alpha = 9^{o}$ 108

29a Impact Pressure Survey on Leeside of Delta Wing, $\alpha = 15^{o}$ 109

29b Impact Pressure Survey on Leeside of Delta Wing, $\alpha = 15^{o}$ 110

30 Cross-flow Streamline Plot as Projected on ξ-η Plane for Hypersonic Flow Above a Planar Delta Wing, $\alpha = 0^{o}$ 111

31 Cross-flow Streamline Plot as Projected on ξ-η Plane for Hypersonic Flow Above a Planar Delta Wing, $\alpha = 9^{o}$ 112

32 Cross-flow Streamline Plot as Projected on ξ-η Plane for Hypersonic Flow Above a Planar Delta Wing, $\alpha = 15^{o}$ 113

33 Static Pressure Contour in Cross-flow Plane for Hypersonic Flow Above a Planar Delta Wing, $\alpha = 0^{o}$ . . . 115

34 Static Temperature Contour in Cross-flow Plane for Hypersonic Flow Above a Planar Delta Wing, $\alpha = 0^{o}$ . . . 116

35 Static Pressure Contour in Cross-flow Plane for Hypersonic Flow Above a Planar Delta Wing, $\alpha = 9^{o}$ 117

36 Static Density Contour in Cross-flow Plane for Hypersonic Flow Above a Planar Delta Wing, $\alpha = 15^{o}$ 118

37 Static Pressure Contour in Cross-flow Plane for Hypersonic Flow Above a Planar Delta Wing, $\alpha = 15^{o}$ 119

38 Static Temperature Contour in Cross-flow Plane for Hypersonic Flow Above a Planar Delta Wing, $\alpha = 15^{o}$ 120

39 Spanwise Pressure Distribution on Compression Side of Planar Delta Wing at Supersonic Speeds 123

40 Mach Number Contour in Cross-flow Plane for Supersonic Flow Below a Planar Delta Wing 124

41 Static Pressure Contour in Cross-flow Plane for Supersonic Flow Below a Planar Delta Wing 124

Figure Page

42 Static Temperature Contour in Cross-flow Plane for Supersonic Flow Below a Planar Delta Wing 126

43 Static Density Contour in Cross-flow Plane for Supersonic Flow Below a Planar Delta Wing 126

44 Cross-flow Vector Velocity Plot as Projected on the ξ-η Plane for Supersonic Flow Below a Planar Delta Wing, $\alpha = 15^o$ 127

45 Cross-flow Streamline Plot as Projected on the ξ-η Plane for Supersonic Flow Below a Planar Delta Wing, $\alpha = 15^o$ 127

46 Pitot Pressure Distribution in Spanwise Direction for Supersonic Flow Above a Planar Delta Wing, $\xi = 0.0718$. 130

47 Pitot Pressure Distribution in Spanwise Direction for Supersonic Flow Above a Planar Delta Wing 131

48 Cross-flow Velocity Vector Plot as Projected on the ξ-η Plane for Supersonic Flow Around a Planar Delta Wing, $\alpha = 12^o$ 132

49 Cross-flow Streamline Plot as Projected on the ξ-η Plane for Supersonic Flow Around a Planar Delta Wing, $\alpha = 12^o$ 134

50 Static Pressure Contour in Cross-flow Plane for Supersonic Flow Around a Planar Delta Wing. 135

51 Static Temperature Contour in Cross-flow Plane for Supersonic Flow Around a Planar Delta Wing. 136

52 Static Density Contour in Cross-flow Plane for Supersonic Flow Around a Planar Delta Wing. 137

53 Hypersonic Viscous Layer Development Above a Delta Wing as Determined by Impact Pressure Measurements. . . 140

54 Hypersonic Bow Shock Profile Above a Delta Wing 141

55 Impact Pressure Survey on Leeside of Delta Wing, $\alpha = 0^o$. 143

56a Impact Pressure Survey on Leeside of Delta Wing, $\alpha = 5^o$. 144

56b Impact Pressure Survey on Leeside of Delta Wing, $\alpha = 5^o$. 145

Figure **Page**

57a Impact Pressure Survey on Leeside of Delta Wing, $\alpha = 9^o$ 146

57b Impact Pressure Survey on Leeside of Delta Wing, $\alpha = 9^o$ 147

58a Impact Pressure Survey on Leeside of Delta Wing, $\alpha = 15^o$ 148

58b Impact Pressure Survey on Leeside of Delta Wing, $\alpha = 15^o$ 149

59 Cross-flow Velocity Vector Plot as Projected on the ξ-η Plane for Hypersonic Flow Around a Planar Delta Wing, $\alpha = 0^o$ 151

60 Cross-flow Streamline Plot as Projected on the ξ-η Plane for Hypersonic Flow Around a Planar Delta Wing, $\alpha = 0^o$. 152

61 Cross-flow Velocity Vector Plot as Projected on the ξ-η Plane for Hypersonic Flow Around a Planar Delta Wing, $\alpha = 9^o$ 153

62 Cross-flow Velocity Vector Plot as Projected on the ξ-η Plane for Hypersonic Flow Around a Planar Delta Wing, $\alpha = 11^o$. 154

63 Cross-flow Streamline Plot as Projected on the ξ-η Plane for Hypersonic Flow Around a Planar Delta Wing, $\alpha = 11^o$ 155

64 Cross-flow Velocity Vector Plot as Projected on the ξ-η Plane for Hypersonic Flow Around a Planar Delta Wing, $\alpha = 15^o$. 156

65 Cross-flow Streamline Plot as Projected on the ξ-η Plane for Hypersonic Flow Around a Planar Delta Wing, $\alpha = 15^o$ 157

66 Static Pressure Contour in Cross-flow Plane for Hypersonic Flow Around a Planar Delta Wing, $\alpha = 0^o$. 159

67 Static Temperature Contour in Cross-flow Plane for Hypersonic Flow Around a Planar Delta Wing, $\alpha = 0^o$. 160

68 Static Pressure Contour in Cross-flow Plane for Hypersonic Flow Around a Planar Delta Wing, $\alpha = 5^o$. 161

Figure		Page
69	Static Pressure Contour in Cross-flow Plane for Hypersonic Flow Around a Planar Delta Wing, $\alpha = 9^{o}$	162
70	Static Density Contour in Cross-flow Plane for Hypersonic Flow Around a Planar Delta Wing, $\alpha = 9^{o}$	163
71	Static Pressure Contour in Cross-flow Plane for Hypersonic Flow Around a Planar Delta Wing, $\alpha = 11^{o}$	164
72	Static Pressure Contour in Cross-flow Plane for Hypersonic Flow Around a Planar Delta Wing, $\alpha = 15^{o}$	165
73	Static Temperature Contour in Cross-flow Plane for Hypersonic Flow Around a Planar Delta Wing, $\alpha = 15^{o}$	166

List of Tables

Table Page

1 Grid Increments for Hypersonic Flow Field Calculation 100

2 Computer Storage Requirements and Numerical Damping Constants 168

Nomenclature

Symbol	Meaning
a	Local speed of sound
a'	Eigenvalue of A' matrix defined in Appendix C
A	Vector in linearized governing equations defined in Appendix C
A'	Vector defined in Appendix C
A_{ij}	Element of Vector A which is defined in Appendix D
b'	Eigenvalue of B' matrix defined in Appendix C
B	Vector in linearized governing equations defined in Appendix C
B_{ij}	Element of Vector B which is defined in Appendix D
c	Maximum eigenvalue for the C matrix defined in Appendix C (This definition applies only in Appendix C)
c	Adjustable constant for maximum time step as defined in Equation 87
C	Vector in linearized governing equations defined in Appendix C
C_{ij}	Element of Vector C which is defined in Appendix D
C_1	Nondimensionalized constant for Sutherland's equation as defined in Equation 45
C_o	Experimental constant for Sutherland's viscosity equation
c_ℓ	Directional constants for density damping terms
c_p	Coefficient of specific heat at constant pressure
c_v	Coefficient of specific heat at constant volume
d	Maximum eigenvalue for the D matrix defined in Appendix C
D	Vector in linearized governing equations defined in Appendix D

Symbol	Meaning
D_{ij}	Element of Vector D which is defined in Appendix D
$D^{n}_{i,j}$	Density smoothing term defined by Equation 88
e'	Specific internal energy
e	Total energy
E	Vector in linearized governing equations defined in Appendix C
$\bar{E}$	Vector in governing equations (x coordinate) defined by Equation 15
E_{ij}	Element of Vector E which is defined in Appendix D
F	Vector defined by Equation 30
F	Vector in linearized governing equations defined in Appendix C. (This definition applies only in Appendices C and D).
$\bar{F}$	Vector in governing equations (y coordinate) defined in Equation 15
F_i	Body forces
F_{ij}	Element of Vector F which is defined in Appendix D
G	Amplification matrices defined in Appendix C (This definition applies only in Appendix C)
G	Vector defined by Equation 30
$\bar{G}$	Vector in governing equations (z coordinate) defined by Equation 15
h	Eigenvalue of H matrix defined in Appendix C
H	Vector sum of E and F in linearized governing equations defined in Appendix C. (This definition applies only in Appendix C).
H	Vector defined by Equation 30
$\bar{H}$	Vector in governing equations (constant terms) defined by Equation 21
J	Jacobian
k	Coefficient of thermal conductivity

Symbol	Meaning
K_i^n	Variable smoothing coefficient defined by Equations 90 and 91
L	Reference length
M	Total Mach number
M_c	Cross-flow Mach number
M_x	Mach number in x direction
M_y	Mach number in y direction
M_z	Mach number in z direction
N	2 PrRe
N_o	Sphere around a point
P, p	Pressure
P_{t_2}	Pitot pressure
Pr	Prandtl number (0.72 for air)
$\dot{q}$	Heat transfer rate
$\dot{q}_{ri}$	Radiation heat vector
Q	Total normal heat flux and stress terms for Equation 76
r	Radial coordinate
R	Universal gas constant
Re	Reynolds number as defined in Equation 27
Re_x	Free stream Reynolds number at L=x
t	Time in the physical domain
T	Temperature
u	Velocity in x direction

Symbol	Meaning
U	Time vector defined by Equation 30
$\bar{U}$	Time vector in governing equations defined by Equation 15
$\tilde{U}$	Finite-difference representation of the U vector
v	Velocity in y direction
V	Total velocity $(u^2+v^2+w^2)^{\frac{1}{2}}$
V_c	Magnitude of conical velocity vector projected on ξ-η plane as defined in Equation F1
V_{max}	Maximum adiabatic velocity
w	Velocity in z direction
x	Longitudinal distance along delta wing surface, or cone axis, measured from vertex
y	Distance normal to x and z axes
z	Distance normal to x and y axes

Special Notation

α	Angle of attack
β	Normal stress damping constant
γ	Ratio of specific heats (1.40 for air)
γ_c	Cross-flow vector angle with positive η axis
δ	Boundary layer thickness
δ_i	First-order forward-difference operator defined by Equation 92
δ_{ij}	Kronecker delta
Δ	Incremental value
Δ_i	First-order backward-difference operator defined by Equation 93

Special Notation

ε	$\frac{\gamma-1}{2\gamma}$
$\bar{\varepsilon}$	Convergence criteria
ζ	Conical direction coordinate in computational domain
η	Cross-flow direction coordinate in computational domain
θ	Conical angle
θ_c	Cone half angle
λ	Second coefficient of viscosity
λ	Courant number for Equations 49 and 50 only
μ	Absolute viscosity
ν	Kinematic viscosity
ξ	Cross-flow direction coordinate in computational domain
ρ	Density
σ	Maximum eigenvalue of coefficient matrix
Σ	Summation notation
τ_{ij}	Stress tensor
ϕ	Circumferential angle in spherical coordinate system
$\phi^n_{i,j}$	Iteration parameter
Φ	Dissipation function
$\bar{\chi}$	Hypersonic similarity parameter defined in Equation 1
[ ]	Dimensional analysis term

Subscripts	Meaning
c	Cone
e	Boundary layer edge
(i,j)	Mesh point location in (η,ξ) plane
l	Lower delta wing surface
n	Normal direction
o	Free stream isentropic total conditions
s	Wingtip side edge of delta wing surface
t	Total
u	Upper delta wing surface
w	Wall or surface value
x	Partial derivative with respect to x-coordinate
xx	Second partial derivative with respect to x-coordinate
xy	Second cross-partial derivative with respect to x and y coordinates
xz	Second cross-partial derivative with respect to x and z coordinates
y	Partial derivative with respect to y-coordinate
yy	Second partial derivative with respect to y-coordinate
yz	Second cross-partial derivative with respect to y and z coordinates
z	Partial derivative with respect to z-coordinate
zz	Second partial derivative with respect to z-coordinate
DF	Diffusion part of linearized governing equations
INV	Inviscid part of linearized governing equations
L	Reference length
MAX	Maximum value

Subscripts	Meaning
MXD	Mixed derivative part of linearized governing equations
η	Pertaining to η coordinate
ξ	Pertaining to ξ coordinate
∞	Free stream quantity

Superscripts	
n	Time step number
$\bar{n}$	Time step number for a predictor step
$'$	Quantity normalized by corresponding or stagnation quantity

A NUMERICAL SOLUTION OF
SUPERSONIC AND HYPERSONIC VISCOUS
FLOW FIELDS AROUND THIN
PLANAR DELTA WINGS

by

Guion S. Bluford, Jr., Ph.D.
Major USAF

Major Roger Crawford, Advisor

A numerical technique was used to compute the supersonic and hypersonic, viscous flow fields around thin planar delta wings. These solutions were obtained by solving the Navier-Stokes equations subject to a conical approximation. The integration technique used was the second-order accurate, finite-difference scheme by MacCormack. This numerical integration was performed on a constant step size array generated by a conical coordinate transformation. Solutions were obtained for the upper-only, lower-only, and total flow fields around delta wings with supersonic leading edges. These solutions span a Mach number range of 2.94 to 10.17, a local Reynolds number range of 3.345×10^5 to 5.0×10^6, and various angles of attack from -15° to $+15^\circ$. Numerical oscillations, due to shock capturing, were reduced by applying normal stress damping and a fourth-order density damping term to the finite-difference equations. A stability criteria was developed and used which accounted for both the viscous and inviscid flow regions. Good agreement was obtained between the numerical results and the experimental flow field data by Cross, Spurlin, and

Bannink. The shock-induced vortex within the viscous region and the hypersonic viscous "bubble" on top of the boundary layer were computed, for the first time. A unique examination was made of the vortical singularities in the conical cross-flow plane of the delta wing. This investigation demonstrated the feasibility of applying the conical approximation to the Navier-Stokes equations in order to solve flow fields around thin delta wings.

A NUMERICAL SOLUTION OF
SUPERSONIC AND HYPERSONIC VISCOUS
FLOW FIELDS AROUND THIN
PLANAR DELTA WINGS

I. Introduction

Aerodynamicists have been investigating the supersonic and hypersonic flow fields around delta wings for a number of years. These flow fields are essentially conical at high Reynolds numbers and thus are of great interest both theoretically and experimentally. Initial efforts at studying this problem were directed towards analyzing the lower surface or compression side flow field. However, from recent experiments, it was seen that the most striking features of the flow exist in the upper surface or leeside flow field. At angle of attack, an embedded shock is formed on the expansion side of the delta wing. The interaction of this embedded shock wave with the attached boundary layer at hypersonic speeds generates two important features of the leeside flow field. These include embedded streamwise vortices in the boundary layer at low angles of attack and flow separation at large angles of attack. Both of these features increase the temperature and pressure gradients on the upper surface of the wing. The purpose of this investigation is to develop numerical solutions for this flow field which are valid for both supersonic and hypersonic speeds. The delta wing which is being modeled in this study is a thin planar wing with supersonic leading edges. Solutions to this problem for both the upper and lower surface flow fields are of great practical importance, since lifting re-entry vehicles such as the Space Shuttle have delta wing configurations.

Description of Flow

For a comprehensive understanding of this complex flow, it is necessary to examine the flow fields on both the compression and expansion sides of a planar delta wing at subsonic, supersonic, and hypersonic speeds. Particular attention is placed on the leeward side of the wing, since this flow has a significant effect on the lift, drag, stability, and control effectiveness of the vehicle.

Subsonic Flow Field. Several investigators (Refs 1-4) have examined the flow characteristics around a slender delta wing. At subsonic speeds, the flow around a thin delta wing with sharp leading edges changes significantly with angle of attack. At small angles of attack, the flow remains attached, but as the angle of attack is increased beyond some critical value, the flow field becomes dominated by a large region of separated flow. The principal features of this separated flow are illustrated in Figure 1. The primary flow separation occurs at the leading edge where a vortex sheet is formed. This vortex sheet curves upward and inward and eventually rolls up into conical spirals that form concentrated vortex cores above the wing surface. The vortex causes a reattachment of the flow inboard of the leading edges, creating two flow patterns, a primary vortex flow and a secondary vortex flow. The primary vortex flow consists of concentric spirals about the core, the core flow, and the flow over the wing surface. The core flow is a highly rotational flow field, in which the velocity and pressure fields are approximately axially symmetric (Refs 5-11). The viscous effects and compressibility effects are confined to a region near the vortex axis. The spanwise flow next to the wing surface is initially induced outward toward the leading edge. Shortly after the fluid passes underneath the

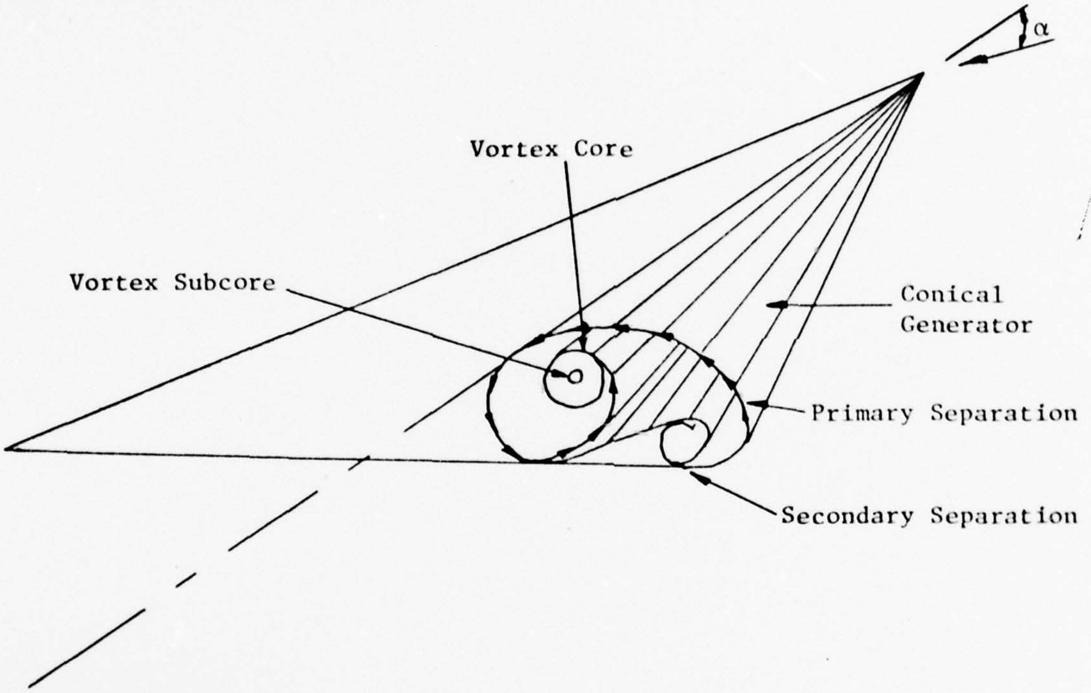
α
Vortex Core
Vortex Subcore
Conical Generator
Primary Separation
Secondary Separation

Fig. 1. Subsonic Flow Field Over Leeside of Planar Delta Wing With a Leading Edge Separation.

vortex core, the adverse pressure gradient causes the boundary layer to separate and form a secondary vortex just inboard and above the leading edge. The circulation of this very weak secondary vortex is opposite in sense to the primary vortex and has a circulation of approximately five percent of the primary vortex (Ref 6).

Supersonic Flow Field. As the Mach number is increased, the flow on the leeward side of the delta wing transitions from a separated flow to one characterized by a Prandtl-Meyer expansion in the cross-flow plane. The conditions under which this transition occurs depends on a number of parameters, such as leading edge shape, airfoil profile, and angle of attack (Ref 12). Intuitively, the range of conditions over which transition occurs for various wing configurations is approximately centered around $M_n = 1.0$ (where M_n is the Mach number normal to the leading edge). For thin wings, the transition occurs well before the leading edge becomes supersonic. On thick wings, at relatively low angles of attack, a strong detached shock wave forms in front of the leading edge with a subsonic region behind it. In this case, the wing leading edge is actually subsonic even though $M_n = 1.0$. Thus, for a wing of finite thickness, it is possible to have leading edge flow separation for a supersonic and hypersonic free stream.

In this investigation, we are concerned with the supersonic and hypersonic flow fields around a delta wing with supersonic leading edges. This study will examine both the flow in the boundary layer as well as the flow in the inviscid regions. The inviscid flow field is approximately conical (Refs 13-18) on both sides of the delta wing. The general features of the flow are shown in Figure 2. On the lower surface, the attached shock wave at the leading edge produces a cross-flow

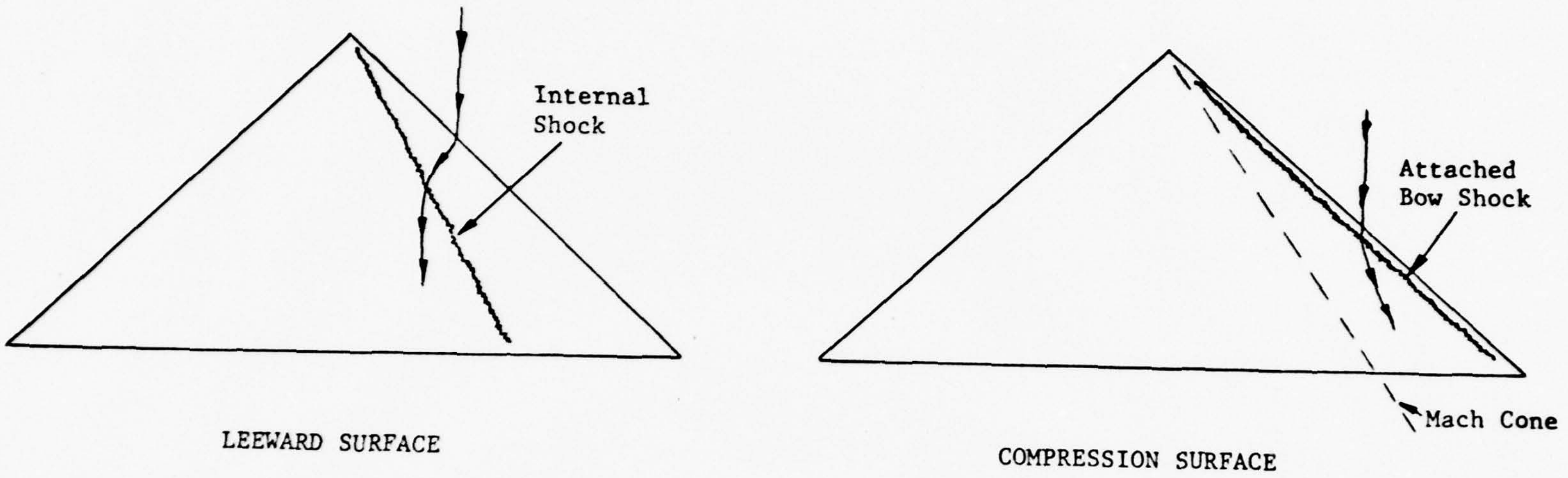
Internal
Shock
Attached
Bow Shock
Mach Cone

LEEWARD SURFACE

COMPRESSION SURFACE

Fig. 2. General Flow Field Features Above and Below a Thin Delta Wing at Supersonic Speeds.

away from the plane of symmetry. Inside the Mach cone, the flow expands and eventually becomes parallel to the plane of symmetry. On the expansion side, the region between the Mach cone and the leading edge contains attached isentropic flow. The Prandtl-Meyer expansion of the free stream velocity component normal to the leading edge causes a deflection of the total velocity vector toward the wing root chord. An internal shock wave along a radial from the vertex realigns the flow with the plane of symmetry so that no flow crosses the center plane. If the internal shock is weak, the deflected flow remains attached. However, if the shock wave is strong, the boundary layer will separate resulting in a rolled-up vortex sheet.

Since the inviscid flow around the delta wing is conical, the flow field in any plane normal to the wing chord has a similar solution. Thus, the entire flow field can be represented by selecting a cross-flow plane normal to the axis of symmetry. By neglecting the viscous effects, a qualitative sketch of this cross-flow plane is shown in Figure 3 (Ref 15).

On the expansion side of the wing, the region bounded by ABDG is hyperbolic. Elliptical equations describe the flow in the region OCBDG. The line BD is the cross-flow sonic line which merges into the internal oblique shock DEG. The Prandtl-Meyer expansion is confined to the area ABD where the line AB represents the first ray of the expansion fan. The line BFE is the reflection of this expansion ray from the surface of the Mach cone BC which emanates from the vertex of the wing. Expansion waves travel along the straight characteristics in the Prandtl-Meyer expansion and are reflected as compression waves at the cross-flow sonic line. In the region between the cross-flow sonic line and

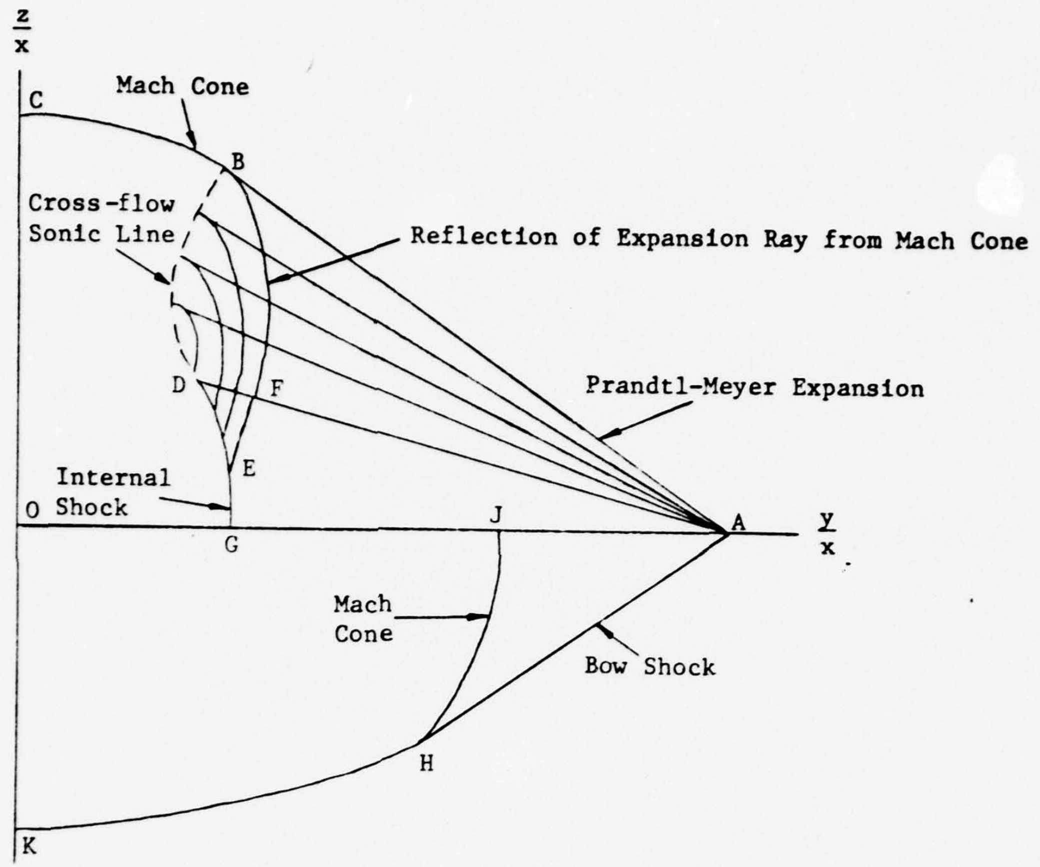
z/x
Mach Cone
C
B
Cross-flow Sonic Line
Reflection of Expansion Ray from Mach Cone
D
F
Prandtl-Meyer Expansion
E
Internal Shock
O
G
J
A
y/x
Mach Cone
Bow Shock
H
K

Fig. 3. Qualitative Sketch of the Inviscid Cross-flow Pattern

BF, the expansion waves are along one family of characteristics and the compression waves are along the other family. The compression waves below the characteristic AFD are straight characteristics which are eventually absorbed by the internal shock wave. The line OGA is the wing surface and the line COK represents the plane of symmetry (Refs 14-15).

For the compression side of the delta wing, the line AHK is a bow shock wave. The curvature of the shock wave at KH makes the flow rotational in the central region OKHJ. The strength of the shock is reduced between the point H and the plane of symmetry. The flow in the region AHJ (within the bow shock wave) is isentropic and uniform with the area JHKO being subject to the influence of the wing vertex. The Mach cone or sonic line JH intersects the shock wave AHK at the point H where the shock begins to bend.

The spherical cross-flow streamline pattern for the inviscid flow field is shown in Figure 4. Outside the influence of the delta wing, the velocity and entropy are constant and the cross-flow streamlines are a family of straight lines that intersect at a point on the plane of symmetry. However, when the cross-flow streamlines cross a shock wave, these streamlines become curved lines that terminate at one or more singularity points called vortical singularities. These points are cross-flow stagnation points where the entropy is multivalued (Refs 19-21). Thus, Figures 3 and 4 depict areas of interest for which the numerical solution of the problem is desired.

In this description of the supersonic flow field, the viscous effects and the shock wave-boundary layer interaction effects were ignored. The bow shock was depicted on the compression side of the

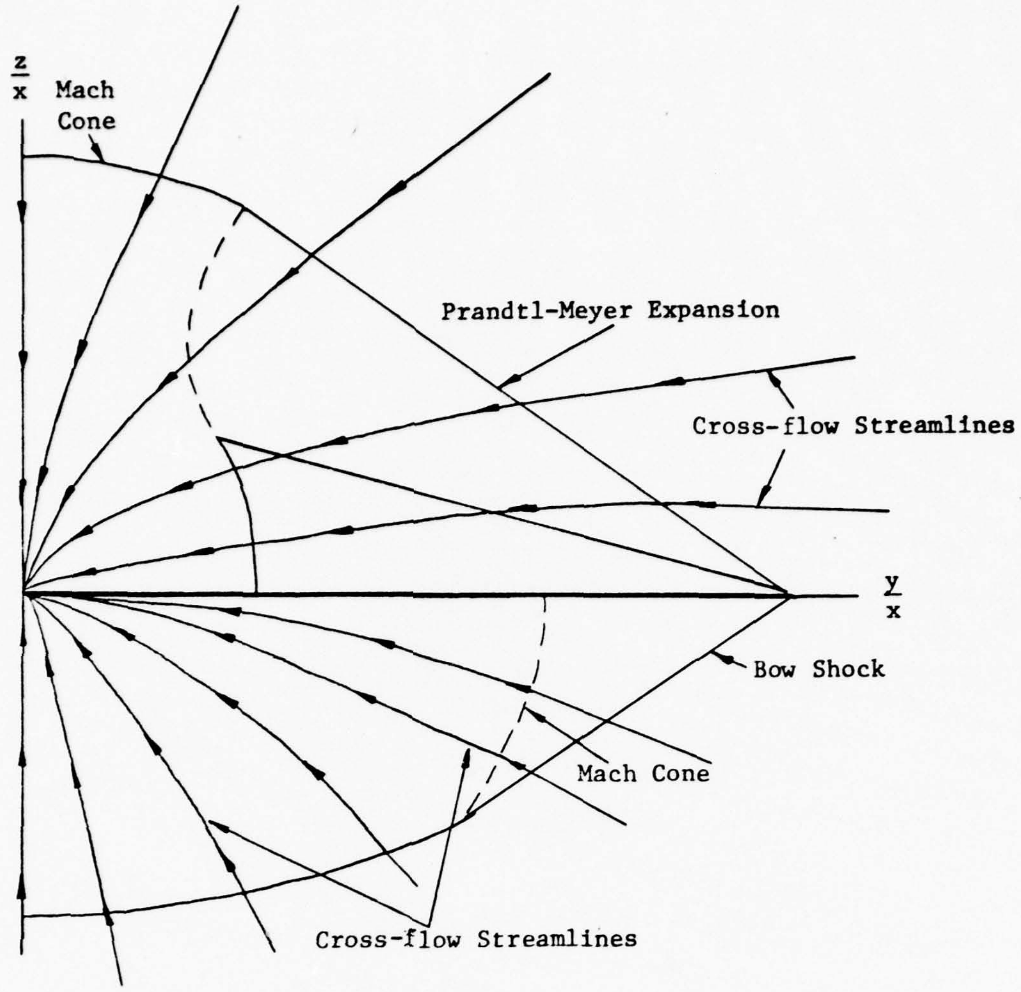
z/x
Mach Cone
Prandtl-Meyer Expansion
Cross-flow Streamlines
y/x
Bow Shock
Mach Cone
Cross-flow Streamlines

Fig. 4. Inviscid Streamline Pattern in Conical Cross-flow Plane of a Delta Wing at Angle of Attack.

delta wing and was attached at the leading edge. The boundary layer was very thin for high Reynolds number flow and thus the supersonic flow field could be approximated as an inviscid conical flow field. However, it was found by experiment (Refs 14-15) that a weak shock wave does exist on the expansion side of the delta wing near the leading edge. This very weak shock occurs because the boundary layer as well as a finite leading edge thickness prevents the compression side shock wave from attaching itself at the leading edge, thus forcing it to partially encircle the expansion flow field. A qualitative sketch of this cross-flow pattern with viscous effects at low Reynolds number is shown in Figure 5.

Hypersonic Flow Field. As the flow is accelerated to hypersonic speeds, the shock waves become stronger and the boundary layer becomes thicker. The interaction of the inner shock with the attached boundary layer is responsible for two of the most important features of the lee-side flow field. These are the generation of embedded vortices in the boundary layer at small angles of attack (Ref 22) and the shock induced flow separation at large angles of attack (Refs 17, 18, 23-24). The embedded vortices lie fully within the attached boundary layer and are convected downstream through the boundary layer. The interaction of these vortices with the upper wing surface results in increased shear and heat transfer. Experimental measurements (Refs 18 and 20) indicate that these vortices occur at small values of the viscous interaction parameter

$$\bar{\chi} = M_\infty^3 / \sqrt{Re_L} \qquad (1)$$

such as $\bar{\chi} = 0.1$.

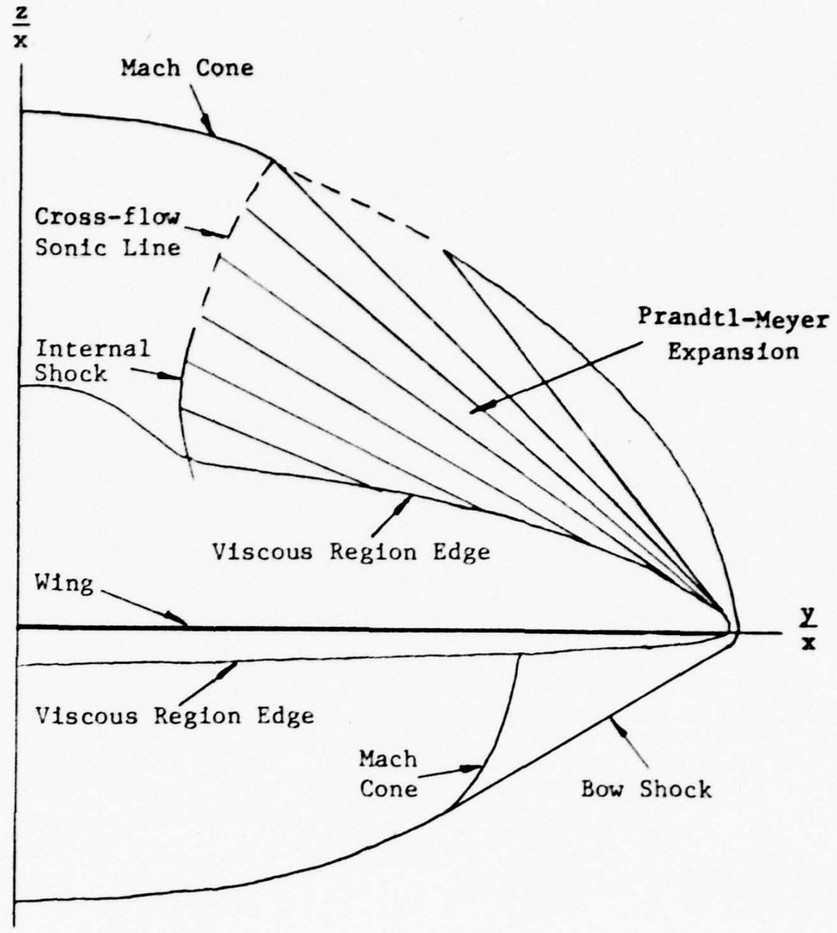

$\frac{z}{x}$
Mach Cone
Cross-flow Sonic Line
Internal Shock
Prandtl-Meyer Expansion
Viscous Region Edge
Wing
$\frac{y}{x}$
Viscous Region Edge
Mach Cone
Bow Shock

Fig. 5. Qualitative Sketch of the Viscous Cross-flow Pattern.

For shock induced separation, the shear layer rolls up into a pair of conically growing vortices as seen in Figure 6. These vortices remain fully submerged in the boundary layer at low Reynolds number and form a large viscous bubble inboard of the internal shock. With an increase in angle of attack, the internal shock and boundary layer separation line move outboard until eventually the separation line reaches the leading edge. The flow pattern in this case resembles the classical subsonic leading edge separation pattern as shown in Figure 1. Increased pressure and heat transfer rates are produced on the leeward side where the vortices impinge on the surface. Under some conditions, as the embedded shock increases in strength the reattached flow underneath the primary vortex might give rise to a secondary vortex as it moves outward from the centerline and separates. Experimental measurements made by Cross (Ref 17) and Narayan (Ref 25) at $M \simeq 0(1)$ exhibit the characteristics of shock induced separated flow. Further discussions on the flow field details are presented in the following sections.

Experimental Flow Field Studies

Because of the complexity of this problem, particularly at hypersonic speeds, a large amount of experimental data exists on delta wings. However, most of this information is surface pressure and heat transfer measurements (Refs 25-55). The majority of the boundary layer and flow field data comes from shadowgraphs, schlieren photographs, oil flow pictures, and vapor screen techniques. Only a small amount of published detailed information has been found for the supersonic and hypersonic flow over delta wings with supersonic leading edges. Some of this detailed data consists of pitot pressure measurements made in the plane of symmetry (Refs 22 and 26). Most of this information consists

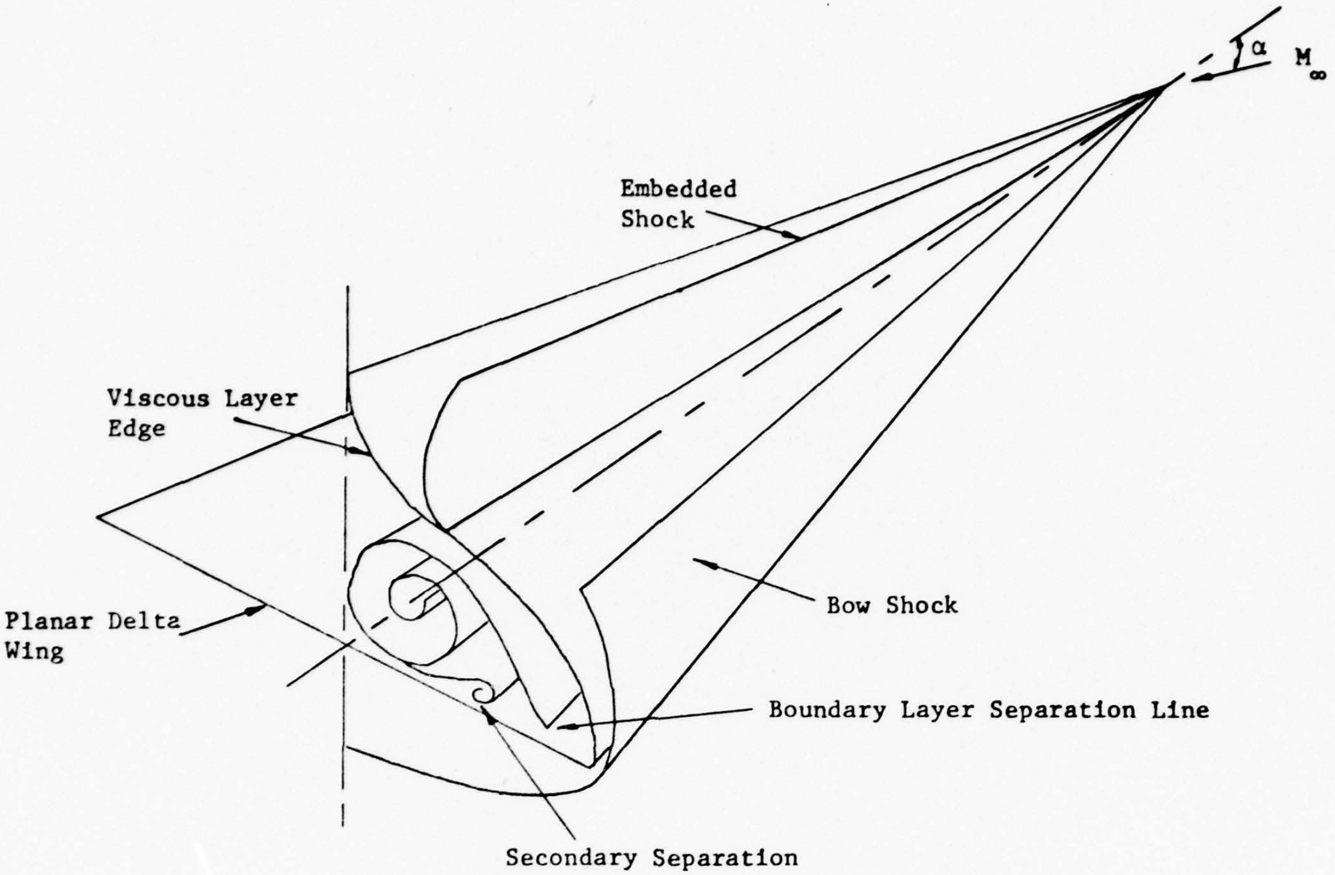
α
M_∞
Embedded Shock
Viscous Layer Edge
Planar Delta Wing
Bow Shock
Boundary Layer Separation Line
Secondary Separation

Fig. 6. Viscous Hypersonic Flow Field Around a Planar Delta Wing.

of impact pressure surveys made in the expansion flow of a delta wing. These pressure measurements were made by Fowell (Ref 13), Bannink et al (Refs 14 and 15), Spurlin (Ref 16), Cross (Ref 17) and Monnerie and Werle (Ref 18). Fowell and Bannink examined the supersonic inviscid flow field over a delta wing while Spurlin, Cross, Monnerie and Werle investigated the hypersonic flow regime.

Fowell (Ref 13) used a pressure rake to measure the spanwise pitot pressure above a flat delta wing. His measurements were made at a Mach number of 2.5 and at an angle of attack of $10^{\circ}\ 5'$. He found that an internal shock does exist on the expansion side of the delta wing and that it increases in strength as the angle of attack is increased. The strength of the internal shock was quite small, being of the same order as the weak bow shock on the expansion side of the wing.

Bannink, Nebbeling, and Reyn (Ref 14) did a more detailed investigation of the supersonic flow over a delta wing. Spanwise pitot pressure measurements were made in several planes perpendicular to the wing surface at various distances from the wing vertex. These measurements focused on determining the location and shape of the internal shock. It was found that the internal shock was approximately conical and that, away from the wing surface, it bends towards the plane of symmetry of the wing.

In 1971, Bannink and Nebbeling (Ref 15) repeated their investigation of supersonic, inviscid flow field over a flat delta wing. Tests were conducted at a Mach number of 2.94 and at a Reynolds number of 2.65×10^{6}. The main purpose of this study was to determine the shape and location of the internal shock and of the conical-sonic line, the latter being the locus of points where the conical Mach number is equal to one.

A comparison of pressure measurements was made in different planes normal to the root chord to show that the inviscid flow is approximately conical. The conical streamlines were traced and were found to end at the wing root chord. Thus, the conical stagnation point or vortical singularity is very near the origin. The results of this investigation suggest that the internal shock wave ends with zero strength at the point where the conical-sonic line begins.

Spurlin, Cross, Monnerie, and Werle examined the expansion flow over a sharp leading edge delta wing at hypersonic speeds. Monnerie and Werle (Ref 18) made static and pitot pressure measurements of the flow field at a Mach number of 7.0 and a Reynolds number of 4.5×10^6. The angle of attack was varied from 0^o to 20^o with flow separation occurring at $\alpha = 5^o$. The impact pressure data was presented as contour curves on the conical plane. No specific experimental point data was given in the reference. Spurlin (Ref 16) made impact pressure measurements at a Mach number of 10.13 and a Reynolds number of 4.28×10^5. This data was used to supplement the experimental data Cross obtained for the same flow conditions (Ref 17). Qualitative flow information was obtained from shadowgraphs, schlierens, vapor screen, and oil flow pictures. Surface pressures, surface temperatures, and impact pressures were measured at various points in the leeside flow field to determine the magnitude and extent of the flow phenomena. The character of the hypersonic flow was separated into three different regimes by several specific and dominant flow properties. The first regime, which occurred for angle of attack in the range $\alpha \leq 7^o$, was dominated by an attached, quasi-parallel flow across the surface. The second regime was dominated by a conical, shock-induced separation of the viscous layer for the range

$7^{\circ} \leq \alpha \leq 20^{\circ}$. Finally, the third region was identified by a base pressure induced separation of the upper surface flow for $\alpha \geq 20^{\circ}$, which eventually resulted in the separation of the entire surface flow. Because of the conical nature of the second flow regime, most of the comparison of numerical and experimental hypersonic results was done for this regime.

For angles of attack from $\alpha = 9^{\circ}$ to 20°, the upper surface flow field was dominated by a shock-boundary layer interaction that caused a separation of most of the wing boundary layer. Separation of the boundary layer was caused by the internal shock which was located near the Mach cone. A viscous bubble occurred near the plane of symmetry as a result of this shock-induced separation. The surface flow between the wing leading edge and the separation line was attached and characterized by a two-dimensional Prandtl-Meyer expansion. Results of the impact pressure survey indicated that to a good approximation, the flow was conical, thus making possible a theoretical or numerical analysis of the flow in two dimensions.

Theoretical Flow Field Studies

Several analytical techniques have been developed to describe the supersonic and hypersonic flow around delta wings. Most of these methods provided satisfactory solutions for a limited number of flow conditions. Very few techniques have been developed which can solve the complete supersonic and hypersonic flow field around delta wings with supersonic leading edges.

Supersonic Flow Field.

Initial efforts at solving the supersonic problem were directed towards using linearized conical flow theory.

Busemann (Ref 56) introduced this procedure and Stewart (Ref 57) and Lagerstrom (Ref 58) extended it to thin delta wings. This method was applicable to thin conical delta wings with weak shock waves. Clarke and Wallace (Ref 59) extended the linear theory to second order in incidence, still based on potential approximations. However, with increasing Mach number and angle of attack, nonlinear effects became important and the results of linearized theory were of little value. In fact, at high Mach numbers even the second order theory was not adequate. Therefore, in order to obtain meaningful results, nonlinear effects were included in the theoretical analyses.

One of the first nonlinear solutions to the delta wing problem was obtained by Maslen (Ref 60). In his treatment of the problem, he assumed that the expansion side had no shocks and thus was irrotational. Maslen computed the flow field characteristics in the hyperbolic region by using the Prandtl-Meyer relations and the method of characteristics. The remaining subsonic domain was solved by using relaxation methods. On the compression side of the delta wing, the supersonic flow properties were calculated by using shock tables while the remaining elliptical region was solved by relaxation techniques. The sonic line location was determined empirically by using the free stream Mach angle and the shock wave angle from a wedge. The primary difficulty encountered in Maslen's technique was that the relaxation procedure did not converge at high supersonic speeds.

Fowell (Ref 13) improved on Maslen's treatment of the problem by solving the governing equations for steady inviscid supersonic flow over a plane delta wing with supersonic leading edges. He showed that two solutions exist for the flows over the expansion surfaces; a continuous solution for flows below a critical angle of attack and a discontinuous solution for flows above this angle of attack. An exact solution was determined for the flow over the compression surface and for the continuous flow over the expansion surface. The Prandtl-Meyer equations were used to calculate the flow properties outside the Mach cone while the relaxation techniques were used to determine the flow properties within the vertex domain. An interactive procedure was needed to locate the curved shock on the compression side.

For the discontinuous flow over the leeward side of the delta wing, an approximate solution was developed by Fowell. He assumed the existence of a planar shock normal to the wing surface and of such strength to change the direction of the outboard velocity vector to parallel the wing root chord. Two-dimensional shock relations were used to determine the flow states on either side of the shock wave. Fowell verified his prediction of an internal shock wave by experimental study on the expansion side of a supersonic delta wing.

It was argued by Reyn (Refs 61-63) that if an irrotational solution for the flow on the expansion side of the delta wing did exist, this wave pattern would lead to limit-line singularities. This conical limit-line would consist of the line BFE (Fig 3) extending as a straight line to the wing surface. Since limit-lines do not exist in real flows, Bulakh (Ref 64) expected a shock wave to occur in the flow field. Bulakh introduced a shock wave upstream of BFEG (Fig 3) and indicated that a shock wave upstream of BC (Fig 3) may also be introduced. The numerical calculations following such a procedure were made by Babaev (Ref 65) and the shock wave vanished along BC (Fig 3) and along the characteristic BFE (Fig 3). A straight shock wave perpendicular to the wing surface and extending to the characteristic BFE (Fig 3) was found. Babaev showed that it was impossible to have a continuous flow solution over the expansion side of the delta wing, as described by Fowell (Ref 13).

In his theoretical development, Babaev used the Prandtl-Meyer relations and the method of characteristics to determine the hyperbolic flow field properties on the expansion side of the delta wing (Ref 65). He obtained the elliptical flow field properties from the irrotational potential flow theory by using the method of successive approximations. On the compression side, Babaev (Ref 66) applied the oblique shock relations to the uniform flow bounded by the plane shock, the Mach cone, and the wing. The flow properties in the central region OKHJ (Fig 3) were calculated by the method of successive corrections similar to the method used for the upper wing surface.

South and Klunker (Ref 67) improved on the compression side flow field results of Babaev, by using the method of lines. In their work, the flow region was transformed into a rectangular domain with an orthogonal coordinate grid. The shock wave and body surface were mapped as parallel boundary lines in the transformed plane. On each grid line, the system of equations was reduced to ordinary differential equations which were integrated by a fourth-order Runge-Kutta method. The results of this technique were compared with the numerical results of Voskresenskii (Ref 88) and were found to be in good agreement.

Hypersonic Flow Field. For hypersonic flow, most of the theoretical analysis was focused on the compression side flow field. Only two references were found which attempted to calculate the leeside hypersonic flow properties (Refs 17 and 68). In Cross' experimental investigation

(Ref 17), a simplified analytical model was developed to describe the significant flow properties over a delta wing. Beeman and Powers (Ref 68) used a three-dimensional method of characteristics to describe both the expansion and compression side flow fields. Both methods provided a fair agreement with experimental results, even though neither technique included viscous and rotational effects. More significant variations between theoretical and experimental results were noted in regions of viscous-inviscid interaction.

For the compression side flow field, several methods were used to calculate flow field characteristics. Thin shock layer theory was used by Messiter (Ref 69) and others to determine surface pressure distributions and shock shapes. This theory assumed that the shock wave lies very close to the body and that the pressure on the body is determined primarily by the shock shape. Under these conditions, the flow variables in the intervening shock layer can be written as a series expansion in ϵ, where ϵ is the density ratio across a plane shock lying at the same angle of attack as the wing. The zeroth-order solution of these series gives the well-known Newtonian results, modified possibly by the Busemann correction for body curvature. Messiter derived a set of approximate nonlinear equations for the conical flow and produced limited results for the lifting flat delta wing with a detached shock. He pointed out that in the case when the shock wave is attached to leading edges, difficulties may arise in matching the uniform flow near the leading edges with the nonuniform flow in the central or wing root region. This work was expanded by Hida (Ref 70), who made an approximate allowance for wing thickness. Squire (Refs 71 and 72) and Shanbhag (Ref 73) obtained the exact numerical solutions to the governing equations for the flow, with detached shocks, on the compression surface. Their results showed excellent agreement with experiment, as did also the work by Hillier (Refs 74 and 75), who extended the analysis to include the effects of yaw. Squire (Ref 76), Woods (Refs 77 and 78), Roe (Refs 79 and 80), and Gonor (Refs 81 and 82) all considered conical flows for attached shocks, again showing good agreement with the limited experimental results and exact solutions available.

For hypersonic flow at low angles of attack on the compression side, the thin shock layer theory is not valid. In this regime, linearized hypersonic small disturbance theory was used by Malmuth (Ref 83), Ter-Minasyants (Ref 84), and Hui (Refs 85 and 86) to treat planar delta wings of moderate aspect ratio. Malmuth calculated the pressures on the compression side of a planar delta wing at infinite Mach number. He assumed that the flow inside of the Mach cone differed slightly from the corresponding two-dimensional flow over a flat plate at the same angle of attack. Based on this assumption, a linear perturbation method was used to calculate the nonlinear flow inside the Mach cone. Ter-Minasyants (Ref 84) and Hui (Refs 85 and 86) calculated the flow field on both sides of the Mach cone at Mach numbers less than infinity. They used a linearized perturbation technique to calculate the flow within the Mach cone and then used Lighthill's strained coordinate technique to match this solution with the exact solution of the uniform flow outside of the Mach cone. When compared with available exact numerical solutions, this method gave almost identical results, except near the cross-flow sonic line, where the numerical methods failed to describe the discontinuous flow. At the sonic line, this technique predicted the discontinuity and showed that the discontinuous pressure slope has a square root singularity similar to that described by supersonic linear theory.

Numerical Flow Field Studies

Several references (Refs 87-93) were found which used finite-difference techniques to solve the supersonic flow around delta wings. Most of these references presented a detailed analysis and description of this conical flow problem. These references included several papers by Voskresenskii (Refs 87 and 88), Kutler (Refs 89-91) and Bazzhin (Ref 92).

Voskresenskii used a three-dimensional implicit finite-difference scheme to determine the bow shock shape and the pressure distribution on the lower wing surface. On the leeward side, the Prandtl-Meyer relations were used to calculate the flow near the leading edge while the implicit numerical scheme was used to calculate the flow within the Mach cone. In this well-posed initial value problem, Voskresenskii approximated the initial shock wave shape and flow conditions near the wing vertex and then numerically integrated the governing equations until conical similarity conditions were sufficiently satisfied. This technique produced a satisfactory solution for both the expansion flow field (Ref 87) and the compression flow field (Ref 88), even though it required a large amount of computer storage and time.

Kutler numerically computed the supersonic, inviscid, expansion side flow over a planar delta wing. He used the MacCormack finite-difference scheme and a shock capturing technique to calculate this flow field. The numerical integration was done in the conical coordinate direction, since the governing equations were hyperbolic in that direction. His numerical results showed excellent agreement with the experimental data by Bannink and Nebbeling (Ref 15) as well as with the method of characteristics results by Beeman and Powers (Ref 68).

Bazzhin (Ref 92) used the MacCormack finite-difference scheme to solve the time-dependent governing equations for the supersonic flow around a thin delta wing at low angles of attack. He used a coarse grid in the computational plane and thus was unable to obtain a true solution in the vicinity of the leading edge. This loss of accuracy did not prevent him from obtaining an accurate solution in other areas of the flow field. His numerical results compared quite favorably with the analytical solutions by Voskresenskii (Refs 87-88).

Present Approach

Although quite a few solutions were found for the supersonic and hypersonic flow over delta wings, none of these solutions provided a complete description of the flow field. A number of exact and approximate methods were discovered which could accurately calculate the inviscid flow field around a delta wing. However, no satisfactory theory was found which could describe the expansion side flow over a delta wing with shock-induced separation (Ref 3). Thus, the purpose of this research was to develop a numerical solution for the supersonic and hypersonic flow around a thin delta wing which could adequately describe the viscous interaction phenomena of the flow with shock-induced separation.

In order to solve this problem, it was assumed that the flow was both conical and laminar. A locally conical approximation, developed by McRae (Ref 94), was successfully applied to the governing equations for a compressible, viscous, heat conducting fluid. Both a time-dependent finite-difference method and a shock-capturing technique were used to solve these equations. A computer program was written to solve the governing equations in a generalized conical coordinate plane. In order to verify the accuracy of this computer code, the supersonic flow around a cone was solved and these results were compared with both experimental data and computed numerical results. The conical, viscous approximation was tested next by computing both the expansion and compression flow fields of a delta wing at supersonic and hypersonic speeds. The results of these calculations, when compared with experimental data, verified the applicability of this technique for solving the flow above and below a planar delta wing. Finally, the total flow field around a thin delta wing was solved at supersonic and hypersonic speeds to determine the interaction between the upper and lower surface flow fields. These numerical calculations were compared with experimental data. The results of this research demonstrated the feasibility of obtaining solutions to both the supersonic and hypersonic viscous flow fields over a planar delta wing by solving the conical governing equations.

II. Governing Equations

In this chapter, the unsteady governing equations for a viscous, compressible fluid are defined along with the basic fluid flow assumptions. The equations are transformed into generalized conical coordinates by using the relations in Appendix A. A conical approximation is applied to the resulting equations and then these equations are put in nondimensionalized conservative form.

Navier-Stokes Equations

The fundamental governing equations for a compressible, viscous, heat conducting fluid in Cartesian tensor form are given by

Continuity:

$$\frac{\partial \rho}{\partial t} + \frac{\partial(\rho u_i)}{\partial x_i} = 0 \tag{2}$$

Momentum:

$$\rho\left[\frac{\partial u_i}{\partial t} + u_j \frac{\partial u_i}{\partial x_j}\right] = - \frac{\partial p}{\partial x_i} + F_i + \frac{\partial \tau_{ij}}{\partial x_j} \tag{3}$$

Energy:

$$\frac{\partial Q}{\partial t} + \Phi - \frac{\partial \dot{q}_i}{\partial x_i} - \frac{\partial \dot{q}_{ri}}{\partial x_i} = \rho\left[\frac{\partial e'}{\partial t} + u_i \frac{\partial e'}{\partial x_i}\right] + p \frac{\partial u_i}{\partial x_i} \tag{4}$$

where

$$\tau_{ij} = \mu \left[\frac{\partial u_i}{\partial x_j} + \frac{\partial u_j}{\partial x_i}\right] + \lambda\delta_{ij} \frac{\partial u_k}{\partial x_k} \tag{5}$$

$$\phi = \tau_{ij} \frac{\partial u_i}{\partial xj} \tag{6}$$

$$\dot{q}_i = - k \frac{\partial T}{\partial x_i} \tag{7}$$

$$e = c_v T + \frac{u_i^2}{2} \tag{8}$$

$$e' = c_v T \tag{8a}$$

In addition to the above equations which express the conservation of mass, momentum, and energy, it is necessary to include a state equation which, for a perfect gas, is given by

$$p = \rho RT \tag{9}$$

The viscosity coefficient μ is a function of temperature and is adequately approximated by Sutherland's semi-empirical equation

$$\mu = \mu_\infty \left(\frac{T}{T_\infty}\right)^{\frac{1}{2}} \left[\frac{1 + C_o/T_\infty}{1 + C_o/T}\right] \tag{10}$$

where the constand C_o has been experimentally determined to be 198.6°R for air. The Sutherland law takes into account the weak attraction field surrounding the molecule and therefore provides a more rapid viscosity variation than the rigid sphere result of kinetic theory which gives the result $\mu \simeq T^{\frac{1}{2}}$.

Equations 2 through 10 provide seven basic equations in the seven unknowns, u, v, w, ρ, T, p, and μ, if the bulk viscosity coefficient μ_B is set equal to zero. This implies that the second coefficient of viscosity λ is equal to $- {}^2/_3\ \mu$. For a monatomic gas, this step is justified since the bulk viscosity coefficient vanishes when the molecule has no internal degrees of freedom. However, for a polyatomic gas, the bulk viscosity effect is not always zero and can be of the same order of magnitude as the molecular viscosity in sound propagation and shock wave structure. A more detailed discussion of the significance of bulk viscosity is given by Vincenti and Kruger (Ref 95). In the present investigation it is neglected since the numerical grid spacing used in the shock transition region is too coarse to allow resolution of the shock structure. This lack of resolution causes numerical difficulties which will be discussed in chapter three.

There are several approaches which may be used to derive the governing equations. However, the most commonly used method is the continuum approach. In this approach, a volume of arbitrary dimensions is fixed in space and enclosed by an imaginary surface through which a fluid is flowing. The continuity equation is derived from the law of conservation of mass which states that mass can neither be created or destroyed (Eulerian Method). Therefore, the time rate of change of mass within the volume must equal the net inward rate at which mass crosses the surface. The Navier-Stokes or momentum equations are applications of Newton's law of motion which equates the total force acting on the mass in the arbitrary volume to the rate of change of linear momentum. The total force consists of the pressure, the body force, and the viscous stress which is assumed to be linearly related to the rate of strain. The energy equation is based on the first law of thermodynamics which states that the increase in internal energy of the mass of fluid in the volume is equal to the sum of the heat added and work done on the fluid mass. In the absence of chemical reaction and radiation heat flux, the heat added is due to conduction and is given by the Fourier law of heat conduction. The work done on the fluid is that due to the pressure and shear stress acting on the volume surface. A more detailed discussion of this approach of deriving the governing equations may be found in Schlichting (Ref 96), Yuan (Ref 97), and Chow (Ref 98).

In this investigation, the following assumptions are applied to the governing equations:

1. The specific heats, c_p and c_v, are both constant and thus the specific heat ratio $\gamma = \frac{c_p}{c_v}$ is also constant.

2. The Prandtl number $Pr = \mu c_p/k$ is constant throughout the flow at a given value not necessarily unity.

3. The coefficient of thermal conductivity is computed from

$$k = \frac{\mu c_p}{Pr} \tag{11}$$

4. Dissociation and ionization effects are not present in the flow.

5. Stokes' relationship between the first and second viscosity coefficients is valid.

6. There is no external heat addition.

7. The body forces are negligible.

8. There are no chemical reactions and radiation heat flux.

From the above assumptions, it can be seen that the real gas effects associated with high Mach number and high temperature flows are neglected. However, for comparison with wind tunnel data, the calculated impact pressures are corrected for real gas effects by using the caloric imperfection charts in NACA Report 1135.

Conservative Form

In order to process the discontinuities in the flow field correctly, the conservative form of the governing equations is required. This conservative form was initially used by Courant and Friedrichs (Ref 99) for inviscid, compressible flow. Later Lax (Ref 100) applied this form to a finite-difference scheme. Gary (Ref 101) and Abbett (Ref 102) showed that using the non-conservative equations produced significant errors in shock speed and location, while Longley (Ref 103) showed that the conservative form yielded the correct shock speed for a variety of finite-difference schemes.

When the governing differential equations are placed in conservative form, the independent variables become ρ, ρu, ρv, ρw, and ρe. The use of these variables in conservative finite-difference schemes assures the conservation of mass, momentum, and energy across a shock wave. This can be easily demonstrated by considering a stationary normal shock wave. The truncation error of a finite-difference scheme depends on the size of the higher derivatives in the Taylor series expansions for the differentials. In the variables ρ, u, v, w, and T, the shock causes discontinuities in the continuum solution, but the solution is continuous in several of the conservative variables. Since Rankine-Hugoniot relations for normal shocks are based on global conservation of fluid properties, these equations are independent of the details within the shock structure. As a result, the conservative finite-difference techniques applied to the governing equations satisfy the Rankine-Hugoniot relations and thus predict the correct shock conditions across a shock.

The continuity equation is already in conservative form. The conservative form of the momentum equations may be derived by adding the term $u_i \left[\frac{\partial \rho}{\partial t} + \frac{\partial (\rho u_i)}{\partial x_i} \right]$ to the Navier-Stokes equations. Thus, the conservative momentum equations become

$$\frac{\partial (\rho u_i)}{\partial t} + \frac{\partial}{\partial x_j} (\rho u_i u_j + p\, \delta_{ij} - \tau_{ij}) = 0 \tag{12}$$

The energy equation can be put in conservative form by adding the term $e \left[\frac{\partial \rho}{\partial t} + \frac{\partial (\rho u_i)}{\partial x_i} \right]$ to the energy equation. Thus the conservative form of the energy equation becomes

$$\frac{\partial (\rho e)}{\partial t} + \frac{\partial}{\partial x_j} (\rho e u_j + p u_j - u_i \tau_{ij} + \dot{q}_j) = 0 \tag{13}$$

If we put the conservative equations in matrix form, then the governing equations become

$$\frac{\partial \bar{U}}{\partial t} + \frac{\partial \bar{E}}{\partial x} + \frac{\partial \bar{F}}{\partial y} + \frac{\partial \bar{G}}{\partial z} = 0 \tag{14}$$

where

$$\bar{U} = \left| \begin{matrix} \rho \\ \rho u \\ \rho v \\ \rho w \\ \rho e \end{matrix} \right| \qquad \bar{E} = \left| \begin{matrix} \rho u \\ \rho u^2 - \tau_{xx} + p \\ \rho u v - \tau_{xy} \\ \rho u w - \tau_{xz} \\ (\rho e - \tau_{xx} + p)\, u - \tau_{xy} v - \tau_{xz} w \\ + \dot{q}_x \end{matrix} \right|$$

$$\bar{F} = \begin{vmatrix} \rho v \\ \rho uv - \tau_{xy} \\ \rho v^2 - \tau_{yy} + p \\ \rho vw - \tau_{yz} \\ (\rho e - \tau_{yy} + p)\,v - \tau_{xy}u - \tau_{yz}w \\ + \dot{q}_y \end{vmatrix} \tag{15}$$

$$\bar{G} = \begin{vmatrix} \rho w \\ \rho uw - \tau_{xz} \\ \rho vw - \tau_{yz} \\ \rho w^2 - \tau_{zz} + p \\ (\rho e - \tau_{zz} + p)w - \tau_{xz}u - \tau_{yz}v \\ + \dot{q}_z \end{vmatrix}$$

Conical Coordinates

The general transformation from the physical plane (x, y, z) to the conical transformed plane (ζ, η, ξ) is given by

$$\begin{vmatrix} \zeta \\ \eta \\ \xi \end{vmatrix} = \begin{vmatrix} \zeta(r) \\ \eta(\frac{y}{x},\frac{z}{x}) \\ \xi(\frac{y}{x},\frac{z}{x}) \end{vmatrix} \tag{16}$$

where

$$r = \sqrt{x^2 + y^2 + z^2}$$

Assuming that an inverse exist, then

$$\begin{vmatrix} x \\ y \\ z \end{vmatrix} = \begin{vmatrix} x(\zeta,\eta,\xi) \\ y(\zeta,\eta,\xi) \\ z(\zeta,\eta,\xi) \end{vmatrix} \tag{17}$$

Thus, the Jacobian determinant is given by

$$J(\zeta,\eta,\xi) = \begin{vmatrix} \frac{\partial x}{\partial \zeta} & \frac{\partial x}{\partial \eta} & \frac{\partial x}{\partial \xi} \\ \frac{\partial y}{\partial \zeta} & \frac{\partial y}{\partial \eta} & \frac{\partial y}{\partial \xi} \\ \frac{\partial z}{\partial \zeta} & \frac{\partial z}{\partial \eta} & \frac{\partial z}{\partial \xi} \end{vmatrix} . \tag{18}$$

It is important that the transformation equations define a mapping which establishes a one-to-one correspondence between each point in the physical plane to one and only one point in the transformed plane, and conversely. This condition is satisfied if (a) the transformation functions are continuously differentiable and (b) if the Jacobian of the transformation is nonsingular at each point. When these conditions occur, there is a sphere N_o about the point such that the inverse function exists for all x, y, z in N_o. Thus, the transformation is guaranteed in a local fashion only, and the functions in Eq 16 must be selected so that they possess desirable characteristics in the region of interest.

By applying the chain rule of differential calculus, the differential operators become

$$\begin{aligned} \left.\frac{\partial}{\partial x}\right|_{y,z} &= \frac{\partial \zeta}{\partial x}\frac{\partial}{\partial \zeta} + \frac{\partial \eta}{\partial x}\frac{\partial}{\partial \eta} + \frac{\partial \xi}{\partial x}\frac{\partial}{\partial \xi} \\ \left.\frac{\partial}{\partial y}\right|_{x,z} &= \frac{\partial \zeta}{\partial y}\frac{\partial}{\partial \zeta} + \frac{\partial \eta}{\partial y}\frac{\partial}{\partial \eta} + \frac{\partial \xi}{\partial y}\frac{\partial}{\partial \xi} \\ \left.\frac{\partial}{\partial z}\right|_{x,y} &= \frac{\partial \zeta}{\partial z}\frac{\partial}{\partial \zeta} + \frac{\partial \eta}{\partial z}\frac{\partial}{\partial \eta} + \frac{\partial \xi}{\partial z}\frac{\partial}{\partial \xi} \end{aligned} \tag{19}$$

A comprehensive set of transformed derivatives is given in Appendix A.

Once the transformed coordinates are generated for a given physical domain, the set of partial differential equations and their associated boundary conditions are transformed utilizing the relations given in

Appendix A. Substitution of the above differential operators into the conservative Cartesian equations transforms the governing equations into the (ζ,η,ξ) coordinate system. The resulting equations in weak conservation law form (Refs 104-105) are given as follows

$$\begin{aligned}\frac{\partial \bar{U}}{\partial t} &+ \frac{\partial}{\partial \eta}\left[\frac{\partial \eta}{\partial x}\,\bar{E} + \frac{\partial \eta}{\partial y}\,\bar{F} + \frac{\partial \eta}{\partial z}\,\bar{G}\right] \\ &+ \frac{\partial}{\partial \xi}\left[\frac{\partial \xi}{\partial x}\,\bar{E} + \frac{\partial \xi}{\partial y}\,\bar{F} + \frac{\partial \xi}{\partial z}\,\bar{G}\right] + \bar{H} = 0\end{aligned} \tag{20}$$

where

$$\begin{aligned}\bar{H} = &- \frac{\partial}{\partial \eta}\left(\frac{\partial \eta}{\partial x}\right)\bar{E} - \frac{\partial}{\partial \eta}\left(\frac{\partial \eta}{\partial y}\right)\bar{F} - \frac{\partial}{\partial \eta}\left(\frac{\partial \eta}{\partial z}\right)\bar{G} \\ &- \frac{\partial}{\partial \xi}\left(\frac{\partial \xi}{\partial x}\right)\bar{E} - \frac{\partial}{\partial \xi}\left(\frac{\partial \xi}{\partial y}\right)\bar{F} - \frac{\partial}{\partial \xi}\left(\frac{\partial \xi}{\partial z}\right)\bar{G} \\ &+ \frac{\partial \zeta}{\partial x}\,\frac{\partial \bar{E}}{\partial \zeta} + \frac{\partial \zeta}{\partial y}\,\frac{\partial \bar{F}}{\partial \zeta} + \frac{\partial \zeta}{\partial z}\,\frac{\partial \bar{G}}{\partial \zeta}\end{aligned} \tag{21}$$

Conical Approximation

The definition for supersonic conical flow, given by Liepmann and Roshko (Ref 106), is one in which the fluid properties are invariant along each ray emanating from a vertex. An essential element which follows from this definition is that conical flow problems do not involve a characteristic length. A body is called conical if its surface is made up of rays from a vertex. Boundary conditions are conical if the boundary values of the fluid properties are constant along rays from an origin. All natural features of the flow field are conical such as embedded shocks, bow shocks, and contact surfaces.

The basic theorem of conical flow is "a flow field is conical if the boundary conditions are conical." This fundamental theorem applies to linearized potential flows as well as compressible, inviscid flows. It does not hold, however, for viscous fluids. The theorem can be demonstrated quite easily by applying dimensional analysis. Since a conical boundary does not contain a characteristic length, then it can be shown that no combination of fluid properties given at infinity can be constructed to give a dimension of length. This is not true, if viscosity is considered since $\left[{}^{\nu}/_{u}\right] = \left[\,L\cdot\,\right]$. Thus, the boundary layer over a delta wing is a function of the distance from the vertex.

In this investigation, a conical approximation is applied to the governing equations. It is assumed that the viscous region thickness is much smaller than the length scale L of the wing. The leading edge of the delta wing is assumed to be sharp and the boundary layer is laminar and attached at the leading edge (see Fig 7). Since the viscosity effect in the boundary layer introduces a length scale, which appears only in the Reynolds number and radial derivatives, then at large Reynolds numbers, the gradients in the radial direction are much smaller than those in the cross flow directions (θ,ϕ). Hence,

$$\begin{aligned} \frac{\partial}{\partial r} &<< \frac{1}{r}\frac{\partial}{\partial\theta} \\ \frac{\partial}{\partial r} &<< \frac{1}{r}\frac{\partial}{\partial\phi} \end{aligned} \tag{22}$$

This is the mathematical definition of a locally conical flow. Gradients do exist in the radial direction, but they are sufficiently small to be neglected. When this requirement is imposed on the generalized transformed coordinates, it becomes

$$\begin{aligned} \frac{\partial}{\partial\zeta} &<< \frac{\partial}{\partial\eta} \\ \frac{\partial}{\partial\zeta} &<< \frac{\partial}{\partial\xi} \end{aligned} \tag{23}$$

Thus, the flow properties ρ, u, v, w, p, and T are approximately invariant along rays of constant $\zeta(r)$. However, it should be noted that the Reynolds number is a function of ζ and therefore a characteristic

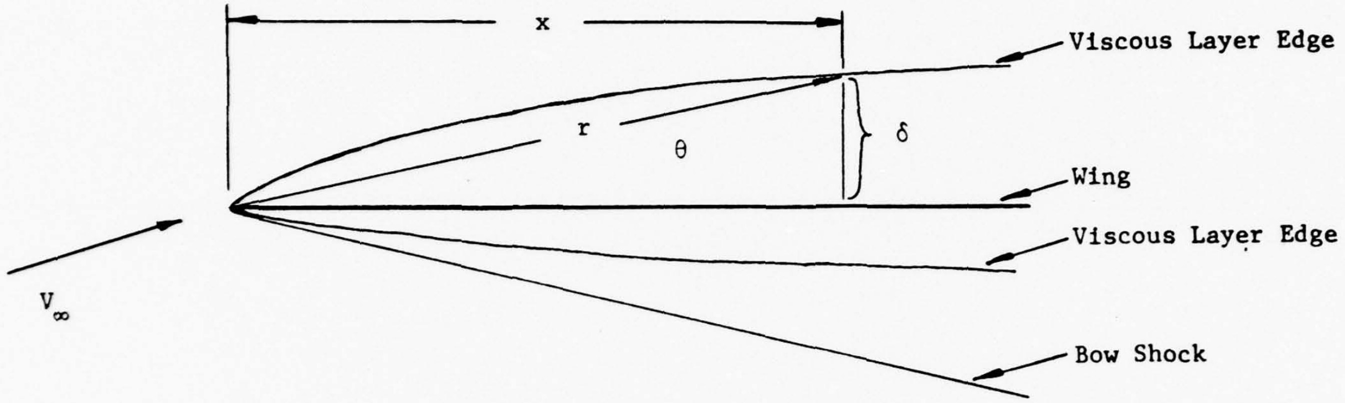
x
Viscous Layer Edge
r
θ
δ
Wing
Viscous Layer Edge
V_∞
Bow Shock

Fig. 7. Physical Implications of the Conical Flow Assumptions on the Boundary Layer of a Flat Delta Wing.

length must be included in the computation.

Anderson (Ref 107) was the first to introduce this conical approximation and McRae (Ref 94) later demonstrated it in his calculations of supersonic, viscous flows over a cone. From experimental data by Cross (Ref 18) and from discussions with Barber (Ref 31), it was found that the viscous layer is laminar and approximately conical under certain hypersonic flow conditions. For high Reynolds number supersonic flow, the boundary layer is so thin that its effect on the total flow field is minimal. Thus, a locally conical flow approximation for the viscous-inviscid flow field over a delta wing is adequate to model the test cases being considered.

Nondimensionalization

Before numerically solving the resulting governing equations, it is advantageous to write these equations and other relationships in nondimensional form. The pressure and density are made dimensionless with respect to free stream stagnation conditions while velocity and total energy are nondimensionalized with respect to the maximum adiabatic velocity

$$V_{MAX} = \sqrt{\frac{2\gamma}{\gamma-1} RT_o} \qquad (24)$$

The normalizing length scale L is the characteristic length used in determining the free stream Reynolds number.

The following nondimensional relationships are used in the governing equations:

$$
\begin{aligned}
&x' = \frac{x}{L} && y' = \frac{y}{L} && z' = \frac{z}{L} \\
&u' = \frac{u}{V_{MAX}} && v' = \frac{v}{V_{MAX}} && w' = \frac{w}{V_{MAX}} \\
&e' = \frac{e}{V_{MAX}^2} && p' = \frac{p}{p_o} && \rho' = \frac{\rho}{\rho_o} \\
&t' = \frac{t}{L/V_{MAX}} && T' = \frac{T}{T_o} && \tau' = \frac{\tau}{\rho_o V_{MAX}^2}
\end{aligned}
\tag{25}
$$

where

$$\rho_o = \left(\frac{2\gamma}{\gamma-1}\right)\frac{P_o}{V_{MAX}^2} \tag{26}$$

and where the subscript "o" refers to free stream isentropic total conditions.

We also define a reference Reynolds number as

$$Re = \frac{\rho_o V_{MAX} L}{\mu} \tag{27}$$

and a Prandtl number as

$$Pr = \frac{\mu c_p}{k} \tag{28}$$

If we drop the prime notation with the understanding that all quantities are nondimensional values unless otherwise indicated, then the final form of the governing equation is

$$\frac{\partial U}{\partial t} + \frac{\partial F}{\partial \eta} + \frac{\partial G}{\partial \xi} + H = 0 \tag{29}$$

where

$$
\begin{aligned}
U &= \bar{U} \\
F &= \frac{\partial \eta}{\partial x}\bar{E} + \frac{\partial \eta}{\partial y}\bar{F} + \frac{\partial \eta}{\partial z}\bar{G} \\
G &= \frac{\partial \xi}{\partial x}\bar{E} + \frac{\partial \xi}{\partial y}\bar{F} + \frac{\partial \xi}{\partial z}\bar{G} \\
H &= \bar{H}
\end{aligned}
\tag{30}
$$

The nondimensionalized heat flux and stress terms are

$$\tau_{xx} = -\varepsilon p - \bar{\Phi} + \frac{2}{Re}\left[\frac{\partial\eta}{\partial x}\frac{\partial u}{\partial\eta} + \frac{\partial\xi}{\partial x}\frac{\partial u}{\partial\xi}\right] \tag{31}$$

$$\tau_{yy} = -\varepsilon p - \bar{\Phi} + \frac{2}{Re}\left[\frac{\partial\eta}{\partial y}\frac{\partial v}{\partial\eta} + \frac{\partial\xi}{\partial y}\frac{\partial v}{\partial\xi}\right] \tag{32}$$

$$\tau_{zz} = -\varepsilon p - \bar{\Phi} + \frac{2}{Re}\left[\frac{\partial\eta}{\partial z}\frac{\partial w}{\partial\eta} + \frac{\partial\xi}{\partial z}\frac{\partial w}{\partial\xi}\right] \tag{33}$$

$$\tau_{xy} = \frac{1}{Re}\left[\frac{\partial\eta}{\partial y}\frac{\partial u}{\partial\eta} + \frac{\partial\xi}{\partial y}\frac{\partial u}{\partial\xi} + \frac{\partial\eta}{\partial x}\frac{\partial v}{\partial\eta} + \frac{\partial\xi}{\partial x}\frac{\partial v}{\partial\xi}\right] \tag{34}$$

$$\tau_{yz} = \frac{1}{Re}\left[\frac{\partial\eta}{\partial z}\frac{\partial v}{\partial\eta} + \frac{\partial\xi}{\partial z}\frac{\partial v}{\partial\xi} + \frac{\partial\eta}{\partial y}\frac{\partial w}{\partial\eta} + \frac{\partial\xi}{\partial y}\frac{\partial w}{\partial\xi}\right] \tag{35}$$

$$\tau_{xz} = \frac{1}{Re}\left[\frac{\partial\eta}{\partial x}\frac{\partial w}{\partial\eta} + \frac{\partial\xi}{\partial x}\frac{\partial w}{\partial\xi} + \frac{\partial\eta}{\partial z}\frac{\partial u}{\partial\eta} + \frac{\partial\xi}{\partial z}\frac{\partial u}{\partial\xi}\right] \tag{36}$$

$$\dot{q}_x = -\frac{1}{N}\left[\frac{\partial\eta}{\partial x}\frac{\partial T}{\partial\eta} + \frac{\partial\xi}{\partial x}\frac{\partial T}{\partial\xi}\right] \tag{37}$$

$$\dot{q}_y = -\frac{1}{N}\left[\frac{\partial\eta}{\partial y}\frac{\partial T}{\partial\eta} + \frac{\partial\xi}{\partial y}\frac{\partial T}{\partial\xi}\right] \tag{38}$$

$$\dot{q}_z = -\frac{1}{N}\left[\frac{\partial\eta}{\partial z}\frac{\partial T}{\partial\eta} + \frac{\partial\xi}{\partial z}\frac{\partial T}{\partial\xi}\right] \tag{39}$$

where

$$\begin{aligned}\bar{\Phi} = \frac{2}{3Re}\Bigg[&\frac{\partial\eta}{\partial x}\frac{\partial u}{\partial\eta} + \frac{\partial\xi}{\partial x}\frac{\partial u}{\partial\xi} + \frac{\partial\eta}{\partial y}\frac{\partial v}{\partial\eta} \\ &+ \frac{\partial\xi}{\partial y}\frac{\partial v}{\partial\xi} + \frac{\partial\eta}{\partial z}\frac{\partial w}{\partial\eta} + \frac{\partial\xi}{\partial z}\frac{\partial w}{\partial\xi}\Bigg]\end{aligned} \tag{40}$$

$$\varepsilon = \frac{\gamma-1}{2\gamma} \tag{41}$$

$$N = 2\,Pr\,Re \tag{42}$$

The normalized equation of state becomes

$$P = \rho T \tag{43}$$

and the nondimensional form of the Sutherland viscosity formula is

$$\mu = T^{3/2}\left[\frac{1 + C_1}{T + C_1}\right] \tag{44}$$

where

$$C_1 = {}^{C_o}/T_o \tag{45}$$

Coordinate Transformations

Although this problem is developed for generalized conical coordinate transformations, only two specific coordinate transformations are used. These include a cylindrical-type coordinate transformation for flow over a cone and a conical coordinate transformation for flow over a delta wing.

For the flow field calculations over a cone, the coordinate transformation is

$$\zeta = x \qquad \eta = \tan^{-1}\left(\frac{z}{y}\right) \qquad \xi = \frac{\sqrt{y^2 + z^2}}{x} - \tan\theta_c \tag{46}$$

The physical and computational planes are shown in Figures 8a and 8b, respectively. The transformation derivatives, which are used in the calculations, are developed in Appendix A.

For the flow field around a thin, planar delta wing, a constant spaced grid is used in the physical plane. The conical coordinate transformation is

$$\zeta = x \qquad \eta = \frac{y}{x} \qquad \xi = \frac{z}{x} \tag{47}$$

where the physical and computational domains are depicted in Figures 9a and 9b, respectively. The transformation derivatives are given in Appendix A.

These coordinate transformations and their derivatives are applied to the conical governing equations for a compressible, laminar, viscous flow. The equations are solved by a numerical finite-difference procedure which is discussed in the next chapter.

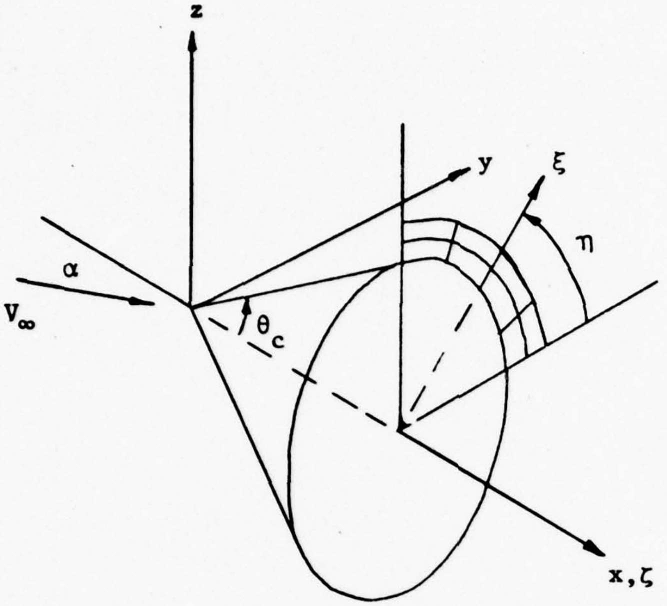
z
y
ξ
η
α
V∞
θc
x,ζ

Fig. 8a. Physical Domain of Cone.

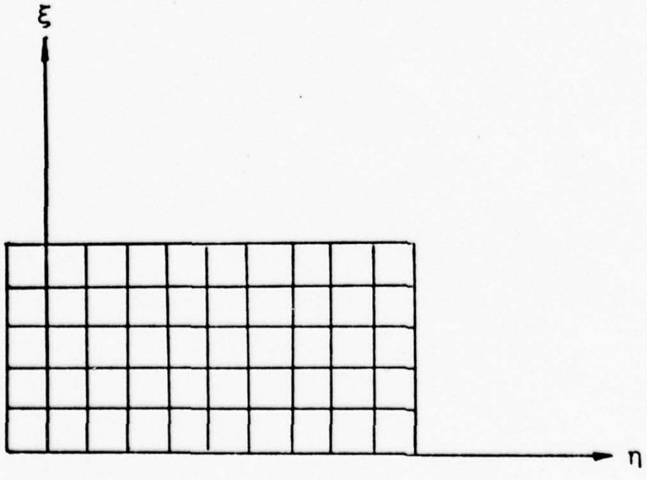

Fig. 8b. Computational Domain of Cone.

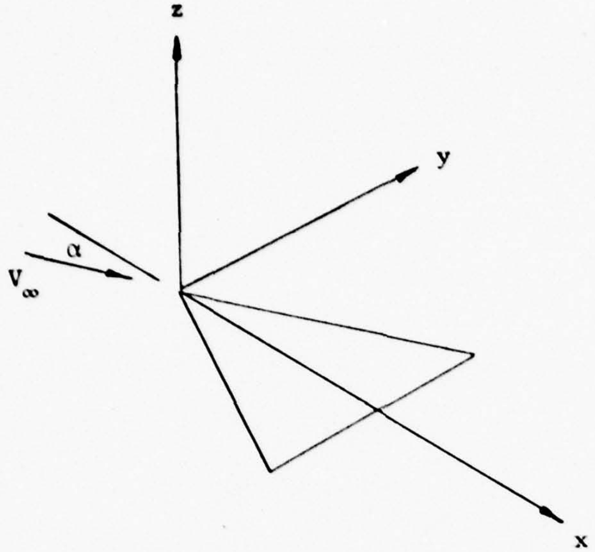
z
y
x
α
V_∞

Fig. 9a. Physical Domain of Delta Wing.

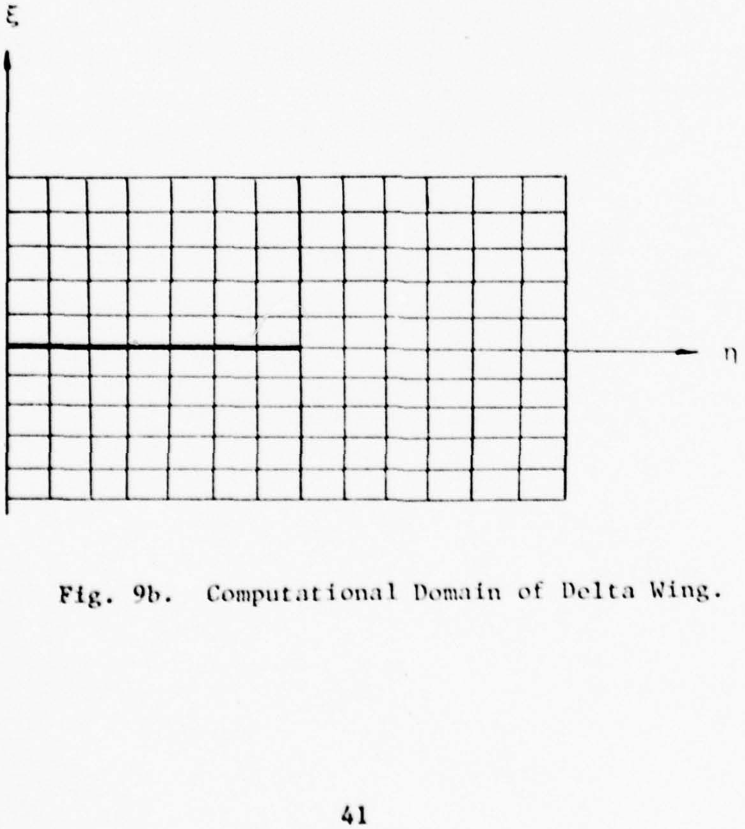

Fig. 9b. Computational Domain of Delta Wing.

III. Numerical Methods

In this chapter, several basic concepts of numerical methods are discussed for solving time-dependent, multi-shock flow field problems. The MacCormack finite-difference scheme is examined and then applied to the fundamental governing equations. Several numerical models are used to represent the initial and boundary conditions. The requirements of stability, consistency, and convergence are derived and discussed for solving the resulting numerical equations.

Basic Concepts

For this conical flow problem, the steady state solution is sought by numerically solving the unsteady flow equations. This steady state solution is determined when all the time derivative terms in the governing equations vanish in the limit of large times. Such a procedure for obtaining the steady state solution is sometimes referred to as the "asymptotic" method (Ref 108). This method was advocated by such early proponents as J. von Neumann and R. Richtmyer (Ref 109) because it represents the physical situation more naturally than the method of solving the steady state governing equations. The successive iterations needed to determine the "steady" state solution may be looked upon as the evolution of the flow field with time.

Under the conical flow approximation, the radial derivatives of the flow properties can be set equal to zero. This reduces the number of independent variables in the transformed plane to three, which include time and the two cross-flow spatial coordinates $\eta\left(\frac{y}{x},\frac{z}{x}\right)$ and $\xi\left(\frac{y}{x},\frac{z}{x}\right)$. This conical flow problem is then solved as an initial value problem. Initial conditions are specified at t=0 along with appropriate boundary conditions, and the solution is numerically integrated in time until steady state conditions are reached. Elimination of $\zeta(r)$ as one of the independent variables in the problem reduces the amount of storage space, numerical computation, and resulting computer time of the problem.

By applying finite-difference techniques, the partial differential operators in the governing equations are replaced by finite-difference quotients. This allows the governing equations to be approximately represented by a set of difference equations. Solutions to the difference equations are obtained at the intersection points of the computational grid lines. These nodal points (η_i, ξ_j) may be specified by a double subscript (i,j) and a superscript n, where n refers to times $t=n\Delta t$ and where Δt is the time step that the solution is advanced during each cycle. All the dependent variables at the nodal points are initially prescribed as free stream values and the unknown values at $t>0$ are calculated during numerical integration. Figure 10 illustrates the mesh of nodal points in the transformed plane.

There are several types of finite-difference quotients which may be used to represent the partial derivatives. An implicit difference quotient approximates the partial derivative at an advanced point in time and is written so that the dependent variable is expressed in terms of its neighboring values and known previous values. This implicit representation requires the solution of a set of simultaneous equations in order to calculate the dependent unknown as each time step is taken. The implicit form has the advantage of universal stability for $t>0$, however the method requires a more complicated computational procedure.

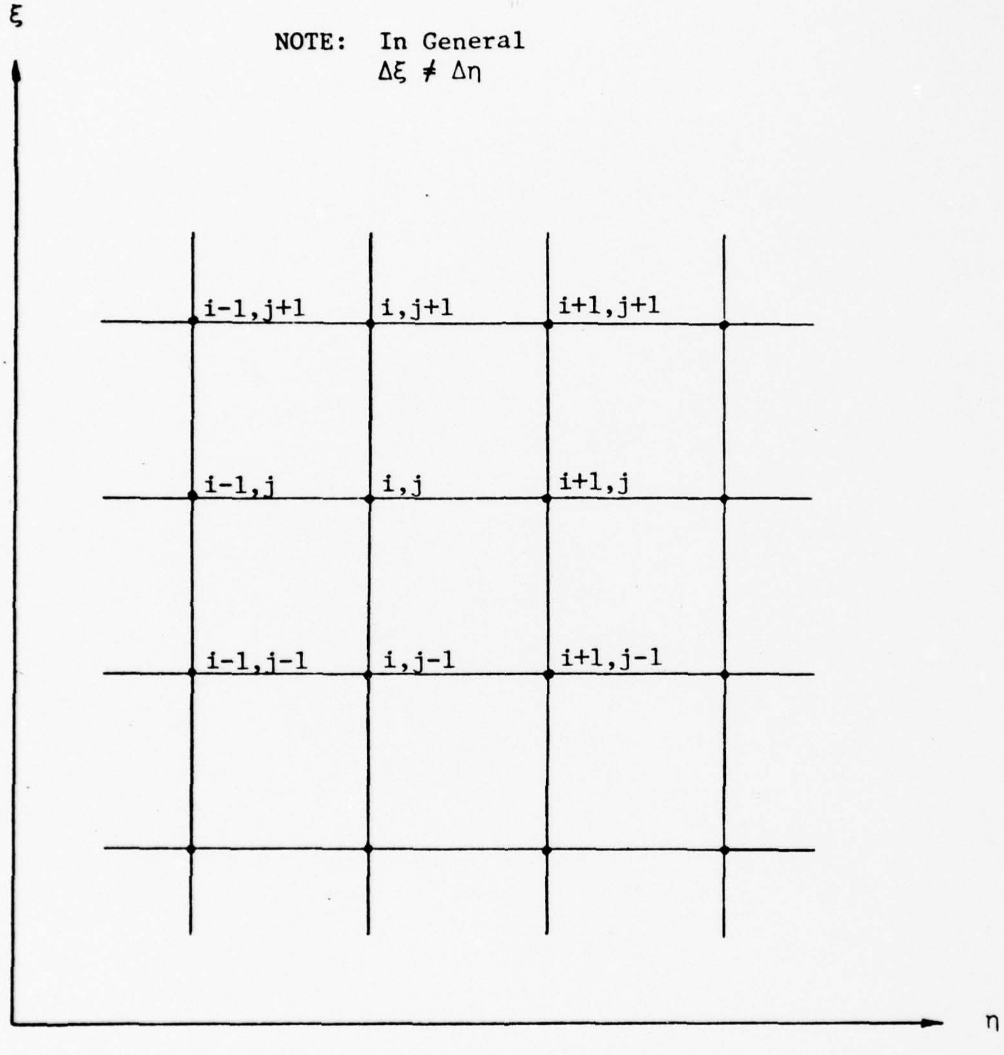
ξ
NOTE: In General
Δξ ≠ Δη
i-1,j+1
i,j+1
i+1,j+1
i-1,j
i,j
i+1,j
i-1,j-1
i,j-1
i+1,j-1
η

Fig. 10 System of Nodal Points Used in the Finite-Difference Method.

The explicit differential quotient represents a partial differential operator with only one unknown. The explicit form is solved directly (explicitly) in terms of known previous values and boundary conditions. As each step in time is taken, the unknown quantities are calculated one at a time. The explicit difference quotient has the advantage of programming simplicity, although there are stability restrictions on its use. Because of its successful application to compressible, viscous multiple shock flows, only the explicit finite-difference quotients are used in this investigation.

Two distinct approaches are used to compute multishock flow fields. One is referred to as a shock-fitted technique and the other as a shock-capturing method. For shock-fitting, the shock is transformed onto a coordinate surface and treated as a discontinuity. The values at the shock surface are determined by explicitly solving the Rankine-Hugoniot relations. Although it is conceptually possible to treat all shocks as discontinuities, this method involves complex logic to fit all the internal and bow shocks.

The shock-capturing technique is a method by which multiple shocks can be accurately determined numerically without knowing initially where the shocks will form. Shock waves are automatically allowed to form and decay without employing any special shock-fitting procedures which involve explicit use of the Rankine-Hugoniot equations. The shock-capturing technique requires that the governing equations be differenced in weak conservative form. Shocks which exist or do form are generally spread over 3 or 4 mesh intervals. Thus, a finer mesh interval is required in order to specify the shock location. This method also has a tendency to give spurious fluctuations of flow field quantities in the vicinity of the shock. These fluctuations can be dampened by use of an artificial viscosity term. Unfortunately, additional shock smearing occurs. However, the results obtained by using this method have been shown to be quite accurate when compared to shock-fitting methods outside of the immediate shock location. Therefore, in this investigation shock-capturing techniques are used to compute the conical flow field around a delta wing.

Finite-Difference Scheme

The selection of the numerical shock-capturing algorithm involves considering such factors as accuracy, computational speed, storage requirements, and programming complexity. Unfortunately, there is no generally accepted optimal scheme, even when the order of the numerical approximation is specified. A survey of various first and second-order schemes by Kutler (Ref 110) shows that the highly dissipative nature of the first order accurate methods makes them generally unsuitable for shock-capturing calculations. Among the second-order schemes, the predictor-corrector combination by MacCormack was found to be the best. Anderson (Ref 111) compared the second-order MacCormack method with both the third-order Rusanov and Kutler-Lomax-Warming methods. He applied these numerical methods to a set of one-dimensional hyperbolic equations

$$\frac{\partial E}{\partial t} + \frac{\partial F}{\partial x} = 0 \tag{48}$$

where E and F are n-component vectors and x is an arbitrary direction. By utilizing von Neumann's stability analysis, the stability criterion for these equations was found to be

$$| \lambda | \leq 1 \tag{49}$$

where λ is the Courant number given by

$$\lambda = \sigma \frac{\Delta t}{\Delta x} \tag{50}$$

and σ represents the maximum eigenvalue of the Jacobian matrix $\frac{\partial F}{\partial E}$. Anderson discovered that the second-order MacCormack method gave acceptable results for most cases. For a Courant number of approximately one, the second-order MacCormack scheme provides the best results from among the examples tested. However, when the Courant number varies appreciably, third-order schemes provide better results. In certain critical flow regions, such as multiple shock flows in which shock waves of various strengths are located close together, the third-order schemes are capable of obtaining results where second-order methods would fail (Ref 112). Since these critical flow regions requiring third-order methods are not expected to be encountered in this study, MacCormack's method was selected for the numerical integration of he flow field.

The second-order MacCormack scheme is a non-centered, preferential, predictor-corrector algorithm (Ref 113) which has been used for a wide variety of flow calculations. The method is a variant of the two-step Lax-Wendroff method (Ref 114), but because of its non-centered nature, the dependent variables need not be evaluated at half-mesh intervals. When the MacCormack two-step explicit method is applied to the normalized conservative equations

$$\frac{\partial U}{\partial t} + \frac{\partial F}{\partial \eta} + \frac{\partial G}{\partial \xi} + H=0 \tag{51}$$

the following predictor-corrector equations result:

Predictor

$$\begin{aligned}\overline{U_{i,j}^{n+1}} = U_{i,j}^{n} - \frac{\Delta t}{\Delta\eta}\Big\{ & (1-\varepsilon_\eta)\, F_{i+1,j}^{n} - (1-2\varepsilon_\eta)\, F_{i,j}^{n} \\ & - \varepsilon_\eta\, F_{i-1,j}^{n} \Big\} - \frac{\Delta t}{\Delta\xi}\Big\{ (1-\varepsilon_\xi)\, G_{i,j+1}^{n} \\ & - (1-2\varepsilon_\xi)\, G_{i,j}^{n} - \varepsilon_\xi\, G_{i,j-1}^{n} \Big\} - \Delta t\, H_{i,j}^{n}\end{aligned} \tag{52}$$

Corrector

$$\begin{aligned}U_{i,j}^{n+1} = \frac{1}{2}\Big\{ & U_{i,j}^{n} + \overline{U_{i,j}^{n+1}} - \frac{\Delta t}{\Delta\eta}\Big[\varepsilon_\eta\, \overline{F_{i+1,j}^{n+1}} \\ & + (1-2\varepsilon_\eta)\, \overline{F_{i,j}^{n+1}} + (\varepsilon_\eta-1)\, \overline{F_{i-1,j}^{n+1}} \Big] \\ & - \frac{\Delta t}{\Delta\xi}\cdot\Big[\varepsilon_\xi\, \overline{G_{i,j+1}^{n+1}} + (1-2\varepsilon_\xi)\, \overline{G_{i,j}^{n+1}} \\ & + (\varepsilon_\xi-1)\, \overline{G_{i,j-1}^{n+1}} \Big] - \Delta t\, \overline{H_{i,j}^{n+1}} \Big\}\end{aligned} \tag{53}$$

where

$$\eta = i\Delta\eta \quad \xi = j\Delta\xi \quad t = n\Delta t \tag{54}$$

and

$$F_{i,j}^{n} = F(U_{i,j}^{n}) \quad \overline{F_{i,j}^{n+1}} = F(\overline{U_{i,j}^{n+1}}), \text{ etc} \tag{55}$$

This scheme permits four possible variations for replacing the time derivatives in the predictor and corrector steps:

$$\begin{aligned} \text{I:} &\quad \varepsilon_\eta = 0 \quad \varepsilon_\xi = 0 \\ \text{II:} &\quad \varepsilon_\eta = 1 \quad \varepsilon_\xi = 1 \\ \text{III:} &\quad \varepsilon_\eta = 0 \quad \varepsilon_\xi = 1 \\ \text{IV:} &\quad \varepsilon_\eta = 1 \quad \varepsilon_\xi = 0 \end{aligned} \tag{56}$$

Each version yields a slightly different result. For this reason, it is termed a preferential scheme. MacCormack (Ref 113) suggested that the four combinations be cyclically permuted in order to obtain the most unbiased result. However, it has been shown that for shocks which propagate away from a body surface in the computational plane, method I tends to yield the best results (Refs 110 and 115). Since the shocks in this flow field problem originate at the body surface, method I was used for the numerical integrations. Thus, the following predictor-corrector equations were used.

Predictor

$$U^{\overline{n+1}}_{i,j} = U^{n}_{i,j} - \frac{\Delta t}{\Delta \eta}\left\{ F^{n}_{i+1,j} - F^{n}_{i,j} \right\} - \frac{\Delta t}{\Delta \xi}\left\{ G^{n}_{i,j+1} - G^{n}_{i,j} \right\} - \Delta t \; H^{n}_{i,j} \tag{57}$$

Corrector

$$U^{n+1}_{i,j} = \frac{1}{2}\left\{ U^{n}_{i,j} + U^{\overline{n+1}}_{i,j} - \frac{\Delta t}{\Delta \eta}\left[F^{\overline{n+1}}_{i,j} - F^{\overline{n+1}}_{i-1,j} \right] - \frac{\Delta t}{\Delta \xi}\left[G^{\overline{n+1}}_{i,j} - G^{\overline{n+1}}_{i,j-1} \right] - \Delta t \; H^{\overline{n+1}}_{i,j} \right\} \tag{58}$$

In this version, forward differences are used in the predictor step to approximate $\frac{\partial F}{\partial \eta}$ and $\frac{\partial G}{\partial \xi}$ derivatives while backward differences are used for these terms in the corrector step. This method minimizes the post and precursor oscillations near the shock.

In order to evaluate the shear stress and heat flux terms appearing in the F and G matrices, backward differences are used in the predictor step and forward differences in the corrector step. A central difference operator is used for τ_{ij} and $\dot{q}_j$ in the H matrix. This differencing procedure results in a central difference approximation with second-order accuracy for all shear stress and heat flux terms (Ref 116). For example, if we consider the F matrix containing the velocity gradient $\frac{\partial u}{\partial \eta}$, then the predictor term is

$$\frac{\Delta t}{\Delta \eta} \left[F^n_{i+1,j} - F^n_{i,j} \right] \qquad (59)$$

and the velocity gradient terms can be written as

$$\frac{u^n_{i+1,j} - u^n_{i,j}}{\Delta \eta} \quad \text{for the } F^n_{i+1,j} \text{ term} \qquad (60)$$

and

$$\frac{u^n_{i,j} - u^n_{i-1,j}}{\Delta \eta} \quad \text{for the } F_{i,j} \text{ term} \qquad (61)$$

For the corrector term, we have

$$\frac{\Delta t}{\Delta \eta} \left[\overline{F^{n+1}_{i,j}} - \overline{F^{n+1}_{i-1,j}} \right] \qquad (62)$$

where the velocity gradient terms are

$$\frac{\overline{u^{n+1}_{i+1,j}} - \overline{u^{n+1}_{i,j}}}{\Delta \eta} \quad \text{for the } \overline{F^{n+1}_{i,j}} \text{ term} \qquad (63)$$

and

$$\frac{\overline{u^{n+1}_{i,j}} - \overline{u^{n+1}_{i-1,j}}}{\Delta \eta} \quad \text{for the } \overline{F^{n+1}_{i-1,j}} \text{ term} \qquad (64)$$

This results in a finite-difference quotient of second-order accuracy for the $\frac{\partial^2 u}{\partial \eta^2}$ derivative centered at (i,j).

When the cross derivative is calculated i.e., $\frac{\partial u}{\partial \xi}$ inside the F matrix, then the velocity gradient terms for the predictor are

$$\frac{u^{n}_{i+1,j+1} - u^{n}_{i+1,j-1}}{2\Delta\xi} \quad \text{for the } F^{n}_{i+1,j} \text{ term} \tag{65}$$

and

$$\frac{u^{n}_{i,j+1} - u^{n}_{i,j-1}}{2\Delta\xi} \quad \text{for the } F^{n}_{i,j} \text{ term} \tag{66}$$

and for the corrector

$$\frac{u^{\overline{n+1}}_{i,j+1} - u^{\overline{n+1}}_{i,j-1}}{2\Delta\xi} \quad \text{for the } F^{\overline{n+1}}_{i,j} \text{ term} \tag{67}$$

and

$$\frac{u^{\overline{n+1}}_{i-1,j+1} - u^{\overline{n+1}}_{i-1,j-1}}{2\Delta\xi} \quad \text{for the } F^{\overline{n+1}}_{i-1,j} \text{ term} \tag{68}$$

This approximation results in a finite-difference quotient of second-order accuracy for the derivative $\frac{\partial^2 u}{\partial\eta\partial\xi}$ centered at (i,j).

By using these finite-difference equations, the calculations are advanced in time from the initial conditions until the steady state solutions are achieved. At each time step of the integration process, it is necessary to calculate the vectors F, G, and H, which are functions of the dependent and independent flow variables. The dependent normalized flow variables are obtained at each interior grid point by decoding the U vector

$$U = \left|\begin{matrix} U_1 \\ U_2 \\ U_3 \\ U_4 \\ U_5 \end{matrix}\right| = \left|\begin{matrix} \rho \\ \rho u \\ \rho v \\ \rho w \\ \rho e \end{matrix}\right| \tag{69}$$

In this decoding procedure, the primitive flow variables are solved for in the following manner

$$\begin{aligned} \rho &= U_1 \\ u &= U_2/U_1 \\ v &= U_3/U_1 \\ w &= U_4/U_1 \\ e &= U_5/U_1 \\ P &= 2\gamma\rho\,(e - \frac{u^2 + v^2 + w^2}{2}) \\ T &= \frac{P}{\rho} \end{aligned} \tag{70}$$

After the decoding, the boundary conditions are determined on the body surface and at the plane of symmetry. Thus, with the free stream and boundary conditions as the initial starting solution, Eq 51 is integrated with respect to time and the flow variables are advanced from $t=t^n$ to $t=t^n + \Delta t$. If the flow variables in the $t=t^n$ plane and the $t=t^n + \Delta t$ plane do not satisfy the convergence criteria, then the computed flow variables at $t=t^n + \Delta t$ are transferred to the $t=t^n$ plane and become the new starting solution. This iteration process is continued until there is little change between the flow variables at $t=t^n + \Delta t$ for two subsequent cycles. At this point, the solution is assumed to have converged. The following inequality is used as the termination criteria

$$\left|\frac{\phi^n_{i,j} - \phi^{n+1}_{i,j}}{\phi_r}\right| \le \bar{\varepsilon} \tag{71}$$

for $1 \le i \le i_{max}$ and $1 \le j \le j_{max}$, where $\phi^n_{i,j}$ represents each primitive variable at $t=t^n$, ϕ_r is a constant, and $\bar{\varepsilon}$ is the convergence criteria (typically 10^{-5}). Further discussions on the concept of iterative convergence and the determination of iteration errors can be found in Appendix B.

Boundary Conditions

An important aspect in the successful application of the MacCormack finite-difference method is the proper treatment of the boundary conditions. There are numerous schemes available for simulating the various types of physical boundaries encountered in a fluid flow problem (Refs 102, 117, 118). However, there is no rigorous mathematical theory concerning which numerical boundary conditions to select in order to get a unique solution. Thus, one must examine the physical flow field situation and take into account the mathematical nature of the governing equations in order to select which numerical boundary conditions to apply.

In this investigation, there are four types of boundary conditions which require numerical modeling. These are:

1. Body Surface
2. Symmetry Plane
3. Free Stream Boundaries
4. Singularity Points

The finite-difference equations used to describe these boundary conditions are developed in the following subsections.

Body Surface Boundary Conditions.

On the surface of the delta wing and the cone, the boundary conditions are

$$u = v = w = 0 \tag{72}$$

and

$$T = T_{wall} \quad \text{or} \quad \frac{\partial T}{\partial \xi} = 0 \tag{73}$$

Equation 72 guarantees that the velocity component tangent to the surface satisfies the viscous no-slip conditions and that the velocity component normal to the body surface is zero. The thermal conditions on the surface are either isothermal or adiabatic, as indicated by Eq 73. The isothermal boundary condition requires that a temperature be specified at the surface nodal points. The adiabatic boundary condition requires that a first or second-order, one-sided, finite-difference term be used to model the zero temperature derivative. In this investigation, all surfaces are isothermal.

The surface pressure or density cannot be obtained from the boundary conditions, and thus must be calculated. There are several methods for calculating the surface pressure or density; however, only two methods seem preferable. Either the continuity equation must be satisfied, for which an iteration for the density at the body surface is accomplished, or the normal momentum equation must be satisfied for the component of the pressure gradient normal to the surface.

The first technique consists of calculating the density at the surface from the continuity equation

$$\left.\frac{\partial\rho}{\partial t}\right|_{wall} = -\rho\frac{\partial\xi}{\partial x}\frac{\partial u}{\partial\xi} - \rho\frac{\partial\xi}{\partial y}\frac{\partial v}{\partial\xi} - \rho\frac{\partial\xi}{\partial z}\frac{\partial w}{\partial\xi} \qquad (74)$$

where the velocity and the gradients parallel to the surface are zero. This method has the advantage of being simple and convenient when using suitable second-order one-sided difference quotients for the spatial derivatives and a first-order forward time difference quotient for $\frac{\partial\rho}{\partial t}$. However, this technique may lead to divergence of the numerical results for $t\to\infty$. This is particularly true for separated flows and flows near a leading edge.

The second method, which is used in this study, consists of evaluating the pressure gradients normal to the surface by applying the ξ-momentum equation at the surface. The equation for p_ξ is

$$
\begin{aligned}
\frac{\partial p}{\partial \xi} = Q = &-\frac{2}{3\varepsilon}\frac{\partial}{\partial \xi}\left(\frac{1}{Re}\right)\left[\frac{\partial \xi}{\partial x}\frac{\partial u}{\partial \xi} + \frac{\partial \xi}{\partial y}\frac{\partial v}{\partial \xi} + \frac{\partial \xi}{\partial z}\frac{\partial w}{\partial \xi}\right] \\
&+ \frac{2}{3\varepsilon}\left(\frac{1}{Re}\right)\left[\frac{\partial \eta}{\partial x}\frac{\partial^2 u}{\partial \xi \partial \eta} + \frac{\partial}{\partial \xi}\left(\frac{\partial \xi}{\partial x}\right)\frac{\partial u}{\partial \xi} + \frac{\partial \xi}{\partial x}\frac{\partial^2 u}{\partial \xi}\right. \\
&+ \frac{\partial \eta}{\partial y}\frac{\partial^2 v}{\partial \xi \partial \eta} + \frac{\partial}{\partial \xi}\left(\frac{\partial \xi}{\partial y}\right)\frac{\partial v}{\partial \xi} + \frac{\partial \xi}{\partial y}\frac{\partial^2 v}{\partial \xi^2} + \frac{\partial \eta}{\partial z}\frac{\partial^2 w}{\partial \xi \partial \eta} \qquad (75) \\
&\left. + \frac{\partial}{\partial \xi}\left(\frac{\partial \xi}{\partial z}\right)\frac{\partial w}{\partial \xi} + \frac{\partial \xi}{\partial z}\frac{\partial^2 w}{\partial \xi^2}\right] - \frac{2}{\varepsilon}\frac{\partial}{\partial \xi}\left(\frac{1}{Re}\right)\frac{\partial \xi}{\partial z}\frac{\partial w}{\partial \xi} \\
&- \frac{2}{\varepsilon}\left(\frac{1}{Re}\right)\left[\frac{\partial \eta}{\partial z}\frac{\partial^2 w}{\partial \xi \partial \eta} + \frac{\partial}{\partial \xi}\left(\frac{\partial \xi}{\partial z}\right)\frac{\partial w}{\partial \xi} + \frac{\partial \xi}{\partial z}\frac{\partial^2 w}{\partial \xi^2}\right] \\
&- \frac{1}{\varepsilon}\left(\frac{1}{\partial \xi / \partial z}\right)\left[\frac{\partial \eta}{\partial x}\frac{\partial}{\partial \eta}\left(\tau_{xz}\right) + \frac{\partial \eta}{\partial y}\frac{\partial}{\partial \eta}\left(\tau_{yz}\right)\right. \\
&\left. + \frac{\partial \eta}{\partial z}\frac{\partial}{\partial \eta}\left(\tau_{zz}\right) + \frac{\partial \xi}{\partial x}\frac{\partial}{\partial \xi}\left(\tau_{xz}\right) + \frac{\partial \xi}{\partial y}\frac{\partial}{\partial \xi}\left(\tau_{yz}\right)\right] \\
&+ \frac{\partial \zeta}{\partial x}\frac{\partial}{\partial \zeta}\left(\tau_{xz}\right) + \frac{\partial \zeta}{\partial y}\frac{\partial}{\partial \zeta}\left(\tau_{yz}\right) + \frac{\partial \zeta}{\partial z}\frac{\partial}{\partial \zeta}\left(\tau_{zz}\right)
\end{aligned}
$$

This equation is numerically modeled by using a one-sided, second-order accurate finite-difference algorithm to calculate the surface points of interest. The surface pressure is calculated by

$$P^n_{i,j} = \frac{4}{3} P^n_{i,j\pm1} - \frac{1}{3} P^n_{i,j\pm2} + Q(u,v,w)\,\Delta\xi \qquad (76)$$

with $j = j_{wing}$ and $1 \leq i \leq i_{wing}$. The numerical representation, Q, of the stress terms in Eq 75 uses second-order central difference terms for those graidents not on the surface.

For the total delta wing, the same wing grid points model both the upper and lower transformed wing surfaces. When the MacCormack predictor and corrector terms are applied to the computational plane below the wing, the wing nodal points model the lower surface. When the integration is occurring above the wing, the wing modal points model the upper surface values. The leading edge is treated as a singularity point and is discussed in a later subsection.

For the cone, a simplier boundary condition is used to calculate the surface pressure. From boundary layer theory, we know that $Q \simeq 0$, thus the pressure gradient normal to the surface is zero and the pressure can be calculated by the finite-difference equation

$$P^n_{i,j} = \frac{4}{3} P^n_{i,j+1} - \frac{1}{3} P^n_{i,j+2} \tag{77}$$

For both bodies, the density at the surface is determined by applying the surface pressure and temperature in the equation of state.

Symmetry Boundary Conditions. A symmetry boundary condition exists in the transformed plane for both the delta wing and the cone, where

$$\frac{\partial u}{\partial \eta} = 0 \qquad v = 0 \quad \frac{\partial w}{\partial \eta} = 0 \tag{78}$$

$$\frac{\partial p}{\partial \eta} = 0 \qquad \frac{\partial T}{\partial \eta} = 0$$

The "reflection" method is used to calculate the primitive variables on the plane of symmetry. The finite-difference equations used for this reflection technique are

$$v_{i=1,j} = v_{i+1,j} \tag{79}$$

$$v_{i,j} = 0$$

and

$$\phi_{i-1,j} = \phi_{i+1,j} \tag{80}$$

where $i = 2$ and $\phi = u, w, p, \rho$, and e. The $i - 1$ column represents an additional column of grid points placed next to the plane of symmetry. This column of grid points causes the integration along the line of symmetry to perceive that a mirror image solution is evolving from the opposite side of the symmetry plane. This technique provides an accurate solution for the flow field qualities on the plane of symmetry with a minimal amount of computation.

Free Stream Boundary Conditions. The free stream boundary conditions are applied on the extremities of the computational domain. These conditions are applied under the assumption that the free stream or infinity boundaries completely encompass the disturbed flow region of the body. The flow through these boundaries must be supersonic with respect to the transformed coordinates. When this condition is satisfied, the variables at the exterior grid points can be set equal to the free stream conditions and held fixed during the entire integration process. These free stream conditions for uniform flow at an angle of attack are

$$u = \frac{V_\infty \cos\alpha}{V_{max}} = \left[\frac{\frac{\gamma-1}{2} M_\infty^2}{1 + \frac{\gamma-1}{2} M_\infty^2}\right]^{\frac{1}{2}} \cos\alpha \tag{81}$$

$$v = 0$$

$$w = \frac{V_\infty \sin\alpha}{V_{max}} = \left[\frac{\frac{\gamma-1}{2} M_\infty^2}{1 + \frac{\gamma-1}{2} M_\infty^2}\right]^{\frac{1}{2}} \sin\alpha \tag{83}$$

$$p = \frac{p_\infty}{p_o} = \left[1 + \frac{\gamma-1}{2} M_\infty^2\right]^{\frac{\gamma}{\gamma-1}} \tag{84}$$

$$\rho = \frac{\rho_\infty}{\rho_o} = \left[1 + \frac{\gamma-1}{2} M_\infty^2\right]^{\frac{1}{\gamma-1}} \tag{85}$$

$$e = \frac{1}{2\gamma}\frac{p}{\rho} + \frac{1}{2}\left(u^2 + v^2 + w^2\right) \tag{86}$$

where α is the angle of attack, M_∞ is the free stream Mach number, and V_{max} is the characteristic reference velocity.

Leading Edge Singularity. The leading edge singularity point requires special attention. The boundary conditions at this point are identical to the surface boundary conditions. However, numerical considerations require (Ref 119) that the properties at this singularity point be triple valued in the numerical computation.

The no-slip conditions and the isothermal conditions are applied at the leading edge. The pressure and density are triple valued at the point. The three values of pressure are denoted as upper, side, and lower values (P_u, P_s, and P_L) and are assumed to exist simultaneously at the leading edge. These values are calculated from the ξ and η momentum equations. The three values of density are determined from the equation of state.

Initial Conditions

To initiate the numerical integration, the flow field quantities at each grid point in the computational plane must be specified. It has been numerically shown that two-step finite-difference schemes may be unstable if these initial conditions differ greatly from the steady state solution (Refs 120 and 121). Since the stability of linear systems is not affected by the choice of initial conditions, then this phenomenon represents a nonlinear instability in the governing equations. As a result of this nonlinear instability, the MacCormack finite-difference scheme is not absolutely convergent. This means that for an arbitrary initial vector $X^{(o)}$, where X is an n-component vector, the vector sequence $X^{(k)}$ may not always converge. In fact, theorems which prescribe the sufficient conditions for convergence of nonlinear iterative methods (Ref 122) generally require that the initial vector $X^{(o)}$ closely approximate the presumed final solution, A, of the converged flow field. This "nearness" is usually expressed in terms of the vector norm $||X^{(o)} - A||$.

In this investigation, the initial starting conditions are specified at each interior grid point on the computational plane. These grid points are assigned values of the free stream conditions given by Eqs 81-86. The integration time step is determined from the von Neumann stability criteria as discussed in Appendix C.

The numerical integration is initiated by an "impulsive" start in which the body is instantaneously accelerated from rest to free stream conditions. The no-slip boundary conditions on the body surface creates either a compression or expansion wave that propagates into the flow field and eventually settles down as the solution converges. If the compression or expansion wave is strong, then numerical oscillations are created which may lead to program failure. However, by applying numerical damping through the addition of an artificial viscosity, these nonlinear instabilities can be sufficiently dampened so that a steady state solution can be achieved.

An alternative method was used when a series of angles of attack for the same flow conditions were investigated. The previous converged solution was used as the initial condition for the next angle of attack case. Convergence time was reduced by 10% using this method.

Stability Analysis

The numerical solution of the governing equations approximates the exact solution, if the finite-difference equations and their solutions satisfy the requirements of stability, consistency, and convergence. In this investigation, stability is directly associated with the size of the time step in the marching direction. The maximum time increment by which the numerical solution may be advanced at any time step is dependent on the spatial coordinate grid size, the location of the nodal grid points, and the solution itself. In order to examine the stability requirements of this finite-difference technique, a definition for stability is needed. Let $U(\eta,\xi,t)$ be the exact solution of the governing equations and let $\tilde{U}(i\Delta\eta,j\Delta\xi,n\Delta t)$ represent the finite-difference solution of the same equations. The error, E, of the finite-difference approximation is defined as $\left|\tilde{U}(i\Delta\eta,j\Delta\xi,n\Delta t) - U(\eta,\varepsilon,t)\right|$. The finite-difference equations are stable if the following two conditions are satisfied: (1) E remains bounded as $n\to\infty$ for a fixed $\Delta\eta$, $\Delta\xi$, and Δt and (2) E remains bounded as the mesh is refined (i.e., as Δt, $\Delta\eta$, and $\Delta\xi\to 0$) for a fixed value of $n\Delta t$. Thus, any finite-difference scheme which allows the growth of the numerical error E with time, eventually "destroys" the true solution of the equations and thus becomes unstable.

In this study, the maximum time step for numerical stability is determined by the Courant-Friedrichs-Lewy (CFL), the diffusion, and the mixed-derivative stability requirements. By applying a von Neumann stability analysis separately to the linearized inviscid, diffusion, and mixed derivative parts of the governing equations, a maximum time step is developed (Ref 123). This time step is

$$\Delta t = \frac{c}{\dfrac{1}{\Delta t_{INV}} + \dfrac{1}{\Delta t_{DF}} + \dfrac{1}{\Delta t_{MXD}}} \tag{87}$$

where c is an adjustable constant and Δt_{INV}, Δt_{DF}, and Δt_{MXD} are defined in Appendix C. A complete development of this stability criteria is given in Appendices C and D.

Several investigators (Refs 122-123), using the shock capturing method, have encountered numerical oscillations in the vicinity of strong shock waves. These nonlinear instabilities can be overcome by adding an artificial viscosity. In this study, two types of artificial viscosity terms are used to dampen oscillations. A normal stress damping term by McRae (Ref 94) is used for initial transients and a fourth-order damping term by MacCormack is used for shocks.

During program startup, large impulsive oscillations are developed near the body surface. These initial transients can be large enough to cause numerical instability. By applying a multiplier to the second coefficient of viscosity, these oscillations are effectively reduced. As the solution progresses in time, this multiplier is gradually reduced to its minimum value of one. This numerical damping technique adversely affects the maximum time step that can be used, as seen in Appendix C.

For numerical oscillations in the vicinity of strong pressure gradients, a fourth-order damping term, suggested by Tannehill et al (Ref 133), is adopted with modifications. Instead of using a rigorous transformation of the second-order derivatives of density into the transformed space, the second-order derivatives are approximated by the derivatives with respect to the transformed independent variables (η,ξ). The net results are two artificial viscosity-like terms of the form

$$D^{n}_{i,j} = \sum_{\ell=i,j} c_{\ell} \left(K_{\ell+1} \delta_{\ell} U^{n} - K_{\ell} \Delta_{\ell} U^{n} \right) \tag{88}$$

$$D^{\overline{n+1}}_{i,j} = \sum_{\ell=i,j} c_{\ell} \left(K^{\overline{n+1}}_{\ell} \delta_{\ell} U^{\overline{n+1}} - K^{\overline{n+1}}_{\ell-1} \Delta_{\ell} U^{\overline{n+1}} \right) \tag{89}$$

where the U's are defined by Eq 30, the summations on ℓ indicate one term for each of the two spatial directions (i,j), the c's are constant coefficients, the K's are variable coefficients defined by

$$K_i^n = \frac{\left|\rho_{i+1,j}^n - 2\rho_{i,j}^n + \rho_{i-1,j}\right|}{\left(\rho_{i+1,j}^n + 2\rho_{i,j}^n + \rho_{i-1,j}\right)} \tag{90}$$

$$K_j^n = \frac{\left|\rho_{i,j\;1}^n - 2\rho_{i,j}^n + \rho_{i,j-1}^n\right|}{\left(\rho_{i,j+1}^n + 2\rho_{i,j}^n + \rho_{i,j-1}^n\right)} \tag{91}$$

and the $\delta_\ell(\quad)$ and $\Delta_\ell(\quad)$ operators are forward and backward differences, respectively, defined by

$$\delta_i U^n = U_{i+1,j}^n - U_{i,j}^n \tag{92}$$

$$\Delta_i U^n = U_{i,j}^n - U_{i-1,j}^n \tag{93}$$

When smoothing is desired $D_{i,j}^n$ is added to Eq 57 on the predictor step and $D_{i,j}^{\overline{n+1}}$ is added inside the outer brackets of Eq 58 on the corrector step.

The variable K_ℓ coefficients are composed of a normalized second-order difference of flow field density. The K_ℓ subscript indicates which direction the difference is in (i or j) and also the center of the difference. The K_ℓ superscript indicates the time level used for the values of density. This variable coefficient is essentially zero in smooth regions of the flow field and approaches a maximum value of one in regions of large point-wise oscillations. The theoretical maximum value of the coefficient product $c_\ell K_\ell$ is less than or equal to 0.5 to prevent this term from causing an instability itself. The K_ℓ coefficients can theoretically reach a value of one, causing c_ℓ coefficients to be restricted to a value of one-half or less. However, since K_ℓ coefficients are usually much smaller than one, the c_ℓ coefficients can be larger than one-half. Smaller amounts of damping or damping in only one of the two spatial directions can also be used. This is achieved by independently setting the constant coefficients in each of the two directions equal to the appropriate values.

Consistency and Order of Accuracy

In order to examine the consistency and order of accuracy of a finite-difference scheme, it is necessary to understand what partial differential equation is, in fact, being solved by the finite-difference algorithm. This differential equation is called the modified equation and aside from the round-off error, actually represents the original partial differential equation when a numerical solution is computed. The modified equation is derived by first expanding each term of the finite-difference equation in a Taylor series and then eliminating time derivatives of higher than first-order (including mixed time and space derivatives) by the algebraic manipulations described by Warming and Hyett (Ref 124). The terms appearing in the modified equation which are not in the original partial differential equation represent a form of truncation error introduced by the finite-difference scheme. These error terms allow one to determine the order of accuracy and consistency of the finite-difference approximation.

If we examine the linearized form of the governing equation, we find that the modified equation is

$$\begin{aligned} &\frac{\partial U}{\partial t} + A\frac{\partial U}{\partial \eta} + B\frac{\partial U}{\partial \xi} + C\frac{\partial^2 U}{\partial \eta^2} + D\frac{\partial^2 U}{\partial \xi^2} \\ &+ E\frac{\partial}{\partial \eta}\left(\frac{\partial U}{\partial \xi}\right) + F\frac{\partial}{\partial \xi}\left(\frac{\partial U}{\partial \eta}\right) = \\ &\left(\frac{1}{2}A^3\Delta t^2 - \frac{1}{6}A\Delta_\eta^2\right)\frac{\partial^3 U}{\partial \eta^3} + \frac{3}{2}A^2B\Delta t^2\,\frac{\partial^3 U}{\partial \eta^2 \partial \xi} \\ &+ \frac{3}{2}AB^2\Delta t^2\,\frac{\partial^3 U}{\partial \eta \partial \xi^2} + \left(\frac{1}{2}B^3\Delta t^2 - \frac{1}{6}B\Delta\xi^2\right)\frac{\partial^3 U}{\partial \xi^3} + \cdots \end{aligned} \tag{94}$$

where the matrices A,B,C,D,E, and F are defined in Appendix C. The order of accuracy of the finite-difference scheme is defined by the lowest-order powers of the increments Δt, $\Delta \eta$, and $\Delta \xi$ appearing in the error terms. Thus, according to the modified equation, the MacCormack scheme is a second-order accurate algorithm for the linear governing equations. This definition of order of accuracy is consistent with that used by Richtmyer and Morton (Ref 109) in which truncation error is normally examined.

A finite-difference scheme is defined as consistent if the difference between the partial differential equation (with the initial and boundary conditions) and the finite-difference equation tends to zero as Δt, $\Delta \eta$, and $\Delta \xi$ approach zero in some arbitrarily stable manner. This implies that the error terms in the modified equation approach zero in the limit as Δt, $\Delta \eta$, and $\Delta \xi \rightarrow 0$. By examining Eq 94, it is obvious that for the MacCormack scheme, the finite-difference equation is consistent with the original partial differential equation. If by some special relationship the error terms did not tend to zero as the increments vanish, then the finite-difference scheme is said to be inconsistent. In this situation, the modified equation yields directly the differential equation with which the finite-difference scheme is consistent.

Convergence

In order to show equivalance between the finite-difference equations and the partial differential equations, it is necessary to demonstrate that the MacCormack scheme is convergent. Richtmyer and Morton (Ref 109) define a convergent finite-difference scheme as one in which the numerical solution approaches the solution of the partial differential equation as the step size approaches zero. The proof of convergence is particularly complex for the finite-difference scheme associated with the governing equations. This is especially true when boundary conditions are included in the analysis. Thus, in this investigation, only the linearized form of the governing equations is examined.

According to Lax's Equivalence Theorem for an initial value problem, a finite-difference solution converges to the exact solution if and only if 1) the differential problem is properly posed and therefore possesses a genuine solution, 2) the finite-difference equations are consistent, and 3) the numerical computation is stable. In this analysis, it is assumed that the initial value problem is properly posed. This implies that a solution of the governing equations exists, is unique, and depends continuously on the initial data. Therefore, by satisfying the criteria of Lax's Equivalence Theorem, it is assumed that the MacCormack second-order finite-difference algorithm is convergent for the governing equations.

The numerical analysis of the MacCormack method has been based on the mathematical theory of linear partial differential equations. By examining the linearized form of the governing equations, a heuristic assessment has been made of the MacCormack algorithm as applied to the governing equations. Although there is no guarantee that the linear and nonlinear characteristics of the finite-difference scheme are similar, there is ample evidence which tends to support this assumption. Thus, in the absence of a systematic analysis the numerical schemes associated with the governing equations, it is assumed that the above analysis will provide a practical insight into the characteristics of the MacCormack finite-difference scheme.

IV. Numerical Computation

In order to obtain a numerical solution for the supersonic and hypersonic flow around a delta wing, it is necessary to translate the finite-difference equations and the initial and boundary conditions into a computer code. The purpose of this chapter is to describe, in general terms, the basic structure and operation of the computer codes used in this investigation. These computer codes use the MacCormack finite-difference scheme to solve the conical, viscous governing equations. The input data, sequence of operations, and the calculated results of these codes are discussed in this chapter. A brief description of each subroutine used in the computer programs is given in Appendix E.

Computer Codes

Three basic computer codes are used in this study. These codes are the CONE, DELTA1, and DELTA computer programs. They are used to solve the flows over a circular cone, flat delta wing, and around a thin planar delta wing, respectively. The basic structure and operation of each of these programs are the same. The differences in these codes occur in how the boundary conditions are modeled and in what coordinate transformations are used. Because of the close similarity among the programs, only one code is described in this chapter. This is the DELTA computer program. Differences between the basic computer programs used in this study are highlighted in the description of the DELTA program.

DELTA

The computer code, DELTA, was written to solve the generalized conical governing equations numerically and to validate the conical approximation technique. With only minor changes in the input data and internal code structure, the code is designed to solve any problem which satisfies the conical flow approximation. The program is structured in a modular or subprogram form so that each module or subprogram can be coded and debugged separately. This procedure adds to the total computation time of the program but it minimizes the number of changes needed to solve various conical flow problems and it reduces the time required to debug the program. No major effort was made to reduce the running time or storage requirements of the computer program. The primary emphasis, in developing this code, was to keep the program as flexible and generalized as possible so that various changes in boundary conditions and coordinate transformations could be easily made. This code represents the first step towards development of a user-oriented code which can be used to solve a variety of conical, viscous flow field problems.

The DELTA program begins its calculation by initializing the grid points in the computational plane with free stream and boundary condition values. A constant time step is specified at the beginning of each run and a maximum number of iterations is given as part of the input data. The computer program is run until it reaches the maximum number of iterations or satisfies the convergence criteria. When either of these two conditions are reached, the calculations are terminated and the results are printed out and stored on magnetic tape. If an interim solution is stored on magnetic tape, then this solution is used as the initializing data for the next computer run and the calculations are continued. When the convergence criteria is finally satisfied, the numerical integration is terminated and the final results are printed out and stored on magnetic tape. These final results include:

1. The nondimensional scalar velocity components in the x, y, and z directions.

2. The normalized pressure, density and internal energy as defined in chapter 2.

3. The cross-flow Mach number, M_c, and the slope of the conical streamlines, γ_c, with respect to the η axis as given by

$$M_c = \left(\frac{\left[M_y\xi - M_z\eta\right]^2 + \left[M_z - M_x\xi\right]^2 + \left[M_x\eta - M_y\right]^2}{(1+\eta^2 + \xi^2)} \right)^{\frac{1}{2}} \tag{95}$$

$$\gamma_c = \tan^{-1} \left(\frac{M_x\xi - M_z}{M_x\eta - M_y} \right) \tag{96}$$

These quantities are calculated for each point in the computational plane.

No capability for interpolating between the computational grid nodes is provided in the program. Therefore, it is necessary to insure that a spatial grid point is specified at each location for which flow field data is required.

Sequence of Calculations

In order to initiate the numerical integration, the DELTA program is required to receive:

1. The free stream Mach number and angle of attack. The angle of attack is measured relative to the body coordinate system as shown in

Figures 8a. and 9a.

2. The sweep angle for the DELTA and DELTA1 programs and the cone half angle for the CONE program.

3. The free stream isentropic total temperature and the isothermal surface temperature, in degrees Rankine.

4. The free stream Reynolds number and a reference length. This reference length is defined as the distance from the vertex to the desired y-z plane.

5. The time step size and the maximum number of time step iterations.

6. The number of grid points on the body surface and in the computational plane. The location of these grid points is determined by inputing $\Delta\xi$ and by calculating $\Delta\eta$.

7. The appropriate coordinate transformation, as defined in Appendix A, and the grid location of the η-axis for the DELTA program.

8. The normal stress damping coefficients and the pressure damping coefficients.

Once the above input data is supplied, the DELTA program begins its calculations in the following order:

1. The computational grid points are initialized with free stream and boundary condition values or with an interim flow solution, whichever is appropriate.

2. The coordinate transformation derivatives are calculated next in the COORD subroutine.

3. At this point, the main program DO loop is entered for the repetitive calculation of all the flow field quantities at each time step until convergence or the maximum number of time step iterations is

reached.

4. Within this DO loop, the local Reynolds number is calculated for each grid point.

5. The predictor term of the MacCormack finite-difference scheme is calculated next by calling the subroutine PREDICT. In this subroutine, the surface boundary conditions are computed first by calling subroutine BOUND. After that, a double DO loop is entered wherein the following calculations are made for each grid point (i,j):

(a) The pressure damping terms ($D_{i,j}^{n}$) and ($D_{i,j}^{\overline{n+1}}$) are determined by calling the subroutines DAMPF and DAMPG.

(b) The subroutine VECTOR is called next to solve for the stress and heat conducting terms as well as determine the values of the F, G, and H vectors.

(c) The predicted value of the $U_{i,j}$ vector at the new time level is computed by calling subroutine DECODE.

(d) The subroutine SOLVE is used next to solve for the flow quantities from the calculated $U_{i,j}$ vector at the new time level.

6. The flow quantities on the opposite side of the symmetry plane are determined by calling subroutine SYM.

7. The local Reynolds number is recalculated with the flow quantities from the $U_{i,j}$ vector at the new time level.

8. The corrector term of the MacCormack finite-difference scheme is calculated next by calling subroutine CORRECT. This subroutine duplicates the predictor subroutine (5) except for some changes in the finite-difference representatives and flow quantity levels. The same subroutines and sequence of events are followed.

9. After the corrector step, the SYM subroutine is called to

AD-A056 513 AIR FORCE INST OF TECH WRIGHT-PATTERSON AFB OHIO SCH--ETC F/G 20/4
A NUMERICAL SOLUTION OF SUPERSONIC AND HYPERSONIC VISCOUS FLOW --ETC(U)
JUN 78 G S BLUFORD
UNCLASSIFIED AFIT/DS/AA/78S-1 NL

2 OF 3
AD
A056 513

recalculate the flow quantities on the opposite side of the symmetry plane.

10. The final step in the main DO loop is to test the new solution for convergence. If the new solution is not converged, the numerical integration process is begun again at step (4) until the convergence criteria is met or the maximum number of time steps is reached.

11. At the end of the numerical integration cycle, the flow field results are printed out and the interim or final solution is stored on magnetic tape.

The computational sequence of this code is shown in Figures 11 and 12. This program is repetitively run until a converged solution is obtained.

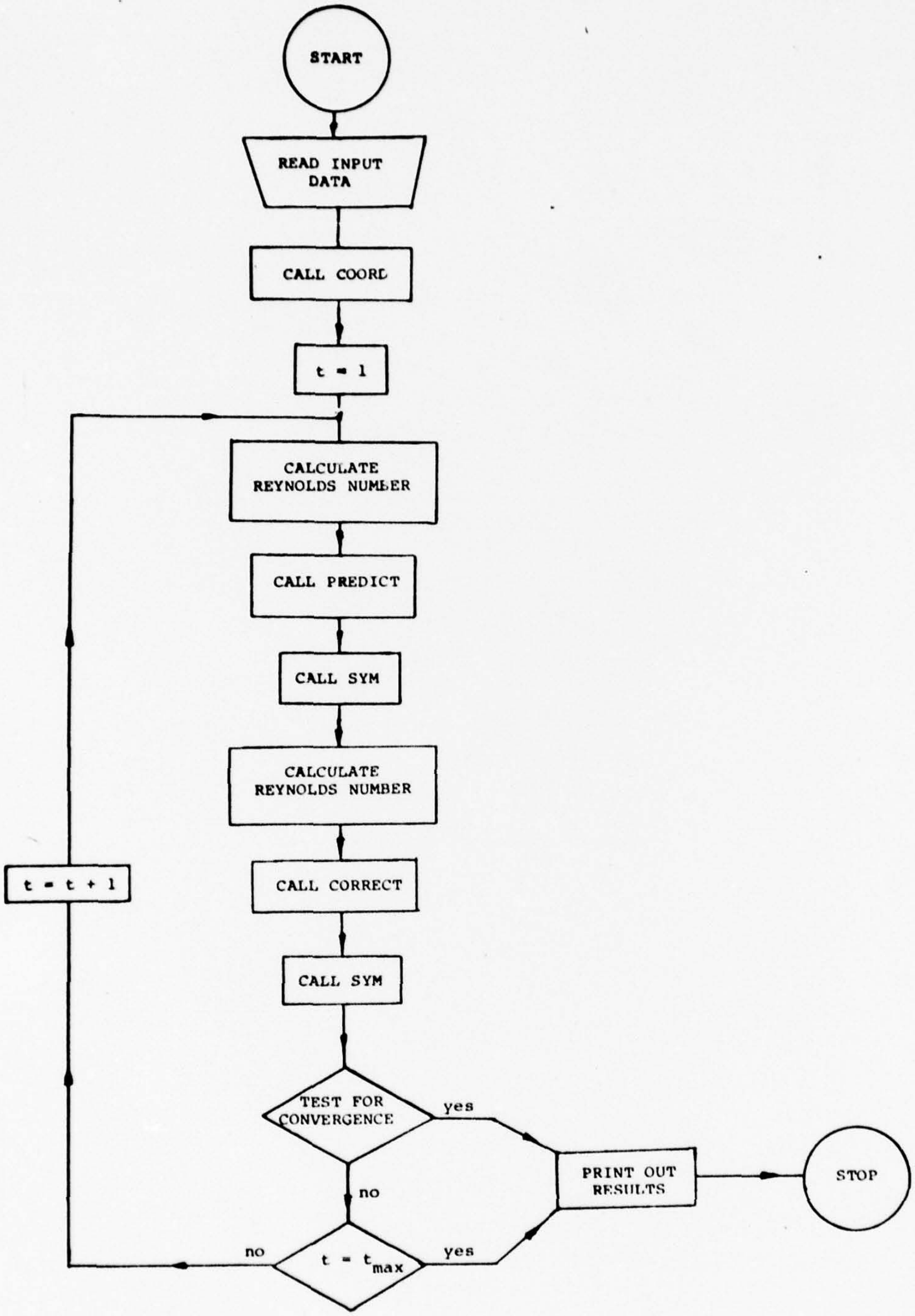
START
READ INPUT DATA
CALL COORD
t = 1
CALCULATE REYNOLDS NUMBER
CALL PREDICT
CALL SYM
CALCULATE REYNOLDS NUMBER
CALL CORRECT
CALL SYM
TEST FOR CONVERGENCE
yes
no
t = t + 1
$t = t_{max}$
no
yes
PRINT OUT RESULTS
STOP

Fig. 11. Schematic Diagram of DELTA Program.

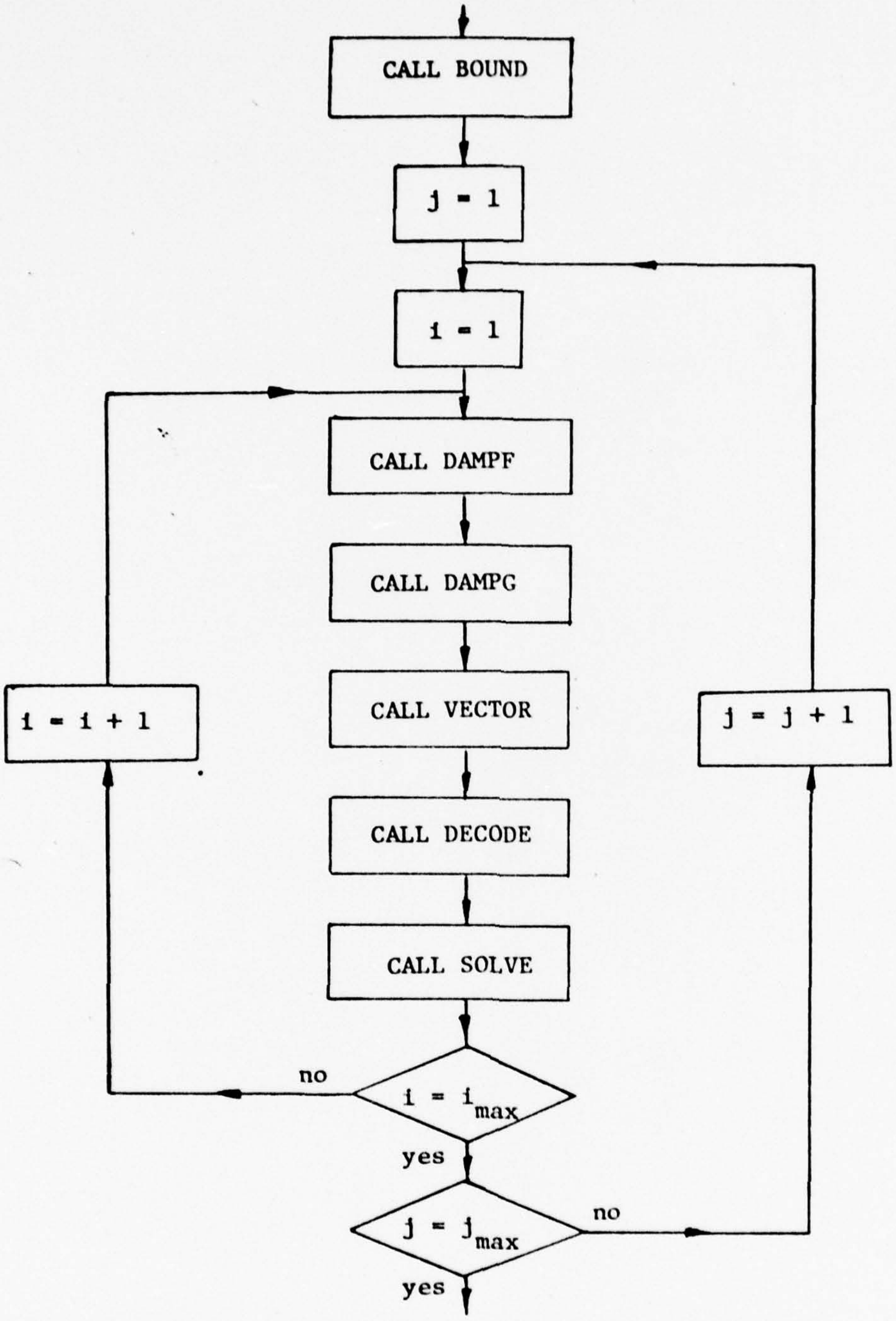
CALL BOUND
j = 1
i = 1
CALL DAMPF
CALL DAMPG
CALL VECTOR
CALL DECODE
CALL SOLVE
i = i + 1
j = j + 1
no
i = i_max
yes
j = j_max
no
yes

Fig. 12. Schematic Diagram of PREDICT and CORRECT Subroutines.

V. Numerical Results

In this chapter, the numerical solutions for both the supersonic flow around a cone and the supersonic/hypersonic flow around a thin planar delta wing are discussed. In each of these cases, the conical, viscous approximation is applied to the governing equations to determine the laminar flow field characteristics. The numerical results of these calculations are compared with various analytical solutions and experimental data.

Cone Flow Analysis

In order to verify the accuracy of the computer codes, the supersonic flow around a cone at zero angle of attack was computed and compared with previous analytical and experimental results. The coordinate transformation used in this calculation is discussed in Appendix A and the physical and transformed planes are shown in Figures 8a and 8b. The free stream and surface boundary conditions chosen for this calculation are

$M_\infty = 7.95$ $\qquad$ $T_o = 1360^\circ R$

$Re_x = 4.2 \times 10^5$ $\qquad$ $P_o = 259.3$ psia

$\theta_c = 10^\circ$ $\qquad$ $\frac{T_w}{T_o} = 0.41$

$Pr = 0.72$ $\qquad$ $\gamma = 1.4$

where the Reynolds number is based on a reference length of x=4.0 inches. These flow conditions are identical to those used by Tracy (Ref 127) in his experimental studies of hypersonic flow over a yawed circular cone.

In this investigation, two different rectangular grid systems were used to calculate the flow field. These included a coarse mesh with a radial step size of $\Delta\xi=0.0079$ and a fine mesh with a step size of $\Delta\xi=0.00395$. A circumferential grid size of $\Delta\eta=3^{o}$ was used in both systems. The computational domains contained 63 equally spaced η grid points ranging from $-3^{o}\leq\eta\leq183^{o}$, and 30 constantly spaced ξ grid points from $\theta_c=10^{o}$ to the free stream boundary surface. The free stream boundaries were located at $\xi=\tan(16.21^{o})$ (fine mesh) and at $\xi=\tan(22.06^{o})$ (coarse mesh). Both of these boundary locations were far enough from the cone surface and bow shock so as not to affect the numerical solution.

Figures 13-16 illustrate a comparison of the numerical results of this technique with the solutions obtained by McRae. The squares and triangles, in these figures, represent the numerical results for $\Delta\xi=0.00395$ and $\Delta\xi=0.0079$, respectively. The solid curve depicts the numerical solution obtained by McRae. In all of these solutions, no numerical damping was used. The undamped solutions were obtained in order to compare the results more easily and to assess the accuracy of the computer code.

The static pressure distribution in the θ direction above the cone surface is shown in Figure 13. The normal pressure gradient in the boundary layer is zero and the numerical solutions near the cone surface are within one percent of each other. If we assume that the attached bow shock location coincides with the static pressure transition centerpoint (a definition used by Tracy), then the experimental shock location is at $\theta-\theta_c=3.56^{o}$ (Ref 127). The numerical shock locations for $\Delta\xi=0.00395$ and $\Delta\xi=0.0079$ are at $\theta-\theta_c=3.57^{o}$ and $\theta-\theta_c-3.52^{o}$, respectively.

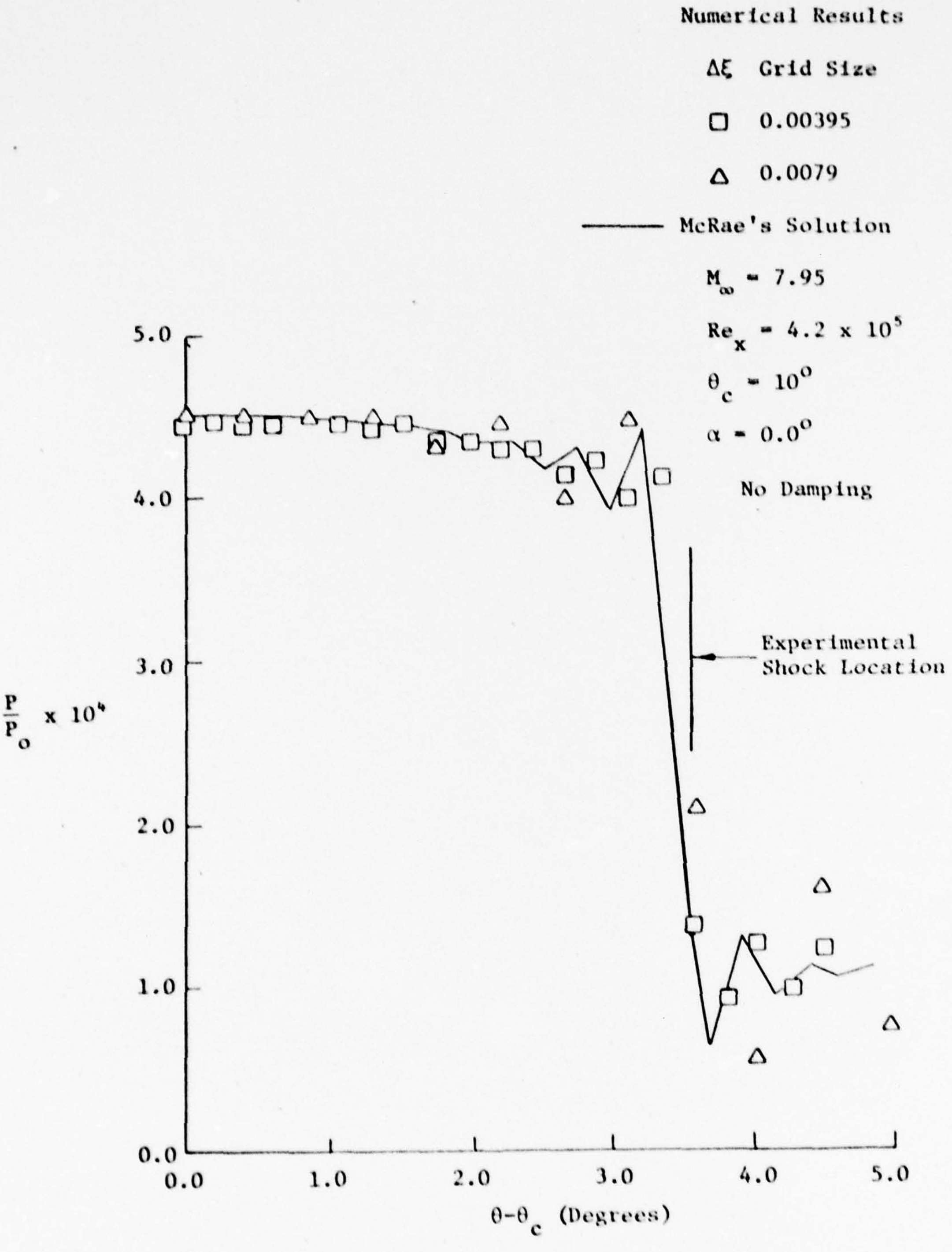

Fig. 13. Comparison of Static Pressure vs. θ Above the Cone Surface for Different Grid Sizes with McRae's Solution.

McRae's solution shows the shock at 3.48° above the cone surface. These results indicate that the fine mesh solution agrees slightly better with experimental data than does the coarser mesh solution. However, both numerical results yield excellent agreement with both McRae's solution and Tracy's experimental data.

The surface pressure on the cone is determined from Eq 77, where the normal pressure gradient is zero. The nondimensionalized surface pressures for both the fine and coarse grid systems are $4.50\text{x}10^{-4}$ and $4.54\text{x}10^{-4}$, respectively. The surface pressure calculated by McRae is $4.53\text{x}10^{-4}$. Experimental results by Tracy show the normalized surface pressure to be $4.62\text{x}10^{-4}$. This discrepancy between calculated and measured results can be attributed to experimental error, instrumentation error, and numerical modeling error. It can be seen that the simplified model of the surface boundary conditions provides excellent agreement with McRae's solution and good agreement with Tracy's experimental data.

In Figure 14, the total velocity distribution in the θ direction is presented for $x=4.0$ inches. The numerical resolution of the boundary layer and bow shock is marginal for the fine grid system and is poor for the coarser grid system. However, the agreement between McRae's calculations and the numerical results is remarkable. In general, there is little difference between the fine and coarse mesh systems, except that the fine mesh solution provides a much better definition of the flow field. Both numerical results yield nearly identical behavior as that noted in similar experimental observations by Tracy.

The static temperature distribution in the θ direction above the cone surface is shown in Figure 15. It can be seen that $\frac{\partial T}{\partial \theta} > 0$ and

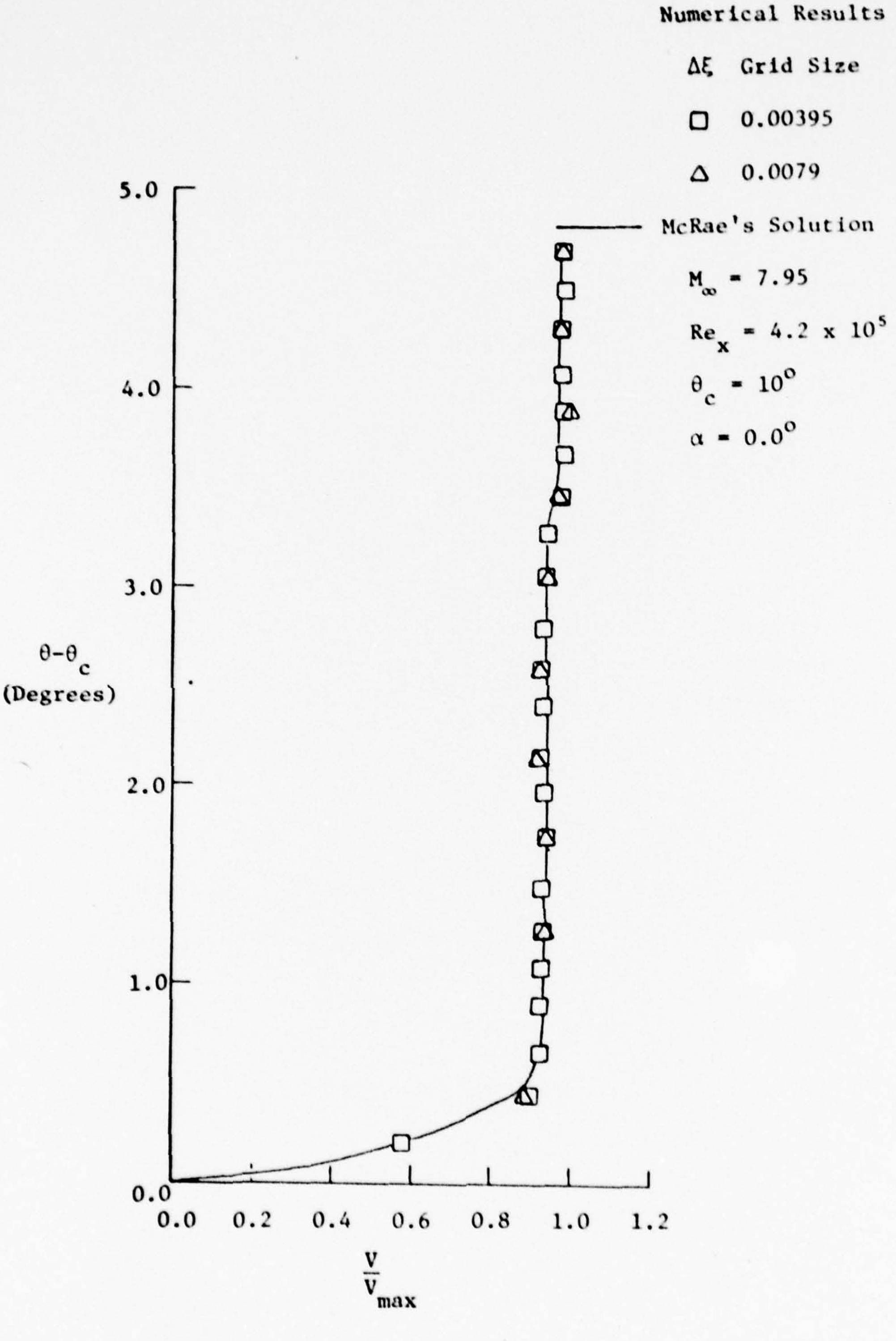

Fig. 14. Comparison of Total Velocity vs. θ Above the Cone Surface for Different Grid Sizes with McRae's Solution.

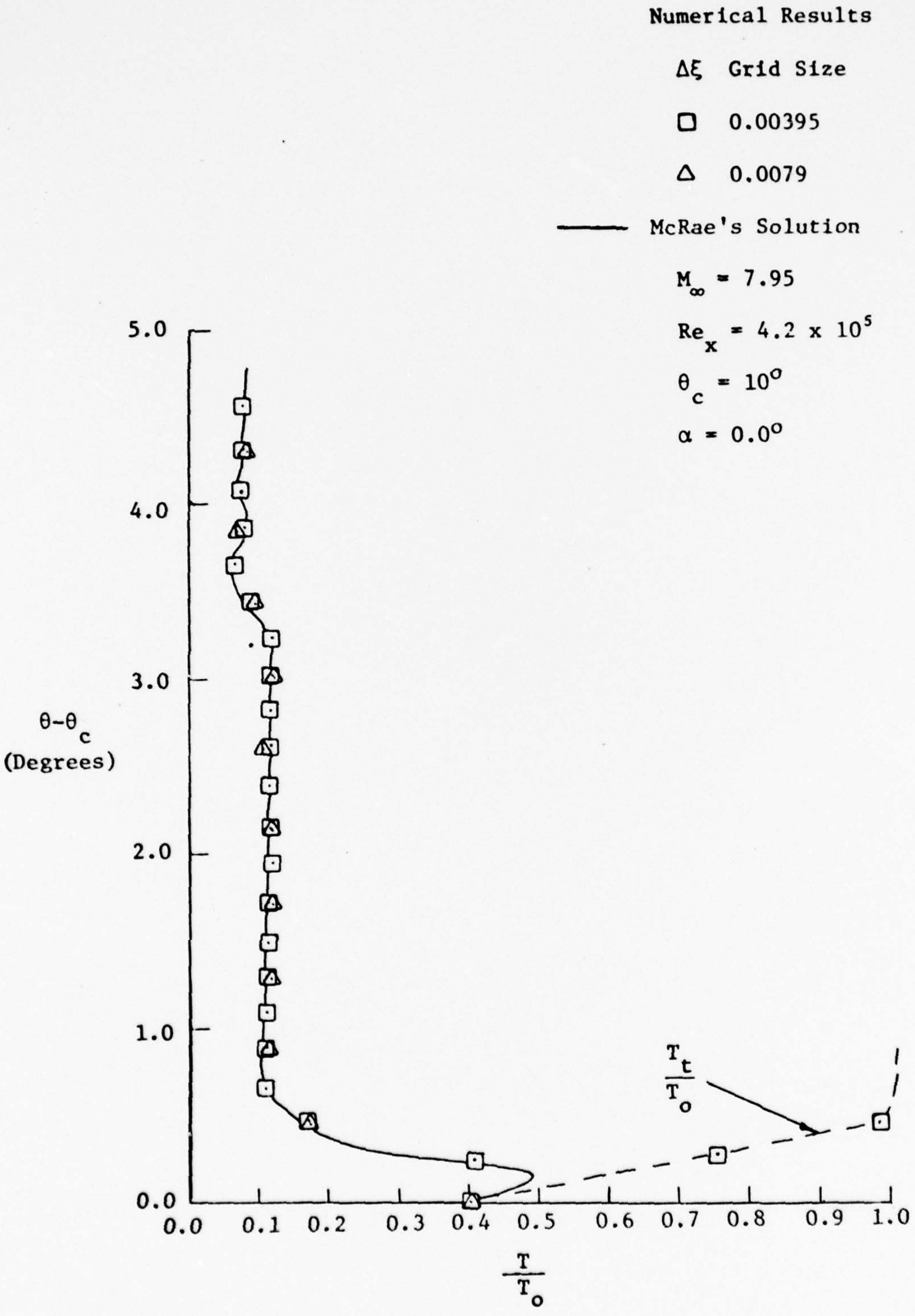

Fig. 15. Comparison of Static Temperature vs. θ Above the Cone Surface for Different Grid Sizes with McRae's Solution.

$\frac{\partial T_t}{\partial \theta} > 0$ at $\theta = \theta_c$, thus indicating that heat is being transferred to the cone surface. This is occurring because of the large amount of frictional heat being generated in the boundary layer, even though $T_w > T_\infty$. Because of the limited number of grid points in the viscous region, a verification of this result was made with a zero-pressure gradient similarity solution of the boundary layer equation. In order to convert the similar solution results given by Low (Ref 136) from the nondimensional Blasius variables to the present nondimensional variables, it was necessary to specify V, ρ, and T at the boundary layer edge as well as at the cone surface. Rather than choose free stream conditions for the outer edge conditions as would be consistent with classical boundary layer theory, the viscous edge conditions were chosen from the fine mesh solution. A survey of calculated impact pressures in the θ direction, as shown in Figure 16, was used to determine the boundary layer edge ($\theta_e - \theta_c = 0.62^\circ$). The normalized surface pressure $p = 4.50 \times 10^{-4}$ was assumed to be constant throughout the viscous region. This pressure coupled with the edge temperature $T_e/T_o = 0.117$ gave the edge density $\rho_e/\rho_o = 3.84 \times 10^{-3}$. From Figures 14 and 16, the edge velocity was found to be $V_e/V_{max} = 0.94$. By applying these edge conditions to the boundary layer equations, a similar temperature profile was obtained, thus confirming the correctness of the numerical results.

The effect of grid refinement in the ξ direction is most significant in the vicinity of the shock wave, as shown in Figures 13 and 16. For $\Delta\xi = 0.00395$ and $\Delta\theta = 0.226^\circ$ (McRae's step size), the numerical oscillations are moderate on both sides of the shock. However, when $\Delta\xi = 0.0079$, the oscillations on the upwind side of the shock become larger. This

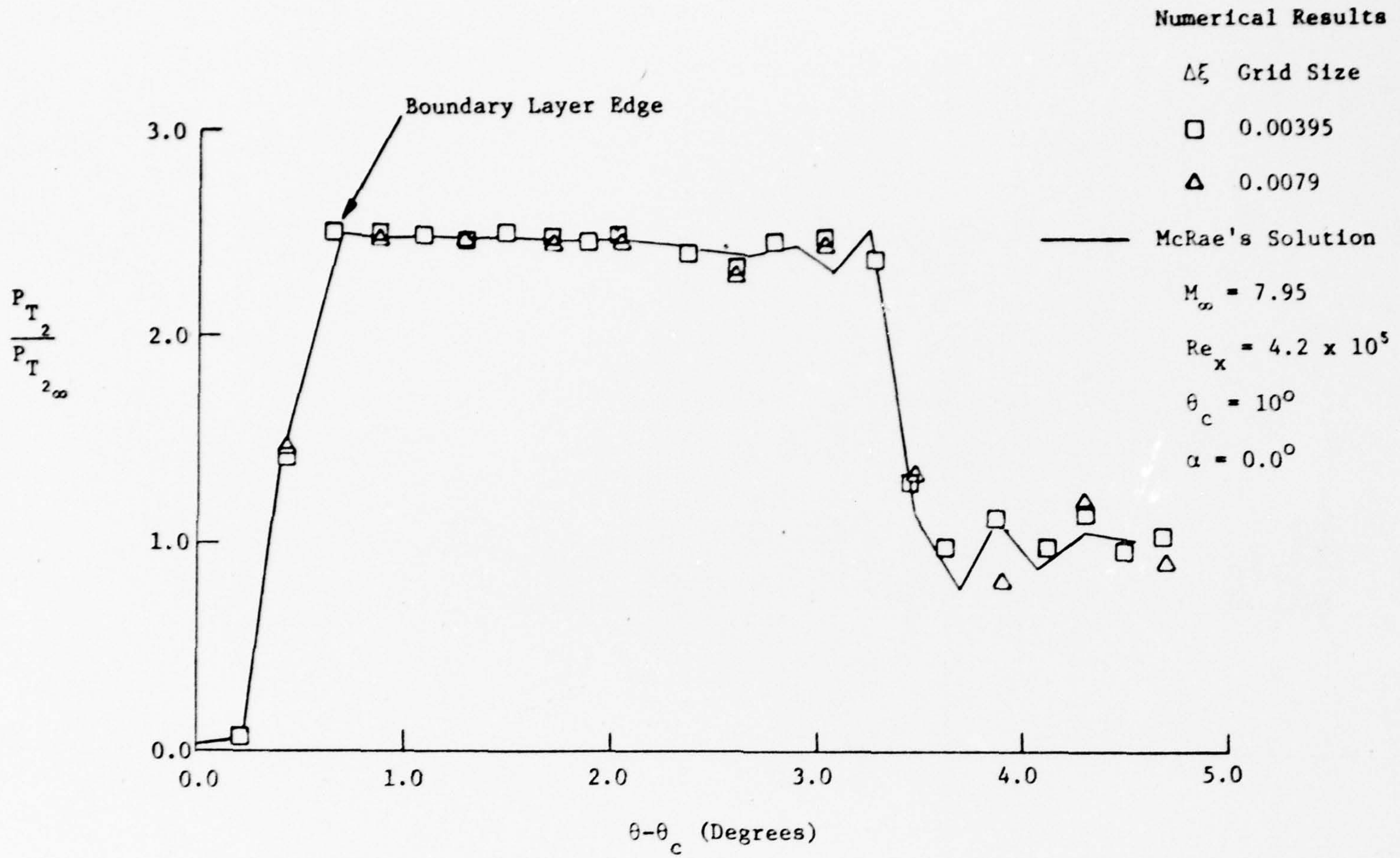

Fig. 16. Comparison of Pitot Pressure vs. θ Above the Cone Surface for Different Grid Sizes with McRae's Solution

causes the numerical instabilities (Gibbs phenomenon) to be spread over a larger distance before they are completely damped out.

In conclusion, it can be seen that this computer code accurately calculates the supersonic, viscous flow field around a cone. The velocity, temperature, and pressure results compare quite favorably with both McRae's solution and Tracy's experimental data. The fine mesh solution provides just enough flow field definition in order to determine the flow characteristics adequately in the boundary layer and near the bow shock.

Delta Wing Expansion Side Flow Analysis

The next phase in this investigation is to examine both the supersonic and hypersonic flows over the leeside of a planar delta wing. The purpose of this analysis is to verify the applicability of the conical, viscous approximation in solving the expansion side flow field. In order to do this, two simplifications were made in modeling the flow. These were (1) to assume the flows above and below the wing surface are independent of each other and (2) to neglect some of the details of the complex flow in the immediate vicinity of the delta wing vertex and leading edge.

In the first assumption, the upper and lower wing flows are independent of each other because the leading edge flow is supersonic. This follows from the fact that in supersonic linear theory, disturbances are propagated downstream in a Mach cone which has its axis aligned with the free stream and which has a semi-angle equal to the free stream Mach angle. Thus, any disturbance generated by either wing surface is confined to a Mach cone which does not intersect the leading edge, since the edge is less swept than the Mach cone. However, in a real flow, this does not hold since the regions of influence are determined by local, rather than free stream conditions (Ref 128). For delta wings, the two surfaces are independent if the bow shock is attached at the leading edge. Wing thickness and viscous development effects can detach the shock wave and thus cause a strong overflow from the compression side of the wing. This overflow influences the supersonic and hypersonic flow on the expansion side of a delta wing, as described in Chapter 1. However, in this numerical model the bow shock is attached to the leading edge and thus the compression side flow does not influence the upper surface flow field characteristics.

The second simplification, which is used throughout this study, is to neglect the three-dimensional flow field effects near the wing vertex and around the leading edges. The flow over the wing vertex, at angle of attack, is characterized by a bow shock, a leading edge Prandtl-Meyer expansion, a pair of internal shock waves, and a developing boundary layer. These flow properties are highly dependent on a number of parameters, such as (1) leading edge geometry, (2) angle of attack, (3) Mach number, (4) Reynolds number, and (5) hypersonic similarity parameter. This complex flow induces vortex generation downstream of the apex region, and the development of a three-dimensional boundary layer.

Vortex generation in the boundary layer depends critically on the cross-flow and viscous-inviscid interaction in the apex region, where the spanwise pressure gradients are strongest (Ref 2). This has been demonstrated by Whitehead and Bertram (Ref 129) and by Rao (Ref 130). The former reduced the cross-flow in the apex region by rounding off the sharp apex, thus, locally "unsweeping" the leading edge. The latter drooped the portion of the wing near the apex in order to align it with the free stream at angle of attack, thus making the local angle of attack in the apex region zero. In both cases, the critical crossflow development in the apex region was reduced which effectively suppressed embedded vortex generation. In addition, experimental measurements have shown that embedded vortices occur when $\bar{\chi}$=0(0.1) (Refs 18 and 131), but not at large values of $\bar{\chi}$, such as $\bar{\chi}\cong 1.0$ (Refs 17 and 25). The reduced spanwise pressure gradient (due to diminished expansion at the leading edge) has the effect of retarding vortex generation. These embedded vortices are different from those formed by shock-induced boundary layer separation at higher angles of attack ($\alpha > 9^o$), as seen in Cross' study.

Rao and Whitehead (Ref 131) examined the hypersonic boundary layer along the centerline of a 75^o delta wing at $\alpha=5^o$ in $M_\infty=6.8$ flow (Re/ft = 1.2×10^6). It was found that the boundary layer thickness, δ, initially develops as a two-dimensional boundary layer; however, a maximum δ is reached and $\frac{d\delta}{dx}$ becomes negative. This decrease in boundary layer thickness is due to the entrainment of low momentum fluid by the presence of vortices in the boundary layer. Further downstream, this "trough" or decrease in δ begins to fill in between the vortices as these vortices move apart. An increase in unit Reynolds number (to 2.0 million per foot and to 3.5 million per foot) moves the δ_{min} upstream.

In conclusion, this investigation assumes that the effects of the viscous interaction around the leading edge and near the wing vertex can be neglected because these flows have only a small effect on the total flow field. McRae (Ref 94) and Hankey (Ref 132) showed that the conical, viscous approximation provides good agreement with experimental results, when viscous interactions are weak ($\bar{\chi} \le O(1)$). Thus, the primary area of interest in this research program is to calculate the conical flow in the weak-interaction region.

Supersonic Flow. In this analysis, only one supersonic case is computed for the expansion side flow field. The free stream conditions chosen for this calculation are

$M_\infty = 2.94$ $T_o = 544^\circ R$

$Re_x = 2.64 \times 10^6$ $P_o = 96$ psia

$Pr = 0.72$ $\gamma = 1.4$

$\alpha = 12.0^\circ$ $T_w = 199.5^\circ R$

$\bar{\chi} = 0.02$

where the Reynolds number is based on a root chord length of 0.173 ft. These flow conditions correspond identically to those used by Bannink and Nebbeling (Ref 15) in their experimental investigation. As part of their study, they used a delta wing model with a flat upper surface and a semi apex angle of 45.3°. The wedge shaped cross-section perpendicular to the leading edge has an apex angle of 7.5°. A conical head probe was used to measure pitot pressure and flow angularity.

The delta wing coordinate transformation, as described in Appendix A, was used in these numerical calculations as well as all other delta wing calculations. The computational domain, on which these calculations were made, consisted of a $26(\eta)\times 30(\xi)$ grid array, similar to the upper half of the grid system shown in Figure 9b. For the sweep angle of 45.3°, the η step size was 0.063158 with 14 grid points on the wing surface. In the ξ direction, a constant, but different, step size was used for each measurement height (pitot pressure measurements by Bannink, Ref 15) so that experimental and numerical results could be compared without interpolation. These constant step sizes ranged from 0.02393 to 0.02775 for different calculations. The results of these calculations are shown in Figures 17-24.

In Figures 17 and 18, several spanwise pitot pressure distributions are shown for various heights above the delta wing. The conical, viscous results of this technique are compared with the inviscid calculations by Kutler (Ref 89) and the experimental measurements by Bannink and Nebbeling (Ref 15). For ξ=0.0718 (Fig 17), the experimental pitot pressure profile across the inboard shock is clearly affected by the interference with the wing boundary layer. At this height, the measured shock strength is slightly less than that measured at higher values of ξ. This numerical technique accurately predicts the shock wave-boundary layer interaction, which is not accounted for in Kutler's solution. Both theoretical methods provide good agreement with experimental data, except in the vicinity of the bow shock. In this region, the current numerical model does not account for the influence of the compression side bow shock near the leading edge. By neglecting the lower surface flow influence, a much weaker leading edge compression wave is computed due to displacement effects of the boundary layer. This very weak shock wave is clearly depicted in the contour plots shown later in Figures 22 and 24.

Since the inviscid flow field and shock wave structure are nearly conical, the velocity components in a spherical coordinate system are used to delineate the three-dimensional flow field. The velocity vectors

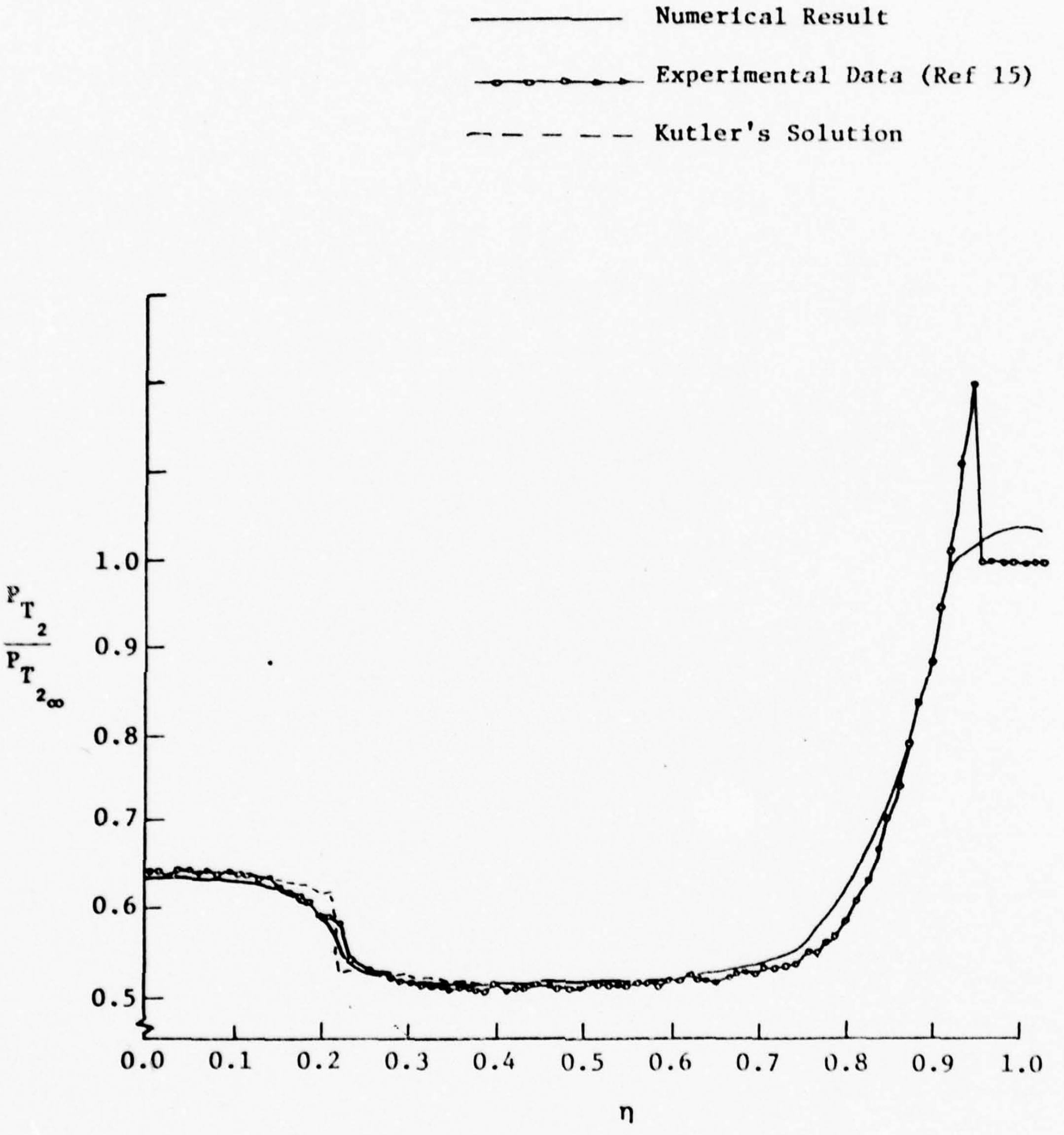

Fig. 17. Pitot Pressure Distribution in Spanwise Direction for Supersonic Flow Above a Planar Delta Wing, $\xi = 0.0718$.

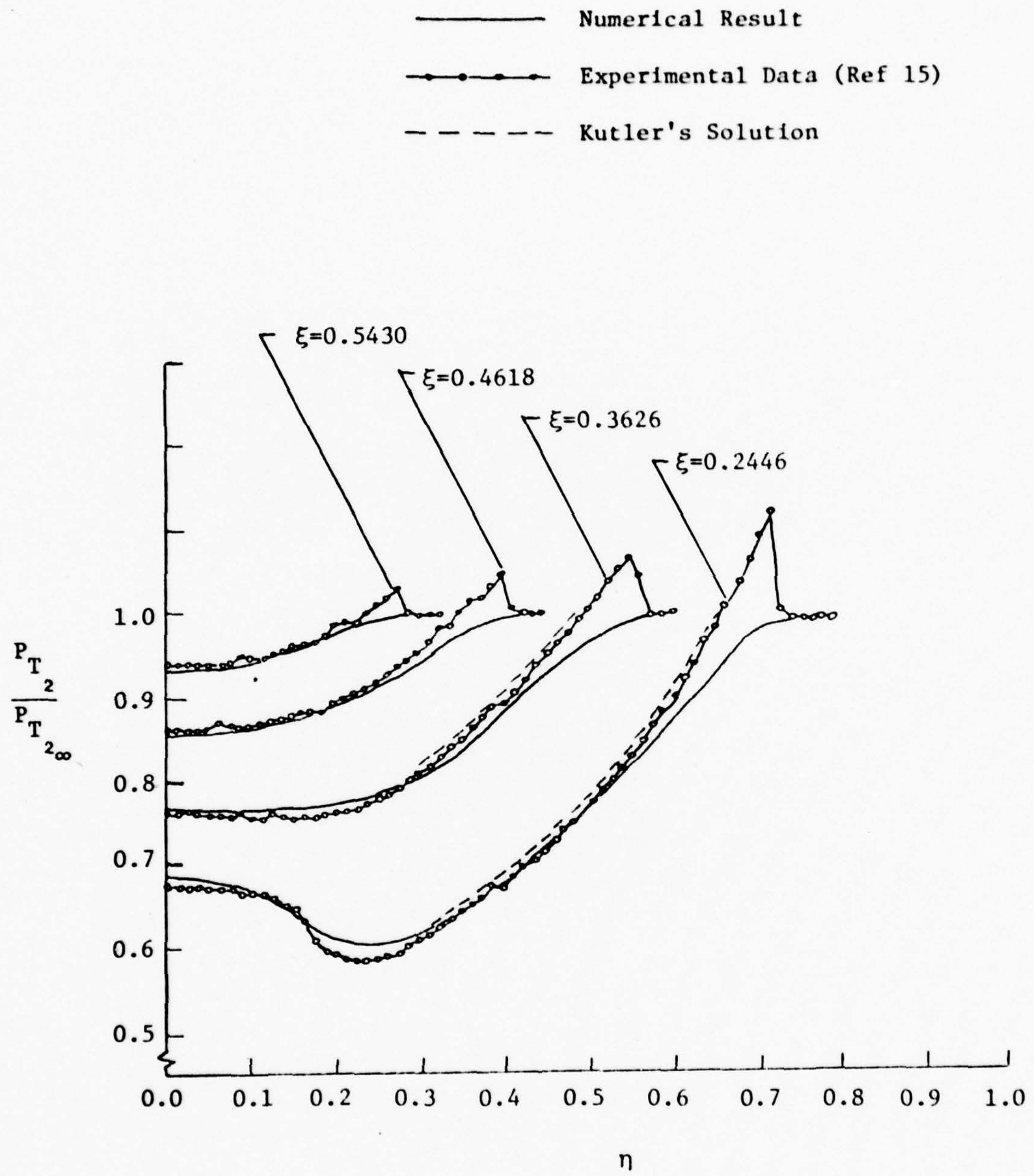

Fig. 18. Pitot Pressure Distribution in Spanwise Direction for Supersonic Flow Above a Planar Delta Wing.

normal to the rays through the vertex of the delta wing are projected on the ξ-η plane as shown in Figure 19. The relative magnitude of these vectors is illustrated for all but the lowest momentum region. The direction of these vectors is given by

$$\tan \gamma_c = \frac{u\xi - w}{u\eta - v} \qquad (97)$$

where γ_c is the angle with the positive η axis (see Appendix F). The locus of these velocity vectors trace out "pseudo" streamlines which converge at a vortical singularity point (cross-flow stagnation point) near the origin. In the unperturbed flow region (upper and right portions of Fig 19), the conical cross-flow velocity vectors point to the origin of the coordinate system. Figure 20 illustrates some of the cross-flow conical streamlines (780 points). A linear interpolation technique, described in Appendix F, is used to determine these steady state path lines. Figure 20 shows more clearly how most of these conical streamlines converge at the vortical singularity point, even though the numerical resolution is marginal. This result is consistent with the experimental observations by Bannink and Nebbeling.

In Figure 21, the calculated position of the internal shock wave and conical sonic line (M_c=1.0) is shown in the computational plane. Superimposed on this plot are the experimental results obtained by Bannink and Nebbeling (Ref 15). The measurement of the pressure rise across a shock wave is dependent on the shock strength and dimensions of the probe. Bannink and Nebbeling (Ref 133) found that for cylindrical pitot probes Tracy's centerpoint criteria was satisfactory, provided that a suitable ratio exists between the inner and outer diameters of the probe. Since Bannink and Nebbeling used a conical shaped probe

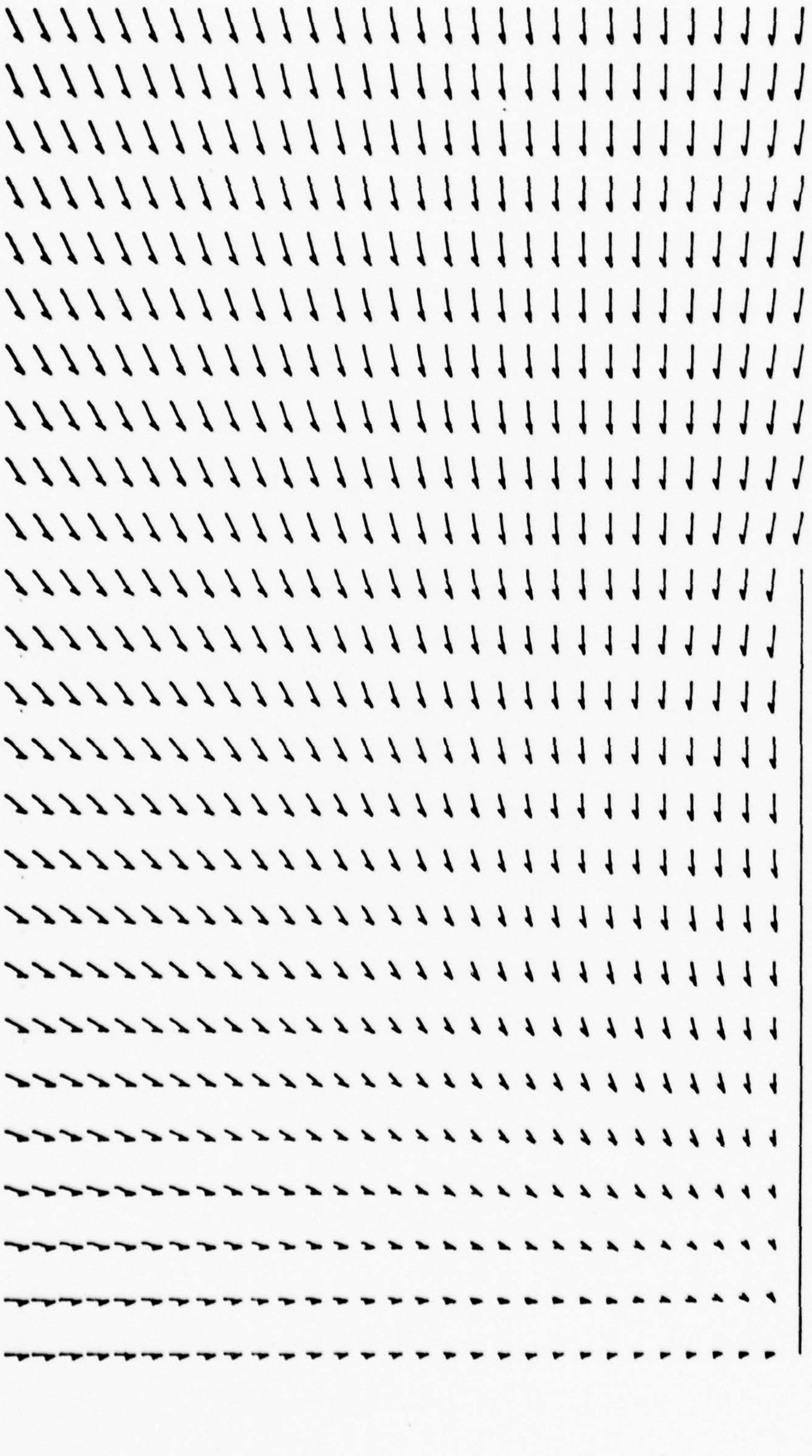

Fig. 19. Cross-Flow Vector Velocity Plot as projected on ξ-η plane for Supersonic Flow Above a Planar Delta Wing, $\alpha = 12^{\circ}$.

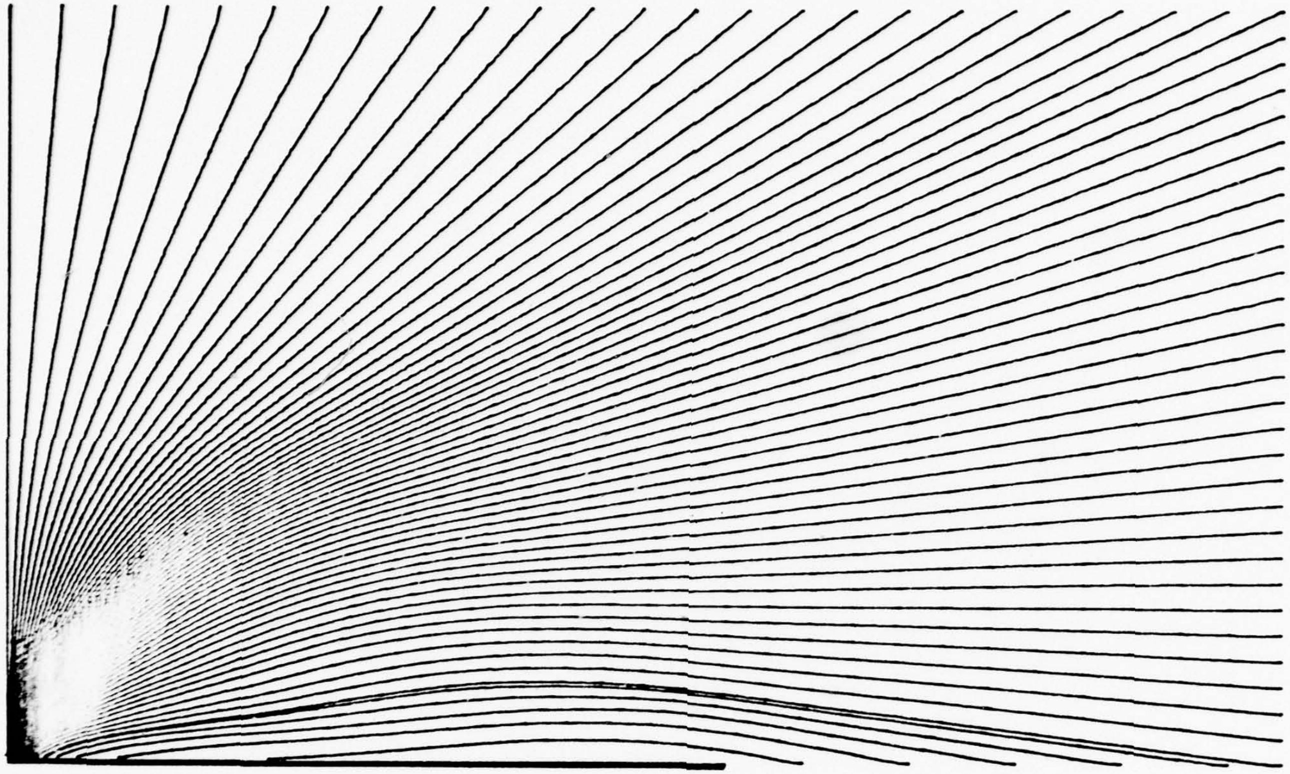

Fig. 20. Cross-Flow Streamline Plot as Projected on ξ-η Plane for Supersonic Flow Above a Planar Delta Wing, $\alpha = 12^{\circ}$.

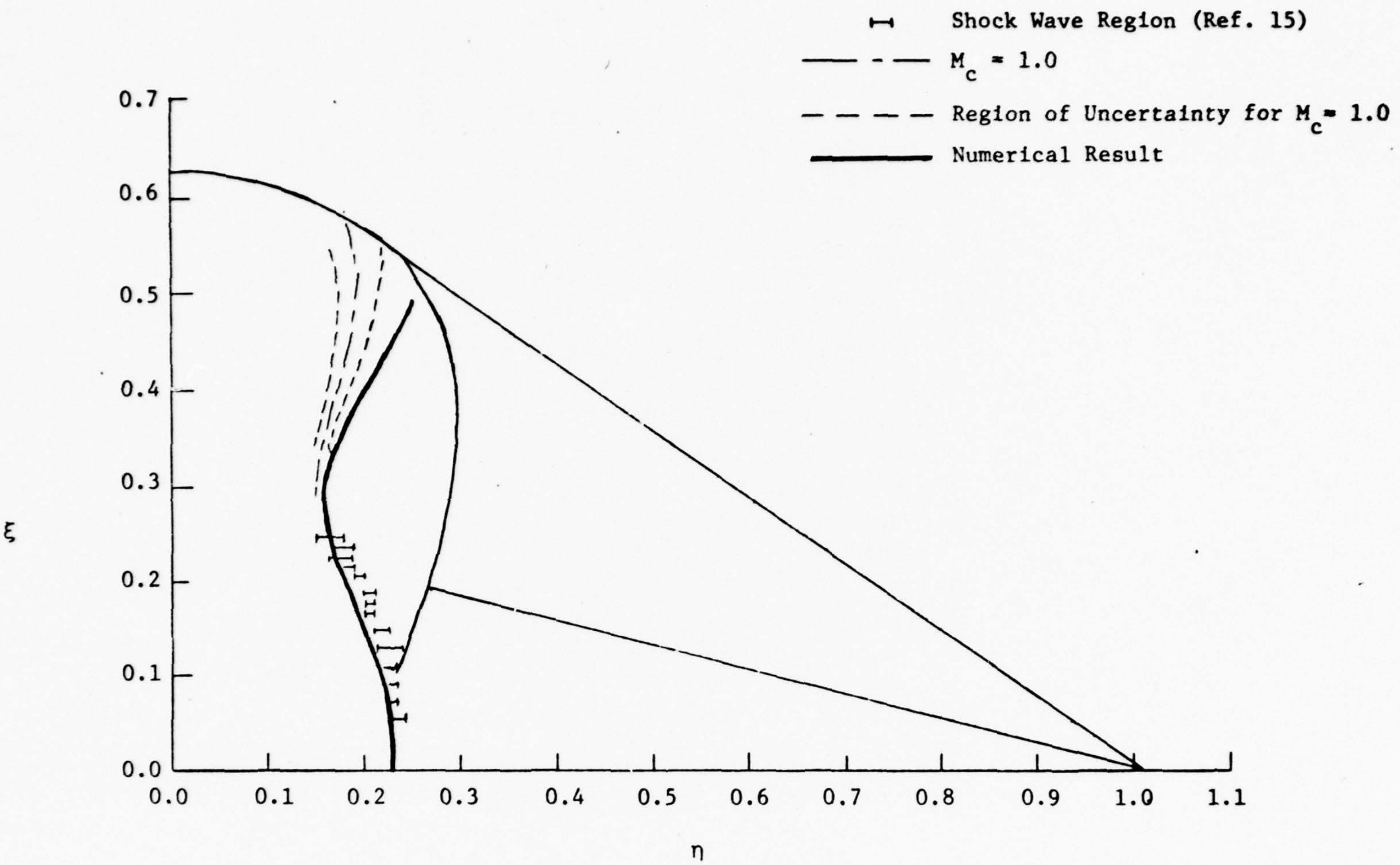

Fig. 21. Location of Shock Wave and Conical Sonic Line for Supersonic Flow Above a Planar Delta Wing, $\alpha = 12^{\circ}$.

in their experimental measurements, the shock location is presented as a band having the width of the observed pressure jump. No attempt is made to define the exact location of the shock wave within this band. In Figure 21, it can be seen that a close correlation exists between the calculated and experimental locations of the inner shock and sonic line below $\xi=0.35$. The small discrepancy between the measured and the calculated conical sonic line in the upper region of the flow field ($\xi>0.35$) is due to the small gradients of M_c in the η direction, since a small inaccuracy in the measurements results in a large η variation. This discrepancy is indicated by the region of uncertainty shown in Figure 21.

The pressure, temperature, and density contours in the η-ξ plane are shown in Figures 22-24, respectively. These contour plots were developed by using a General Purpose Contouring Program (Ref 134) on the CDC 6600 computer. A total of 780 data points were evaluated to produce these figures. The internal shock wave and leading edge expansion fan are clearly depicted in all three figures as highly concentrated contour lines. In Figure 22, the isobars indicate that the inboard shock wave, starting perpendicularly from the wing surface, extends into the central region where the expanded flow is dominant. In this region, the internal shock weakens and eventually becomes a conical sonic line. Along the wing surface, the boundary layer is very thin and the pressure gradient normal to the surface is zero. Beyond the leading edge, a relatively weak bow shock is formed which diminishes very rapidly as it overflows the upper surface of the wing. A strong temperature gradient is formed in the boundary layer, as seen in Figure 23. This gradient is slightly stronger in the region between

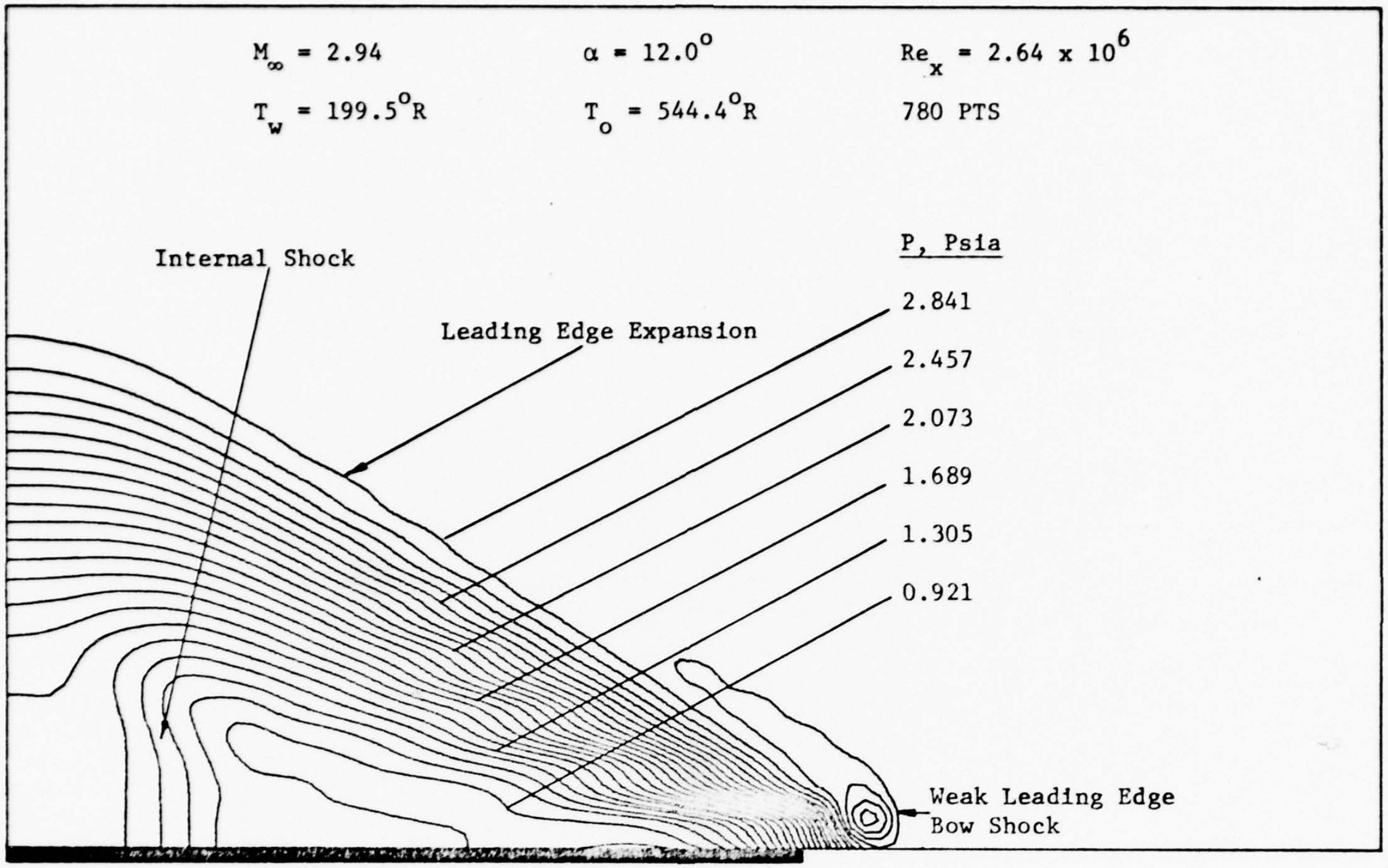

Fig. 22. Static Pressure Contour in Cross-flow Plane for Supersonic Flow Above a Planar Delta Wing.

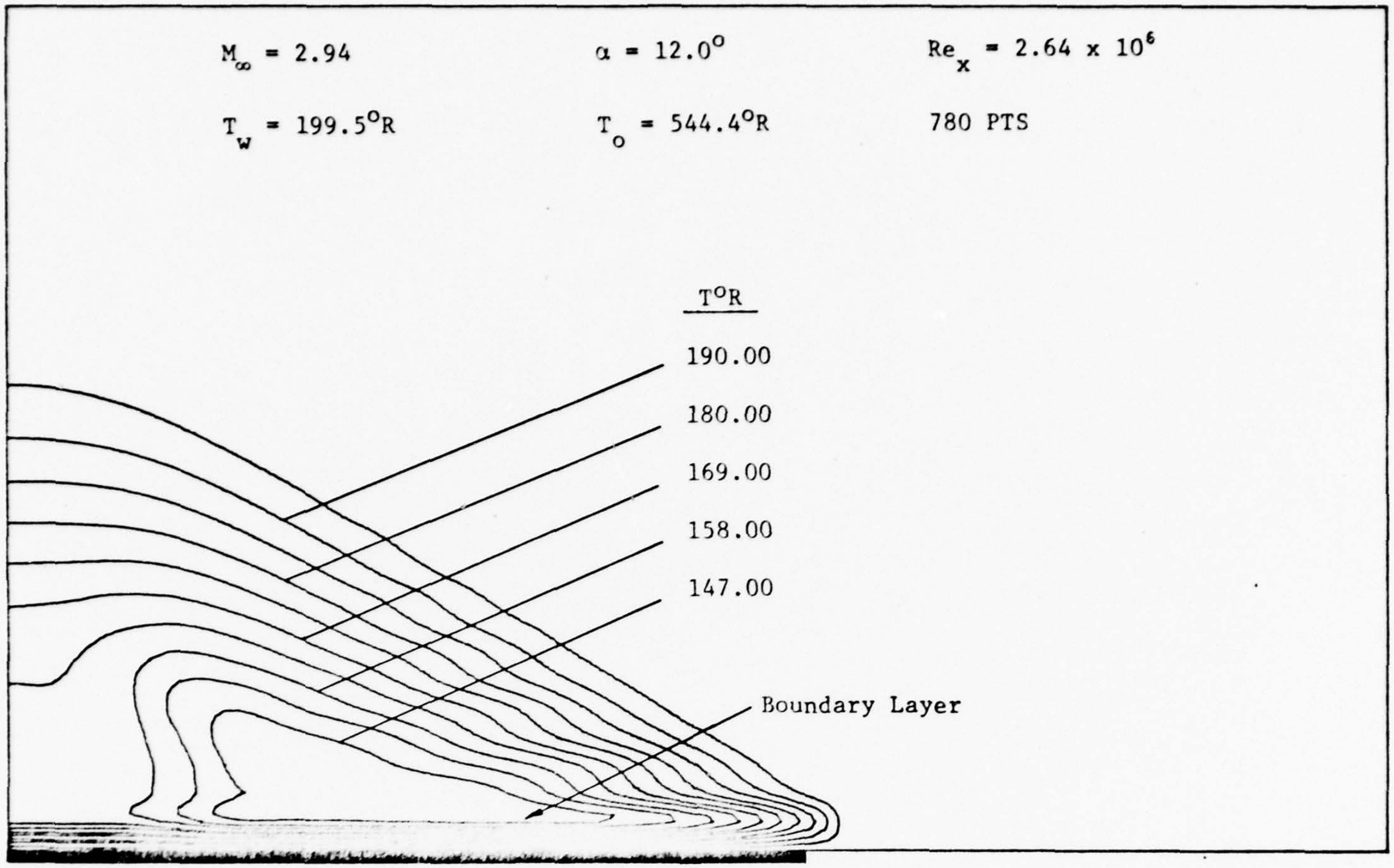

Fig. 23. Static Temperature Contour in Cross-Flow Plane for Supersonic Flow Above a Planar Delta Wing.

the internal shock wave and the leading edge expansion fan. In Figure 24, it can be seen that the shock wave-boundary layer interaction is very weak and no flow separation occurs at the base of the internal shock.

In summary, this numerical technique accurately predicts the basic elements of the supersonic flow over the upper surface of a planar delta wing. The numerical results compare quite favorably with Bannink's experimental data, except in the vicinity of the bow shock. These calculations show that a three-dimensional, supersonic viscous flow over the expansion surface of a planar delta wing can be accurately approximated by using a two-dimensional conical flow field model.

Hypersonic Flow. Cross (Ref 17) conducted a series of experimental studies of the expansion side flow field over a flat delta wing at hypersonic speeds. Several models were used in this investigation. All of these models were geometrically similar flat plate delta wings with sharp leading edges (diameter approximately 0.003 inch). The sweep angles on these models were 75° and the central wing chords varied from 3 to 7 inches with plate thicknesses of up to 0.5 inches. Impact pressures were measured at numerous points in the leeside flow field from $\alpha=0^\circ$ through $\alpha=19^\circ$ in 2° increments. A 0.040 inch outside diameter pitot probe, mounted parallel to the upper wing surface, was used to make these pressure measurements.

In order to simulate Cross' experimental investigation, the following free stream conditions were chosen for this calculation

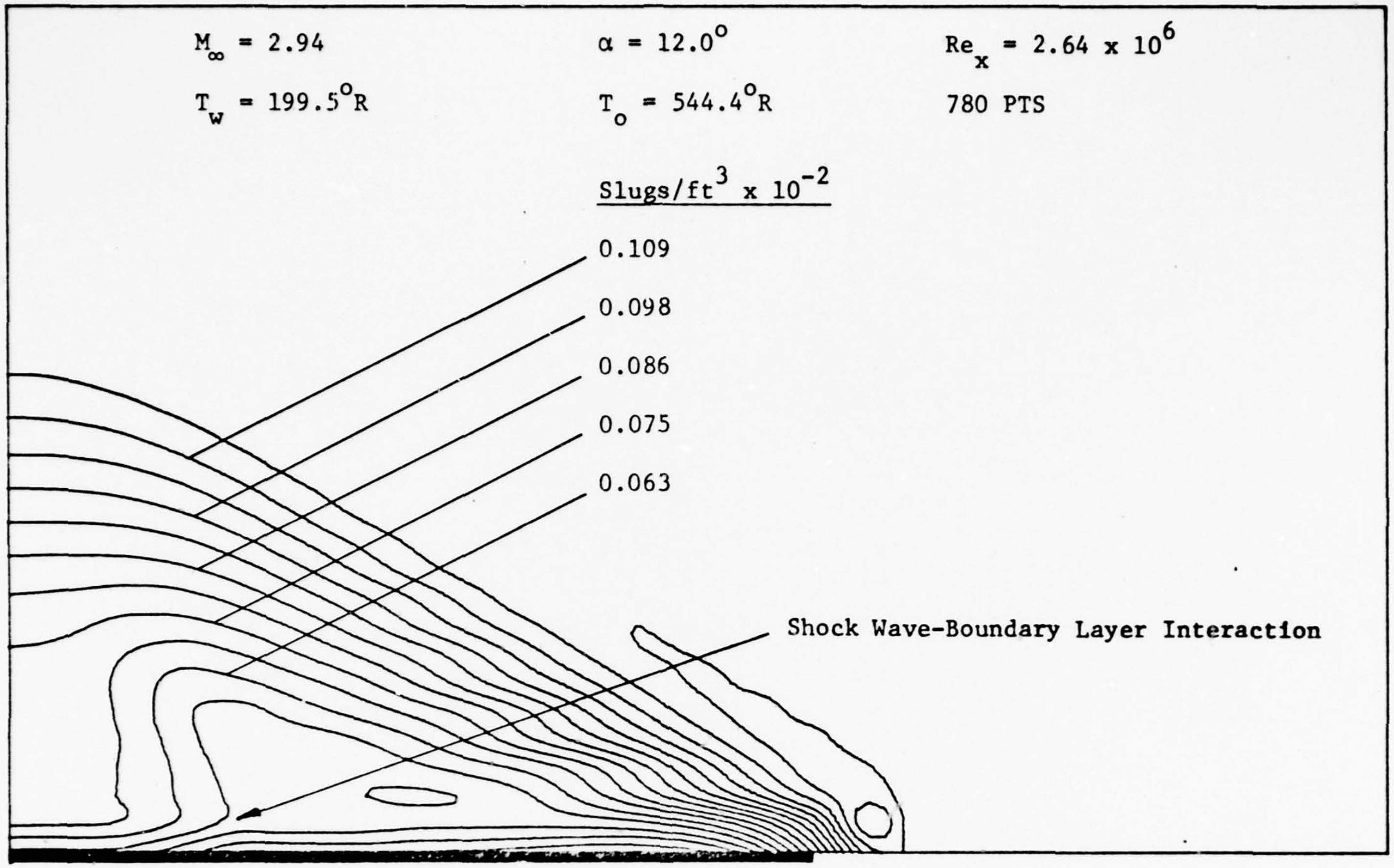

Fig. 24. Static Density Contour in Cross-flow Plane for Supersonic Flow Above a Planar Delta Wing.

$M_\infty = 10.17$ $T_o = 1780^\circ R$

$Re_x = 3.345 \times 10^5$ $P_o = 596$ psia

$Pr = 0.72$ $\gamma = 1.4$

$\bar{\chi} = 1.8$ $T_w = 1259.7^\circ R$

$\alpha = 0^\circ, 5^\circ, 9^\circ, 11^\circ$, and 15°

A constant step size array, identical to the upper half of the grid system in Figure 9b, was used with grid increments as shown in Table 1.

Table I

Grid Increments for Hypersonic Flow Field Calculations

α	$\Delta\eta$	$\Delta\xi$	Grid
0°	0.019139	0.00568	$26\eta \times 45\xi$
5°	0.019139	0.01136	$26\eta \times 30\xi$
9°	0.019139	0.01136	$26\eta \times 30\xi$
11°	0.019139	0.00568	$26\eta \times 76\xi$
15°	0.019139	0.00568	$26\eta \times 76\xi$

The free stream boundaries (upper and right) were located far enough from the upper wing surface as not to affect the numerical solutions. The incremental step sizes were selected so that no interpolation was required in order to compare experimental and numerical results. The results of these calculations are shown in Figures 25-35.

In Figure 25, a comparison is made between the experimental and calculated edge of the viscous region. This viscous profile is

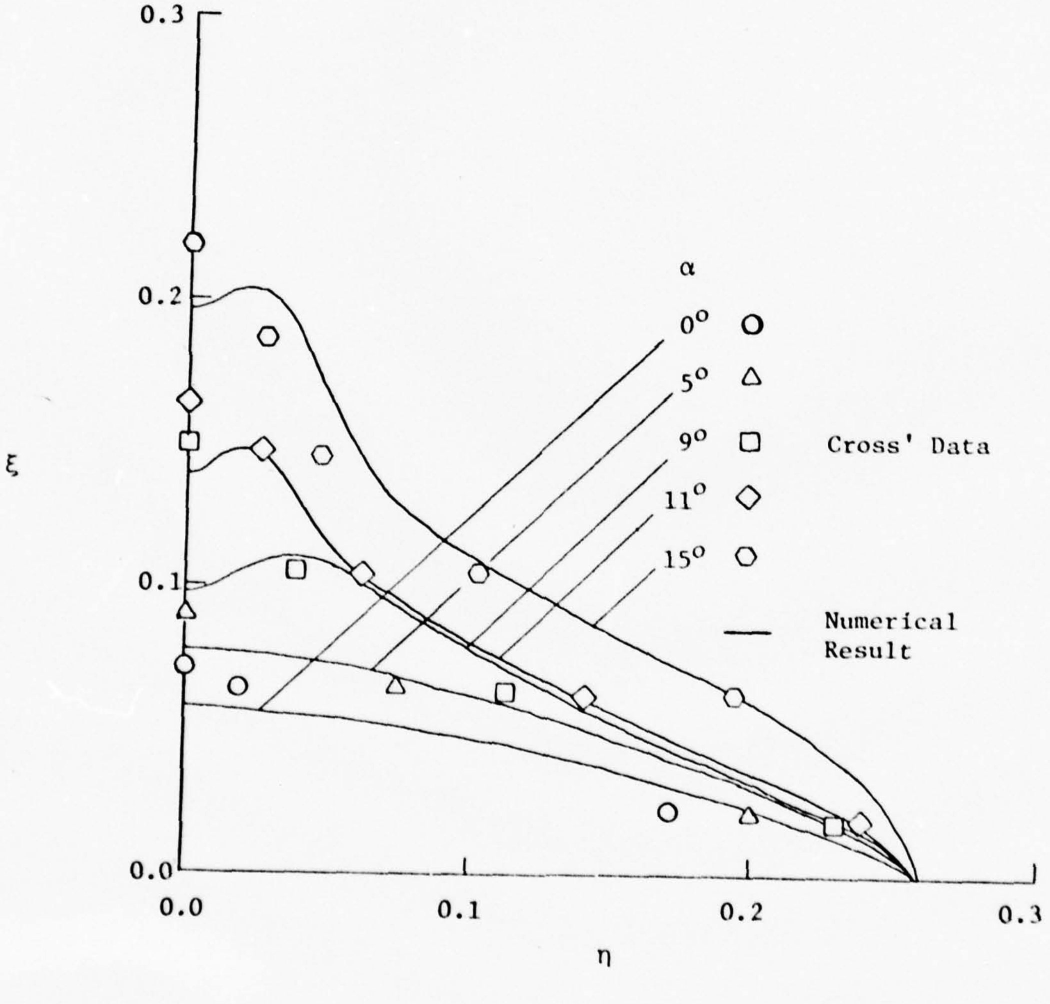

Fig. 25 Hypersonic Viscous Layer Development Above a Delta Wing as Determined by Impact Pressure Measurements

determined by evaluating the impact pressures in the ξ-direction, similar to what is shown in Figure 16. It can be clearly seen (Fig 25) that there is a progressive increase in the extent of the viscous region as the angle of attack is increased. At low angles of attack ($\alpha \leq 5^{\circ}$), the calculated profile can be approximated by $\delta \sim \eta^{\frac{1}{2}}$. This result is similar to the qualitative flow behavior noted by Rao and Whitehead (Ref 131) in their vapor screen studies. However, from Cross' data, the experimental profile is very nearly linear. The largest differences between experimental and calculated results occur at the plane of symmetry, where three-dimensional effects are dominant. For $\alpha \geq 9^{\circ}$, a centerline "trough" appears in the calculated viscous profile. This trough is generated by shock-induced vortices in the viscous region. Cross' data, for $\alpha \geq 8^{\circ}$, shows a large region of low impact pressure developing along the centerline of the wing. This region is located at the projection point of the free stream velocity vector (through the wing vertex) on the ξ-η plane.

The impact pressure distribution for various angles of attack and ξ-position are shown in Figures 26 through 29. Figure 26 depicts a comparison between experimental and calculated impact pressure results for $\alpha=0^{\circ}$. The calculated values are in good agreement with the measured quantities except at one point on the upwind side of the bow shock at $\xi=0.0682$. In this region, the calculated bow shock position is slightly inboard of the actual shock wave. Figures 27a and 27b illustrate the impact pressure results for $\alpha=5^{\circ}$. In these figures, good agreement is again shown between theory and experiment, except in the vicinity of the bow shock and along the centerline of the wing at $\xi=0.0682$. This discrepancy on the symmetry plane occurs because the calculated boundary

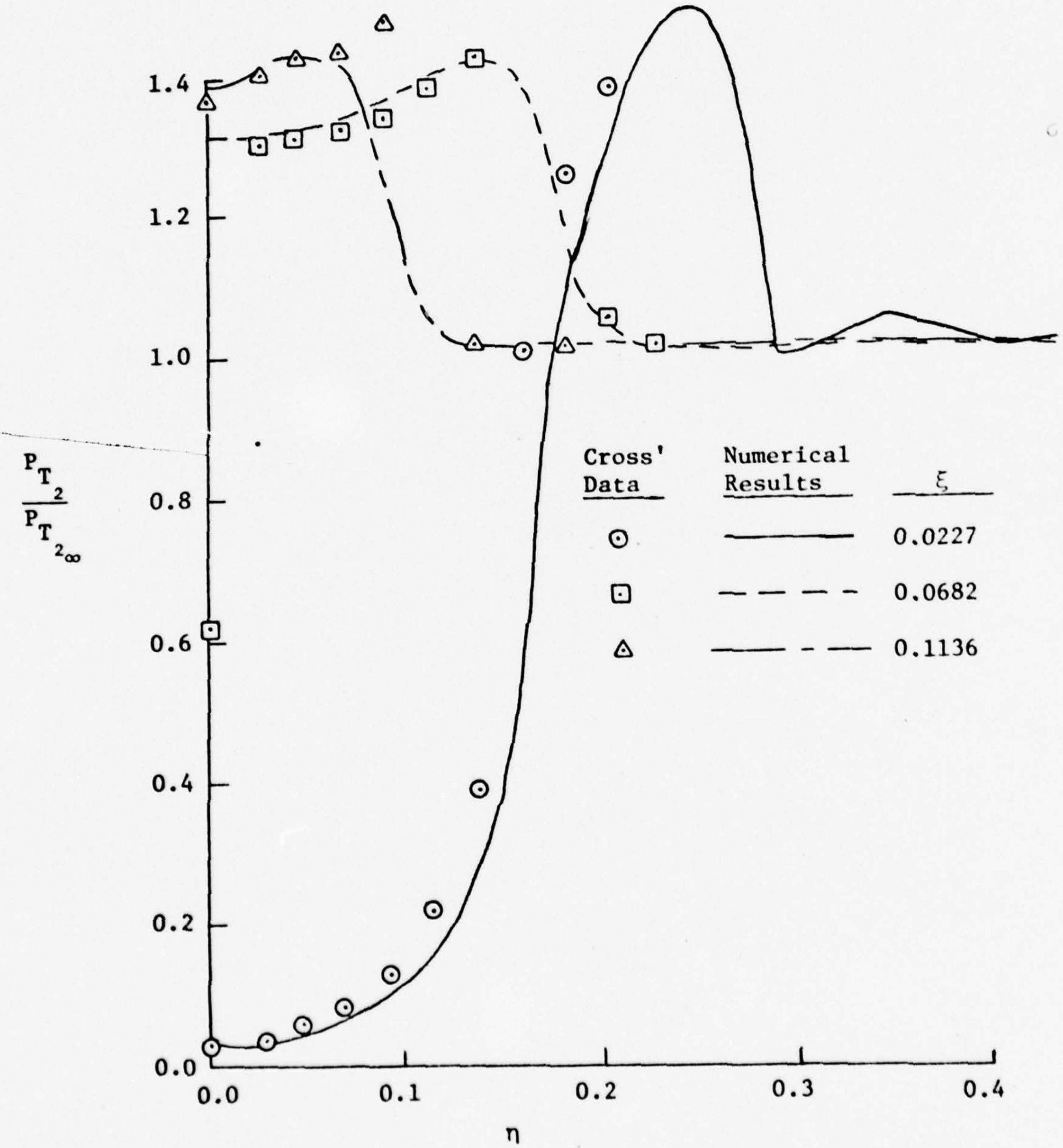

Fig. 26. Impact Pressure Survey on Leeside of Delta Wing, α = 0°

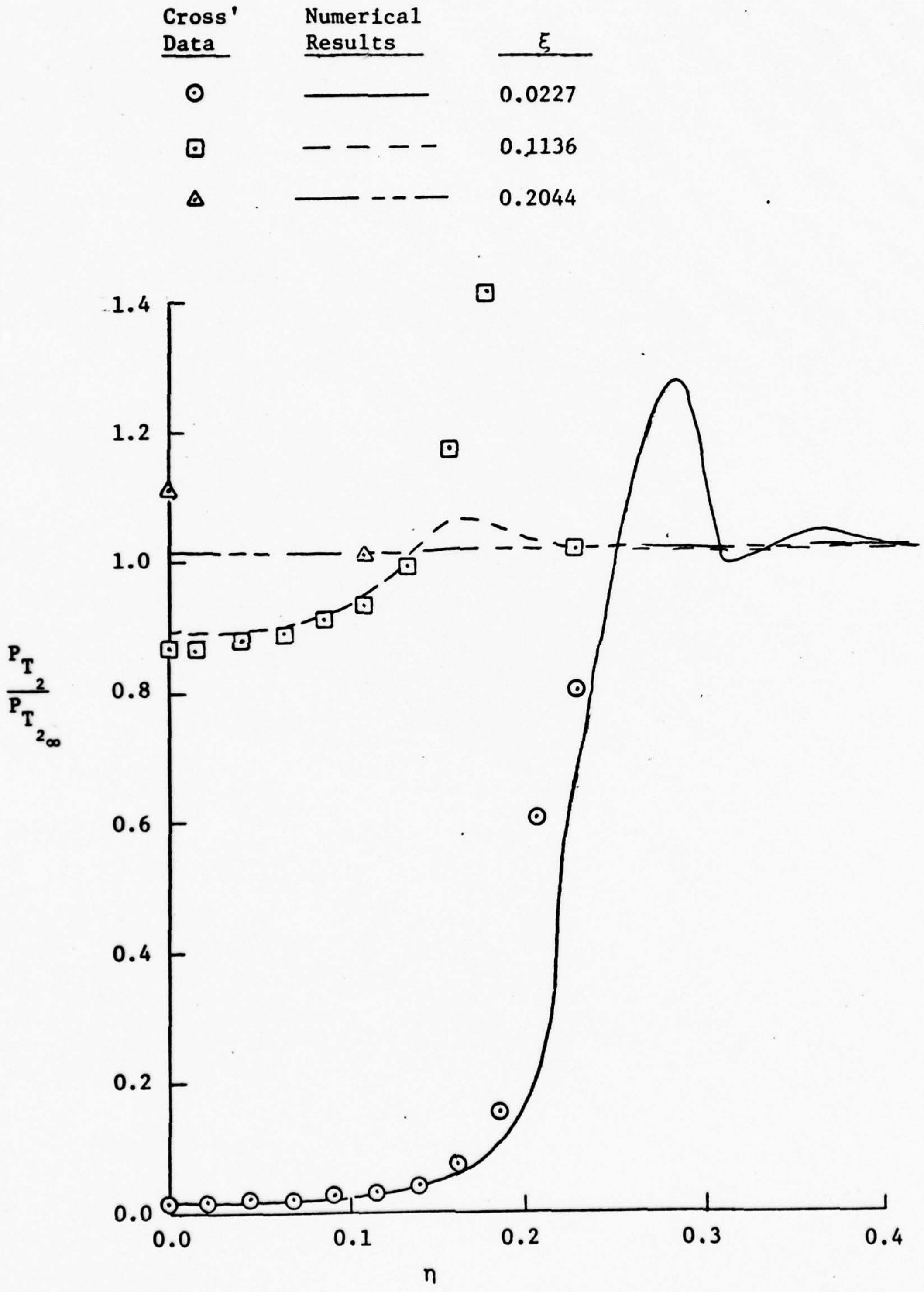

Fig. 27a. Impact Pressure Survey on Leeside of Delta Wing, $\alpha = 5^{\circ}$

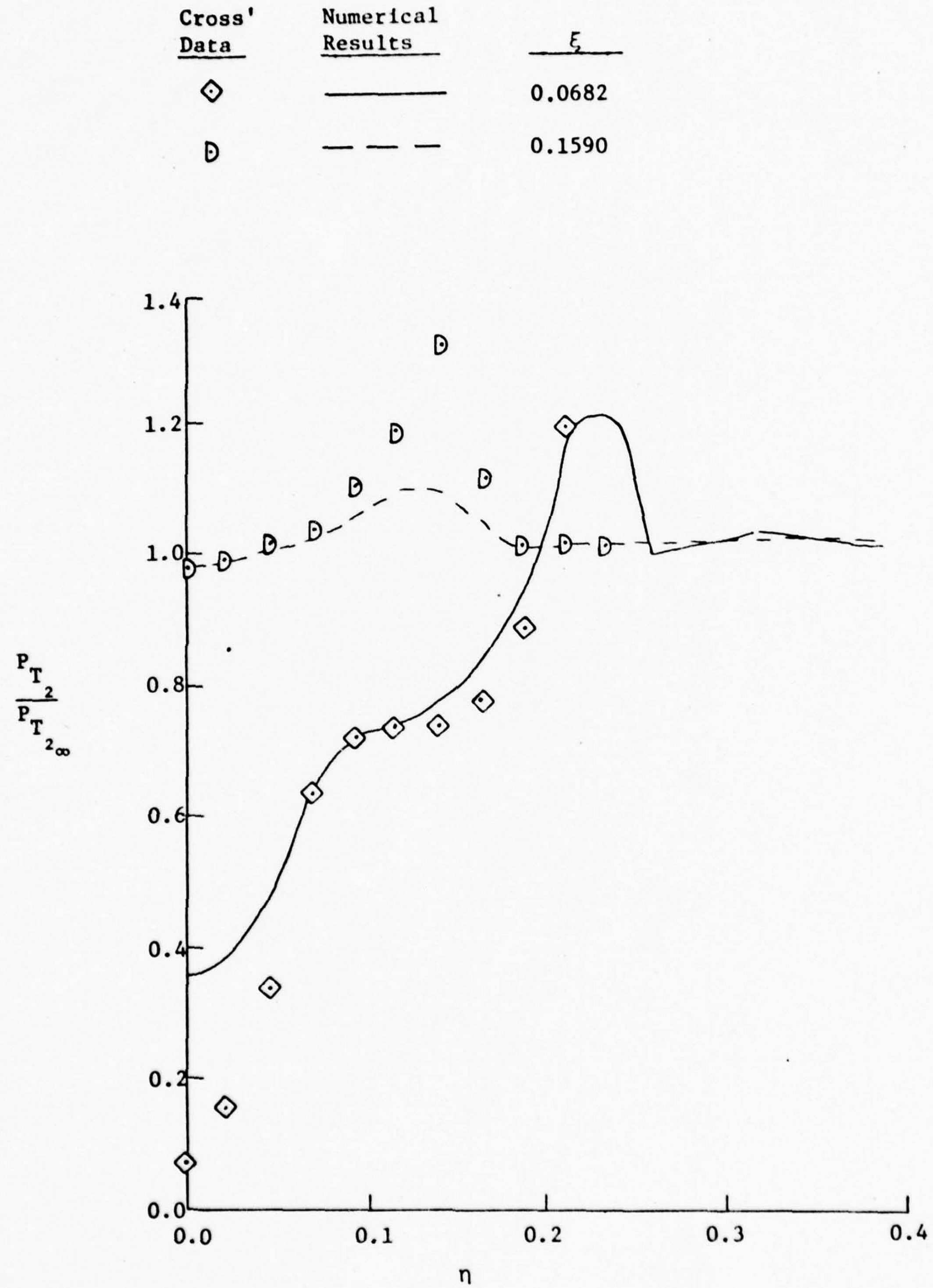

Fig. 27b. Impact Pressure Survey on Leeside of Delta Wing, α = 5°

layer thickness is slightly less than the measured value. The same type of pressure results are also seen for $\alpha=9^{\circ}$ (Figs 28a and 28b), except that at $\xi=0.11505$ the impact pressure disparities are much larger near the centerline. These large disparities are a result of the differences between the calculated boundary layer trough and the measured enlarged low pressure region. Similar discrepancies are seen for $\alpha=15^{\circ}$ (Figs 29a and 29b) at $\xi=0.15904$ and $\xi=0.20454$.

The conical cross-flow streamlines for $\alpha=0^{\circ}$, 9°, and 15° are shown in Figures 30 through 32. At zero angle of attack (Fig 30), a vortical singularity exists near the upper edge of the viscous region. No flow separation is seen along the wing surface and no vortex is formed in the boundary layer. As the angle of attack is increased (as determined in this study), the vortical singularity is forced downward toward the wing surface under the developing influence of a vortex in the viscous region. At $\alpha=5^{\circ}$, the vortical singularity is located at the origin of the coordinate system. All conical streamlines converge toward this cross-flow stagnation point in the η-ξ plane.

At $\alpha=9^{\circ}$ (Fig 31), a small vortex is formed in the boundary layer. This vortex is initially very close to the wing surface and is formed as a result of shock-induced boundary layer separation. Because of the limited number of grid points in the viscous region, only a coarse outline can be seen of this developing vortex. As the angle of attack is increased, the vortex strength is increased and the core of the vortex moves further above the wing. At $\alpha=11^{\circ}$ and $\alpha=15^{\circ}$ (Fig 32), the vortex is well developed in the viscous region and its behavior is very similar to the experimental observations of Cross.

The density, pressure, and temperature contours in the cross-flow

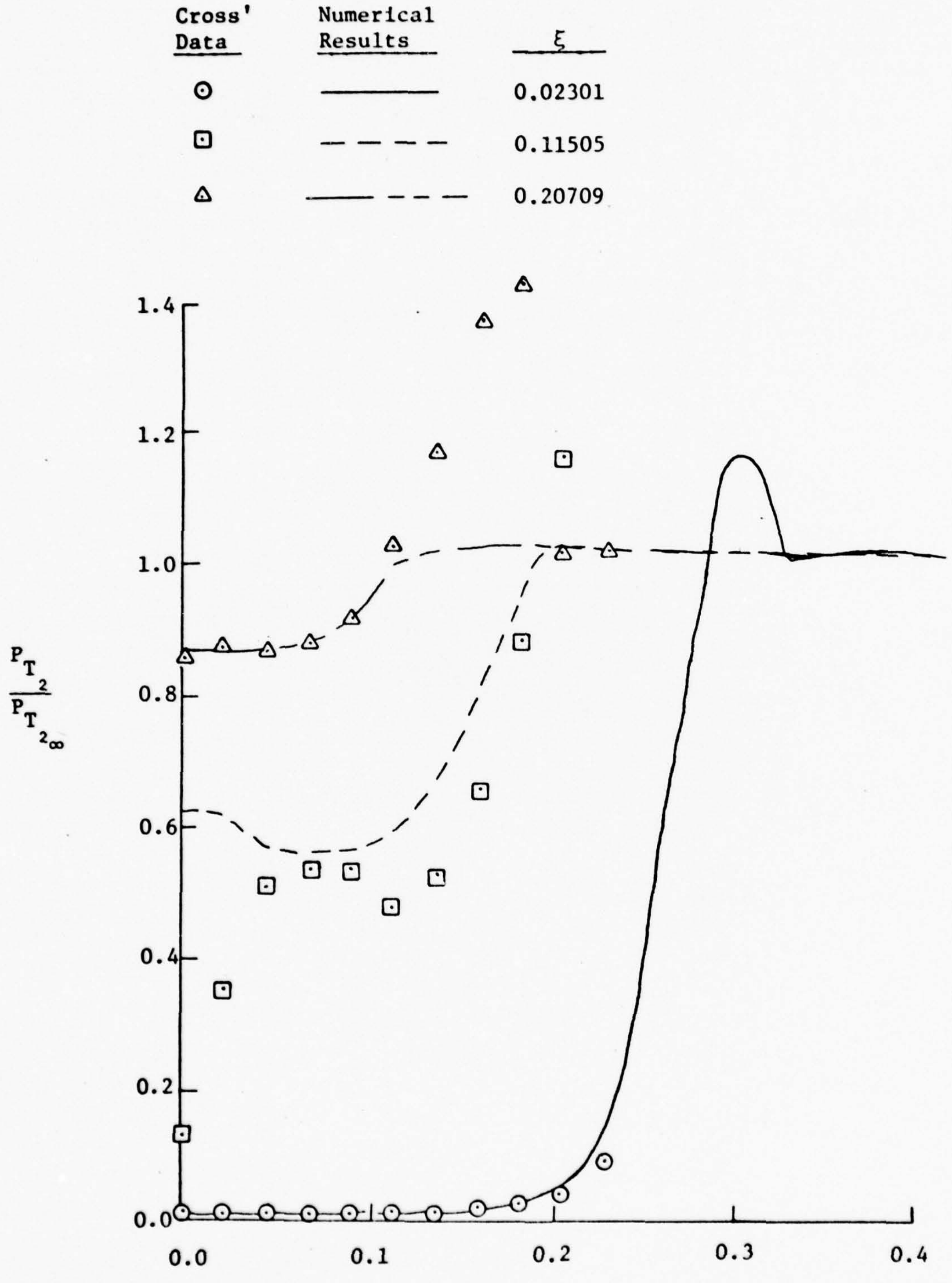

Fig. 28a. Impact Pressure Survey on Leeside of Delta Wing, $\alpha = 9^{o}$

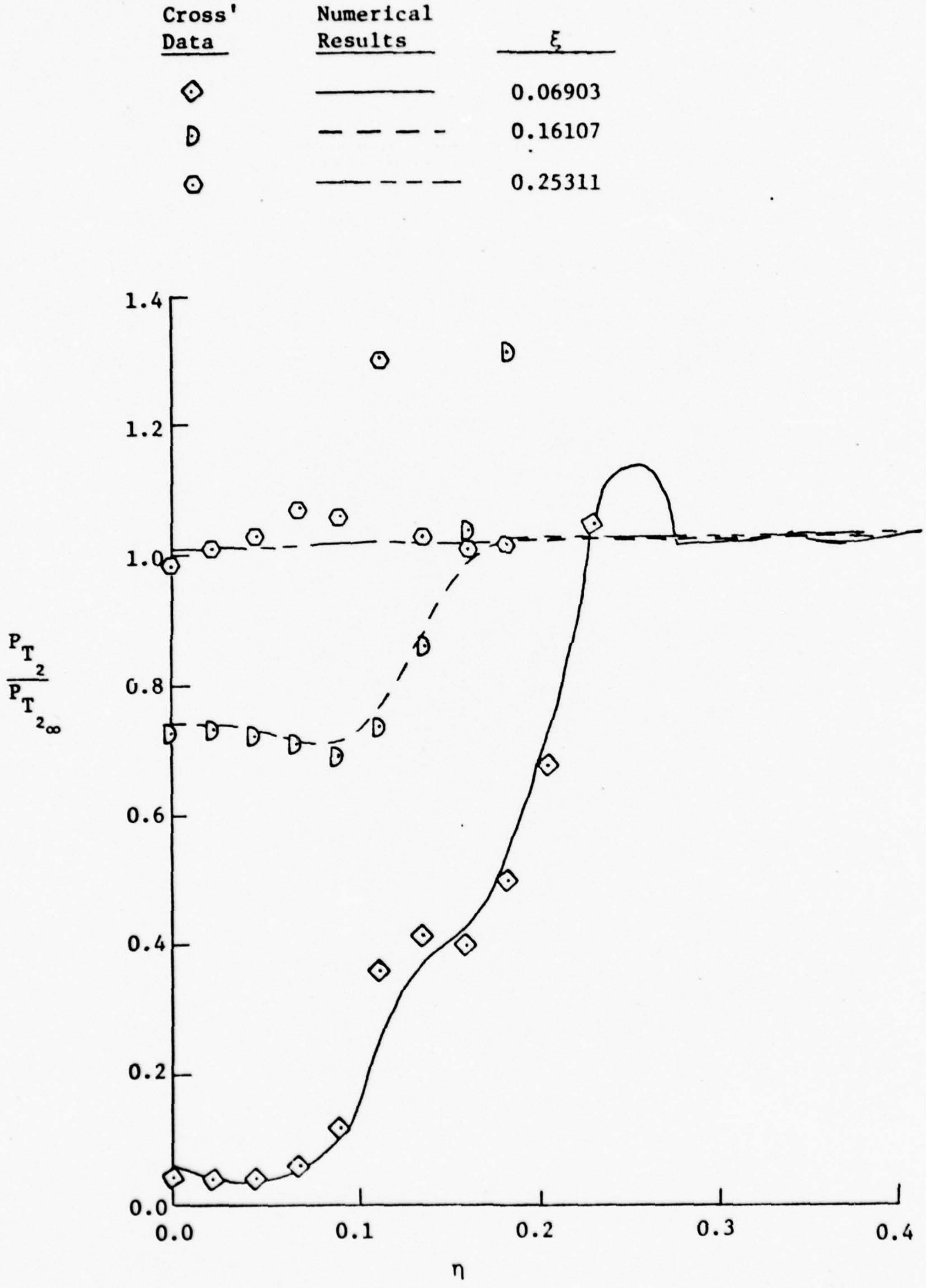

Fig. 28b. Impact Pressure Survey on Leeside of Delta Wing, α = 9°

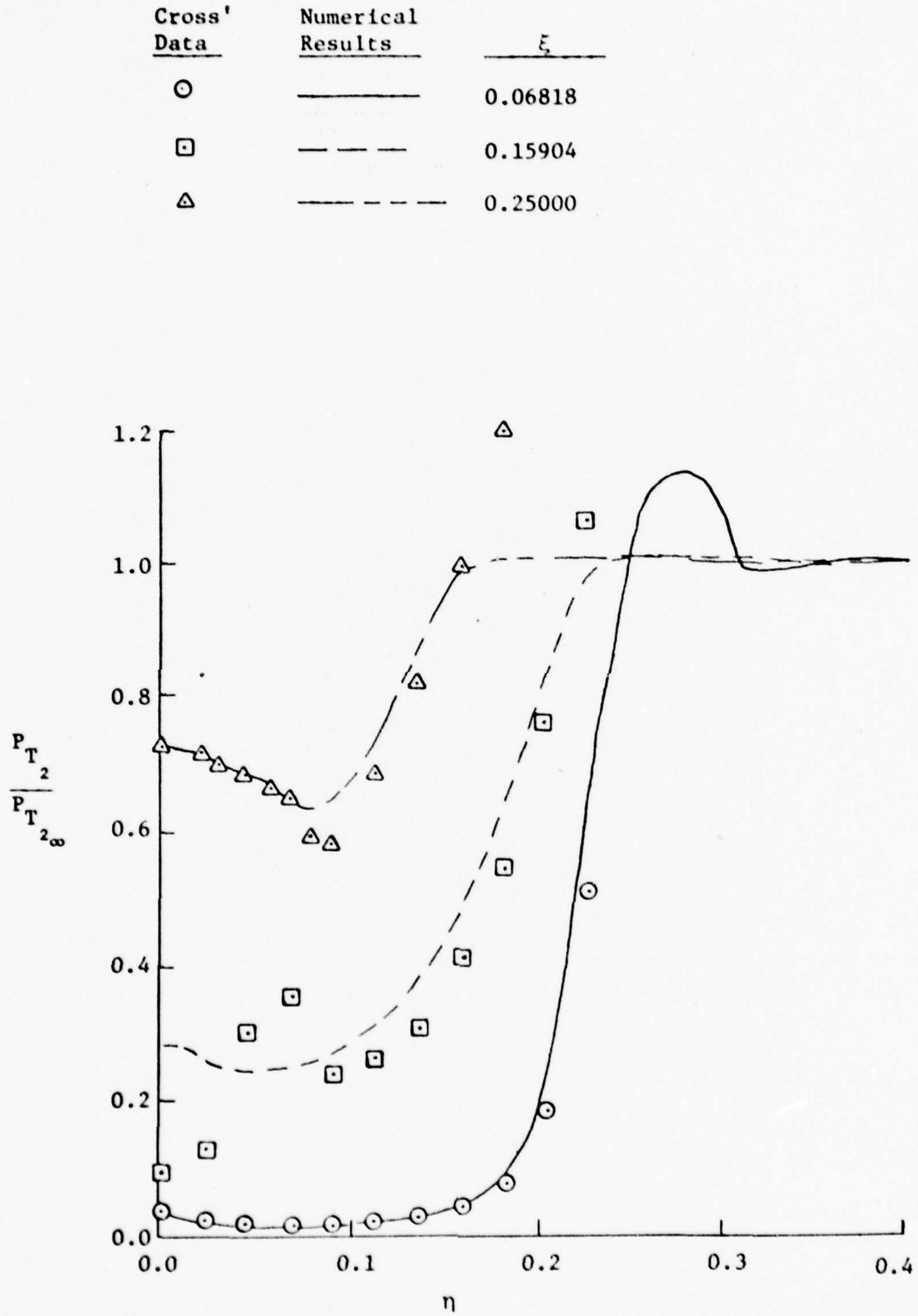

Fig. 29a Impact Pressure Survey on Leeside of Delta Wing, $\alpha = 15^{\circ}$

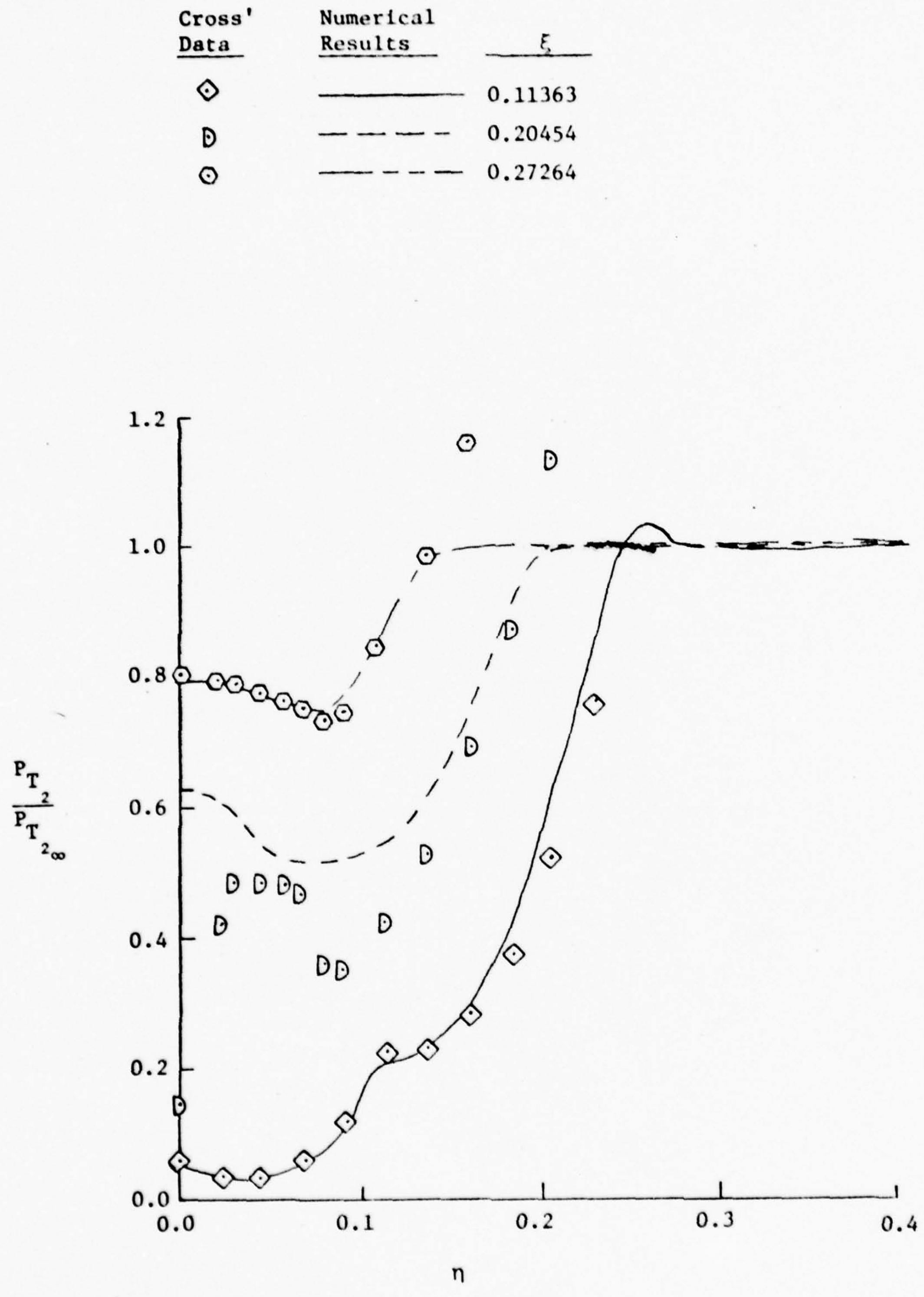

Fig. 29b. Impact Pressure Survey on Leeside of Delta Wing, α = 15°

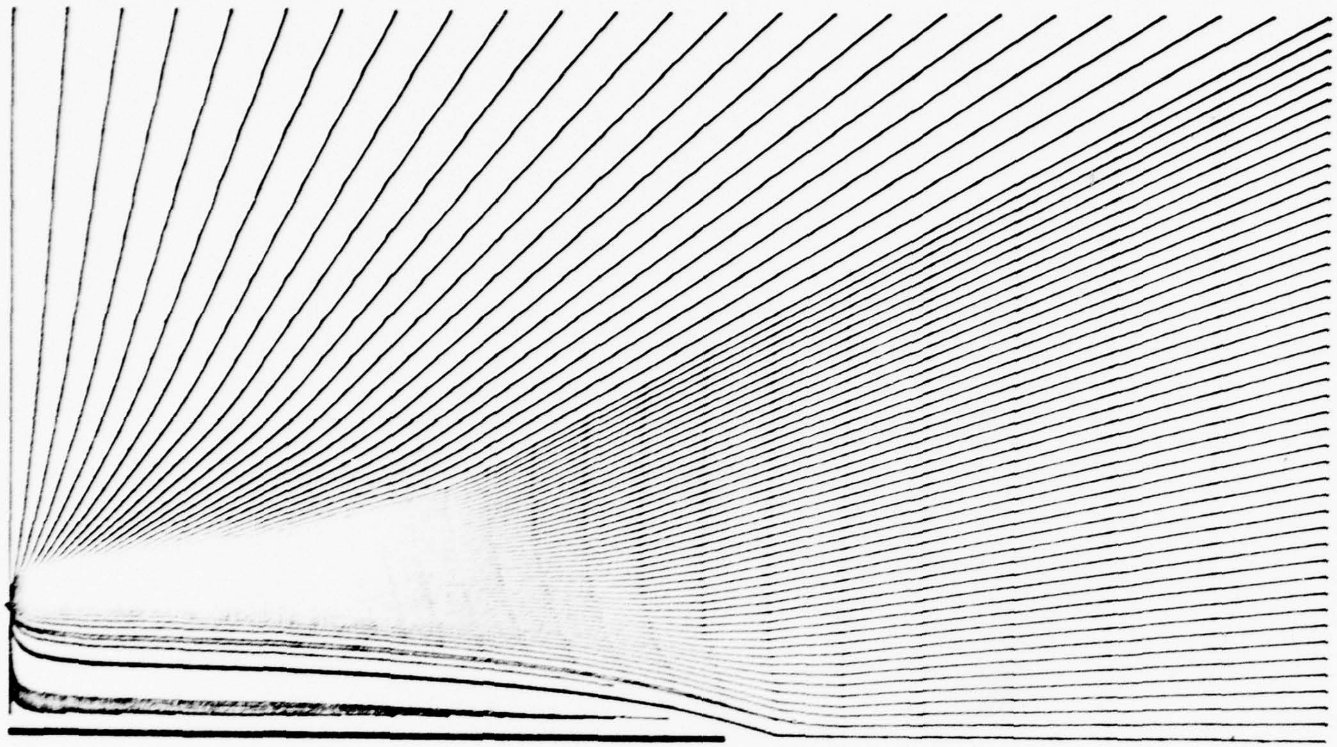

Fig. 30. Cross-Flow Streamline Plot as Projected on ξ-η Plane for Hypersonic Flow Above a Planar Delta Wing, $\alpha = 0^{\circ}$.

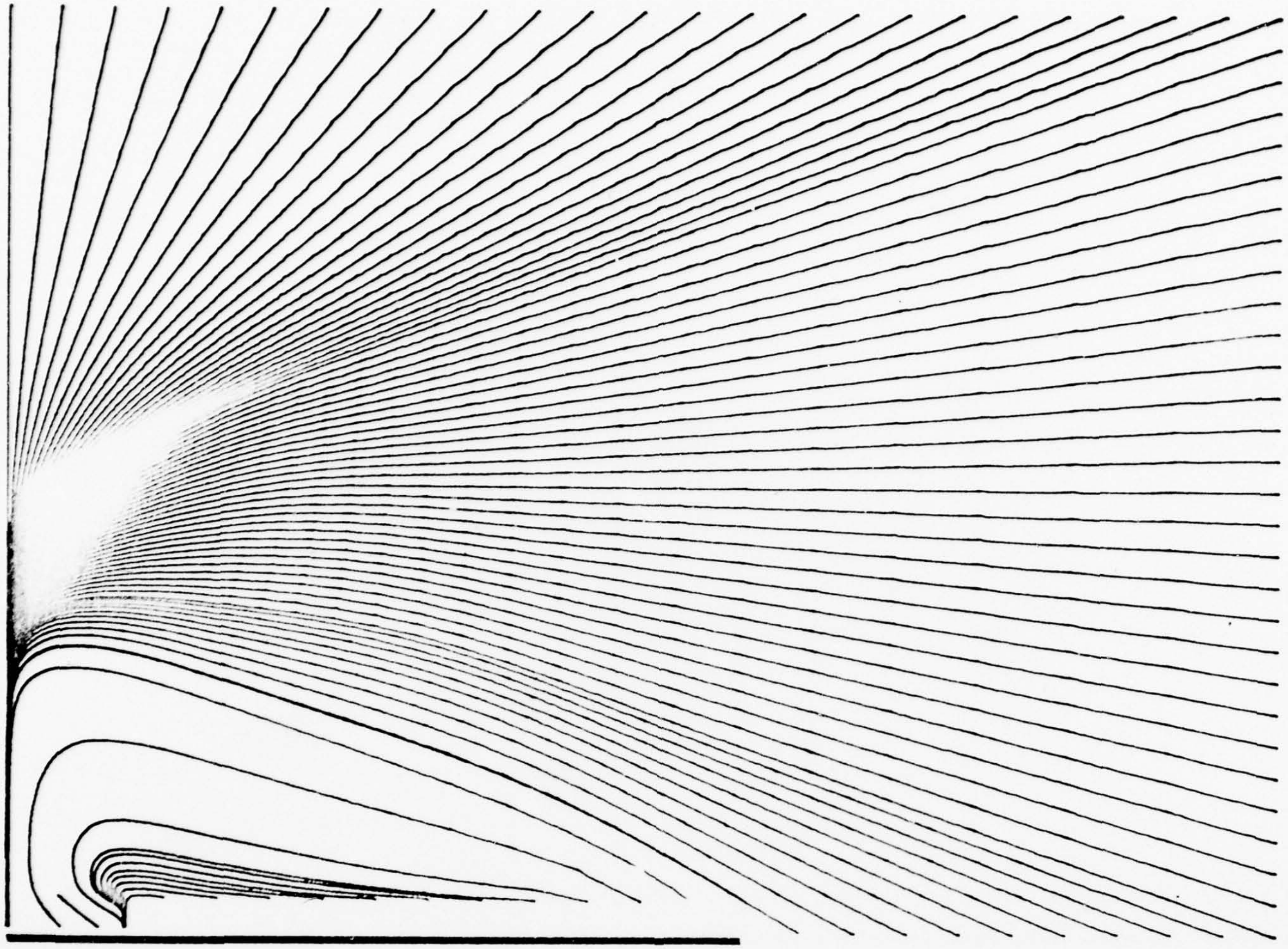

Fig. 31. Cross-flow Streamline Plot as Projected on the ξ-η Plane for Hypersonic Flow Above a Planar Delta Wing, $\alpha = 9^{0}$.

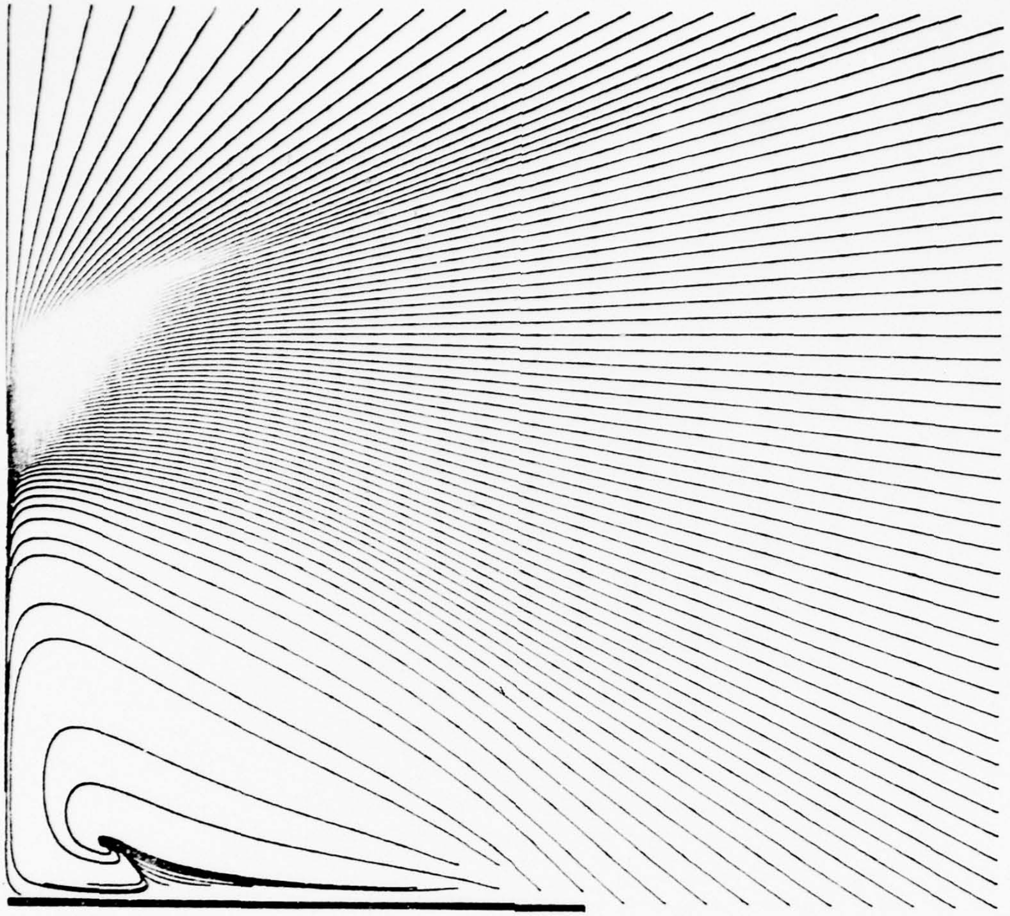

Fig. 32. Cross-flow Streamline Plot as Projected on ξ-η Plane for Hypersonic Flow Above a Planar Delta Wing, $\alpha = 15^\circ$

physical domain are shown in Figures 33 through 38. These contour plots depict the intricate flow field characteristics for $\alpha=0^{\circ}$ to $\alpha=15^{\circ}$. Numerical results from this study show that several significant changes occur in the flow as the angle of attack is increased. At $\alpha=0^{\circ}$, the cross-flow is dominated by a strong leading edge shock wave due to boundary layer displacement thickness (Fig 33). There is no internal shock and thus the boundary layer remains attached on the wing surface. The spanwise temperature distribution, as illustrated in Figure 34, indicates that the heat transfer is a minimum at the centerline and it increases rather sharply at the leading edge. As the angle of attack is increased, the bow shock is gradually weakened by a developing Prandtl-Meyer expansion fan over the leading edge. At $\alpha=9^{\circ}$, an internal shock is formed in the inviscid flow region. This internal shock is nearly normal to the wing surface, and at its lowest edge, is incident upon the upper surface of the viscous region (Fig 35). At $\alpha=15^{\circ}$, the internal shock wave and leading edge expansion fan are very strong, as seen by the highly concentrated density contour lines in Figure 36. The bow shock is weak and the pressure gradient normal to the wing surface in the viscous region is zero (Fig 37). Figure 38 shows a change in the temperature profile from that shown in Figure 34 for attached flow at $\alpha=0^{\circ}$. For separated flows, the temperature gradient (normal to the wing surface) decreases from a peak at the centerline, reaches a minimum and then increases to a maximum at the leading edge. This spanwise temperature behavior is similar to the experimental observations by Narayan (Ref 25) at $\alpha=15^{\circ}$.

In conclusion, it can be seen that the numerical method accurately predicts the basic elements of leeside hypersonic flow over a planar

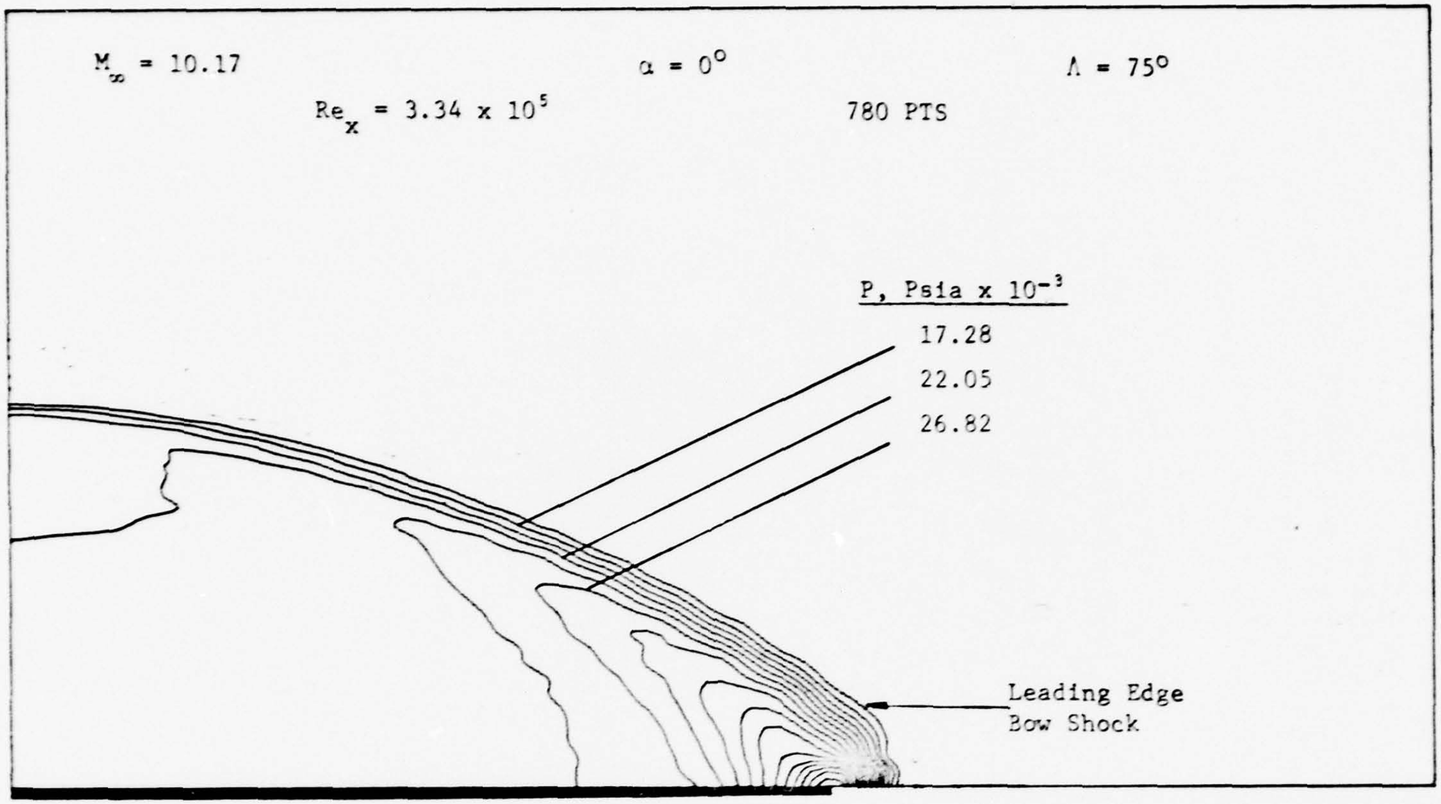

Fig. 33. Static Pressure in Cross-Flow Plane for Hypersonic Flow Above a Planar Delta Wing.

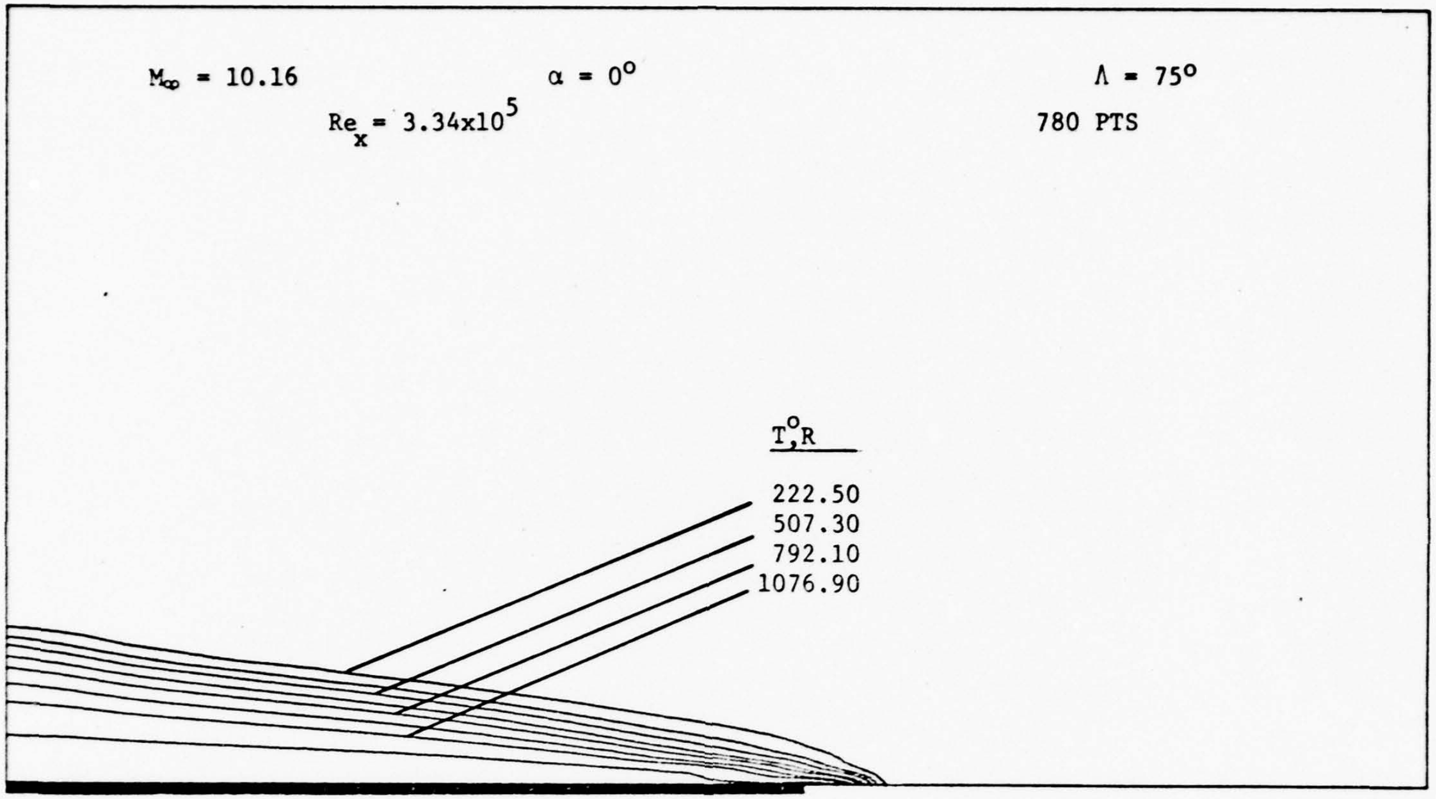

Fig. 34. Static Temperature Contour in Cross-flow Plane for Hypersonic Flow Above a Planar Delta Wing.

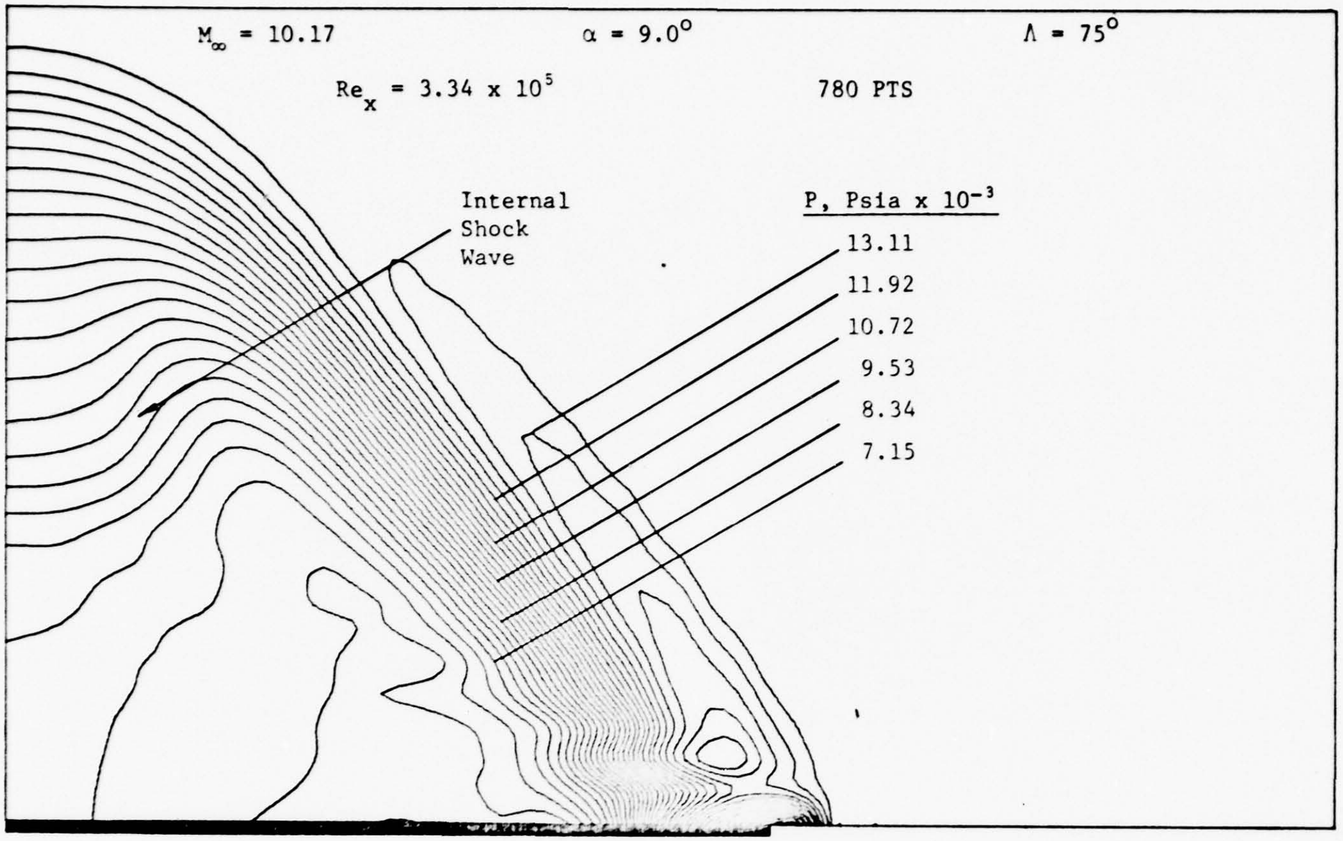

Fig. 35 Static Pressure Contour in Cross-Flow Plane for Hypersonic Flow Above a Planar Delta Wing.

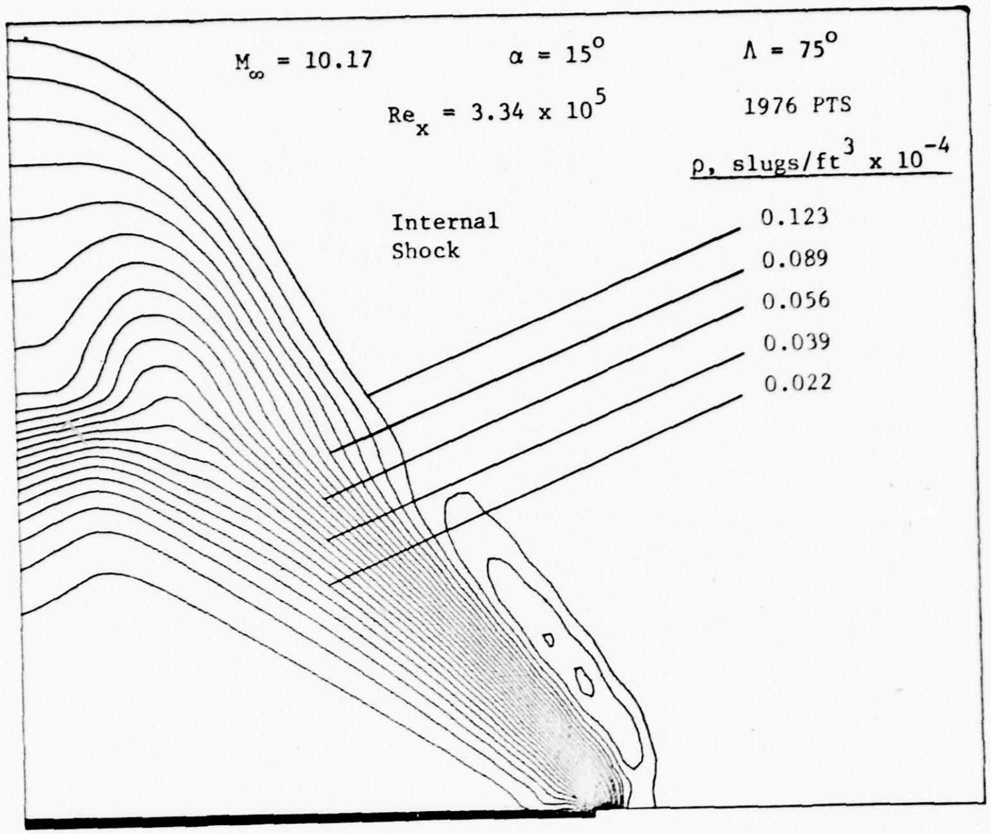

Fig. 36. Static Density Contour in Cross-flow Plane for Hypersonic Flow Above a Planar Delta Wing.

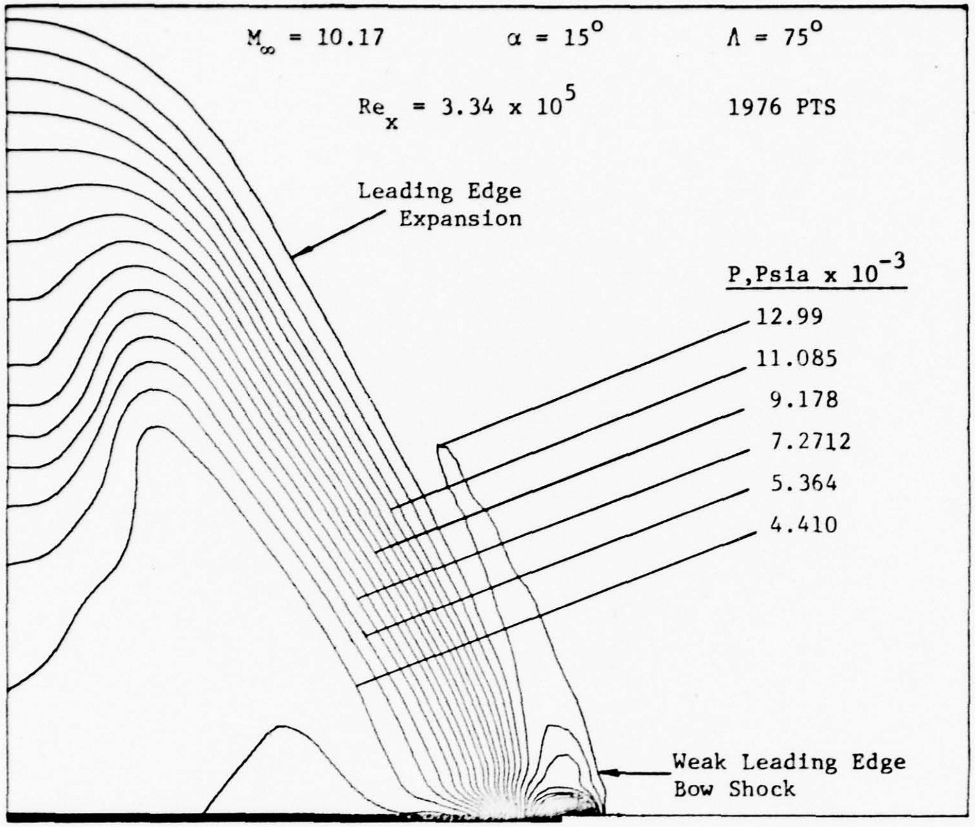

Fig. 37. Static Pressure Contour in Cross-flow Plane for Hypersonic Flow Above a Planar Delta Wing.

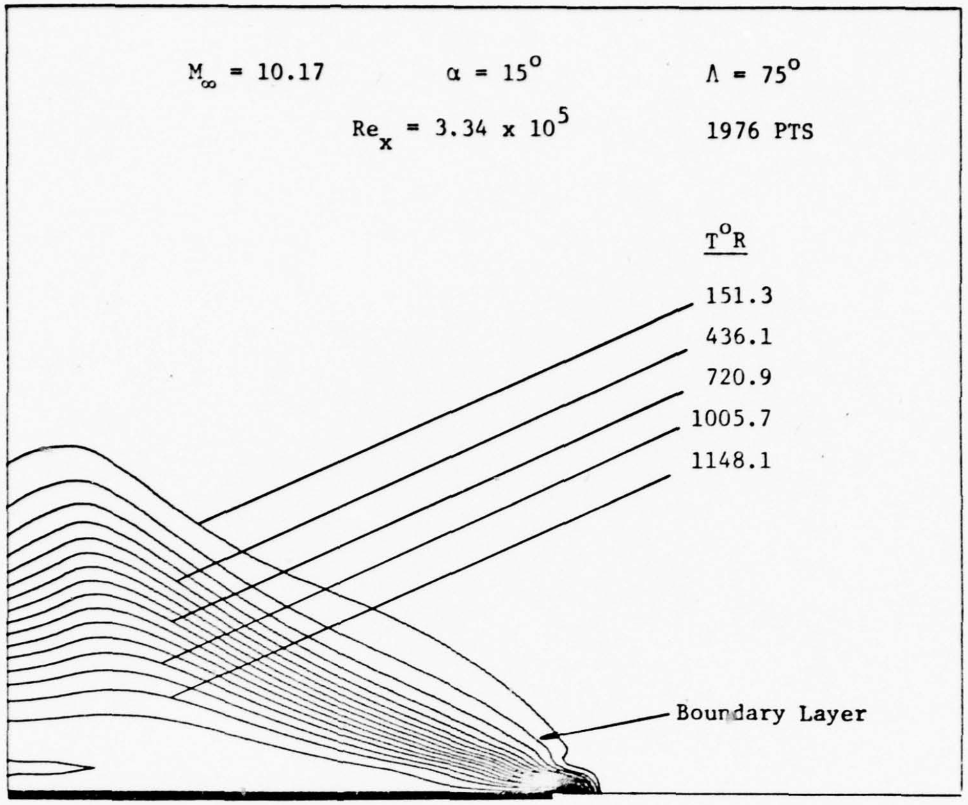

Fig. 38. Static Temperature Contour in Cross-flow Plane for Hypersonic Flow Above a Planar Delta Wing.

delta wing. For the first time in any calculation, the vortex development in the boundary layer of a delta wing is computed based on a strong shock wave-boundary layer interaction. The numerical results compare quite favorably with Cross' data as well as with the qualitative observations by Rao and Whitehead (Ref 131) and by Narayan (Ref 25). The discrepancies between the calculated and experimental results are due to not modeling the compression side flow field and not compensating for the three-dimensional effects around the wing vertex.

Delta Wing Compression Side Flow Analysis

The next phase in this investigation is to apply the conical, viscous flow approximation to a supersonic flow over the windward side of a planar delta wing. The purpose of this effort is to verify the applicability of this method in solving compression side flow fields. The same simplifying assumptions, which were used in the expansion side flow calculations, are applied in this calculation.

For this analysis, only one compression side flow field case is computed. The free stream conditions chosen for this calculation are

$M_\infty = 4.0$ $\Lambda = 50^\circ$

$Re_x = 5.0 \times 10^6$ $T_w = 530^\circ R$

$Pr = 0.72$ $\gamma = 1.4$

$\alpha = 15^\circ$ $\bar{\chi} = 0.028$

where T_w is equal to the free stream stagnation temperature. These flow conditions are identical to those used by Babaev (Ref 66), Voskresenskii (Ref 88), Beeman and Powers (Ref 68), and South and Klunker (Ref 67) in their inviscid analyses.

A 26(η)x45(ξ)array was used in this numerical calculation. This constant step size array was identical to the lower half of the grid system shown in Figure 9b. The η step size was 0.059936 with 14 grid points on the wing surface. The ξ step size was 0.00568. The free stream boundary locations were positioned far enough from the wing surface and bow shock so as not to affect the numerical solution. The results of this calculation are shown in Figures 39-45.

In Figure 39, the coefficient of pressure on the lower surface of a flat delta wing is plotted for various spanwise locations. The primary area of interest, in this figure, is the subsonic cross-flow region, where a variation in surface pressure occurs. The cross-flow sonic line (as seen in Fig 40) serves as a dividing line between the rotational and irrotational portions of the flow. Close agreement is seen between the subsonic numerical calculations and all of the analytical solutions, except Babaev's solution. In Babaev's method, an attempt is made to account for the singularity which occurs at the cross-flow sonic point (on the wing surface). The analytical surface pressure distribution should exhibit a "corner" or slope discontinuity at the cross-flow sonic point. However, Babaev's solution as well as all the other analytical solutions, show a very smooth pressure distribution at this point. Most of the other analytical techniques ignored this weak singularity.

Figures 40 through 43 illustrate the cross-flow Mach number, pressure, temperature, and density contours in the physical cross-flow plane, respectively. In Figure 40, the cross-flow Mach number contours based on the magnitude of the conical cross-flow velocity components are shown.

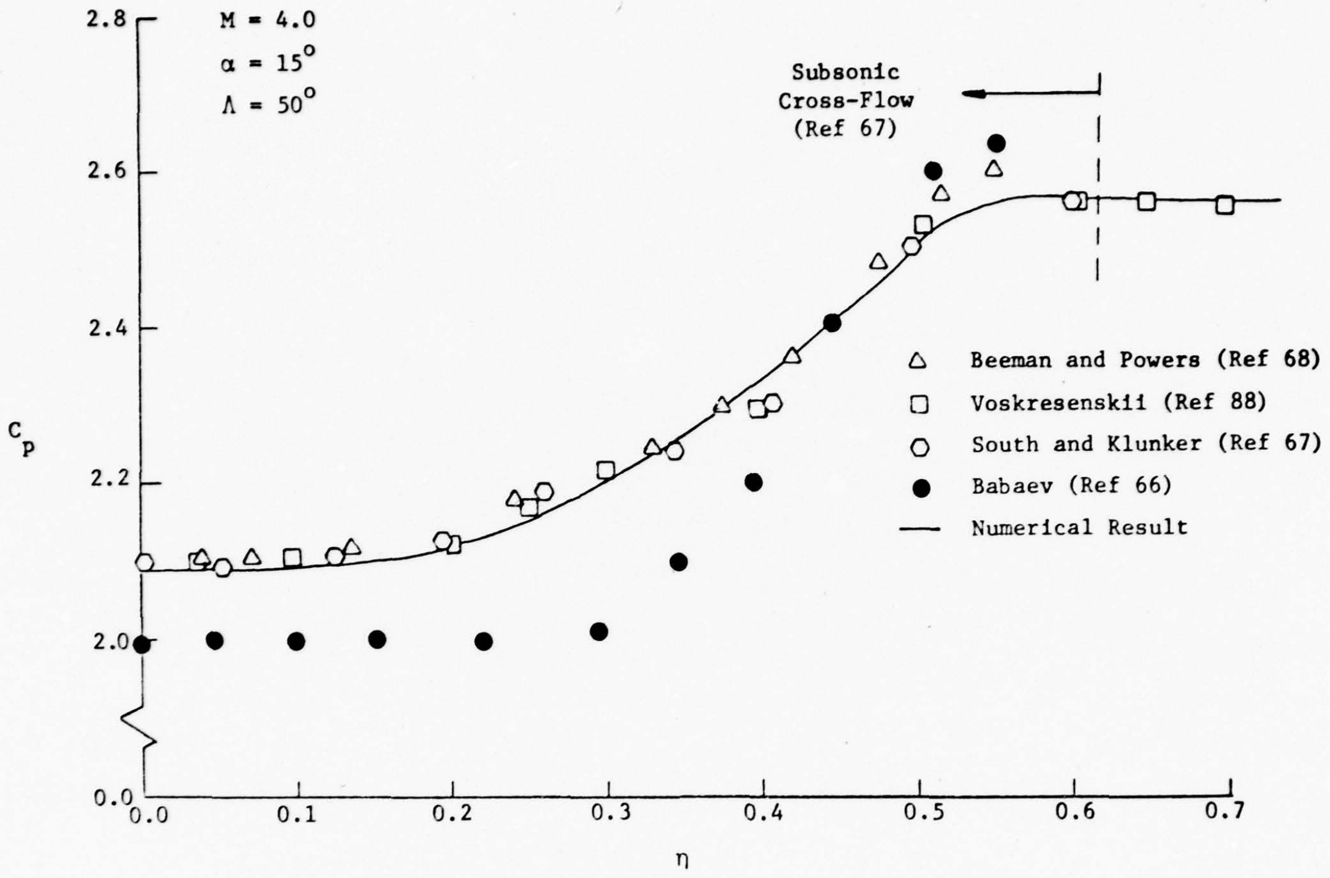

Fig. 39. Spanwise Pressure Distribution on Compression Side of Planar Delta Wing at Supersonic Speeds

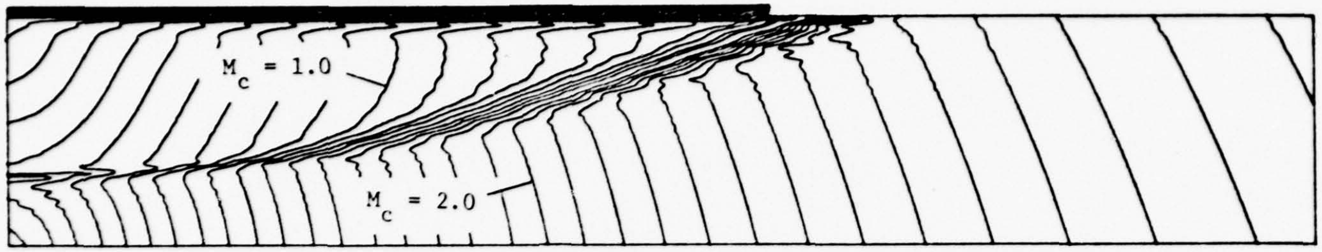

Fig. 40. Mach Number Contour in Cross-flow Plane for Supersonic Flow Below a Planar Delta Wing.

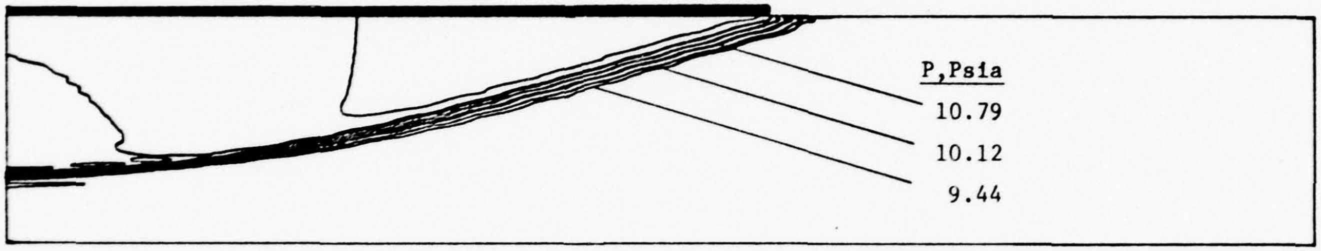

Fig. 41. Static Pressure Contour in Cross-flow Plane for Supersonic Flow Below a Planar Delta Wing.

This figure defines the cross-flow subsonic and supersonic regions and the sonic line that separates these regions. The sonic point is located at the base of the sonic line in the boundary layer or on the wing surface (inviscid solution only). The shock wave from the leading edge to the sonic line is approximately planar, as seen in Figure 41. The inviscid, analytical shock angle, relative to the leading edge, is 21.3° compared with approximately 18.5° numerically. There is no normal pressure gradient in the boundary layer and the shock weakens slightly as it curves toward the wing surface and approaches the plane of symmetry. In Figures 42 and 43, strong density and temperature gradients exist in the thin boundary region.

The cross-flow velocity vectors and resulting conical streamlines are shown in Figures 44 and 45, respectively. The significant change in magnitude and direction of the cross-flow velocity vectors near the shock wave indicate that the compression side bow shock is very strong. The streamline contours show that a vortical singularity exists near the wing surface on the plane of symmetry. This is consistent with the analytical results by Voskresenskii (Ref 88) and Melnik (Ref 19).

In conclusion, it can be seen that this numerical technique accurately predicts the basic characteristics of a compression side flow field. The supersonic numerical results compare quite favorably with several inviscid analytical solutions. These calculations show that this conical, viscous approximation technique can be accurately applied to high Reynolds number, viscous compression side flow fields.

Total Delta Wing Flow Analysis

The final phase in this investigation is to examine and calculate the total supersonic and hypersonic flow field around a thin planar

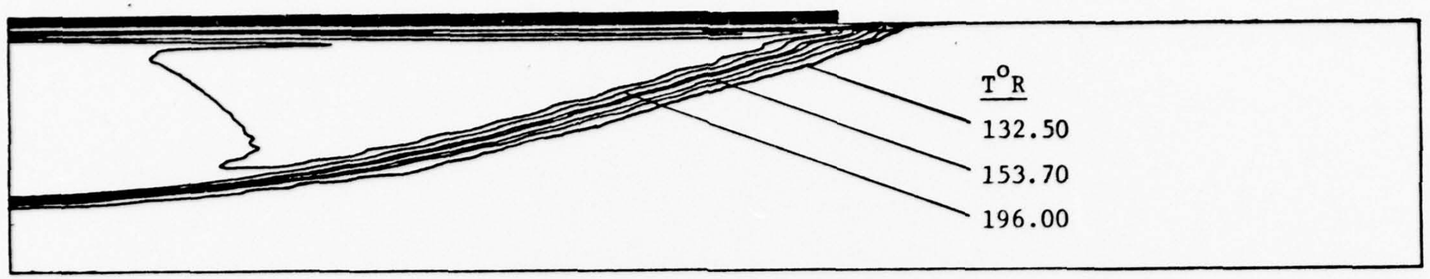

Fig. 42. Static Temperature Contour in Cross-flow Plane for Supersonic Flow Below a Planar Delta Wing

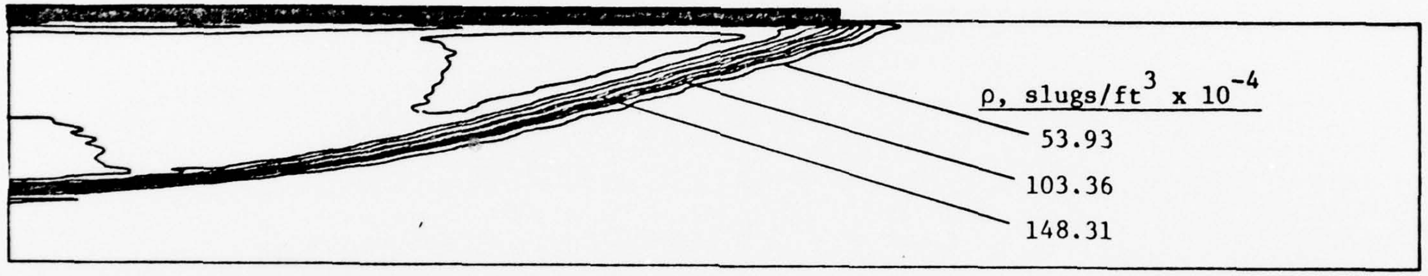

Fig. 43. Static Density Contour in Cross-flow Plane for Supersonic Flow Below a Planar Delta Wing

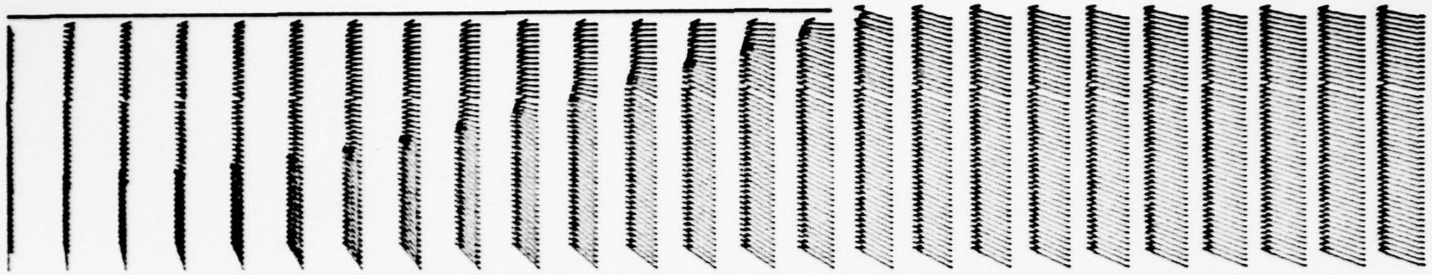

Fig. 44. Cross-flow Vector Velocity Plot as Projected on ξ-η Plane for Supersonic Flow Below a Planar Delta Wing, $\alpha = 15^{\circ}$.

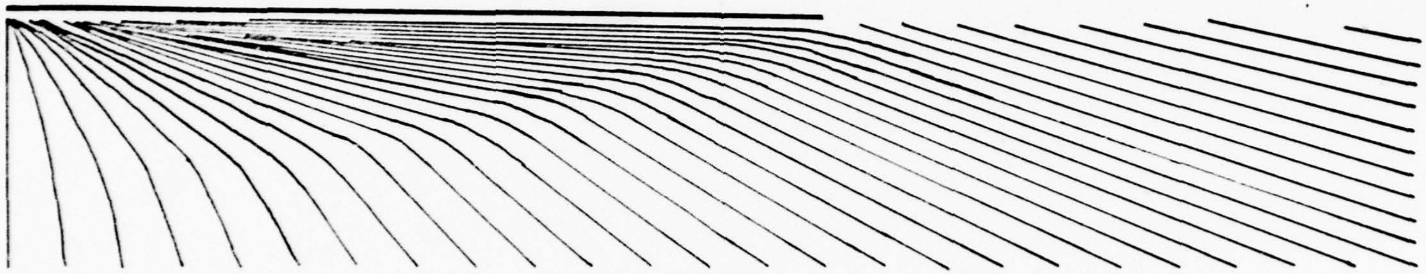

Fig. 45. Cross-flow Streamline Plot as Projected on ξ-η Plane for Supersonic Flow Below a Planar Delta Wing, $\alpha = 15^{\circ}$

delta wing. Previous calculations in this study have demonstrated the applicability of the conical, viscous approximation in separately solving flows over either the leeside and or the compression side of flat delta wings. However, it is still necessary to verify this concept in solving the total flow field around a thin planar delta wing. Thus, the purpose of this analysis is to examine and evaluate the use of the conical, viscous approximation in solving the total delta wing flow field. In this calculation, the upper and lower surface flow fields are allowed to interact with each other in reaching a steady state solution. However, the three-dimensional effects generated by the wing vertex are still neglected in solving this flow problem.

Supersonic Flow. For the supersonic flow analysis, the experimental test conditions used by Bannink and Nebbeling (Ref 15) are applied in this calculation. These flow conditions are

$M_\infty = 2.94$ $\qquad$ $T_o = 544^\circ R$

$Re_x = 2.64 \times 10^6$ $\qquad$ $P_o = 96$ psia

$Pr = 0.72$ $\qquad$ $\gamma = 1.4$

$\alpha = 12^\circ$ $\qquad$ $T_w = 199.5^\circ R$

$\bar{\chi} = 0.02$

where the Reynolds number is based on a root chord length of 0.173 ft. This is the same case examined for the leeside-only solution.

The computational domain, as shown in Figure 9b, consisted of a $26(\eta)\times 59(\xi)$ grid array with 29 rows of ξ grid points above and below the wing surface. The η step size was 0.063158 with 14 grid points used to model the wing. A constant, but different, ξ step size was used for each measurement height (pitot pressure measurements by Bannink, Ref 15) so that experimental and numerical results could be compared without interpolation. The free stream boundaries were located far enough from the wing surface so as not to affect the numerical solution. The results of these calculations are shown in Figures 46-52.

In Figures 46 and 47, several spanwise pitot pressure measurements are shown for various heights above the delta wing. The numerical results are compared with the inviscid solutions by Kutler (Ref 89) and with the experimental data by Bannink and Nebbeling (Ref 15). It can be seen that the total numerical flow field solution is similar to that of the expansion-side-only supersonic solution. The only significant difference is that the bow shock in the leeside flow field is slightly stronger for $\xi \leq 0.3626$. This is due to the influence of the lower surface shock wave as it encircles the leading edge of the wing. The coarse grid spacing and the use of the numerical shock capturing technique results in smearing the shock over several grid points. This causes the leeside shock to be displaced slightly upstream of the measured bow shock location. A similar error was noted by Bazzhin (Ref 92) in his delta wing calculations.

Figure 48 depicts the conical cross-flow velocity components projected on the η-ξ plane. On the compression side, the bow shock is clearly delineated by an abrupt change in strength and direction of the velocity vectors. The locus of the velocity vectors trace out "pseudo" streamlines which converge at two vortical singularity points. These vortical singularity points are located above and below the wing

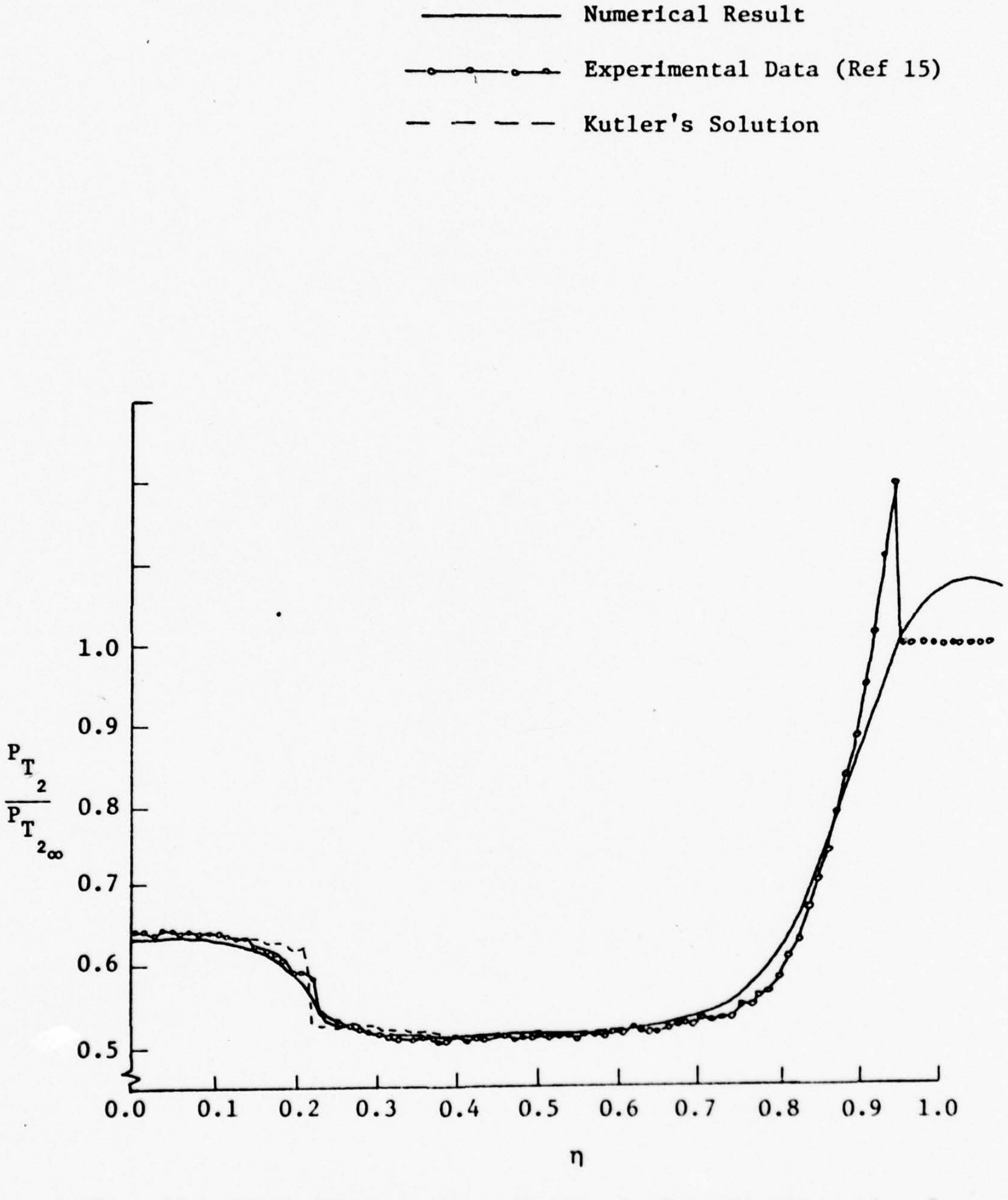

Fig. 46. Pitot Pressure Distribution in Spanwise Direction for Supersonic Flow Above a Planar Delta Wing, $\xi = 0.0718$.

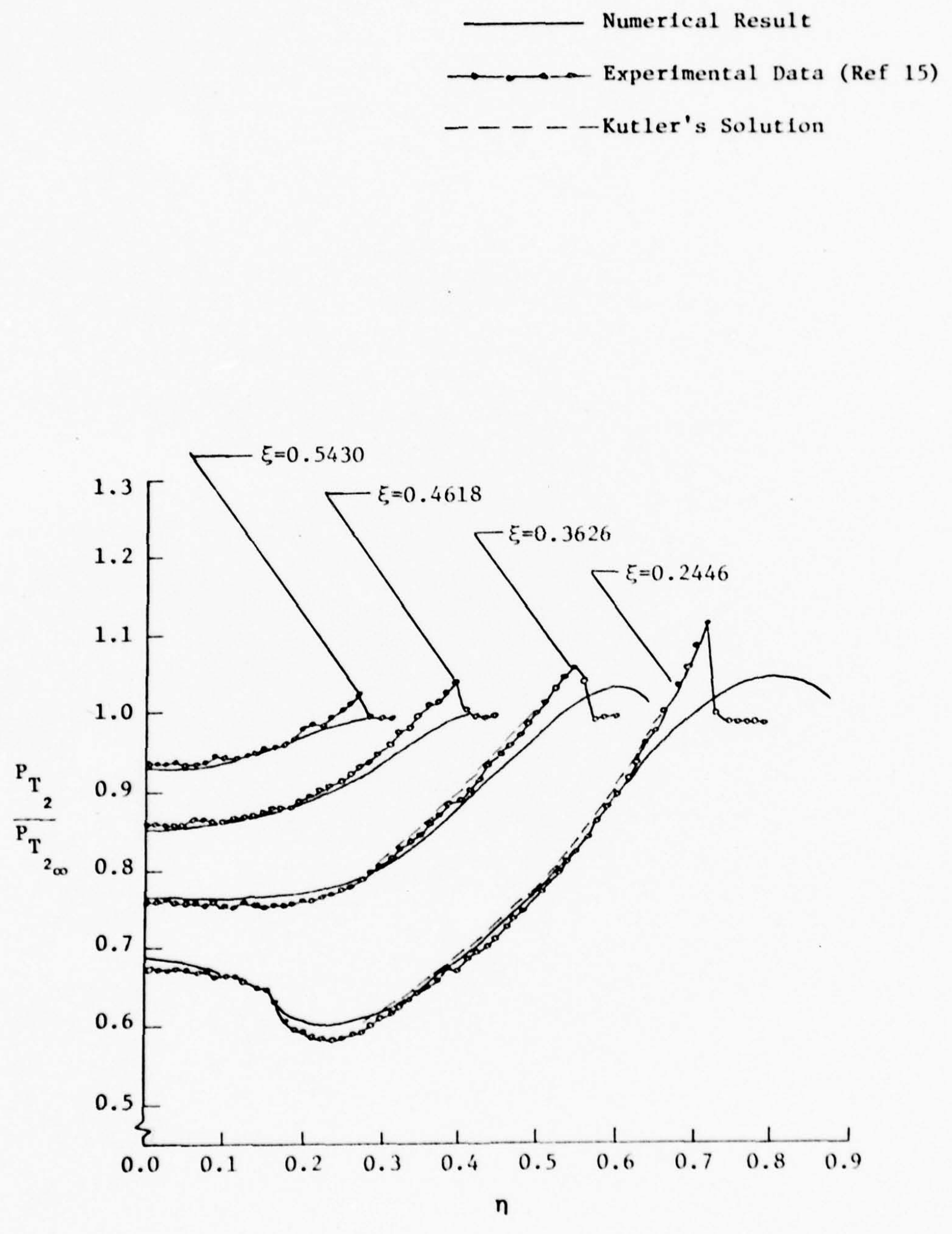

Fig. 47. Pitot Pressure Distribution in Spanwise Direction for Supersonic Flow Above a Planar Delta Wing.

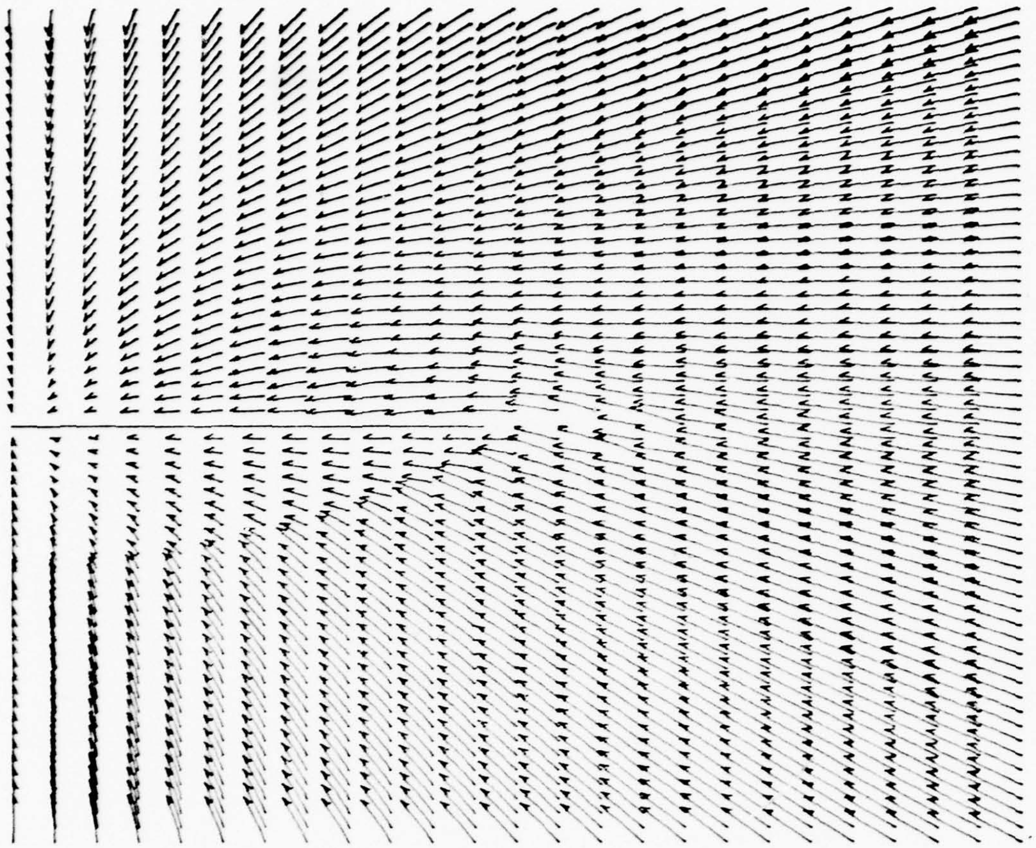

Fig. 48. Cross-flow Velocity Vector Plot as Projected on ξ-η Plane for Supersonic Flow Around a Planar Delta Wing, $\alpha = 12^{\circ}$

surface near the origin of the coordinate system. Figure 49 illustrates some of the conical cross-flow streamlines (1550 points) and how these steady state path lines converge toward the two vortical singularity points. These streamline results are consistent with the inviscid, analytical solutions by Melnik (Ref 19) and with the experimental observations by Bannink and Nebbeling (Ref 15).

The pressure, temperature, and density contour plots for the physical cross-flow plane are shown in Figures 50-52. The wing thickness is exaggerated in these figures in order to clearly depict its location. A total of 1550 data points were used to produce these contours including a set of double-values grid points representing the wing surface. In Figure 50, the isobars indicate that a strong shock wave is formed below the delta wing. This shock wave weakens slightly as it bends toward the wing surface and approaches the plane of symmetry. The influence of this compression wave is felt above the delta wing, as seen by the contour lines encircling the leading edge of the wing. A large leading edge expansion fan is formed above the wing surface and inboard of the bow shock. This expansion fan weakens the leeside internal shock wave and eventually transforms it into a conical sonic line. Along the wing surfaces, the boundary layers are very thin and the pressure gradients normal to these surfaces (in the ξ direction) are zero.

As seen in Figure 51, a strong temperature gradient exists in both boundary layers. This temperature gradient (normal to the wing surface) is particularly strong near the leading edge. In Figure 52, it can be seen that the leeside internal shock wave-boundary layer interaction is very weak and that no flow separation occurs at the base of the shock wave.

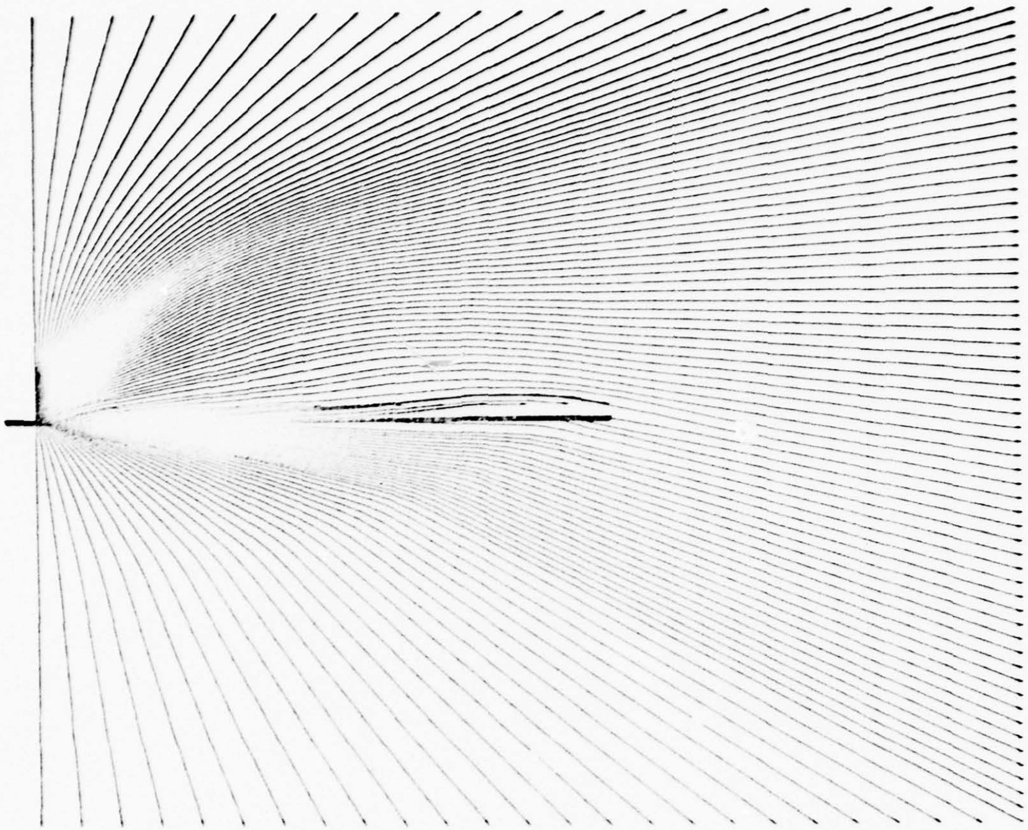

Fig. 49. Cross-flow Streamline Plot as Projected on ξ-η Plane for Supersonic Flow Around a Planar Delta Wing, $\alpha = 12^\circ$

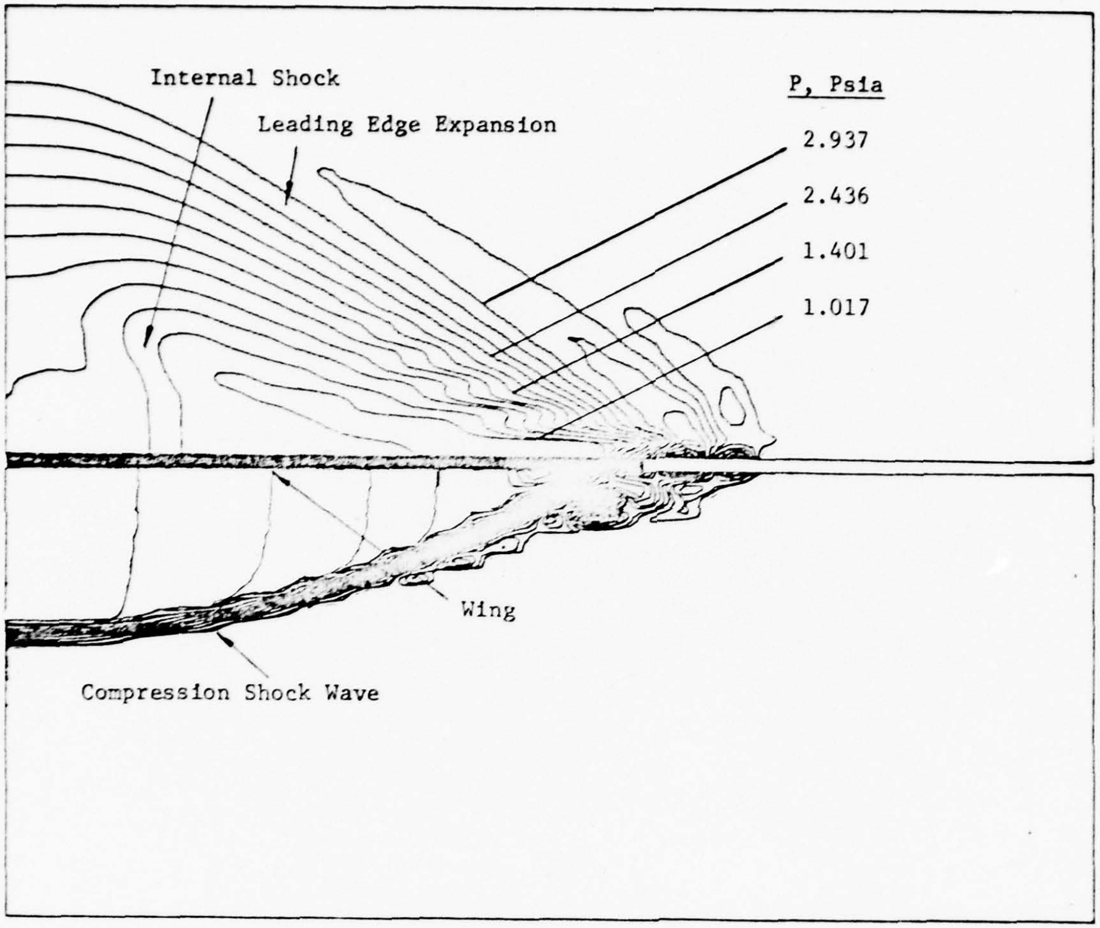

Fig. 50. Static Pressure Contour in Cross-flow Plane for Supersonic Flow Around a Planar Delta Wing.

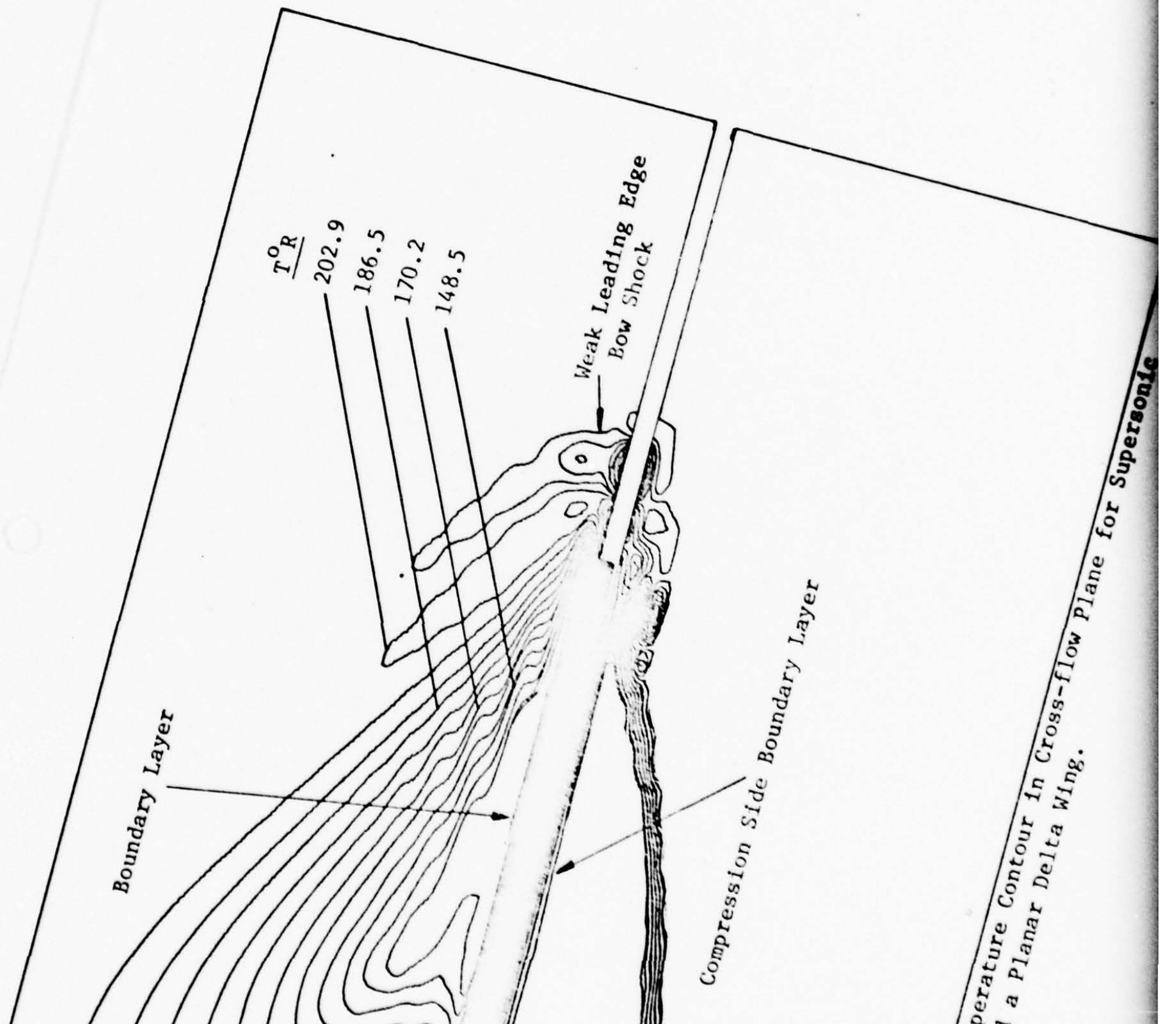

Fig. 51. Static Temperature Contour in Cross-flow Plane for Supersonic Flow Around a Planar Delta Wing.

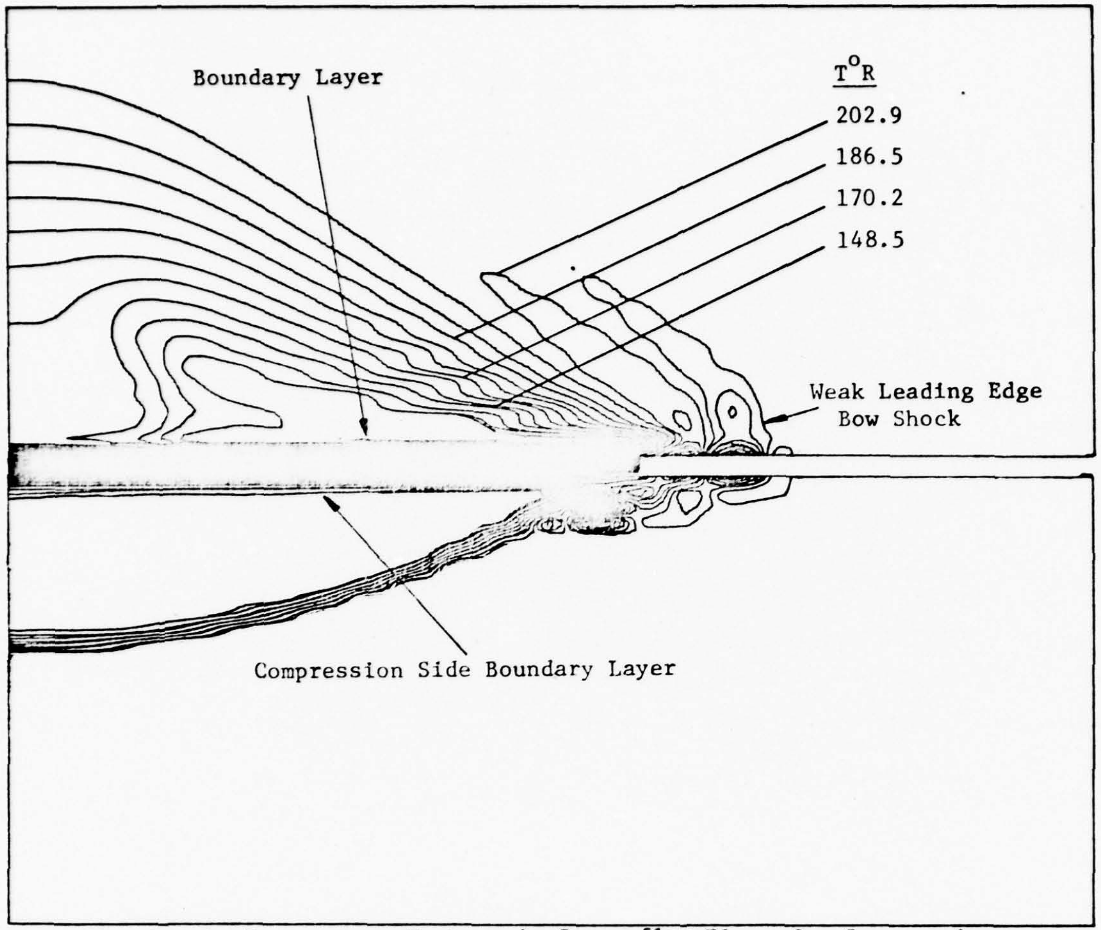

Fig. 51. Static Temperature Contour in Cross-flow Plane for Supersonic Flow Around a Planar Delta Wing.

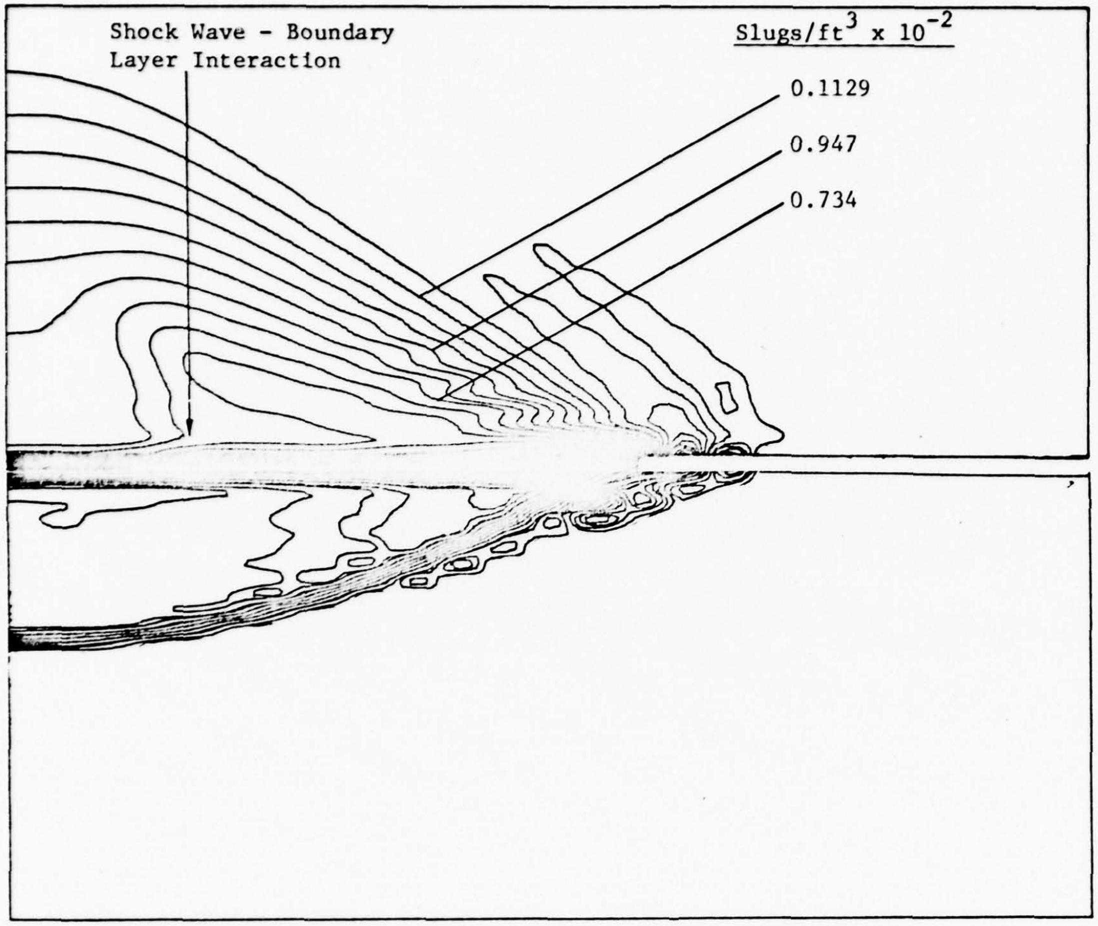

Fig. 52. Static Density Contour in Cross-flow Plane for Supersonic Flow Around a Planar Delta Wing.

In summary, the numerical solution of the supersonic flow around a thin, planar delta wing provides a more accurate and complete solution of the delta wing flow field than does the leeside-only solution. This total flow field solution contains all the basic elements of the flow and these results compare quite favorably with Bannink's experimental data. The discrepancies noted in comparing numerical and experimental results are due to three-dimensional effects in the viscous region, use of a coarse grid in the computational plane, and not properly modeling the delta wing thickness. However, the results indicate that the three-dimensional flow field can be approximated by using a two-dimensional conical, viscous flow field model which would be useful in design applications.

Hypersonic Flow. For the hypersonic flow field analysis, the free stream and surface boundary conditions chosen for this calculation are

$M_\infty = 10.17$ $\quad$ $T_o = 1780^\circ R$

$Re_x = 3.345 \times 10^5$ $\quad$ $P_o = 596$ psia

$Pr = 0.72$ $\quad$ $\gamma = 1.4$

$\bar{\chi} = 1.8$ $\quad$ $T_w = 1259.7^\circ R$

$\alpha = 0^\circ, 5^\circ, 9^\circ, 11^\circ$, and 15° $\quad$ $\Lambda = 75^\circ$

where the Reynolds number is based on a reference length of $x = 5.5 \sec \alpha$ inches. These flow conditions are the same as those used by Cross (Ref 17) in his experimental studies of the hypersonic flow over the leeside of a flat delta wing.

In this investigation, a constant-step size array (Fig 9b) was used to calculate the flow field. This computational domain consisted of a $26(\eta)\times 120(\xi)$ grid array with 75 rows of ξ grid points above the wing and 44 rows below the wing. The η step size was 0.019139 with 14 grid points on the wing surface. The ξ step size, for all the hypersonic cases, was 0.00568. The exterior or free stream boundaries were located far enough from the wing surface so as not to affect the numerical solution. The results of these calculations are shown in Figures 53-73.

In Figure 53, a comparison is made between the measured and calculated edge of the viscous region. This boundary layer profile is determined by evaluating the impact pressure distribution in the ξ-direction similar to what is done in Ref 17. For $\alpha \leq 5^\circ$, the edge of the calculated viscous region is very similar to that predicted by two-dimensional laminar boundary layer theory. The computed boundary layer thickness, δ, for $\alpha = 0^\circ$, is identical to that calculated for the expansion-side-only solution; however, for $\alpha = 5^\circ$, δ is greater and more accurate than the leeside-only result. At $\alpha = 9^\circ$, a centerline trough is computed in the cross-flow viscous profile. This trough is generated by a developing shock-induced vortex in the boundary layer. For $\alpha \geq 11^\circ$, a large viscous bubble or "hump" appears in the plane of symmetry of the boundary layer edge. This viscous bubble occurs as a result of shock-induced separation behind a strong leeside bow shock. This strong bow shock is clearly depicted in the contour plots shown later in Figures 71 and 72. Good qualitative agreement is seen between the experimental and calculated results even though the computed boundary layer thickness is slightly greater than the measured value.

In Figure 54, the bow shock location on the expansion side of the delta wing is shown for various angles of attack. For $\eta \geq 0.1$, the

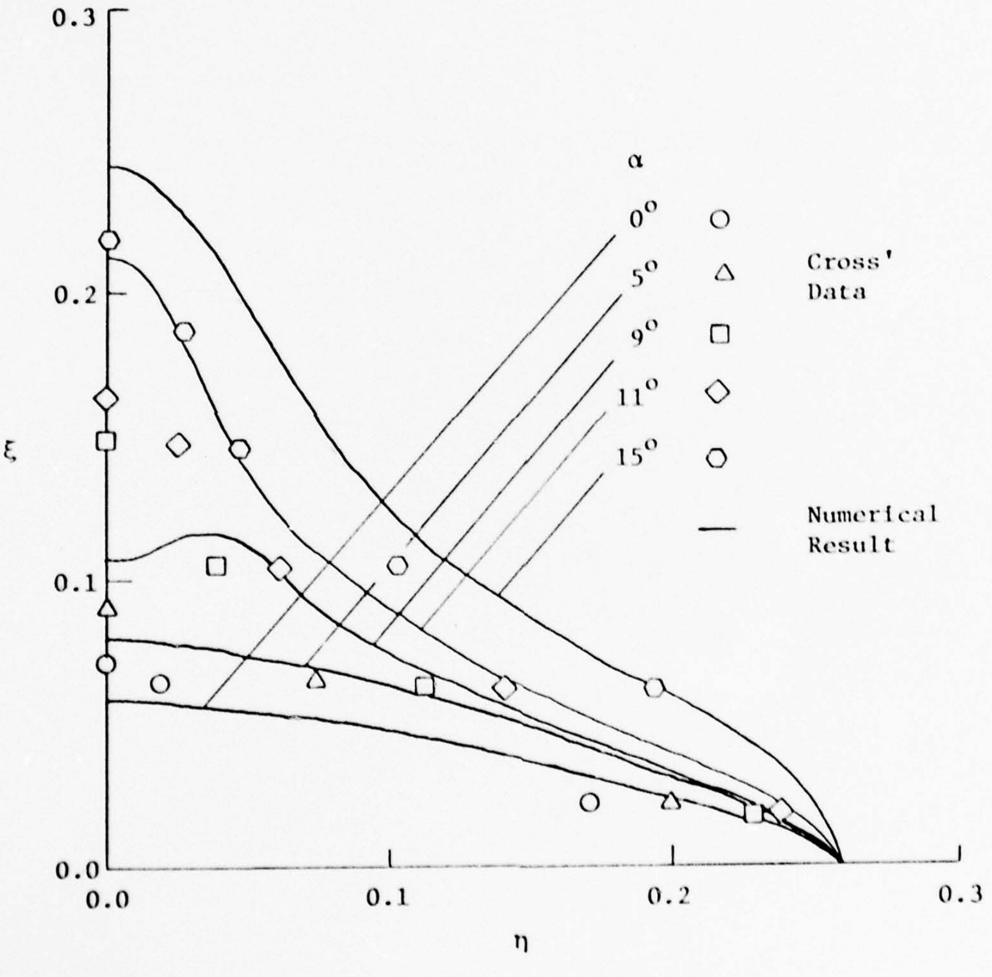

Fig. 53. Hypersonic Viscous Layer Development Above a Delta Wing as Determined by Impact Pressure Measurements.

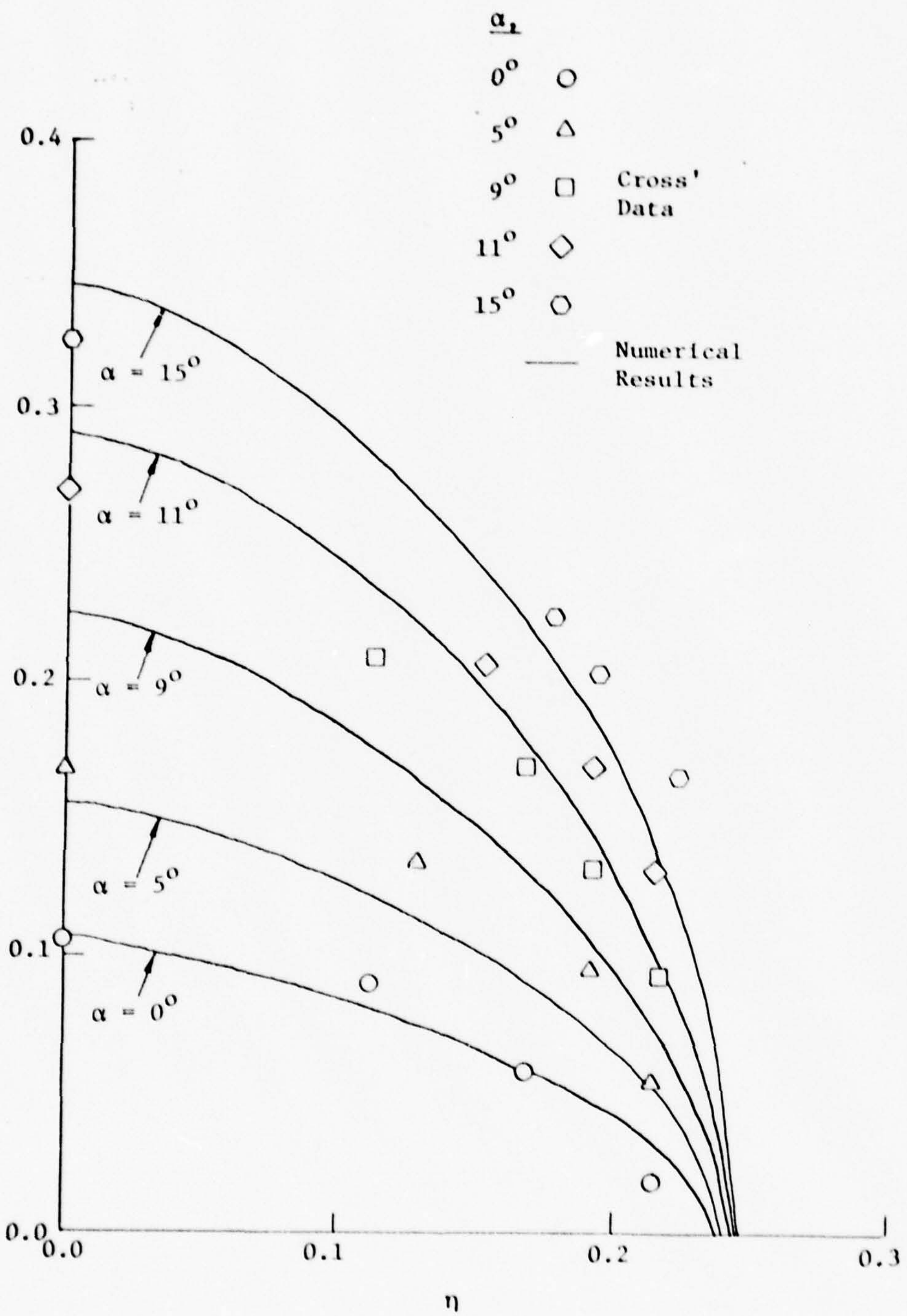

Fig. 54. Hypersonic Bow Shock Profile Above a Delta Wing.

calculated shock profile is slightly less than the measured shock location. This discrepancy occurs because the displacement thickness of the thin, planar delta wing is smaller than that of the actual wind tunnel model. Along the plane of symmetry, good agreement is seen between the calculated and measured shock shape for $\alpha \leq 5^{o}$. However, for $\alpha > 11^{o}$, the numerical shock profile is slightly greater than the experimental value. This error is due to the displacement effects of the calculated boundary layer in the symmetry plane.

The impact pressure distribution for various angles of attack and ξ-positions is shown in Figures 55 through 58. Figure 55 illustrates the comparison between experimental and calculated impact pressure results for $\alpha = 0^{o}$. These results are similar, but more accurate than the leeside-only results, particularly at ξ=0.1136. Along the plane of symmetry, the calculated boundary layer thickness is slightly less than the measured value. This discrepancy is very apparent at ξ=0.0682, where a large difference exists between the measured and calculated impact pressures. Figures 56a and 56b depict the impact pressure results for $\alpha = 5^{o}$. In these figures, a closer agreement is again seen between theory and experiment. The calculated pressure ratio across the bow shock is stronger than that of the leeside-only solution, but weaker than the experimental results. The flow resolution around the shock wave is poor due to shock smearing in the coarse computational grid. Similar results are seen for $\alpha = 9^{o}$ (Figs 57a and 57b) and for $\alpha = 15^{o}$ (Figs 58a and 58b). However, for $\alpha = 15^{o}$, the three-dimensional effects near the centerline are more dominant, as seen at ξ=0.15904 and ξ=0.20454.

The conical cross-flow velocity vectors and streamline plots for

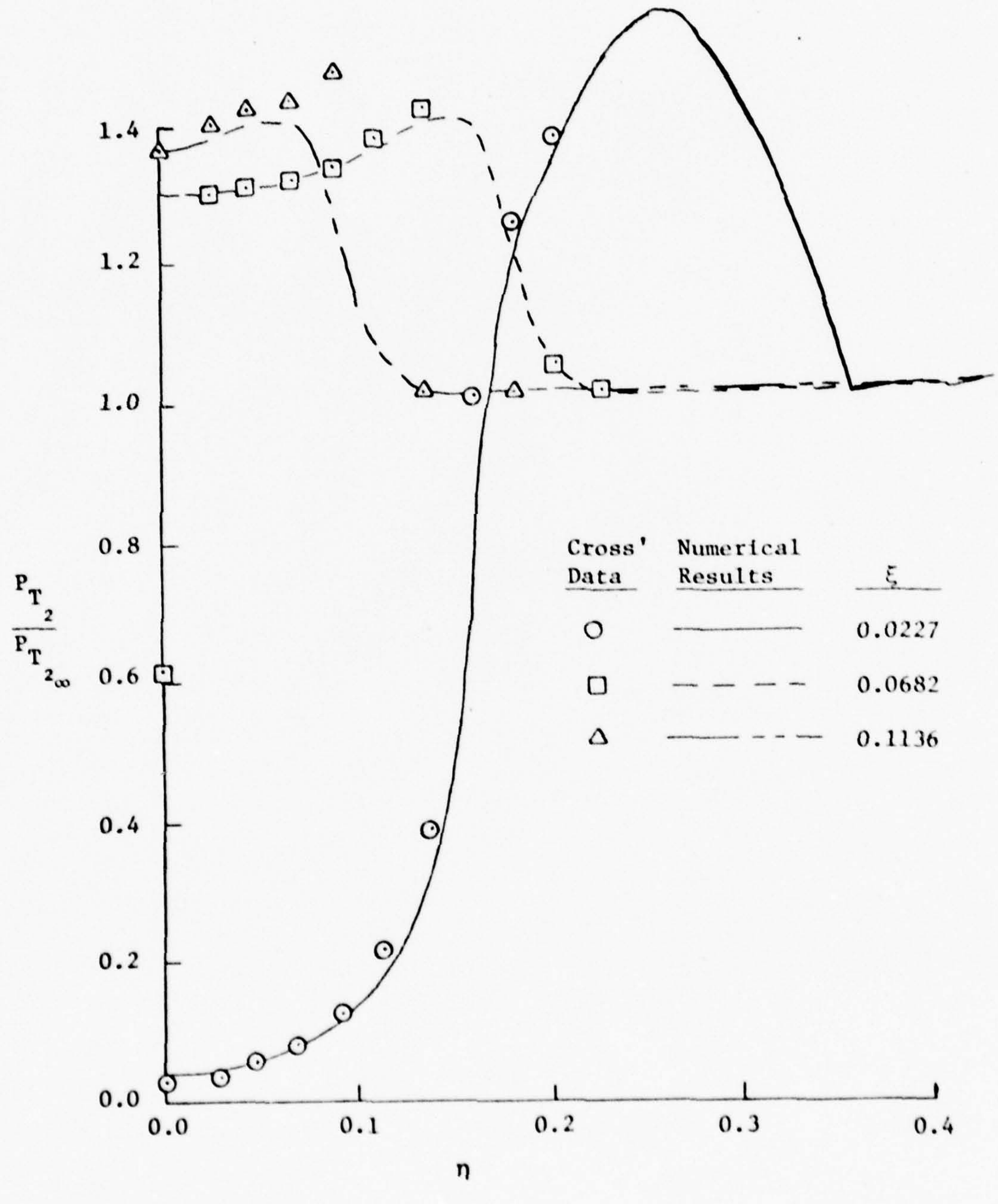

Fig. 55. Impact Pressure Survey on Leeside of Delta Wing, $\alpha = 0^{\circ}$

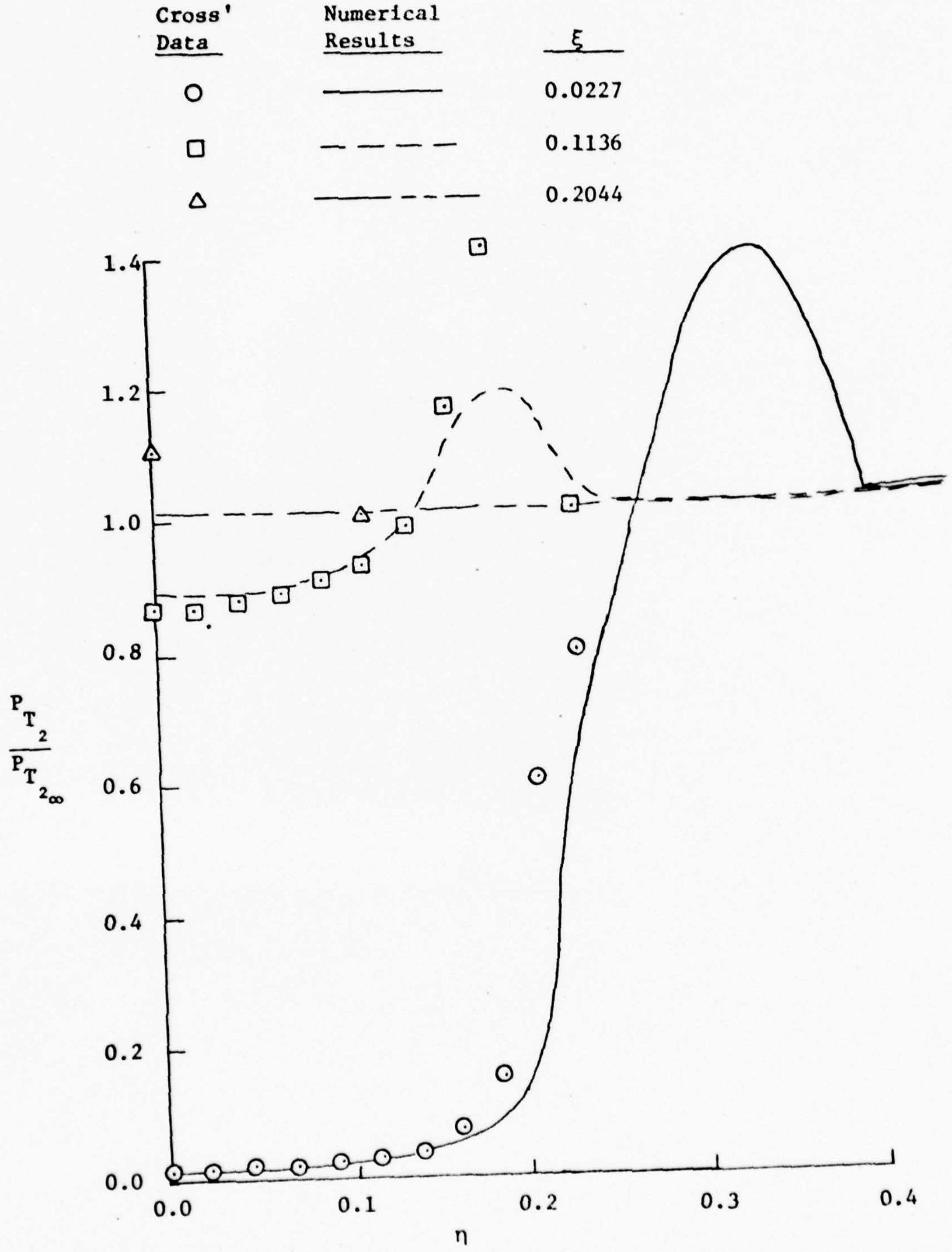

Fig. 56a. Impact Pressure Survey on Leeside of Delta Wing, $\alpha = 5^{\circ}$

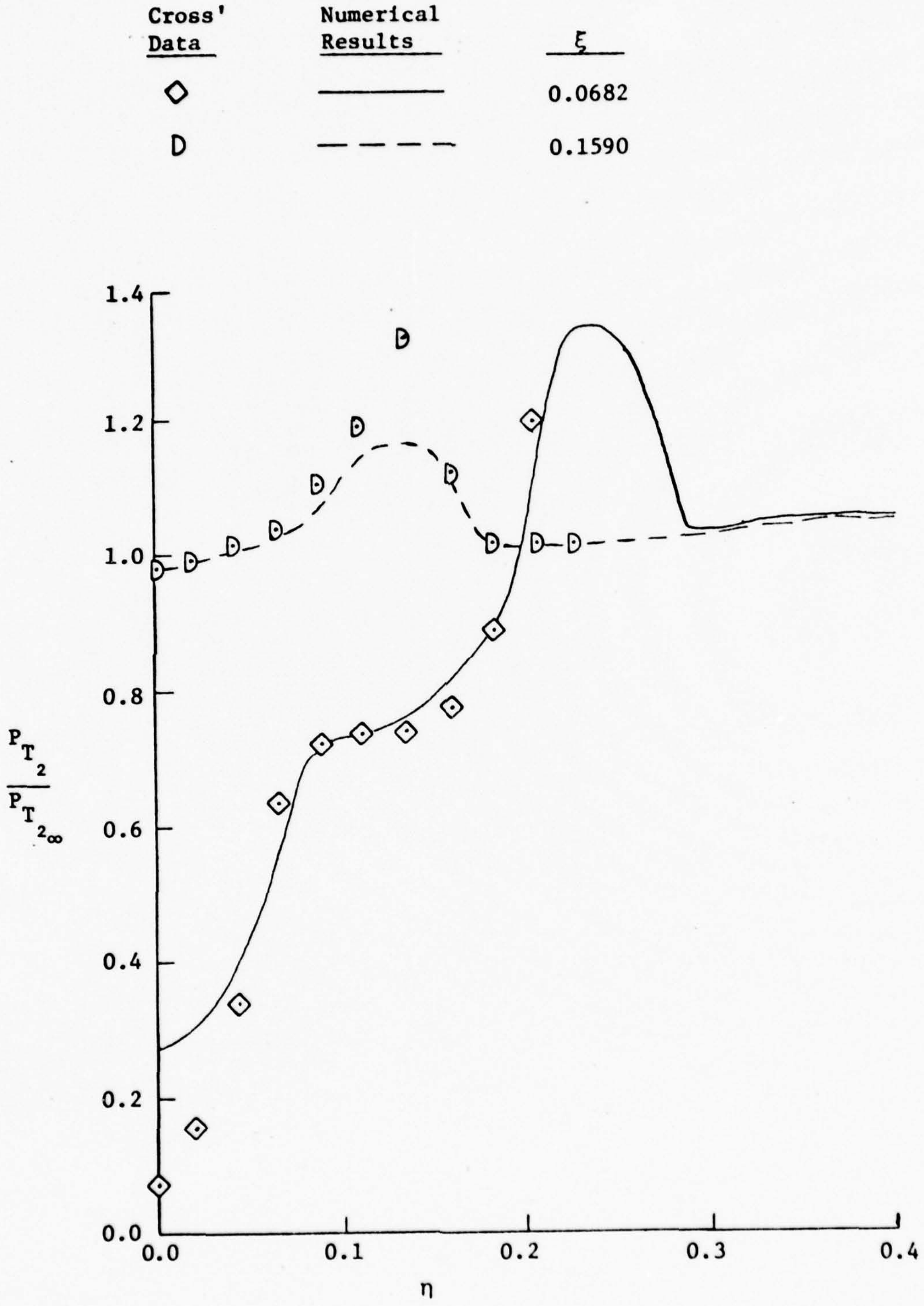

Fig. 56b. Impact Pressure Survey on Leeside of Delta Wing, $\alpha = 5^{\circ}$

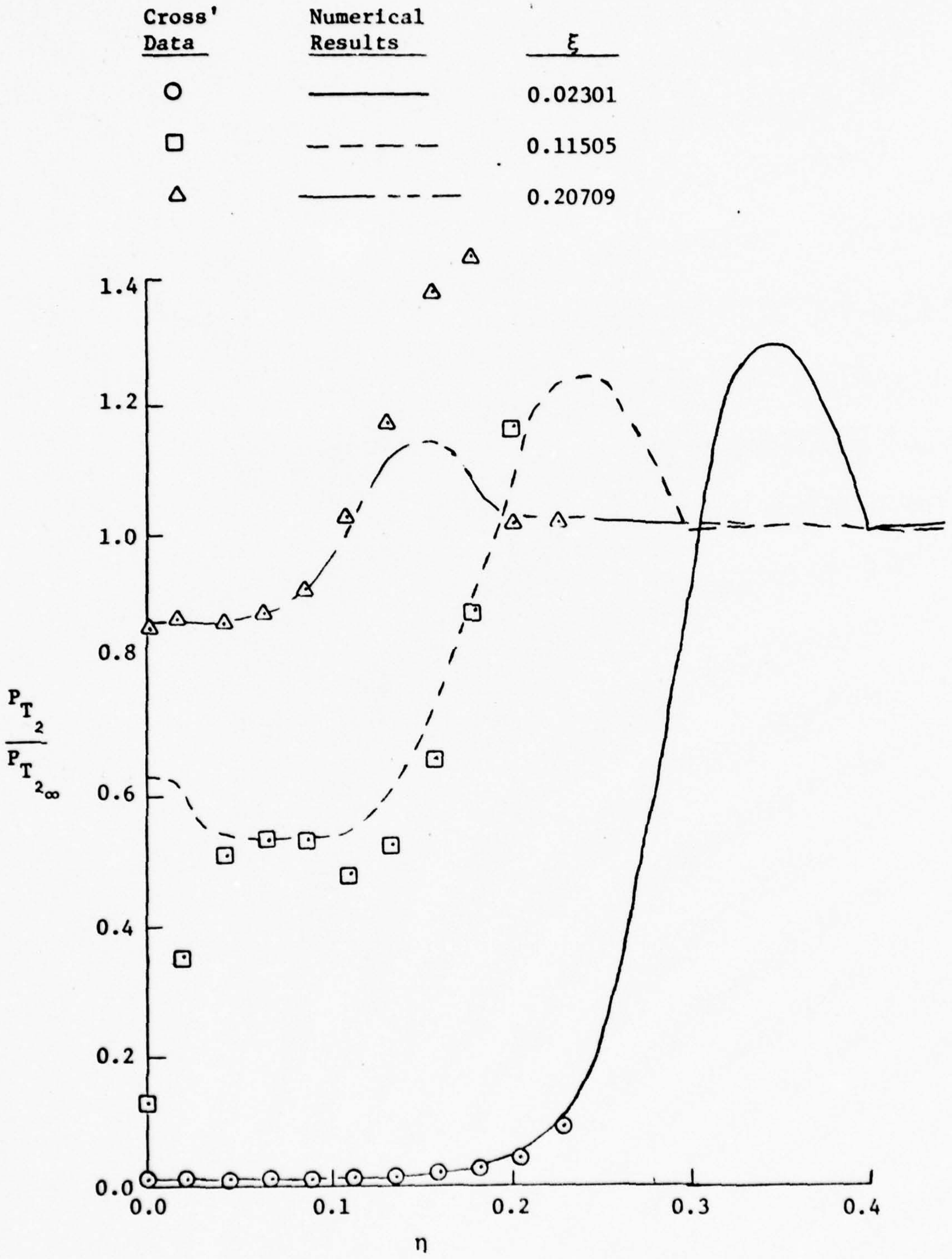

Fig. 57a. Impact Pressure Survey on Leeside of Delta Wing, $\alpha = 9^{\circ}$

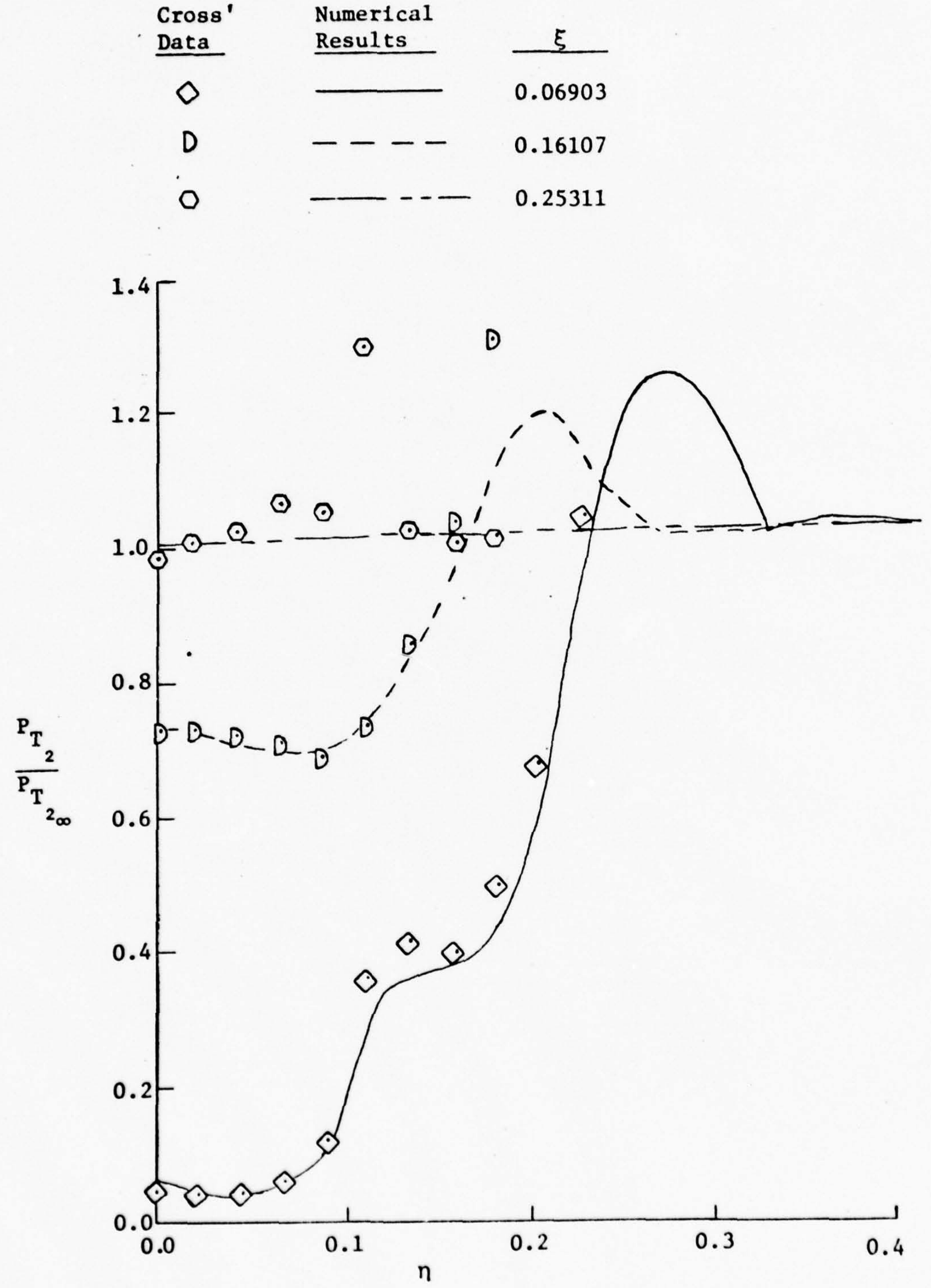

Fig. 57b. Impact Pressure Survey on Leeside of Delta Wing, $\alpha = 9^{\circ}$

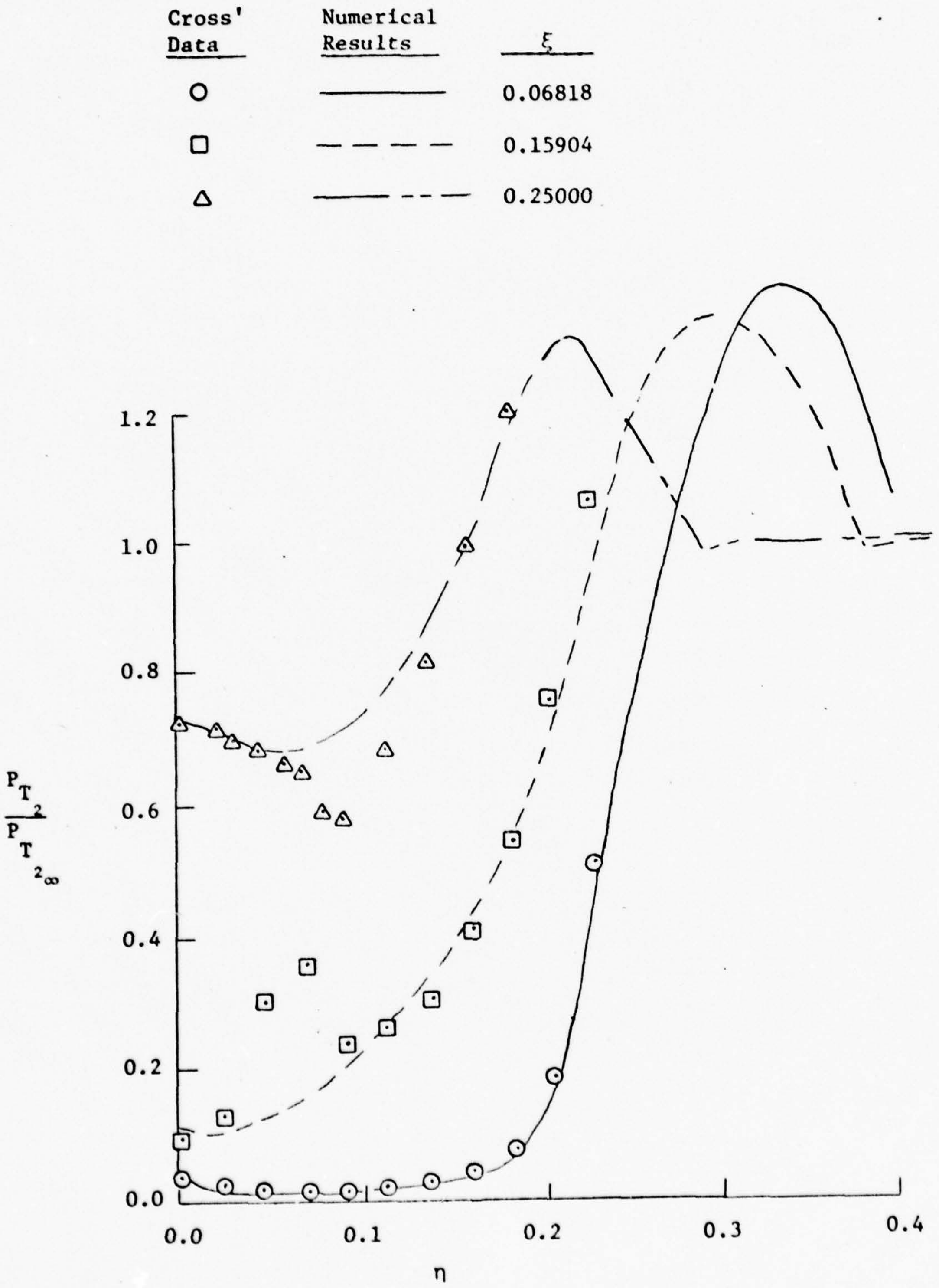

Fig. 58a. Impact Pressure Survey on Leeside of Delta Wing, $\alpha = 15^{\circ}$.

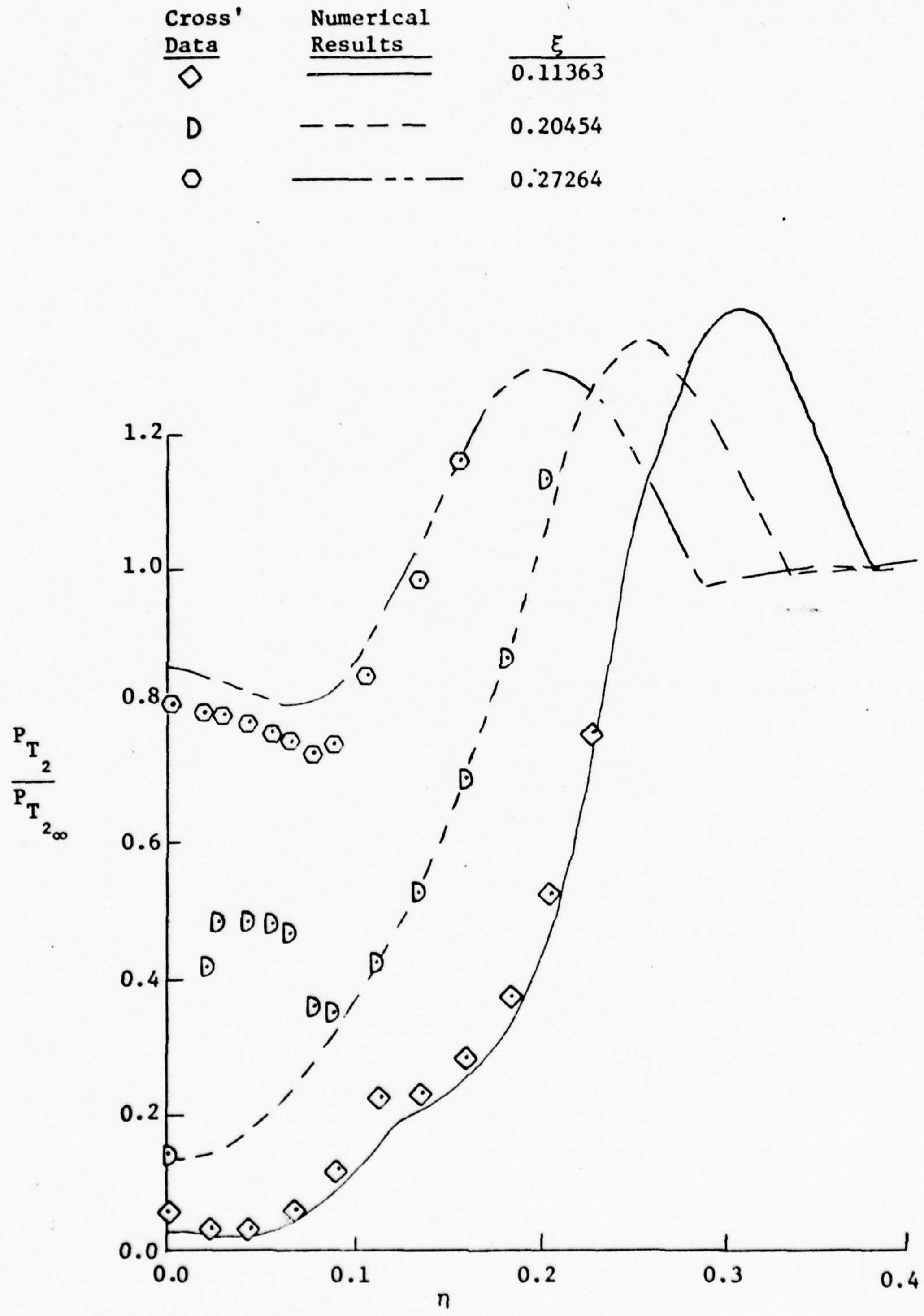

Fig. 58b. Impact Pressure Survey on Leeside of Delta Wing, $\alpha = 15^{\circ}$

$\alpha = 0^\circ$, 9°, 11°, and 15° are shown in Figures 59 through 65. At zero angle of attack (Figs 59-60), vortical singularities occur near the edges of the upper and lower viscous regions. No flow separation is seen along the wing surface and no vortex is formed in the boundary layer. At $\alpha = 5^\circ$ (as determined in this study), these vortical singularities are forced toward the wing surface on both sides of the wing. A further increase in angle of attack to $\alpha = 9^\circ$, results in a detached vortical singularity below the wing surface (Fig 61). The flow, on both sides of the wing, remains attached although there is an increase in circulation (the beginnings of a vortex) on the leeside near the origin at $\alpha = 9^\circ$.

At $\alpha = 11^\circ$, (Figs 62-63), a large reversed flow region or vortex is formed in the boundary layer. This vortex is clearly depicted in the conical streamline plot in Figure 63. Above this vortex near the edge of the leeside boundary layer is a vortical singularity point. Another vortical singularity point is formed below the wing surface near the edge of the viscous region. The leeside cross-flow separation point is at $\eta=0.1206$ with the experimental point at $\eta=0.1166$. As the angle of attack is increased, the vortex strength is also increased and the core of the vortex moves further above the wing. At $\alpha = 15^\circ$ (Fig 64) the cross-flow separation point is at $\eta=0.1301$ while the experimental separation point is at $\eta=0.1432$. The leeside vortical singularity moves further from the wing surface as the boundary layer thickness increases (Fig 65). This behavior of the vortical singularity points is similar to that seen in Tracy's experimental studies on a cone.

The pressure, density, and temperature contours in the cross-flow physical plane are shown in Figures 66 through 73. These figures

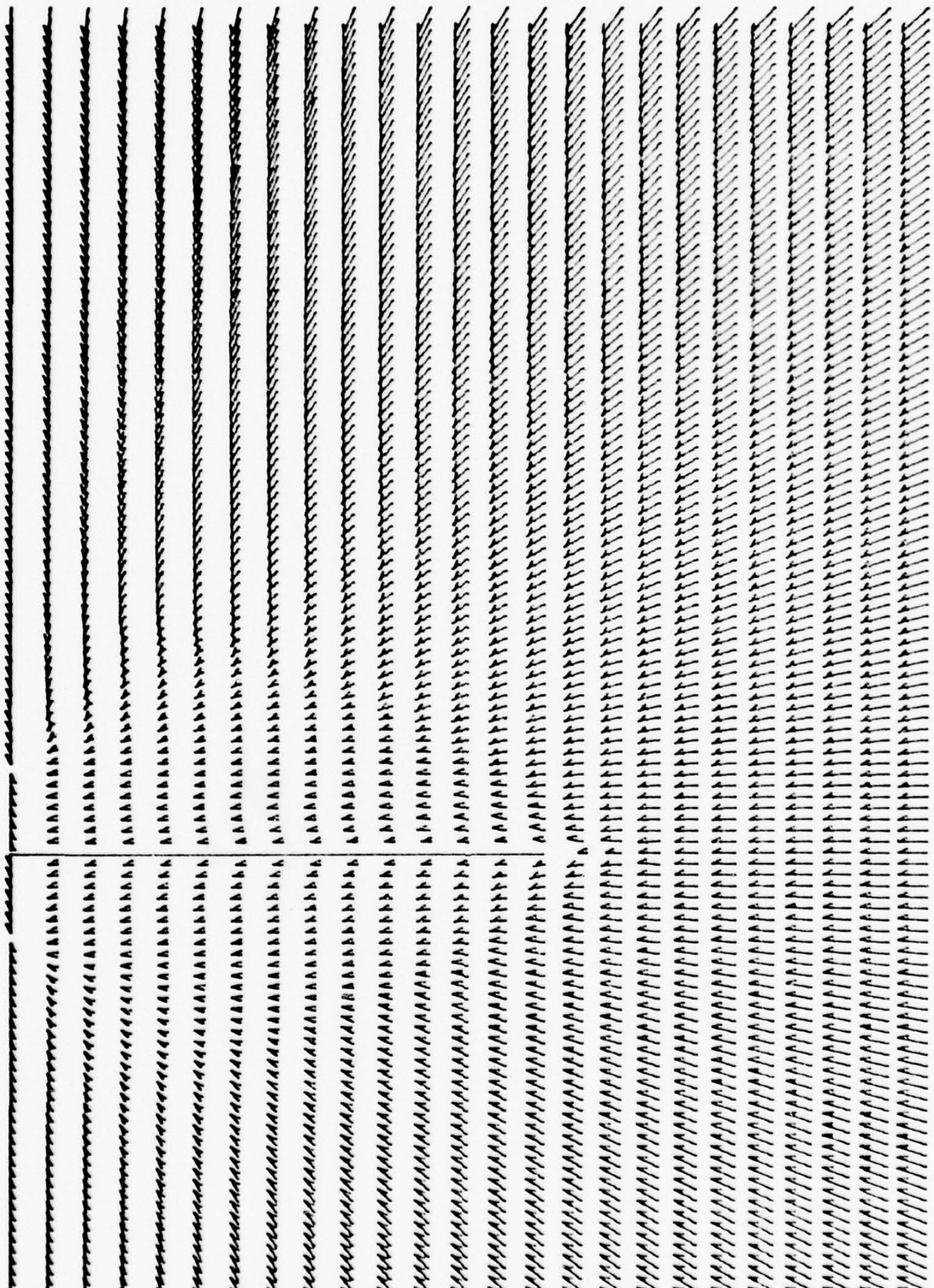

Fig. 59. Cross-flow Velocity Vector Plot as Projected on ξ-η Plane for Hypersonic Flow Around a Planar Delta Wing, $\alpha = 0^{\circ}$.

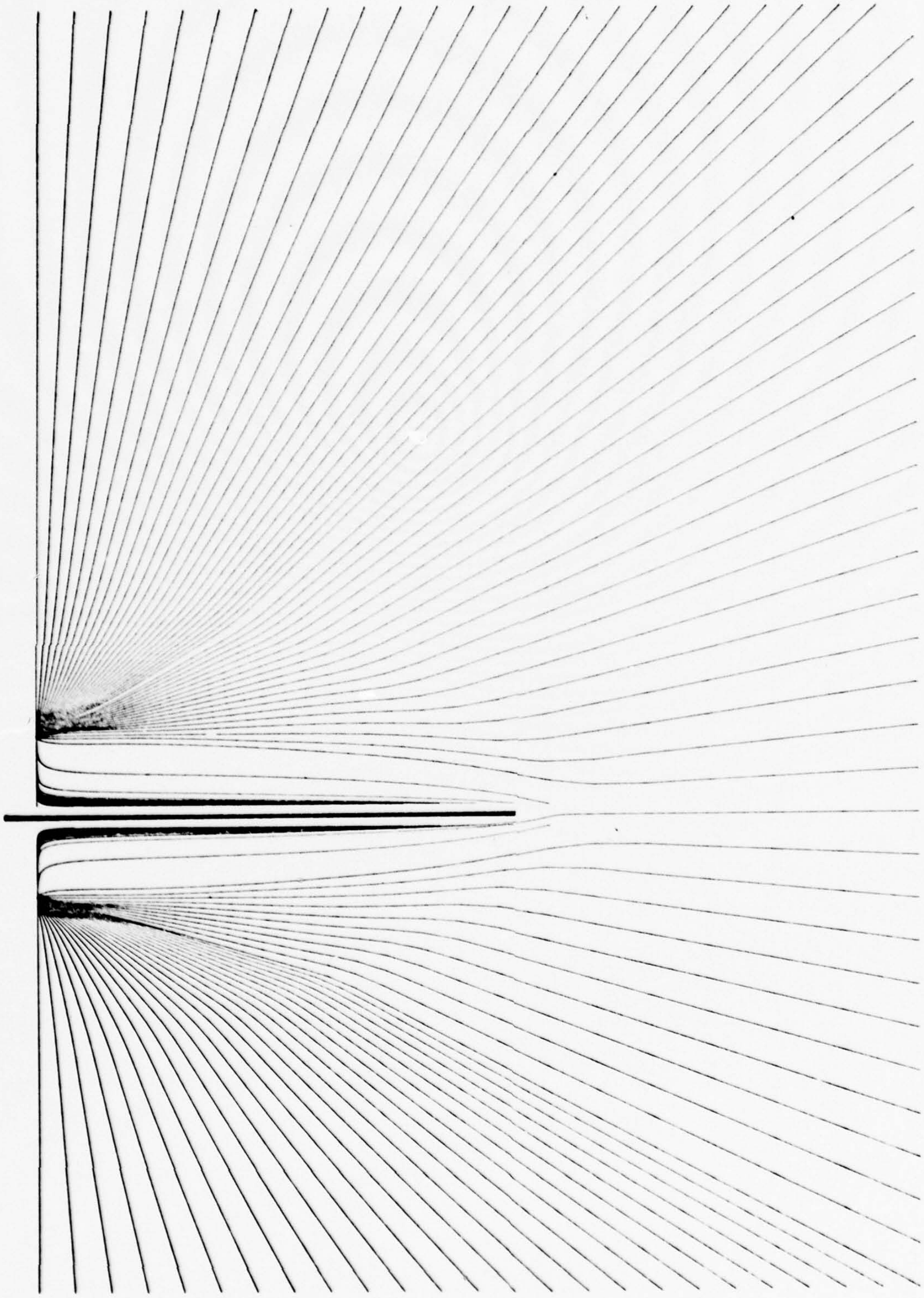

Fig. 60. Cross-flow Streamline Plot as Projected on ξ-η Plane for Hypersonic Flow Around a Planar Delta Wing, $\alpha = 0^{\circ}$.

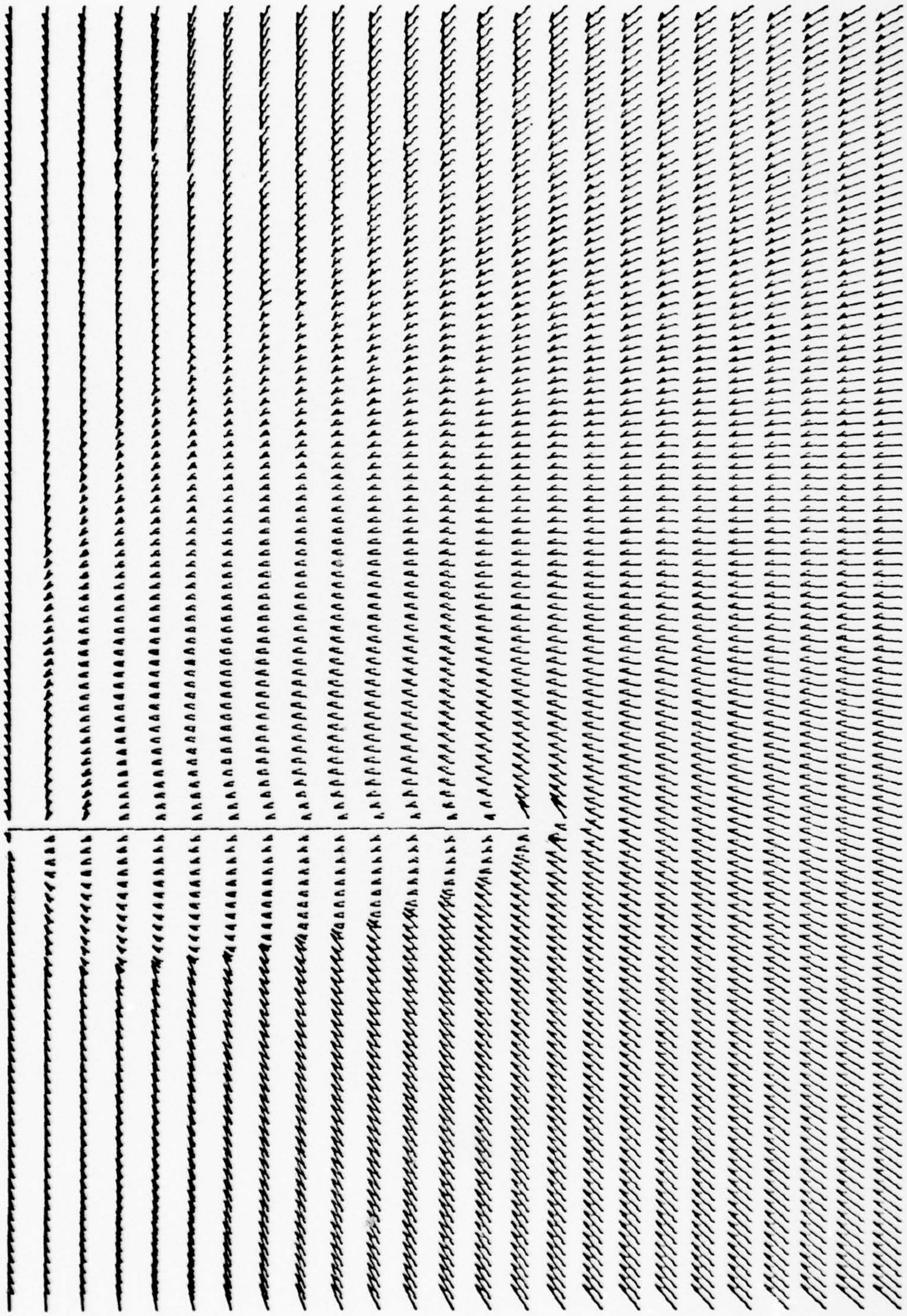

Fig. 61. Cross-flow Velocity Vector Plot as Projected on ξ-η Plane for Hypersonic Flow Around a Planar Delta Wing, $\alpha = 9^{\circ}$.

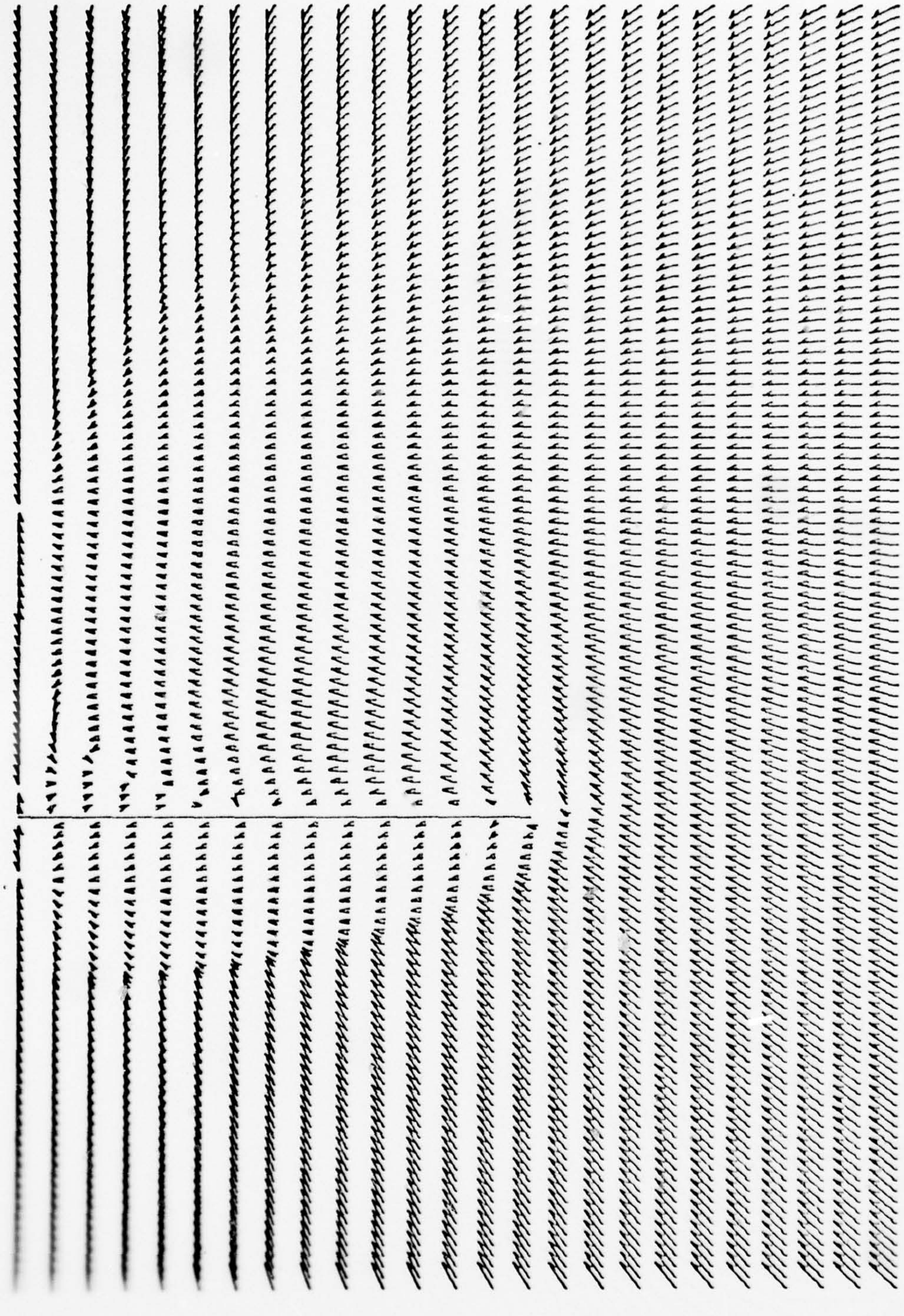

Fig. 62. Cross-flow Velocity Vector Plot as Projected on ξ-η Plane for Hypersonic Flow Around a Planar Delta Wing, $\alpha = 11^{o}$.

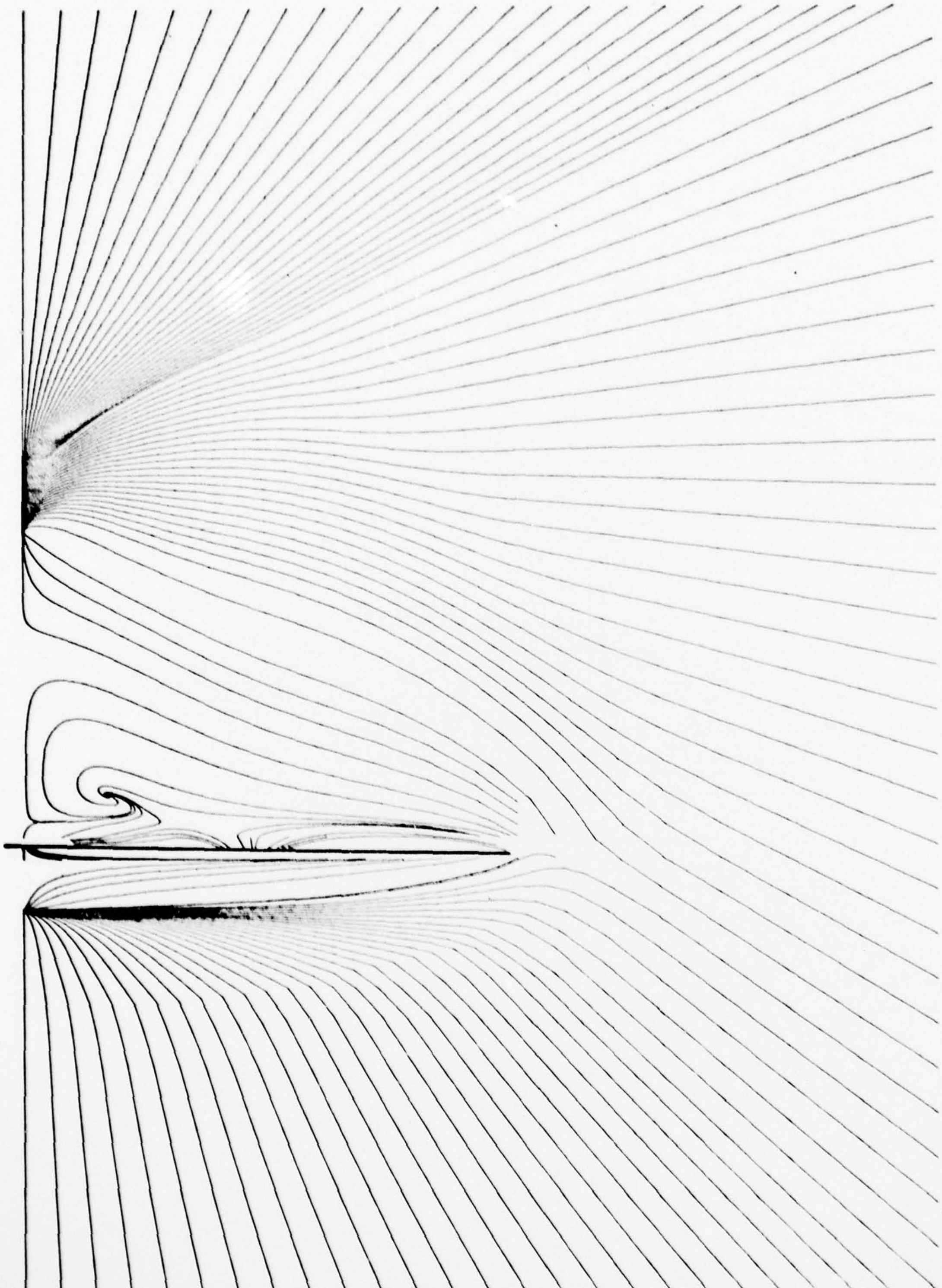

Fig. 63. Cross-flow Streamline Plot as Projected on ξ-η Plane for Hypersonic Flow Around a Planar Delta Wing, $\alpha = 11^\circ$

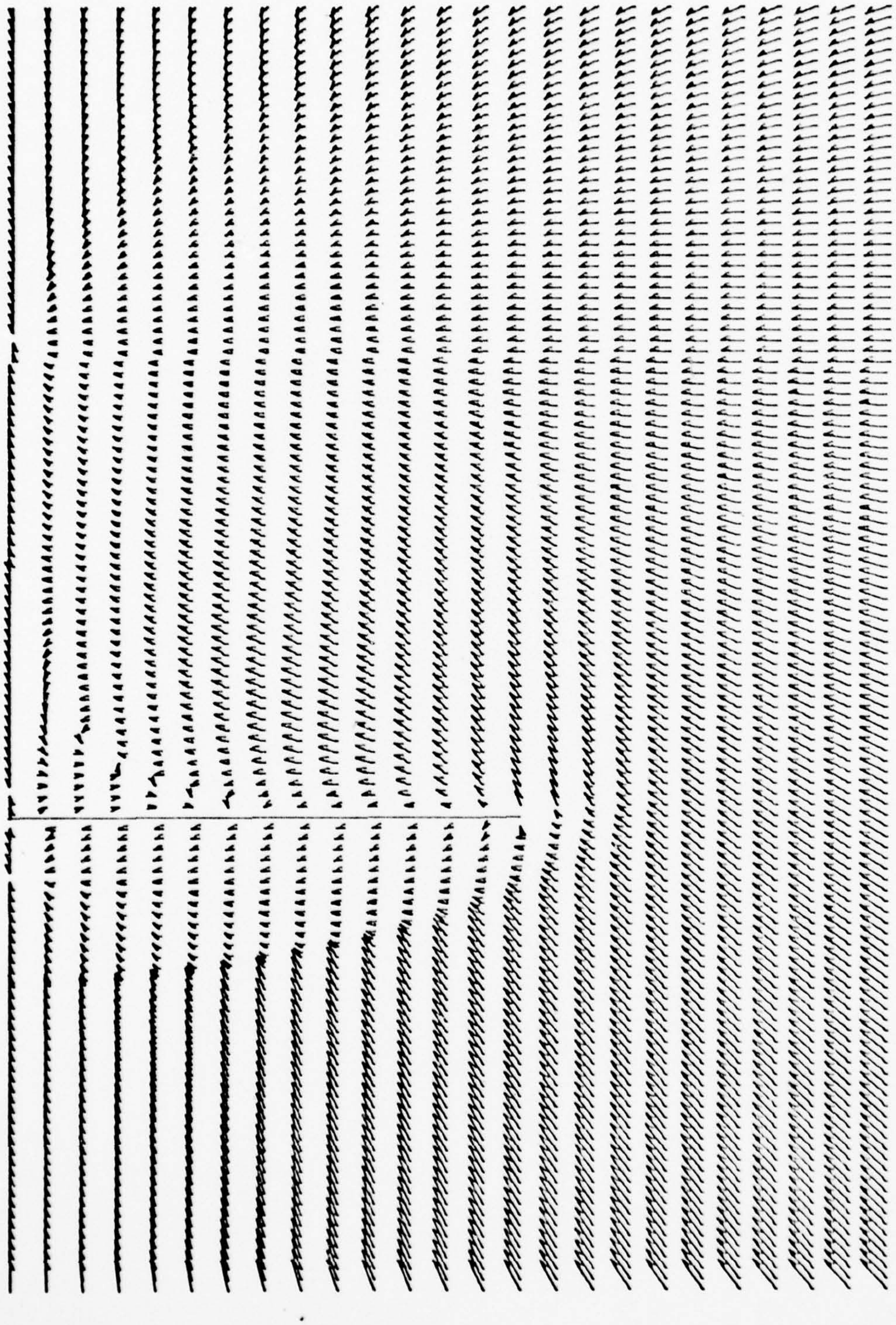

Fig. 64. Cross-Flow Velocity Vector Plot as Projected on ξ-η Plane for Hypersonic Flow Around a Planar Delta Wing, $\alpha = 15°$.

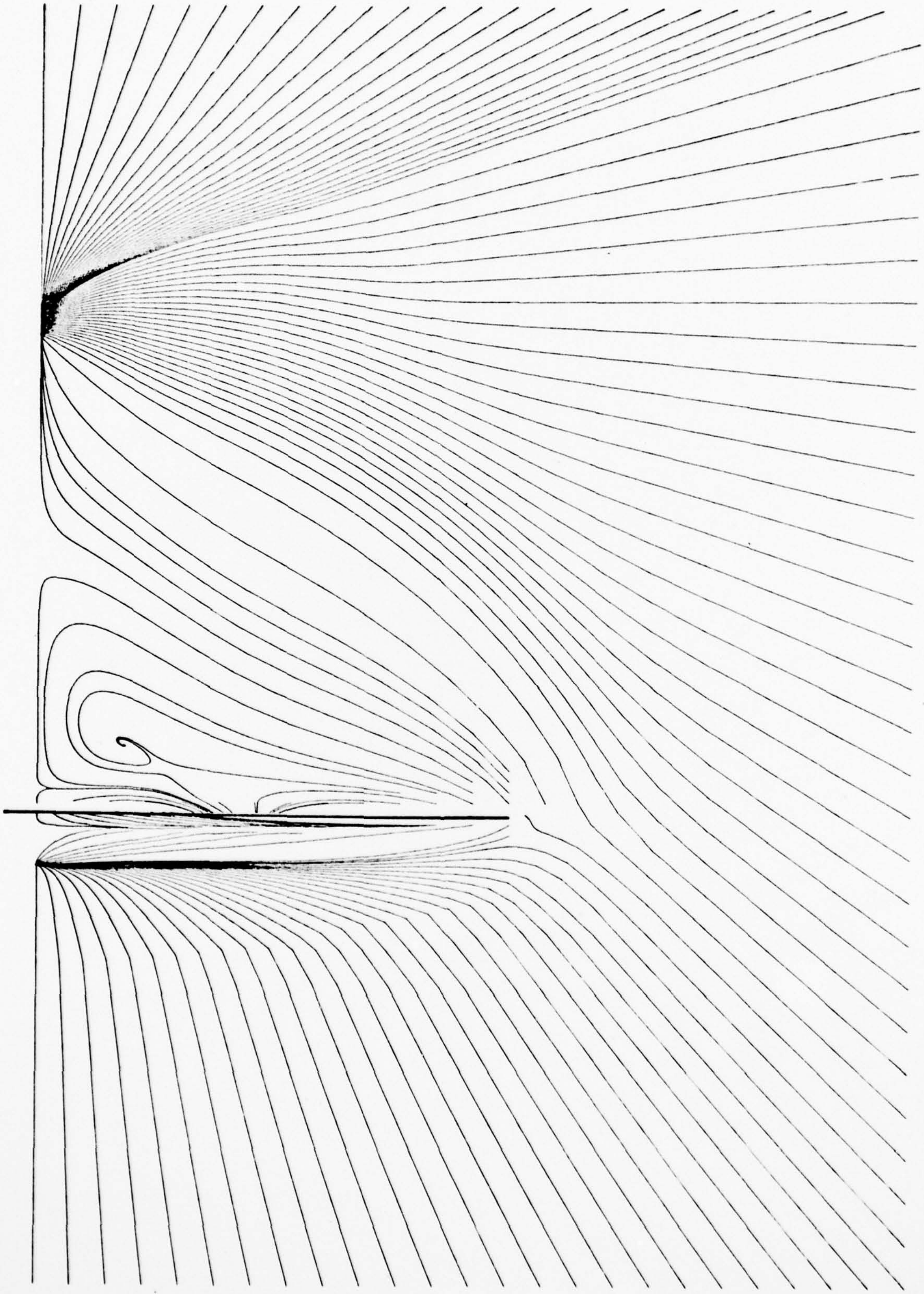

Fig. 65. Cross-flow Streamline Plot as Projected on ξ-η Plane for Hypersonic Flow Around a Planar Delta Wing, $\alpha = 15^{\circ}$.

illustrate the characteristics of the total flow field for $\alpha = 0^{\circ}$ to $\alpha = 15^{\circ}$. At zero angle of attack, the cross-flow is dominated by a strong leading edge shock wave (Fig 66). This shock wave is formed because of the displacement effects of the boundary layer. The spanwise temperature distribution (Fig 67) in the boundary layer indicates that the heat transfer rate gradually increases from a minimum at the centerline to a maximum at the leading edge of the wing. There is no internal shock wave and thus the boundary layer remains attached to the wing surface. As the angle of attack is increased, the pressure ratio across the compression-side shock wave also increases. This shock wave has a strong influence on the leeside bow shock, as seen in Figures 68-69. At $\alpha = 9^{\circ}$, an internal shock is formed on the leeside of the delta wing. This internal shock is normal to the wing surface and, at its lowest point, is incident upon the upper edge of the viscous region (Fig 70). At $\alpha = 11^{\circ}$ (Fig 71), the interaction of the internal shock wave and the boundary layer is so strong that a vortex is formed in the viscous region. The leeside bow shock and Prandtl-Meyer expansion fan are much stronger than those calculated in the leeside-only solution. At $\alpha = 15^{\circ}$, the bow shock and expansion fan are the dominant features of the upper surface flow field (Fig 72). Although an internal shock wave does exist, this shock is much weaker than the internal shock calculated for the leeside-only solution. The pressure gradient (normal to the wing surface) in the boundary layer is zero, except in the separated flow regions. The spanwise temperature distribution (Fig 73), for the separated flow, is similar to that computed for the expansion-side-only solution. The only major difference is that the heat transfer rate for the total flow field is slightly less near the leading edge.

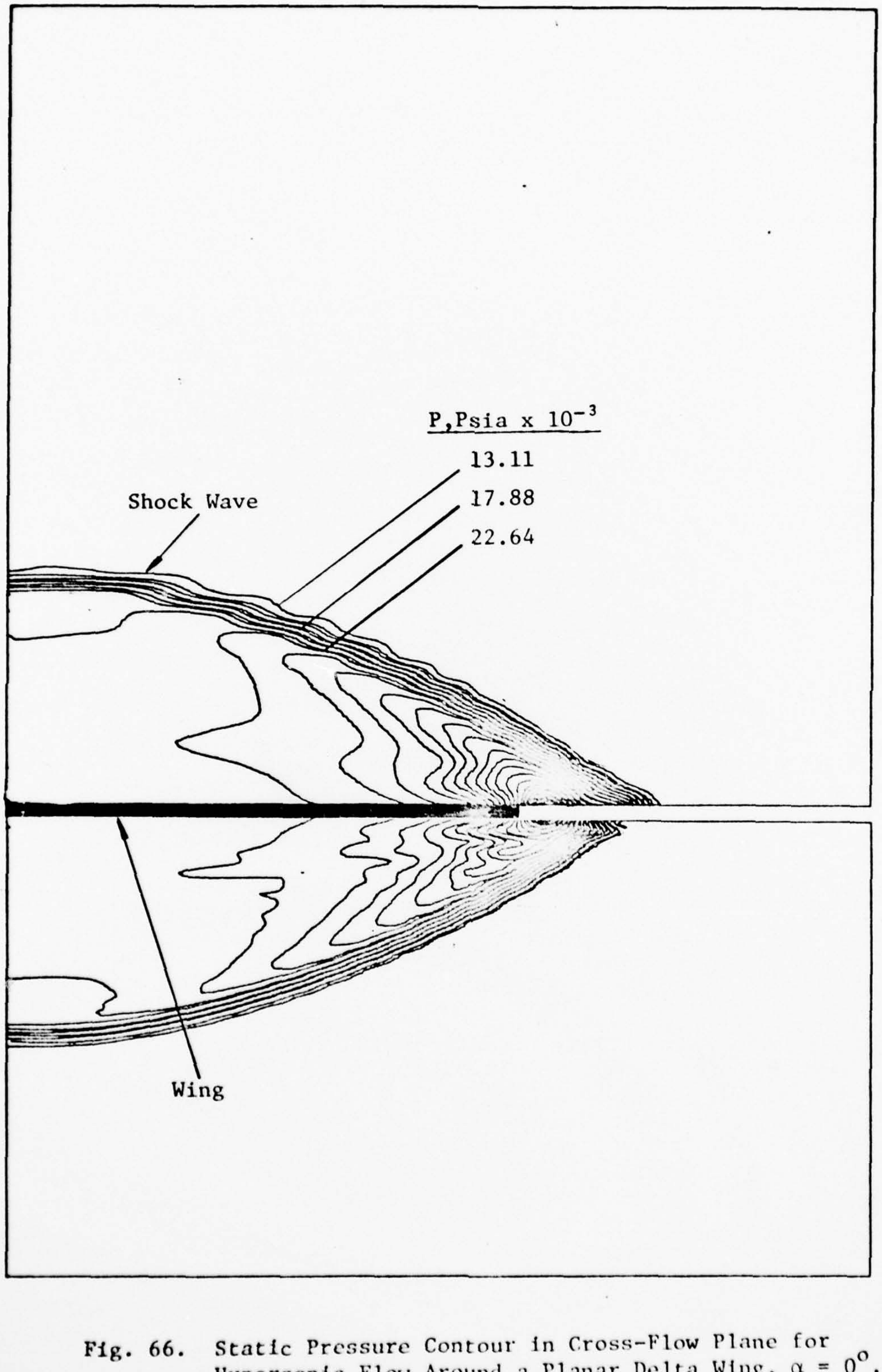

Fig. 66. Static Pressure Contour in Cross-Flow Plane for Hypersonic Flow Around a Planar Delta Wing, $\alpha = 0^o$.

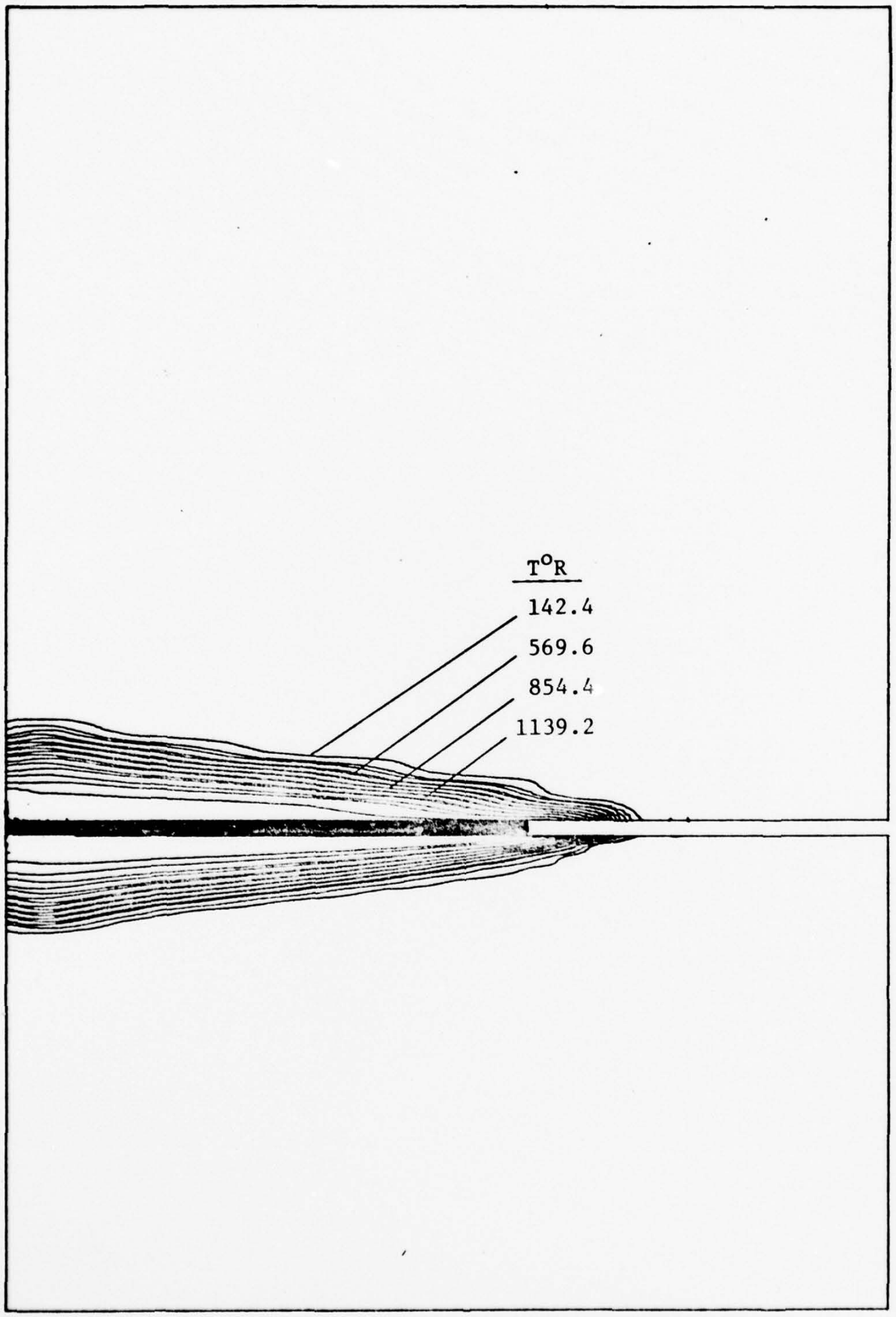

Fig. 67. Static Temperature Contour in Cross-Flow Plane for Hypersonic Flow Around a Planar Delta Wing, $\alpha = 0^{\circ}$.

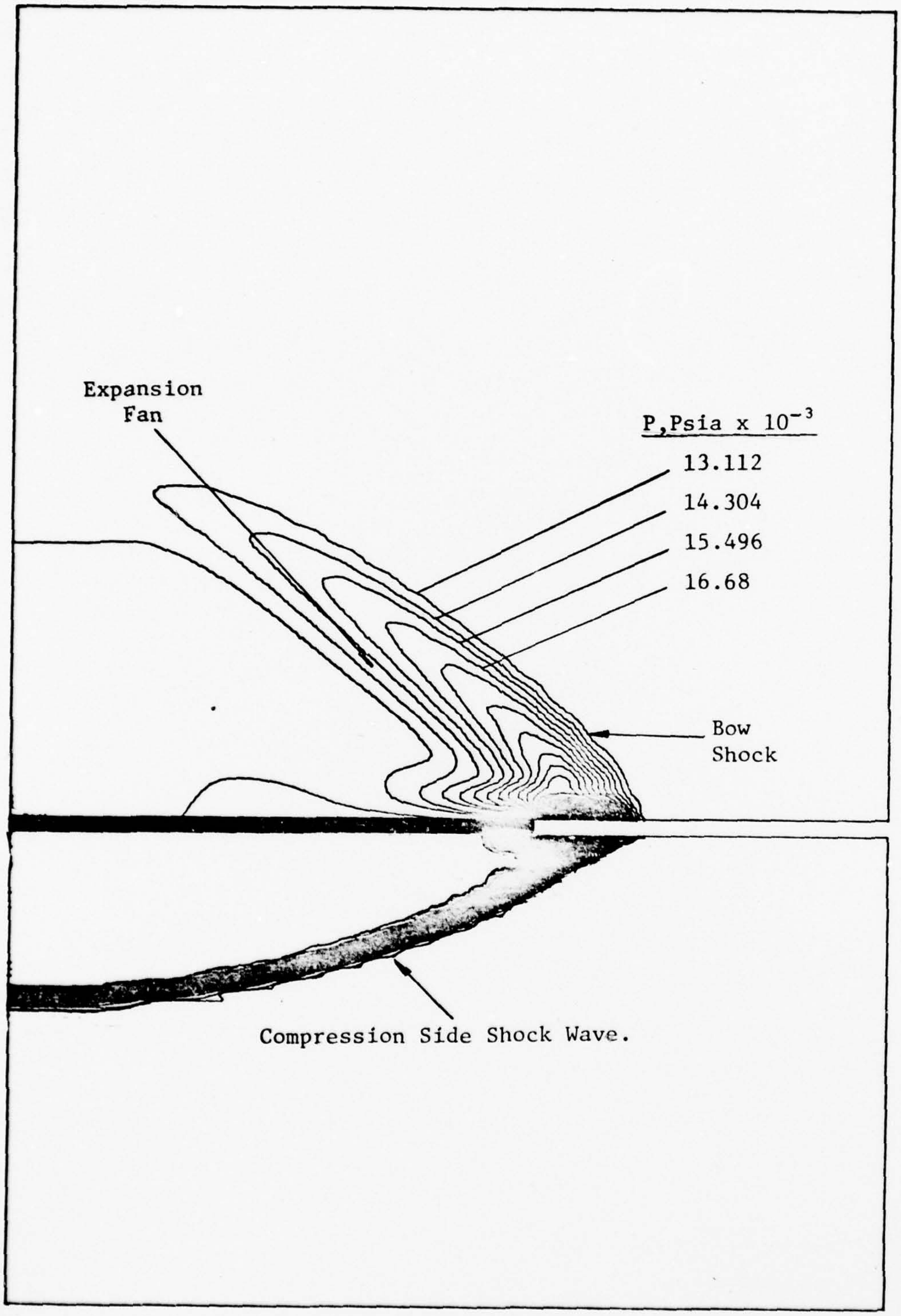

Fig. 68. Static Pressure Contour in Cross-Flow Plane for Hypersonic Flow Around a Planar Delta Wing, $\alpha = 5^{\circ}$.

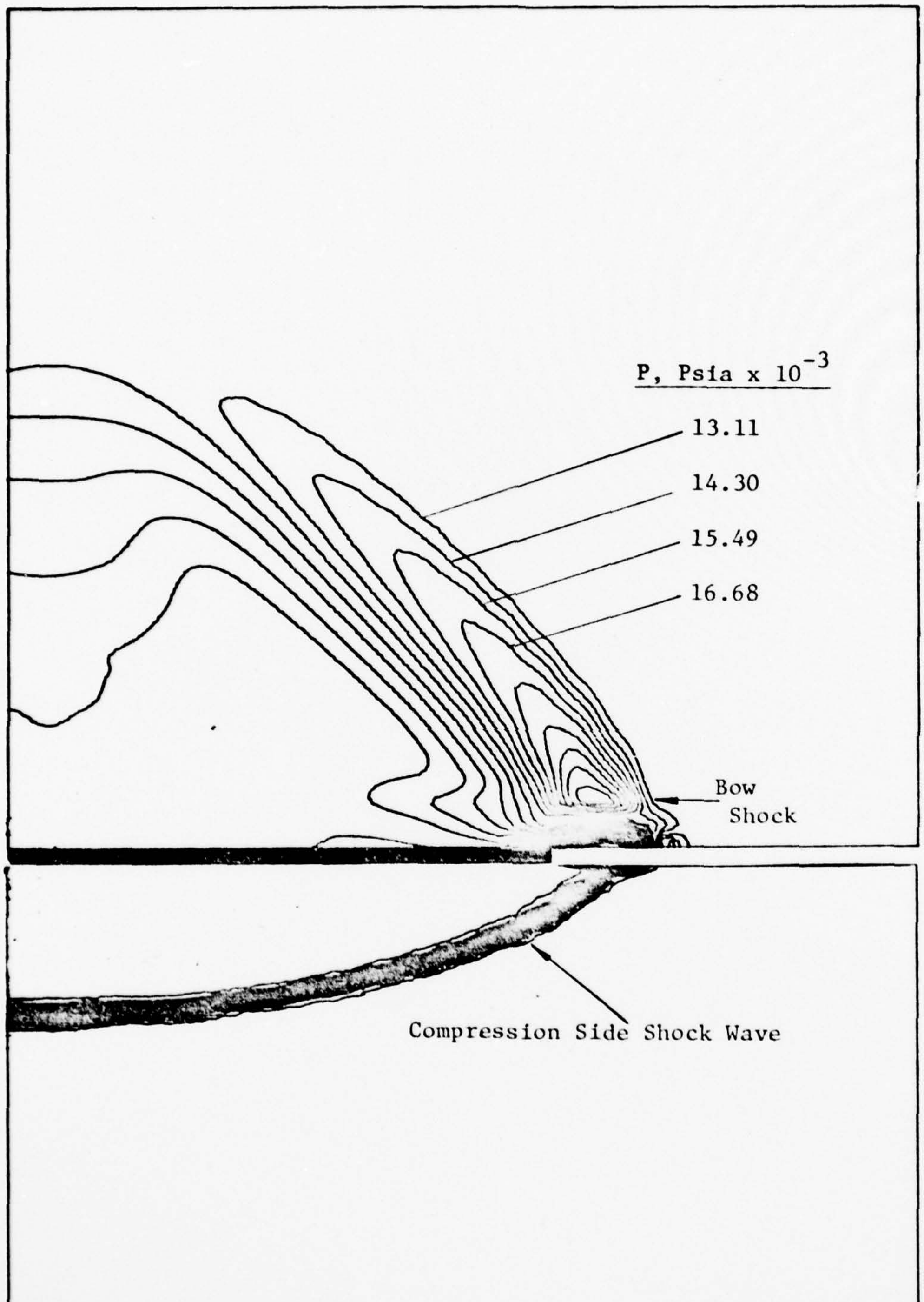

Fig. 69. Static Pressure Contour in Cross-flow Plane for Hypersonic Flow Around a Planar Delta Wing, $\alpha = 9^{\circ}$.

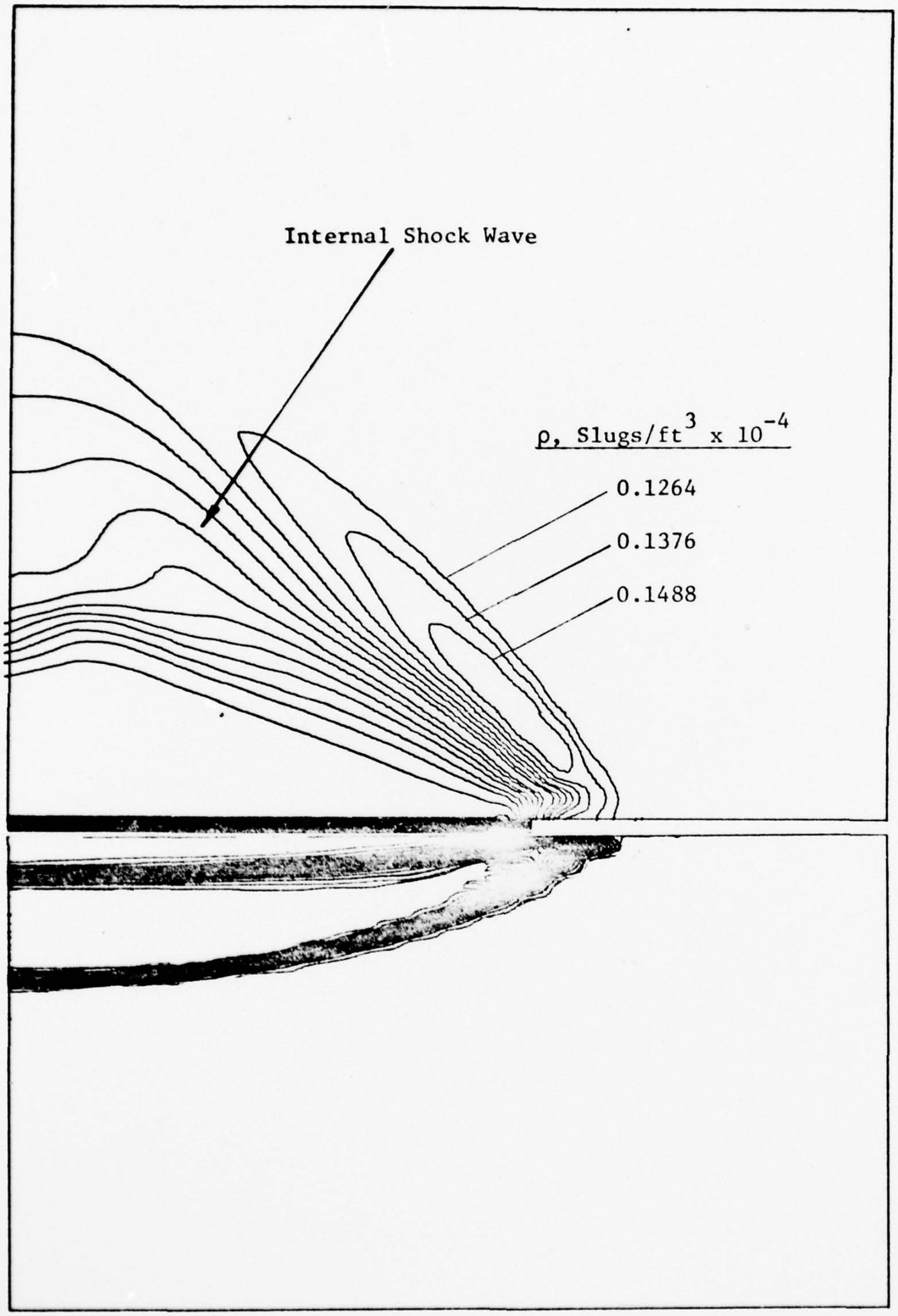

Fig. 70. Static Density Contour in Cross-flow Plane for Hypersonic Flow Around a Planar Delta, $\alpha = 9^\circ$.

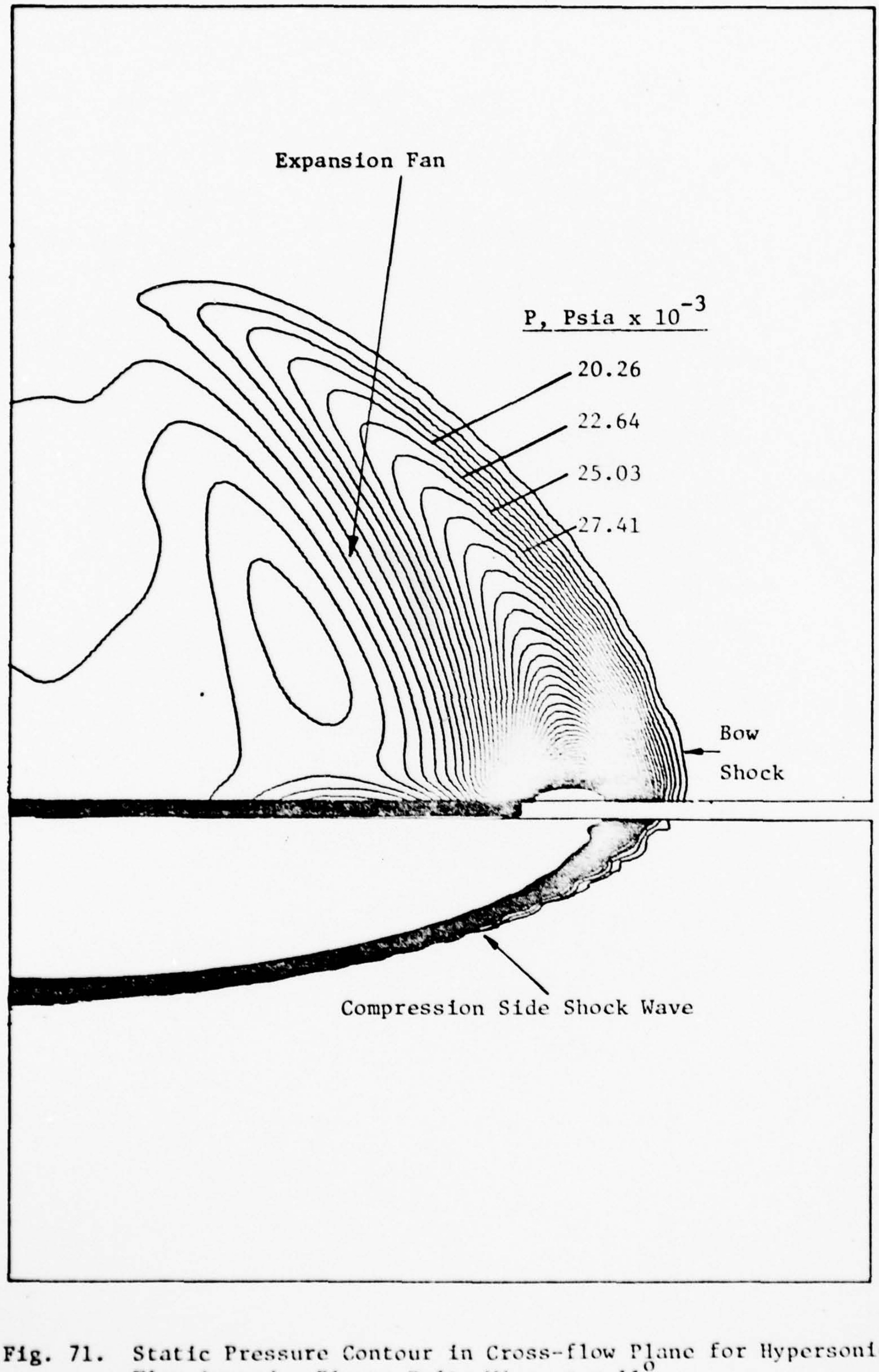

Fig. 71. Static Pressure Contour in Cross-flow Plane for Hypersonic Flow Around a Planar Delta Wing, $\alpha = 11^{\circ}$.

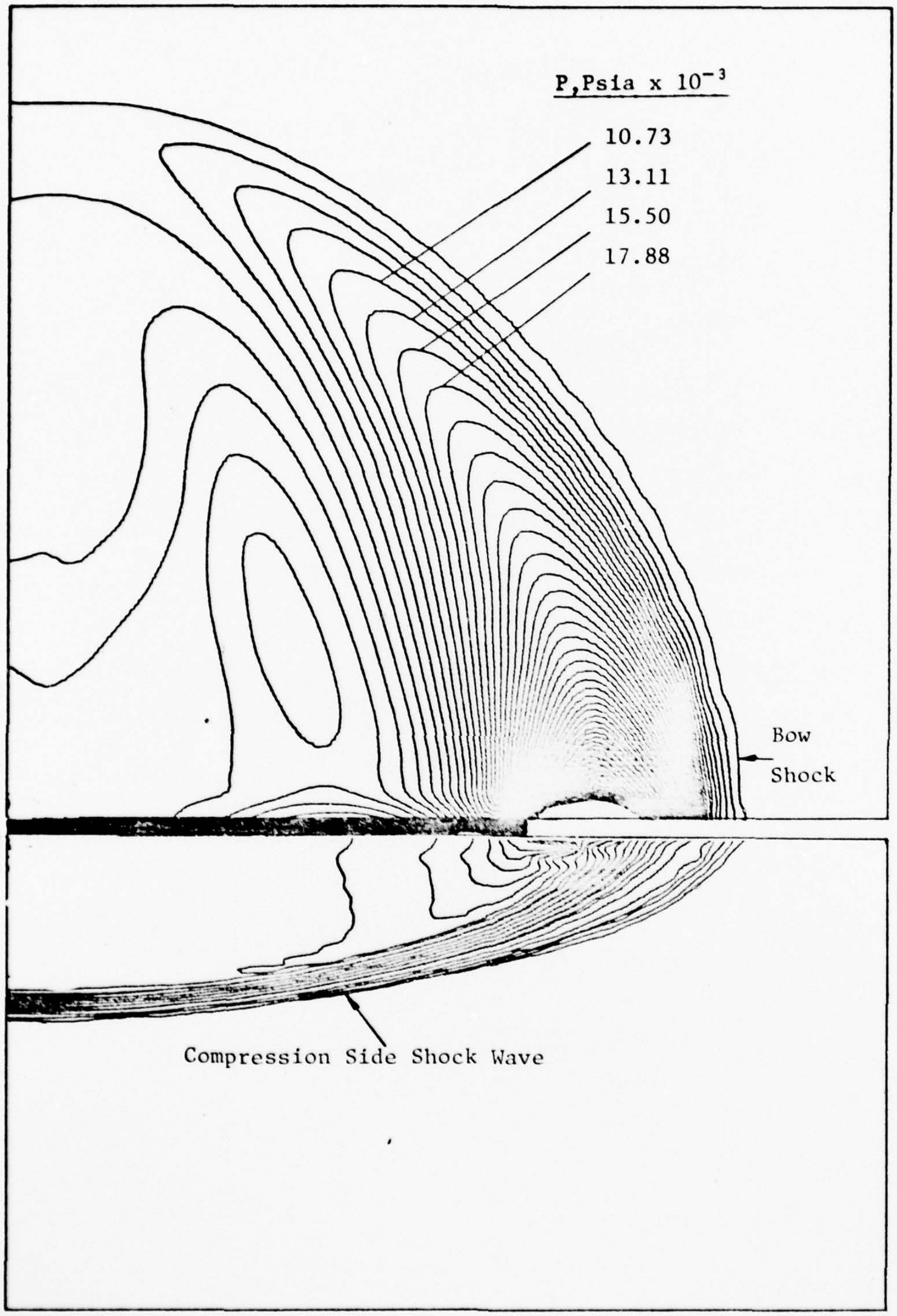

Fig. 72. Static Pressure Contour in Cross-Flow Plane for Hypersonic Flow Around a Planar Delta Wing, $\alpha = 15^{\circ}$.

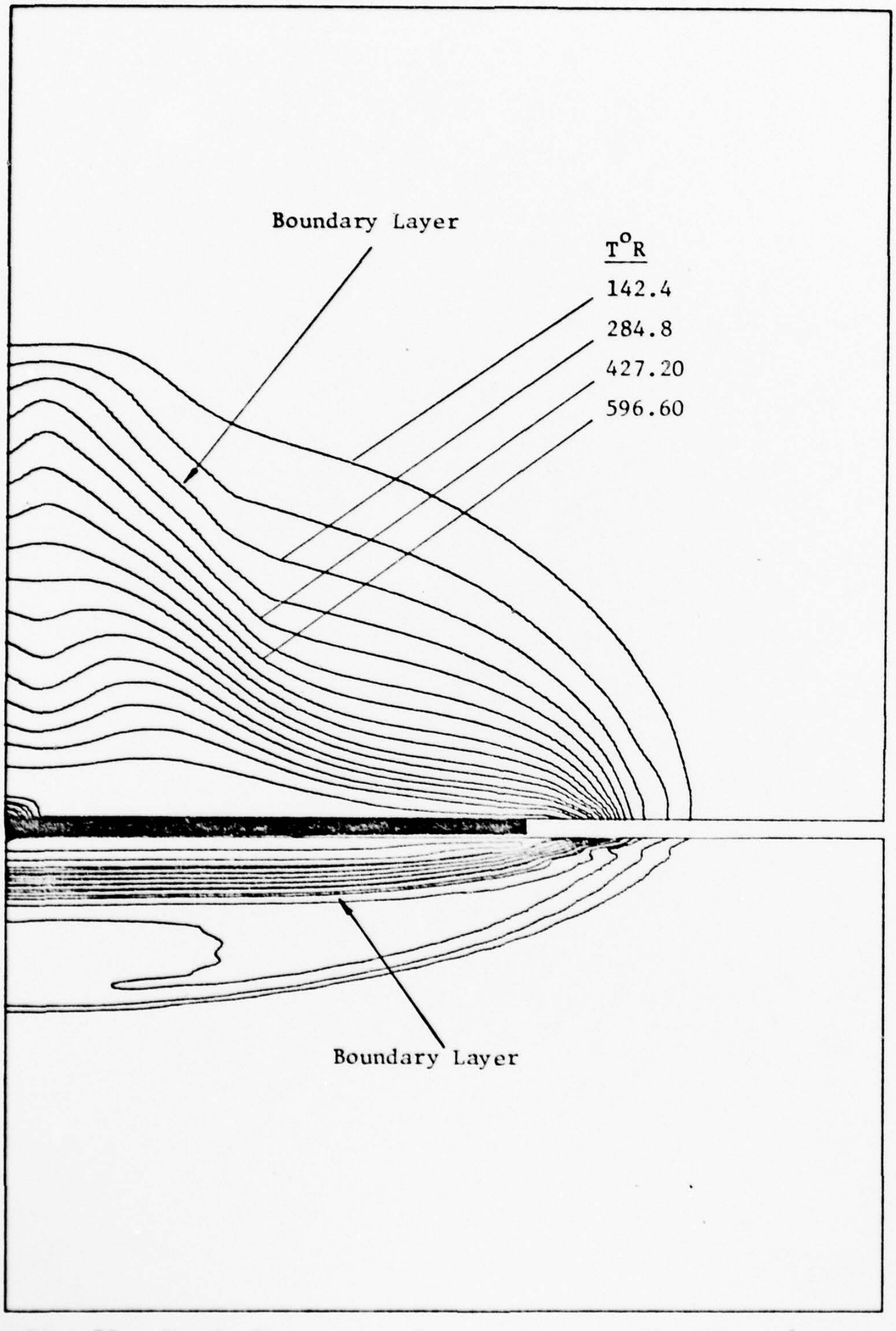

Fig. 73. Static Temperature Contour in Cross-flow Plane for Hypersonic Flow Around a Planar Delta Wing, $\alpha = 15^{\circ}$.

In conclusion, it can be seen that the total flow field solution is more accurate and complete than the leeside-only solution. These numerical results indicate that the compression side flow field has a significant effect on the flow characteristics on the leeside of the wing. The pressure ratio across the upper surface bow shock is stronger than that found in the leeside-only solution. This results in a larger region of reversed flow, a more accurate prediction of the cross-flow separation point, and the calculation of a viscous bubble. The hypersonic numerical results compare quite favorably with Cross' data as well as with the qualitative observations by Rao and Whitehead (Ref 131) and by Narayan (Ref 25). The discrepancies between the calculated and measured results are due to three-dimensional effects in the viscous region and not properly modeling the delta wing thickness. However, these results indicate that the conical viscous approximation technique can be used to adequately predict the three-dimensional flow around a thin delta wing.

Computational Statistics

The two most important statistics for any computer program are the execution time per point and per time step and the storage requirements. These statistics are used to measure the efficiency of the numerical codes and the size of computer needed to run these programs. In this investigation, the computer programs were run on the Control Data Corporation 6600 computer. The execution time for the various numerical solutions ranged from 3.07×10^{-3} to 3.73×10^{-3} sec/grid point/time step. The computer storage requirements and the numerical damping constants varied for each case. These values are shown in Table II.

AD-A056 513 AIR FORCE INST OF TECH WRIGHT-PATTERSON AFB OHIO SCH--ETC F/G 20/4
A NUMERICAL SOLUTION OF SUPERSONIC AND HYPERSONIC VISCOUS FLOW --ETC(U)
JUN 78 G S BLUFORD
UNCLASSIFIED AFIT/DS/AA/78S-1 NL

3 OF 3
AD
A056 513

END
DATE
FILMED
9-78
DDC

Table II

Computer Storage Requirements and Numerical Damping Constants

Case	Grid	Storage (K words)	Damping Constants
Cone	$63\eta \times 30\xi$	167.3K	No Damping
Supersonic Upper, Delta Wing	$26\eta \times 30\xi$	101K	No Damping
Hypersonic Upper, Delta Wing	$26\eta \times 45\xi$ ($\alpha=0^\circ$) $26\eta \times 30\xi$ ($\alpha=5^\circ$, 9°) $26\eta \times 76\xi$ ($\alpha=11^\circ$, 15°)	125.2K 102.2K 174.4K	$\beta=1.0$ $c_i=0.06$ $c_j=0.0$
Supersonic Lower, Delta Wing	$26\eta \times 45\xi$	125.1K	$\beta=1.0$ $c_i=0.12$ $c_j=0.12$
Supersonic Total, Delta	$26\eta \times 59\xi$	151.5K	$\beta=1.0$ $c_i=0.06$ $c_j=0.0$
Hypersonic Total, Delta Wing	$26\eta \times 120\xi$	167.3K	$\beta_1=\beta_2=1.0$ $\beta_3= -20.0$ $c_i=0.40$ $c_j=0.10$

The total execution time for each case varied from 3 to 12 hours, depending on how the stability criteria (Δt) was used, the use and magnitude of the numerical damping terms, the size of the computational mesh, the convergence criteria, and the characteristics of the physical flow field.

VI. Conclusions and Recommendations

A numerical method was used to compute the supersonic and hypersonic, viscous flow fields around a thin, planar delta wing. These solutions were obtained by solving the unsteady governing equations subject to a conical approximation. The integration technique used was the second-order accurate MacCormack finite-difference scheme. This integration was performed on a constant step size array generated by a conical coordinate transformation. The solutions obtained were for a Mach number range of 2.94 to 10.17, a local Reynolds number range of 3.345×10^5 to 5.0×10^6, and angles of attack from -15^o to $+15^o$. Numerical oscillations in these solutions (as a result of shock capturing) were reduced by applying normal stress damping and a fourth-order density damping term to the finite-difference equations. A stability criteria (maximum Δt) was computed and used based on an analysis of the linearized governing equations. The numerical results were compared with experimental data (Ref 15-17), various analytical solutions (Ref 66-68, 88, and 89), and several qualitative observations, such as vapor screen and oil flow techniques (Refs 25 and 131). From these results, the following significant conclusions were drawn based on the present investigation:

(1) This numerical technique accurately predicts the supersonic flow around a thin, planar delta wing, with supersonic leading edges. Good agreement was obtained between calculated results and the experimental data by Bannink (Ref 15). All the basic elements of the flow field (i.e. shock waves, boundary layers, and sonic lines) were calculated and were found to be essentially correct in magnitude and

location. For the first time in any reference, the shock wave-boundary layer interaction was computed and its effects seen in the impact pressure profile for $\xi = 0.0718$ (Figures 17 and 46). The numerical solutions for the leeside-only and the total flow fields were found to be almost identical, except near the bow shock. In this region, the difference in calculated results was due to not modeling the compression side flow field for the upper-surface-only solution. The largest discrepancies between calculated and measured impact pressures also occurred near the leeside bow shock. The maximum impact pressure error for the leeside-only solution was 12.0% while that for the total flow field was 4.0%. These discrepancies were attributed to use of a coarse grid in the computational domain, improper modeling of the delta wing thickness, and neglecting the lower surface flow field influence (leeside-only solution). From these numerical results, it can be seen that the three-dimensional supersonic flow field can be accurately approximated by using a conical, viscous flow field model.

(2) This numerical method adequately modeled the inviscid and viscous hypersonic flow around a thin delta wing. Solutions were obtained for both the upper and total flow fields. These solutions compared quite favorably with Cross' data as well as with the qualitative observations by Rao and Whitehead (Ref 131) and by Narayan (Ref 25). The shock wave-boundary layer interaction was accurately approximated and, for the first time, an embedded vortex was computed in the viscous region. A significant difference was seen between the calculated leeside-only and total flow field solutions (see Figs 32 and 65). This difference was due to the strong interaction which occurs between the upper and lower flow fields. In the total flow field solution, the

detached bow shock and leading edge expansion fan were found to be the dominant features in the upper surface flow field. These flow characteristics caused a weak internal shock wave and a large reversed flow region to form above the wing at $\alpha \geq 11^{\circ}$. For the first time in any calculation, the cross-flow separation point was accurately predicted (within 3.0%) and the viscous "bubble" in the symmetry plane was computed. The total flow field solution provided an improved insight into the behavior of the cross-flow vortical singularities and a more accurate description of the flow field than the leeside-only solution.

(3) A very effective technique was used to calculate the surface conditions at the leading edge of the total delta wing. This method permitted the flow properties to be triple valued at the singularity point. The standard boundary conditions of non-slip at the surface and an isothermal surface were used. The normal momentum equations in the ξ and η directions were used to calculate the upper, side, and lower values of pressure. The three values of density were determined from the equation of state. This numerical modeling of the leading edge or singularity point produced a stable and accurate solution of the flow field in the vicinity of this nodal point.

(4) A satisfactory stability criteria analysis was performed on the finite-difference form of the linearized governing equations. This analysis accounted for both the inviscid and viscous dominant regions in the flow field. A maximum allowable time step was determined and used in the numerical integration of the governing equations.

(5) A normal stress damping term and a fourth-order density damping term were successfully incorporated into the numerical integration procedure. The normal stress damping was used to control the initial

transients due to ill-suited initial conditions. The density damping term was used to reduce numerical oscillations around shock waves and expansion fans. The magnitude of both damping terms was set so as to be effective in the inviscid flow region but not to change the viscous region behavior or modify the effective Reynolds number, appreciably.

Thus, it can be seen that this numerical technique accurately predicts the supersonic and hypersonic flow fields around a thin planar delta wing. These numerical results compare quite favorably with experimental data, various analytical solutions, and several qualitative observations. This investigation has demonstrated the feasibility of using the conical flow approximation in calculating the viscous-inviscid flow fields around thin delta wings for $\bar{\chi} \leq 0(1)$.

Further research in this area is still needed in order to examine the total spectrum of supersonic and hypersonic flows around a thin delta wing. Several recommendations, by the author, are proposed for future work. These include the following:

(1) A faster and more efficient numerical algorithm should be used to solve this flow field problem. Shang (Ref 136) has developed a time-dependent implicit-explicit hybrid scheme which is 8.6 times faster than the current explicit method. This hybrid scheme could be incorporated into the current computer codes in order to produce a faster, but equivalent (accuracy within 4%), result.

(2) A conical, body-fitted, curvilinear coordinate system (Ref 137) should be used to solve flows around thin delta wings of various conical cross-sections. In this coordinate system, the grid system is generated by solving a set of elliptical partial differential equations, with one coordinate being coincident with each boundary contour in the

physical domain. Use of this type of coordinate transformation would result in solutions about delta wings of various cross-sections with the same degree of ease as for planar delta wings.

(3) As a first attempt at calculating the turbulent flow around a planar delta wing, an eddy viscosity model should be incorporated into the governing equations. Several algebraic turbulent models could be used in this study, provided the rate of strain is fairly small and the deviation of the principal axes between the Reynolds stress tensor and the strain-rate tensor is small (Ref 138). This effort should be attempted only when an adequate turbulent experimental data base exists.

(4) Finally, additional experimental data is needed on supersonic and hypersonic flow fields around delta wings. A more detailed examination is required of the viscous region at various angles of attack, and Reynolds numbers. An experimental study should be pursued to investigate the limits of the conical flow approximation in evaluating flows around delta wings. More experimental measurements are needed in order to examine the behavior of vortical singularities in the cross-flow of a low Reynolds number, hypersonic flow field.

Bibliography

1. Stanbrook, A. and L. C. Squire. "Possible Types of Flow at Swept Leading Edges." *The Aeronautical Quarterly*, 15:72-82 (February 1964).

2. Dunavant, J. C., K. Y. Narayan and G. D. Walberg. *A Survey of Leeside Flow and Heat Transfer on Delta Planform Configurations*. AIAA Paper 76-118. New York: American Institute of Aeronautics and Astronautics, January 1976.

3. Squire, L. C. "Flow Regimes Over Delta Wings at Supersonic and Hypersonic Speeds." *The Aeronautical Quarterly*, 27:1-14 (February 1976).

4. Carafoli, E. *Wing Theory in Supersonic Flow*. New York: Pergamon Press Ltd., 1969.

5. Earnshaw, P. B. *An Experimental Investigation of the Structure of a Leading Edge Vortex*. ARC R&M 3281. London: Aeronautical Research Council, March 1961.

6. Hall, M. G. "A Theory for the Core of a Leading Edge Vortex." *Journal of Fluid Mechanics*, 11:209-228 (September 1961).

7. Stewartson, K. "The Inner Viscous Solution for the Core of a Leading Edge Vortex." *Journal of Fluid Mechanics*, 15:306-318 (February 1963).

8. Fink, P. T. and J. Taylor. *Some Early Experiments on Vortex Separation*. ARC R&M 3489. London: Aeronautical Research Council, September 1966.

9. Wentz, W. H. and M. C. McMahon. *An Experimental Investigation of the Flow Fields about Delta and Double-Delta Wings at Low Speeds*. NASA CR 521. Washington: National Aeronautics and Space Administration, August 1966.

10. Wentz, W. H. and M. C. McMahon. *Further Experimental Investigations of Delta and Double-Delta Wing Flow Fields at Low Speeds*. NASA CR 714. Washington: National Aeronautics and Space Administration, February 1967.

11. Brown, S. N. "The Compressible Inviscid Leading-Edge Vortex." *Journal of Fluid Mechanics*, 22:17-32 (May 1965).

12. Rein, J. A. *Flow Over the Suction Surface of Sharp Edge Delta Wings with Detached Leading Edge Shock Waves*. Technical Note HSA. Salisburg, South Australia: Australian Defense Scientific Service, December 1964.

13. Fowell, L. R. "Exact and Approximate Solutions for the Supersonic

Delta Wing." *Journal of the Aeronautical Sciences*, *23*:709-720 (August 1956).

14. Bannink, W. J., C. Nebbeling, and J. W. Reyn. *Investigation of the Flow Field on the Expansion Side of a Delta Wing with Supersonic Leading Edges*. Report VTH-128. Delft, The Netherlands: Technological University Delft, August 1965.

15. Bannink, W. J. and C. Nebbeling. *An Experimental Investigation of the Expansion Flow Field over a Delta Wing at Supersonic Speed*. Report VTH-167. Delft, The Netherlands: Technological University Delft, September 1971.

16. Spurlin, C. J. *Expansion Side Flow Field Impact Pressure Surveys of a 75-Deg Delta Wing at Mach Number 10*. AEDC-TR-68-58. Arnold Air Force Station, Tennessee. Arnold Engineering Development Center, June 1968

17. Cross, E. J. *Experimental and Analytical Investigation of the Expansion Flow Field over a Delta Wing at Hypersonic Speeds*. ARL 68-0027. Wright-Patterson AFB, Ohio: Aerospace Research Laboratories, August 1971.

18. Monnerie, B. and H. Werle. "Etude de L'coulement Supersonique et Hypersonique Autour d'une Aile Elancee en Incidence. *AGARD CP-30*, AGARD Conference on Hypersonic Boundary Layers and Flow Fields (May 1968).

19. Melnik, R. E. "Vortical Singularities in Conical Flow." *AIAA Journal*, *5*:631-637 (April 1967).

20. Melnik, R. E. *A Systematic Study of Some Singular Conical Flow Problems*, Phd Thesis. Brooklyn, New York: Polytechnic Institute of Brooklyn, 1965.

21. Melnik, R. E. *A Conical Thin-Shock Layer Theory Uniformly Valid in the Entropy Layer*. Rept. FDL-TDR-64-82. Wright-Patterson AFB, Ohio: Air Force Flight Laboratory, 1965.

22. Rao, D. M. and A. H. Whitehead Jr. "Leeside Vortices on Delta Wings at Hypersonic Speeds." *AIAA Journal*, *10*:1458-1465 (November 1972).

23. Murray, W. M. and R. L. Stallings. *Heat Transfer and Pressure Distributions on 60° and 70° Swept Delta Wings Having Turbulent Boundary Layers*. NASA TN D-3644. Washington: National Aeronautics and Space Administration, 1966.

24. Thomann, H. *Measurements of Heat Transfer, Recovery Temperature, and Pressure Distribution on Delta Wings at $M=3.0$*. FAA Report 93. Stockholm Sweden: The Aeronautical Research Institute of Sweden, December 1962.

25. Narayan, K. Y. "Leeside Flowfield and Heat Transfer of a Delta Wing at M=10.0." AIAA Journal, 16:160-165 (February 1978).

26. Taswala, M. D. and J. W. Stultz. Flow Field Measurements on an 80 Degree Delta Wing at Moderate Angles of Attack in a Hypersonic Wind Tunnel (Mach = 8.0). Thermodynamics Technical Note No. 41. St. Louis, Mo.: McDonnell Douglas Astronautics Company, 1972.

27. Bertram, M. D. and A. Henderson, Jr. "Recent Hypersonic Studies of Wings and Bodies." American Rocket Society Journal, 31:1129-1139 (August, 1961).

28. Kaatari, G. E. Pressure Distributions on Triangular and Rectangular Wings to High Angles of Attack - Mach Numbers 2.46 and 3.36. NACA RM A54J12. Washington: National Advisory Committee for Aeronautics, 1955.

29. Szodruch, J. and L. C. Squire. Pressure Distributions on the Suction Surface of Some Delta Wings at M=3.5. ARC 35008, FM 4442, Hyp. 956. London: Aeronautical Research Council, 1974.

30. Allegre, J., D. Lartigue, and M. F. Scibilia. "Rarefied Hypersonic Flow Characteristics of Delta Wings and Trailing Edge Spoilers." AIAA Journal, 10:900-905 (July 1972).

31. Barber, E. A. "Some Experiments on Delta Wing in Hypersonic Flow." AIAA Journal, 4:72-83 (January 1966).

32. Bashkin, V. A. "Experimental Study of Flow About Flat Deltas at M=5 and Angles of Attack from 0^{o} to 70^{o}." Izv. AN SSSR. Mekhanika Zhidkosti i Gaza, 2:102-108 (1967).

33. Nagel, A. L., H. D. Fitzsimmons, and L. B. Doyle. Analysis of Hypersonic Pressure and Heat Transfer Tests on Delta Wings with Laminar and Turbulent Boundary Layers. NASA CR-535 Washington: National Aeronautics and Space Administration, 1966.

34. Drougge, G. and P. O. Larson. Pressure Measurements and Flow Investigation on Delta Wings at Supersonic Speed. FFA Report 57. Stockholm, Sweden: The Aeronautical Research Institute of Sweden, November 1956.

35. Randall, R. F., D. Bell, and J. Burk. Pressure Distribution Tests of Several Sharp Leading Edge Wings, Bodies, and Body Wing Combinations at Mach 5 and 8. AEDC TN-173. Arnold Air Force Station, Tennessee: Arnold Engineering Development Center, 1966.

36. Hefner, J. N. and A. H. Whitehead, Jr. Surface Flow, Pressure and Heat Transfer Studies on Two Conical Delta Wings at a Mach Number of 6.0. NASA TM X-2668. Washington: National Aeronautics and Space Administration, December 1972.

37. Bertram, M. H. and P. E. Everhart. An Experimental Study of the

Pressure and Heat Transfer Distribution on a 70° Sweep Slab Delta Wing in Hypersonic Flow. NASA TR R-153. Washington: National Aeronautics and Space Administration, 1963.

38. Hillier, R. Pressure Distributions at M=3.51 and at High Incidences on Four Wings with Delta Planform. ARC CP 1198. London: Aeronautical Research Council, March 1971.

39. Squire, L. C. Pressure Distributions and Flow Patterns at M=4.0 on Some Delta Wings. Part 1: Wings of Inverted "V" Cross-Section. Part 2: "Flat" Wings. ARC R&M 3373. London: Aeronautical Research Council, 1963.

40. Squire, L. C. Pressure Distributions and Flow Patterns on Some Conical Shapes with Sharp Leading Edges and Symmetrical Cross-Sections at M=4.0. ARC R&M 3340. London: Aeronautical Research Council, 1962.

41. Peckham, D. H. Pressure Distribution Measurements on a Series of Slender Delta Body Shapes at Mach Numbers of 6.85 and 8.60. ARC CP-791. London: Aeronautical Research Council, 1964.

42. Little, H. R. Windward Laminar Heating Rates on Conical Segments at Mach Numbers of 10 and 17. AEDC-TR-70-255. Arnold Air Force Station, Tennessee: Arnold Engineering Development Center, December 1970.

43. Matthews, R. K. and C. R. Cauble. Aerodynamic Heating Distributions on Three 80-Degree Swept Delta Lifting Bodies at Mach Number 8. AEDC-TR-70-183. Arnold Air Force Station, Tennessee: Arnold Engineering Development Center, August 1970.

44. Michael, W. H. Jr. Flow Studies on Flat-Plate Delta Wings at Supersonic Speed. NACA TN 3472. Washington: National Aeronautics and Space Administration, 1955.

45. Carter, H. S. Heat Transfer on the Lifting Surfaces of a 60° Delta Wing at Angle of Attack for Mach Number 1.98. NACA RM L56C23. Washington: National Advisory Committee for Aeronautics, 1956.

46. Stallings, R. L., P. B. Burbank, and D. T. Howell. Heat-Transfer and Pressure Measurements on Delta Wings at Mach Numbers of 3.51 and 4.65 and Angles of Attack from -45° to 45°. NASA TN D-2387. Washington: National Aeronautics and Space Administration, 1964.

47. Dunavant, J. C. Investigation of Heat Transfer and Pressure on High Swept Flat and Dihedraled Delta Wings at Mach Numbers of 6.8 and 9.6 and Angles of Attack to 90°. NASA TM X-688. Washington: National Aeronautics and Space Administration, 1962.

48. Royall, J. F. and J. F. Newcombe. Investigation of Heat Transfer on a Simulated 82° Swept Delta Wing in Free Flight at Angle of Attack at Mach Numbers up to 9.8. NASA TM X-622. Washington:

National Aeronautics and Space Administration, 1962.

49. Squire, L. C., J. G. Jones, and A. Stanbrook. *An Experimental Investigation of the Characteristics of Some Plane and Cambered 65° Delta Wings at Mach Numbers from 0.7 to 2.0*. ARC R&M 3305. London: Aeronautical Research Council, July 1961.

50. Stetson, K. F. and N. E. Scaggs. *Shock Detachment From the Leading Edge of Delta Wings*. ARL 72-0079. Wright-Patterson AFB, Ohio: Aerospace Research Laboratories, May 1972.

51. Bertram, M. H., W. V. Feller, and J. C. Dunavant. *Flow Fields, Pressure Distributions, and Heat Transfer for Delta Wings at Hypersonic Speeds*. NASA TM X-316. Washington: National Aeronautics and Space Administration, September 1960.

52. Sliski, N. J. *An Investigation of Aerodynamic Heating Distributions and Boundary Layer Transition on an 80° Swept Delta Planform at Mach=8 and Angles of Attack 0-60°*. AFFDL-TM-74-98. Wright-Patterson AFB, Ohio: Air Force Flight Dynamics Laboratory, March 1974.

53. Stern, I., A. I. Fox, and A. R. Flesher *An Analytical and Experimental Investigation of the Flow Field Around Two Highly Swept Delta Wing Configurations in High Mach Number-Reynolds Number Flight*. AFFDL-TR-70-112. Wright-Patterson AFB, Ohio: Air Force Flight Dynamics Laboratory, September 1970.

54. McElderry, E. D. *A Pressure Distribution Study of Highly Swept Deltas at Hypersonic Speeds from -15 Degrees to +15 Degrees Angle of Attack*. AFFDL-TR-70-82. Wright-Patterson AFB, Ohio: Air Force Flight Dynamics Laboratory, October 1970.

55. Griffith, B. J., W. S. Norman, D. E. Boylan. *Hypersonic Heat Transfer Rates on an AFFDL 80-Deg. Slightly Blunted Delta Wing*. AEDC-TR-70-178. Arnold Air Force Station, Tennessee: Arnold Engineering Development Center, October 1970.

56. Busemann, A. *Infinitesimal Concial Supersonic Flow*. NACA TM-1100. Washington: National Advisory Committee for Aeronautics, 1947.

57. Stewart, H. J. "The Lift of a Delta Wing at Supersonic Speeds". *Quarterly Applied Mathematics*, *4*:246-254 (1946).

58. Lagerstrom, P. A. *Linearized Supersonic Theory of Conical Wings*. NACA TN-1685. Washington: National Advisory Committee for Aeronautics, January 1950.

59. Clarke, J. J. and J. Wallace. "Uniform Second-Order Solution for Supersonic Flow Over Delta Wing Using Reverse-Flow Integral Method". *Journal of Fluid Mechanics*, *18*:255-238 (February 1964).

60. Maslen, S. H. *Supersonic Conical Flows*. NACA TN-2651. Washington: National Advisory Committee for Aeronautics, March 1952.

61. Reyn, J. W. "Differential-Geometric Considerations on the Holograph Transformation for Irrotational Conical Flow." *Anch. Rat. Mech. Am.*, *6*:299-354 (1960)

62. Reyn, J. W. *Further Investigation of the Holograph Transformation for Irrotational Conical Flow*. DI-82-0145. Seattle: Boeing Scientific Research Laboratories, December 1961.

63. Reyn, J. W. "Differential - Geometric Considerations on the Holograph Transformation for Irrotational Conical Flow." *Proc. I.C.A.S.*, *3*:535-552 (1964).

64. Bulakh, B. M. "Remarks on J. W. Reyn's Paper: Differential-Geometric Considerations on the Holograph Transformation for Irrotational Conical Flow." *Journal of Applied Mathematics and Mechanics*, *26*:793-797 (1962).

65. Babaev, D. A. "Numerical Solution of the Problem of Flow Around the Upper Surface of a Triangular Wing by a Supersonic Stream." *USSR Comp. Math. Math. Physics*, *2*:296-308 (1962).

66. Babaev, D. A. "Numerical Solution of the Problem of Supersonic Flow Past the Lower Surface of a Delta Wing." *AIAA Journal*, *1*:2224-2231 (September 1963).

67. South, J. C. and E. B. Klunker. *Method for Calculating Nonlinear Conical Flows*. NASA SP-228. Washington: National Aeronautics and Space Administration, October 1969.

68. Beeman, E. R. and S. A. Powers. *A Method for Determining the Complete Flow Field Around Conical Wings at Supersonic/Hypersonic Speeds*. AIAA Paper 69-646. New York: American Institute of Aeronautics and Astronautics, June 1969.

69. Messiter, A. F. "Lift of Slender Delta Wings According to Newtonian Theory." *AIAA Journal*, *1*:794-802 (April 1963).

70. Hida, K. "Thickness Effect on the Force of Slender Delta Wings in Hypersonic Flow." *AIAA Journal*, *3*:427-433 (March 1965).

71. Squire, L. C. "Calculated Pressure Distributions and Shock Shapes on Thick Conical Wings at High Supersonic Speeds." *The Aeronautical Quarterly*, *18*:185-206 (1966).

72. Squire, L. C. "Calculations of the Pressure Distribution on Lifting Conical Wings with Applications to the Off-Design Behavior of Wave Riders." *AGARD CP 30*. AGARD Conference on Hypersonic Boundary Layers and Flow Fields (May 1968).

73. Shanbhag, V. V. Numerical Studies on Hypersonic Delta Wings with Detached Shock Waves. ARC CP-1277. London:Aeronautical Research Council, 1974.

74. Hillier, R. "The Effects of Yaw on Conical Wings at High Supersonic Speeds." The Aeronautical Quarterly, 21:199-210 (1970).

75. Hillier, R. Some Applications of Thin Shock Layer Theory to Hypersonic Wings. Phd Thesis. Cambridge, England: University of Cambridge, 1970.

76. Squire, L. C. "Calculated Pressure Distributions and Shock Shapes on Conical Wings with Attached Shock Waves." The Aeronautical Quarterly, 19:31-50 (February 1968).

77. Woods, B. A. "Hypersonic Flow with Attached Shock Waves Over Delta Wings." The Aeronautical Quarterly, 21:379-399 (November 1970).

78. Woods, B. A. and C. B. G. McIntosh. "Hypersonic Flow with Attached Shock Waves Over Plane Delta Wings." Journal of Fluid Mechanics, 79:361-377 (February, 1977).

79. Roe, P. L. A Simple Treatment of the Attached Shock Layer on a Delta Wing. ARC 32853. London: Aeronautical Research Council, 1970.

80. Roe, P. L. A Result Concerning the Supersonic Flow Below a Plane Delta Wing. ARC CP-1228. London: Aeronautical Research Council, 1972.

81. Gonor, A. L. "Hypersonic Flow Past a Delta Wing." Journal of Applied Mathematics and Mechanics, 34:452-461 (1969).

82. Gonor, A. L. and N. A. Ostepenko. "Hypersonic Flow Past Delta Wing of Finite Thickness. "Izv. AN SSSR Mekhanika Zhidkosti i Gaza, 5:46-55 (1970).

83. Malmuth, N. D. "Hypersonic Flow Over a Delta Wing of Moderate Aspect Ratio." AIAA Journal, 4:555-556 (March 1966).

84. Ter-Minasyants, S. M. "The Problem of Supersonic Flow Over the Lower Surface of a Triangular Wing." Izv. AN SSSR Mekhanika Zhidkosti i Gaza, 1:147-152 (1966).

85. Hui, W. H. "Supersonic and Hypersonic Flow with Attached Shock Waves over Delta Wings. "Proceedings of the Royal Society of London, Series A, 325:251-268, (1971).

86. Hui, W. H. "Methods for Calculating Nonlinear Flows with Attached Shock Waves over Conical Wings." AIAA Journal, 11:1443-1445 (October 1973).

87. Voskresenskii, G. P. "Numerical Solution of the Problem of the Flow of a Supersonic Gas Stream over the Upper Surface of a Delta Wing in the Expansion Region." Zhurnal Prikladnoi Mekhaniki i Tekhnicheskoi Fiziki, 6:76-81 (November-December 1973).

88. Voskresenskii, G. P. "Numerical Solution of the Problem of a Supersonic Gas Flow Past on Arbitrary Surface of a Delta Wing on the Compression Region." Izv. Akad. Nauk. SSSR Mekh., Zhidk. Gaza, 4:134-142 (1968).

89. Kutler, P. and H. Lomax, "Shock-Capturing Finite-Difference Approach to Supersonic Flows." Journal of Spacecraft and Rockets, 8:1175-1182 (December 1971).

90. Kutler, P. and H. Lomax. A Systematic Development of the Supersonic Flow Fields over and Behind Wings and Wing-Body Configurations Using a Shock-Capturing Finite-Difference Approach. AIAA Paper 71-99. New York: American Institute of Aeronautics and Astronautics, January 1971.

91. Kutler, P. "Computation of Three-Dimensional, Inviscid Supersonic Flows." in Lecture Notes in Physics, edited by H. J. Wirz. Heidelberg Germany: Springer-Verlag, 1975.

92. Bazzhin, A. P. "Flat Slender Delta Wings in Supersonic Stream at Small Angles of Attack." in Lecture Notes in Physics, 35, edited by R. D. Richtmyer. Heidelberg Germany: Springer-Verlag, 1974

93. Walkden, F. and P. Caine. A Shock Capturing Method for Calculating Supersonic Flow Fields. ARC CP-1290. London: Aeronautical Research Council, December 1972

94. McRae, D. S. Numerical Solution of the Conically Symmetric Navier-Stokes Equations for Hypersonic Cone Flow at Angle of Attack. PhD Thesis. Wright-Patterson Air Force Base,Ohio :Air Force Institute of Technology, July 1976. (Available as AD--A028351)

95. Vincenti, W. G. and C. H. Kruger. Introduction to Physical Gas Dynamics New York: John Wiley and Sons, 1965.

96. Schlichting, H. Boundary Layer Theory (Sixth Edition). New York: McGraw-Hill Book Co., 1968.

97. Yuan, S. W. Foundations of Fluid Mechanics. Edgewood Cliffs, New Jersey: Prentice-Hall, Inc., 1967.

98. Chow, Lin-Chen. On Numerical Studies of Time-Dependent Navier-Stokes Equations. PhD Thesis. Tullahoma, Tennessee: University of Tennessee Space Institute, December 1972.

99. Courant, R. and K. O. Friedrichs Supersonic Flow and Shock Waves. New York: Interscience Publishers, Inc., 1948.

100. Lax, P. D. "Weak Solutions of Nonlinear Hyperbolic Equations and Their Numerical Computation." *Communications on Pure and Applied Mathematics*, *7*:159-193 (February 1954).

101. Gary, J. "On Certain Finite Difference Schemes for Hyperbolic Systems." *Mathematics of Computation*, *18*:1-18 (January 1964).

102. Abbett, M. J. *Boundary Condition Computational Procedures for Inviscid Supersonic Steady Flow Field Calculations*. Final Report 71-41. Aerotherm Corp, 1971.

103. Longley, H. J. *Methods of Differencing in Eulerian Hydrodynamics*. LASL Rept. LAMS-2379. Los Alamos: Los Alamos Scientific Laboratory, 1960.

104. Vinokur, M. "Conservation Equations of Gasdynamics in Curvilinear Coordinate Systems." *Journal of Computational Physics*, *14*:105-125 (February 1974).

105. Viviand, H: "Conservative Forms of Gas Dynamic Equations." *LaRecherche Aerospatiale*, 1:65-68 (January - February 1974).

106. Liepmann, H. W. and A. Roshko *Elements of Gasdynamics*. New York: John Wiley and Sons, 1957.

107. Anderson, D. A. "Comments on Numerical Solution of the Axial Corner Flow Problem for Laminar Flow" Private Communication.

108. Crocco, L. "A Suggestion for the Numerical Solution of the Steady Navier-Stokes Equations" *AIAA* Journal, 3:1824-1832, (October 1965).

109. Richtmyer, R. D. and K. W. Morton. *Difference Methods for Initial-Value Problems*. New York: John Wiley and Sons, 1967.

110. Kutler, P. *Application of Selected Finite-Difference Techniques to the Solution of Conical Flow Problems*. Phd Thesis. Ames, Iowa: Iowa State University, 1969.

111. Anderson, D. A. "A Comparison of Numerical Solutions to the Inviscid Equations of Fluid Motion." *Journal of Computational Physics*, *15*:1-20 (May 1974).

112. Warming, R. F., P. Kutler, and H. Lomax. "Second-and Third-Order Noncentered Difference Schemes for Nonlinear Hyperbolic Equations." *AIAA Journal*, *11*:189-196 (February 1973).

113. MacCormack, R. W. *The Effects of Viscosity in Hypervelocity Impact Cratering*. AIAA Paper 69-354. New York: American Institute of Aeronautics and Astronautics, April 1969.

114. Lax, P. D. and B. Wendroff. "Systems of Conservation Laws." *Communications on Pure and Applied Mathematics*, *13*:217-237 (May, 1960).

115. Kutler, P., R. F. Warming, and H. Lomax. "Computation of Space Shuttle Flow Fields Using Noncentered Finite-Difference Schemes." *AIAA Journal*, *11*:196-204 (February 1973).

116. Tannehill, J. C. and R. A. Mohling. *Numerical Computation of the Hypersonic Rarefied Flow Near the Sharp Leading Edge of a Flat Plate*. AIAA Paper 73-200. New York: American Institute of Aeronautics and Astronautics, January 1973.

117. Roache, P. J. *Computational Fluid Dynamics*. Albuquerque, N.M.: Hermosa Publishers, 1972.

118. Carter, J. E. *Numerical Solutions of the Supersonic, Laminar Flow over a Two-Dimensional Compression Corner*. Phd Thesis, Blacksburg, Virginia: Polytechnic Institute and State University, 1971.

119. Burstein, S. Z. "Finite-Difference Calculations for Hydrodynamic Flows Containing Discontinuities." *Journal of Computational Physics*, *1*:198-222. (November 1966).

120. Lapidus, A., "A Detached Shock Calculation by Second-Order Finite Differences." *Journal of Computational Physics*, *2*:154-177. (November 1967).

121. Isaacson, E. and H. B. Keller, *Analysis of Numerical Methods*. New York: John Wiley and Sons, Inc., 1966.

122. Kutler, P., L. Sakell, and G. Aiello. *On the Shock on Shock Interaction Problem*. AIAA Paper 74-524. New York: American Institute of Aeronautics and Astronautics, 1974.

123. MacCormack, R. W. and B. S. Baldwin. *A Numerical Method for Solving the Navier-Stokes Equations with Applications to Shock Boundary Layer Applications*. AIAA Paper 75-1. New York: American Institute of Aeronautics and Astronautics, 1975.

124. Kentzer, C. P. "Stability of Finite-Differnece Methods for Time Dependent Navier-Stokes Equations." *Fluid Dynamics Transactions*, *4*:45-51 (1969).

125. MacCormack, R. W. "Numerical Solution of the Interaction of a Shock Wave with a Laminar Boundary Layer." *Lecture Notes in Physics*, 8:151-163 (1971).

126. Cheng, S. I. "Numerical Integration of Navier-Stokes Equations." *AIAA Journal*, *8*:2115-2122 (December 1970).

127. Tracy, R. R. *Hypersonic Flow over a Yawed Circular Cone*. Technical Memorandum 69. Pasadena, California: California Institute of Technology, August 1963.

128. Squire, L. C. "The Independence of Upper and Lower Wing Flows at Supersonic Speeds." *The Aeronautical Journal*, *80*:452-456 (October 1976).

129. Whitehead, A. H. and M. H. Bertram. "Alleviation of Vortex-Induced Heating to the Leeside of Slender Wings in Hypersonic Flow". AIAA Journal, 9:1870-1872 (September 1971).

130. Rao, D. M. "Hypersonic Lee Surface Heating Alleviation on Delta Wing by Apex-Drooping." AIAA Journal, 9:1875-1876 (September 1971).

131. Rao, D. M. and A. H. Whitehead. "Leeside Vortices on Delta Wings at Hypersonic Speeds." AIAA Journal, 10:1458-1465 (November 1972).

132. Hankey, W. "Comments on Viscous Interaction Parameter." Private Communication.

133. Bannink, W. J. and C. Nebbeling. "Determination of the Position of a Shock Wave from Pitot Tube Experiments." AIAA Journal, 7:796-797 (April 1969).

134. California Computer Products, Inc. A General Purpose Contouring Program - User's Manual. Anaheim, California: Calcomp, April 1971.

135. Burke, G. L. A Study of the Blunt Slab Delta Wing at Hypersonic Speeds and Angles of Attack. AFFDL-TR-71-181. Wright-Patterson AFB, Ohio: Air Force Flight Dynamics Laboratory, June 1972.

136. Shang, J. S., W. L. Hankey and J. S. Petty. Three-Dimensional Supersonic Interacting Turbulent Flow Along a Corner. AIAA Paper 78-1210. New York: American Institute of Aeronautics and Astronautics, July 1978.

137. Thompson, J. F., F. C. Thames, and C. W. Mastin. "Automatic Numerical Generation of Body. Fitted Curvilinear Coordinate System for Field Containing Any Number of Arbitrary Two-Dimensional Bodies." Journal of Computational Physics, 15:299-319 (July 1974).

138. Gessner, F. B., and J. K. Po. "A Reynolds Stress Model for Turbulent Corner Flows - Part I; Comparisons Between Theory and Experiment," Journal of Fluids Engineering, Transactions of ASME, 98: 269-277 (June 1976).

139. Ghia, U. "Comments on Streamline Contour Plotting," Private Communication.

140. Cooper, W. "Comments on Streamline Contour Plotting," Private Communication.

141. Carnahan, B., H. A. Luther, J. O. Wilkes. Applied Numerical Methods. New York: John Wiley and Sons, Inc., 1969.

142. Cooper, J. R. and W. Hankey. Flow Field Measurements in an Asymmetric Axial Corner at M=12.5. AIAA Paper 73-676. New York: American Institute of Aeronautics and Astronautics, July 1973.

143. Levinson, N. and R. M. Redhoffer. Complex Variables. San Francisco, California: Holden Day Publishers, 1970.

APPENDIX A

Transformation Derivatives

This appendix contains a comprehensive set of transformation derivatives used in the numerical integration of the governing equations. Since the intent here is to provide a quick reference only, most of the algebraic development is omitted.

Transformation Derivatives for the Cone

For the flow field calculations over a cone, the coordinate transformation is

$$\zeta = x \qquad \eta = \tan^{-1}\left(\frac{z}{y}\right) \qquad \xi = \frac{\sqrt{y^2 + z^2}}{x} - \tan\theta_c$$

The transformation derivatives are

$$\frac{\partial\zeta}{\partial x} = 1 \qquad \frac{\partial\zeta}{\partial y} = 0 \qquad \frac{\partial\zeta}{\partial z} = 0$$

$$\frac{\partial\eta}{\partial x} = 0 \qquad \frac{\partial\eta}{\partial y} = \frac{-1}{\zeta\xi}\sin\eta \qquad \frac{\partial\eta}{\partial z} = \frac{1}{\zeta\xi}\cos\eta$$

$$\frac{\partial\xi}{\partial x} = \frac{-\xi}{\zeta} \qquad \frac{\partial\xi}{\partial y} = \frac{1}{\zeta}\cos\eta \qquad \frac{\partial\xi}{\partial z} = \frac{1}{\zeta}\sin\eta$$

$$\frac{\partial}{\partial\zeta}\left(\frac{\partial\zeta}{\partial x}\right) = 0 \qquad \frac{\partial}{\partial\zeta}\left(\frac{\partial\zeta}{\partial y}\right) = 0 \qquad \frac{\partial}{\partial\zeta}\left(\frac{\partial\zeta}{\partial z}\right) = 0$$

$$\frac{\partial}{\partial\zeta}\left(\frac{\partial\eta}{\partial x}\right) = 0 \qquad \frac{\partial}{\partial\zeta}\left(\frac{\partial\eta}{\partial y}\right) = 0 \qquad \frac{\partial}{\partial\zeta}\left(\frac{\partial\eta}{\partial z}\right) = 0$$

$$\frac{\partial}{\partial\zeta}\left(\frac{\partial\xi}{\partial x}\right) = \frac{2\xi}{\zeta^2} \qquad \frac{\partial}{\partial\zeta}\left(\frac{\partial\xi}{\partial y}\right) = \frac{-1}{\zeta^2}\cos\eta \qquad \frac{\partial}{\partial\zeta}\left(\frac{\partial\xi}{\partial z}\right) = \frac{-1}{\zeta^2}\sin\eta$$

Transformation Derivatives for the Delta Wing

For the flow around a delta wing, the coordinate transformation is

$$\zeta = x \qquad \eta = \frac{y}{x} \qquad \xi = \frac{z}{x}$$

The transformation derivatives are

$$\frac{\partial\zeta}{\partial x} = 1 \qquad \frac{\partial\zeta}{\partial y} = 0 \qquad \frac{\partial\zeta}{\partial z} = 0$$

$$\frac{\partial\eta}{\partial x} = \frac{-\eta}{\zeta} \qquad \frac{\partial\eta}{\partial y} = \frac{1}{\zeta} \qquad \frac{\partial\eta}{\partial z} = 0$$

$$\frac{\partial\xi}{\partial x} = \frac{-\xi}{\zeta} \qquad \frac{\partial\xi}{\partial y} = 0 \qquad \frac{\partial\xi}{\partial z} = \frac{1}{\zeta}$$

$$\frac{\partial}{\partial\zeta}\left(\frac{\partial\zeta}{\partial x}\right) = 0 \qquad \frac{\partial}{\partial\zeta}\left(\frac{\partial\zeta}{\partial y}\right) = 0 \qquad \frac{\partial}{\partial\zeta}\left(\frac{\partial\zeta}{\partial z}\right) = 0$$

$$\frac{\partial}{\partial\zeta}\left(\frac{\partial\eta}{\partial x}\right) = \frac{2\eta}{\zeta^2} \qquad \frac{\partial}{\partial\zeta}\left(\frac{\partial\eta}{\partial y}\right) = \frac{-1}{\zeta^2} \qquad \frac{\partial}{\partial\zeta}\left(\frac{\partial\eta}{\partial z}\right) = 0$$

$$\frac{\partial}{\partial\zeta}\left(\frac{\partial\xi}{\partial x}\right) = \frac{2\xi}{\zeta^2} \qquad \frac{\partial}{\partial\zeta}\left(\frac{\partial\xi}{\partial y}\right) = 0 \qquad \frac{\partial}{\partial\zeta}\left(\frac{\partial\xi}{\partial z}\right) = \frac{-1}{\zeta^2}$$

APPENDIX B

Convergence of Iterative Methods and Determination of Iteration Errors

All iterative techniques generate a sequence of numbers or vectors. These iterative methods are convergent if their sequences converge to the numbers or vectors which satisfy the given problem. Therefore, given an initial vector $X^{(o)}$, where $X = \left[x_1, x_2, \ldots x_n\right]$,an iterative technique generates a sequence of vectors $X^{(k)}$ which, hopefully, converges to a limit vector, A.

A fundamental theorem of numerical analysis asserts that a sequence converges if and only if it is a Cauchy sequence. A sequence $X^{(k)}$ is a Cauchy sequence.if for every $\bar{\varepsilon} > 0$ there exists a positive number N such that for all integers n, m >N we have

$$||X^{(n)} - X^{(m)}|| < \bar{\varepsilon} \tag{B1}$$

where $|| \quad ||$ is some vector norm. The choice of the particular norm is not important since it can be shown that all vector norms are equivalent (Ref 143).

The importance of the Cauchy property is that the convergence of a sequence can be ascertained without knowledge of the limit vector, A. The significance of this concept with regards to numerical methods in which A is not known is readily apparent.

In this investigation, the numerical convergence method is derived from the definition of a Cauchy sequence and is referred to as the Cauchy method. Numerical iterations are carried out until a condition of the form

$$\frac{\left\|\phi^{(k)} - \phi^{(k-1)}\right\|_{i,j}}{\phi_r} \leq \bar{\varepsilon} \tag{B2}$$

is met where $\phi = u, v, w, \rho, p, e$ and $\bar{\varepsilon}$ is chosen positive number. ϕ_r is defined as $\phi_{i,j}^{(k)}$ for all the primitive variables, except for the velocity terms where V_{max} is used. The local error, $E(x_1, x_2, \ldots x_n, k)$, at iteration k is defined as the vector norm $\left\|X^{(k)} - X^{(k-1)}\right\|_{i,j}$ while the true error at each iteration k is

$$e^{(k)} \equiv X_{i,j}^{(k)} - A \tag{B3}$$

The number $\bar{\varepsilon}$ appearing in Eq B2 is called the convergence criteria. The condition specified by Eq B2 is that for the iterative convergence of the finite-difference technique. The value of the convergence criteria for this investigation is 10^{-5}.

APPENDIX C

Stability Analysis

The theoretical investigation of stability is particularly complex for the difference schemes associated with the governing equations. Approaches to studying this phenomenon are reported in Roache (Ref 117) and Richtmyer and Morton (Ref 109). An approximate method which tends to yield the best results for a set of general nonlinear equations is the amplification matrix theory by von Neumann. This method consists of examining the linearized difference equations for the amplification of short wavelength oscillations superimposed on an exact solution. The growth and decay of these oscillations can be predicted by applying the harmonic analysis of von Neumann. In his analysis, the boundary conditions have no effect on the stability result and the exact solution of the governing equations is smooth. This latter assumption allows the coefficients of the partial differential equations to be treated as constants (locally). The stability conditions predicted by this theory result in a local stability condition which places a bound on the time increment used in the numerical integration.

Richtmyer and Morton (Ref 109) showed that the von Neumann stability conditions for the nonconservative form of the governing equations is the same as that for the conservative form. Since the analysis is easier for the nonconservative form, the following nondimensionalized governing equations, as suggested by MacCormack and Baldwin (Ref 123), were considered:

$$\frac{\partial U}{\partial t} + A \frac{\partial U}{\partial \eta} + B \frac{\partial U}{\partial \xi} + C \frac{\partial^2 U}{\partial \eta^2} + D \frac{\partial^2 U}{\partial \xi^2}$$

$$+ E \frac{\partial}{\partial \eta}\left(\frac{\partial U}{\partial \xi}\right) + F \frac{\partial}{\partial \xi}\left(\frac{\partial U}{\partial \eta}\right) = 0$$

where

$$U = \begin{vmatrix} \rho \\ u \\ v \\ w \\ p \end{vmatrix} \qquad A = \begin{vmatrix} A_{11} & A_{12} & A_{13} & A_{14} & 0 \\ 0 & A_{22} & 0 & 0 & A_{25} \\ 0 & 0 & A_{33} & 0 & A_{35} \\ 0 & 0 & 0 & A_{44} & A_{45} \\ 0 & A_{52} & A_{53} & A_{54} & A_{55} \end{vmatrix}$$

$$B = \begin{vmatrix} B_{11} & B_{12} & B_{13} & B_{14} & B_{15} \\ 0 & B_{22} & 0 & 0 & B_{25} \\ 0 & 0 & B_{33} & 0 & B_{35} \\ 0 & 0 & 0 & B_{44} & B_{45} \\ 0 & B_{52} & B_{53} & B_{54} & B_{55} \end{vmatrix}$$

$$C = \begin{vmatrix} 0 & 0 & 0 & 0 & 0 \\ 0 & C_{22} & C_{23} & C_{24} & 0 \\ 0 & C_{32} & C_{33} & C_{34} & 0 \\ 0 & C_{42} & C_{43} & C_{44} & 0 \\ C_{51} & 0 & 0 & 0 & C_{55} \end{vmatrix}$$

$$D = \begin{vmatrix} 0 & 0 & 0 & 0 & 0 \\ 0 & D_{22} & D_{23} & D_{24} & 0 \\ 0 & D_{32} & D_{33} & D_{34} & 0 \\ 0 & D_{42} & D_{43} & D_{44} & 0 \\ D_{51} & 0 & 0 & 0 & D_{55} \end{vmatrix}$$

$$E = \begin{vmatrix} 0 & 0 & 0 & 0 & 0 \\ 0 & E_{22} & E_{23} & E_{24} & 0 \\ 0 & E_{32} & E_{33} & E_{34} & 0 \\ 0 & E_{42} & E_{43} & E_{44} & 0 \\ E_{51} & 0 & 0 & 0 & E_{55} \end{vmatrix}$$

$$F = \begin{vmatrix} 0 & 0 & 0 & 0 & 0 \\ 0 & F_{22} & F_{23} & F_{24} & 0 \\ 0 & F_{32} & F_{33} & F_{34} & 0 \\ 0 & F_{42} & F_{43} & F_{44} & 0 \\ F_{51} & 0 & 0 & 0 & F_{55} \end{vmatrix}$$

The elements of these matrices can be found in Appendix E.

In the above equations, the Prandtl number, the Reynolds number, and the nodal point locations are assumed to be constant. In addition, the dissipation terms of the energy equation which contain quadratics in first-order derivatives have been deleted based on an analysis by Kentzer (Ref 124).

The stability criteria for the governing equations are determined by examining three distinct parts of these equations: the inviscid, diffusion, and mixed-derivative parts. The magnitude of the eigenvalues of the amplification matrices associated with each of the three parts must be less than or equal to one in order for the numerical equations to be stable.

Inviscid Part

The inviscid part of the governing equations can be written as

$$\frac{\partial U}{\partial t} + A \frac{\partial U}{\partial \eta} + B \frac{\partial U}{\partial \xi} = 0$$

The amplification matrix of this equation, as given by MacCormack (Ref 125), is

$$G = I - i\Delta t \left[\frac{A}{\Delta\eta} \sin\bar{\alpha} + \frac{B}{\Delta\xi} \sin\bar{\beta} \right]$$

$$- \frac{1}{2} (\Delta t)^2 \left\{ \frac{A}{\Delta\eta} (1-e^{-i\bar{\alpha}}) + \frac{B}{\Delta\xi} (1-e^{-i\bar{\beta}}) \right\} \left\{ \frac{A}{\Delta\eta} (1-e^{i\bar{\alpha}}) + \frac{B}{\Delta\xi} (1-e^{i\bar{\beta}}) \right\}$$

where $\bar{\alpha} = k_1 \Delta\eta$, $\bar{\beta} = k_2 \Delta\xi$, and I is the unit matrix. The von Neumann stability condition for this equation is

$$\left| G \right| \leq 1$$

If we look at large values of G, then the G matrix can be approximated as

$$G = I - iA' - \frac{1}{2} (A'^2 + B'^2)$$

where

$$A' = \Delta t \left[\frac{A}{\Delta\eta} \sin\bar{\alpha} + \frac{B}{\Delta\xi} \sin\bar{\beta} \right]$$

and

$$B' = \Delta t \left[\frac{A}{\Delta\eta} + \frac{B}{\Delta\xi} \right]$$

If a' is the eigenvalue of A' and b' is the eigenvalue of B', then the stability condition is satisfied if

$$\frac{1}{4}\ \frac{(a'^2 + b'^2)}{b'} \leq 1$$

Hence, the maximum eigenvalue of the matrix A' helps determine the maximum allowable time increment Δt. Thus, we shall let $\sin\bar{\alpha} = \sin\bar{\beta} = 1$ and A' = B'.

Richtmyer and Morton (Ref 109) introduced a technique by which the eigenvalues of A' and B' may be found. If we consider an axis inclined at an angle θ with respect to the η-axis where θ is given by

$$\cos\theta = \frac{\dfrac{1}{\Delta\eta}}{\sqrt{\left(\dfrac{1}{\Delta\eta}\right)^2 + \left(\dfrac{1}{\Delta\xi}\right)^2}}$$

$$\sin\theta = \frac{\dfrac{1}{\Delta\xi}}{\sqrt{\left(\dfrac{1}{\Delta\eta}\right)^2 + \left(\dfrac{1}{\Delta\xi}\right)^2}}$$

and where the velocity component along this axis is

$$u' = A_{11}\cos\theta + B_{11}\sin\theta$$

then the A' and B' matrices can be written as

$$A' = B' = \sqrt{\left(\frac{1}{\Delta\eta}\right)^2 + \left(\frac{1}{\Delta\xi}\right)^2}\ \left[A\cos\theta + B\sin\theta\right]$$

The eigenvalues for this matrix, in tensor form, are

$$\lambda_1 = \lambda_2 = \lambda_3 = u'\Delta t\sqrt{\left(\frac{1}{\Delta\eta}\right)^2 + \left(\frac{1}{\Delta\xi}\right)^2}$$

$$\lambda_4 = \Delta t \left\{ u' + a \left[\left(\frac{\partial\eta}{\partial x_i}\right)\left(\frac{\partial\eta}{\partial x_i}\right)\cos^2\theta + \left(\frac{\partial\xi}{\partial x_i}\right)\left(\frac{\partial\xi}{\partial x_i}\right)\sin^2\theta \right.\right.$$

$$\left.\left. + 2\left(\frac{\partial\eta}{\partial x_i}\right)\left(\frac{\partial\xi}{\partial x_i}\right)\sin\theta\cos\theta\right]\right\}\sqrt{\left(\frac{1}{\Delta\eta}\right)^2 + \left(\frac{1}{\Delta\xi}\right)^2}$$

$$\lambda_5 = \Delta t \left\{ u' - a \left[\left(\frac{\partial\eta}{\partial x_i}\right)\left(\frac{\partial\eta}{\partial x_i}\right)\cos^2\theta + \left(\frac{\partial\xi}{\partial x_i}\right)\left(\frac{\partial\xi}{\partial x_i}\right)\sin^2\theta \right.\right.$$

$$\left.\left. + 2\left(\frac{\partial\eta}{\partial x_i}\right)\left(\frac{\partial\xi}{\partial x_i}\right)\sin\theta\cos\theta\right]\right\}\sqrt{\left(\frac{1}{\Delta\eta}\right)^2 + \left(\frac{1}{\Delta\xi}\right)^2}$$

By inserting the largest eigenvalue of both the A' and B' matrices into the stability equation, the maximum allowable Δt becomes

$$\Delta t_{INV} \leq \left[\left|u_i \frac{\partial\eta}{\partial x_i}\right|\frac{1}{\Delta\eta} + \left|u_i \frac{\partial\xi}{\partial x_i}\right|\frac{1}{\Delta\xi}\right.$$

$$\left. + a\sqrt{\left(\frac{\partial\eta}{\partial x_i}\right)\left(\frac{\partial\eta}{\partial x_i}\right)\frac{1}{(\Delta\eta)^2} + \left(\frac{\partial\xi}{\partial x_i}\right)\left(\frac{\partial\xi}{\partial x_i}\right)\frac{1}{(\Delta\xi)^2} + 2\left(\frac{\partial\eta}{\partial x_i}\right)\left(\frac{\partial\xi}{\partial x_i}\right)\frac{1}{\Delta\eta\Delta\xi}}\,\right]^{-1}$$

This result indicates that the maximum allowable Δt decreases as η and ξ increase.

Diffusion Part

The diffusion part of the Navier-Stokes equations can be written as

$$\frac{\partial U}{\partial t} + C\frac{\partial^2 U}{\partial\eta^2} + D\frac{\partial^2 U}{\partial\xi^2} = 0$$

By applying the MacCormack scheme to the linearized form of this equation, the finite-difference equation becomes

$$U^{n+1}_{i,j} = U^n_{i,j} - \frac{C\Delta t}{(\Delta\eta)^2}\left\{ U^n_{i+1,j} - 2\,U^n_{i,j} + U^n_{i-1,j} \right\}$$

$$- \frac{D\Delta t}{(\Delta\xi)^2}\left\{ U^n_{i,j+1} - 2U^n_{i,j} + U^n_{i,j-1} \right\}$$

$$+ \frac{1}{2}\left\{ \frac{C\Delta t}{(\Delta\eta)^2} \right\}^2 \left[U^n_{i+2,j} - 4U^n_{i+1,j} + 6U^n_{i,j} - 4U^n_{i-1,j} + U^n_{i-2,j} \right]$$

$$+ \frac{1}{2}\left\{ \frac{D\Delta t}{(\Delta\xi)^2} \right\}^2 \left[U^n_{i,j+2} - 4U^n_{i,j+1} + 6U^n_{i,j} - 4U^n_{i,j-1} + U_{i,j-2} \right]$$

$$+ \frac{1}{2}\left\{ \frac{CD(\Delta t)^2}{(\Delta\eta)^2\ (\Delta\xi)^2} \right\} \left[2U^n_{i+1,j+1} - 4U^n_{i+1,j} + 2U^n_{i+1,j-1} \right.$$

$$\left. - 4U^n_{i,j+1} + 8U^n_{i,j} - 4U^n_{i,j-1} + 2U^n_{i-1,j+1} - 4U^n_{i-1,j} + 2U^n_{i-1,j-1} \right]$$

Substitution of one Fourier component of the solution

$$U(\eta,\xi,\ t) = U_o(t)\ \exp\left[i(k_1\ \eta + k_2\ \xi) \right]$$

into the finite-difference equation gives the amplification matrix, which is defined as

$$G = \frac{U^{n+1}_{i,j}}{U^n_{i,j}} = I - \frac{2C\Delta t}{(\Delta\eta)^2}\ (\cos\bar{\alpha} - 1) - \frac{2D\Delta t}{(\Delta\xi)^2}\ (\cos\bar{\beta} - 1)$$

$$+ \frac{1}{2}\left\{ \frac{C\Delta t}{(\Delta\eta)^2} \right\}^2 \left[2\cos^2\bar{\alpha} - 2\sin^2\bar{\alpha} - 8\cos\bar{\alpha} + 6 \right]$$

$$+ \frac{1}{2}\left\{ \frac{D\Delta t}{(\Delta\xi)^2} \right\}^2 \left[2\cos^2\bar{\beta} - 2\sin^2\bar{\beta} - 8\cos\bar{\beta} + 6 \right]$$

$$+ \frac{1}{2}\left\{ \frac{CD(\Delta t)^2}{(\Delta\eta)^2\ (\Delta\xi)^2} \right\} \left[8\cos\bar{\alpha}\cos\bar{\beta} - 8\cos\bar{\alpha} - 8\cos\bar{\beta} + 8 \right]$$

where $\bar{\alpha} = k_1 \Delta\eta$, $\bar{\beta} = k_2 \Delta\xi$, and I is the unit matrix. If we let c and d be the eigenvalues of the C and D matrices respectively, then the von Neumann stability criterion becomes

$$1 \leq \frac{1}{c + d}$$

The maximum eigenvalue for the C matrix is the larger of the two terms:

$$c = \left| \frac{-2\gamma}{\rho N} \right| \left[\left(\frac{\partial\eta}{\partial x_i} \right) \left(\frac{\partial\eta}{\partial x_i} \right) \right] \frac{\Delta t}{(\Delta\eta)^2}$$

$$c = \left| \frac{2\beta_1 - 6}{3\rho Re} \right| \left[\left(\frac{\partial\eta}{\partial x_i} \right) \left(\frac{\partial\eta}{\partial x_i} \right) \right] \frac{\Delta t}{(\Delta\eta)^2}$$

where β_1 is the maximum local value of the normal stress damping function in the x and y directions. For the D matrix, the maximum eigenvalue is the larger of the two quantities:

$$d = \left| \frac{-2\gamma}{\rho N} \right| \left[\left(\frac{\partial\xi}{\partial x_i} \right) \left(\frac{\partial\xi}{\partial x_i} \right) \right] \frac{\Delta t}{(\Delta\xi)^2}$$

$$d = \left| \frac{2\beta_2 - 6}{3\rho Re} \right| \left[\left(\frac{\partial\xi}{\partial x_i} \right) \left(\frac{\partial\xi}{\partial x_i} \right) \right] \frac{\Delta t}{(\Delta\xi)^2}$$

where β_2 is the maximum local normal stress damping in the x and z directions. Thus, the maximum allowable time increment for the diffusion part of the governing equations is the smaller of the following two terms:

$$\Delta t_{DF} \leq \frac{\rho Pr Re}{\gamma} \left[\left(\frac{\partial\xi}{\partial x_i} \right) \left(\frac{\partial\xi}{\partial x_i} \right) \frac{1}{(\Delta\xi)^2} + \left(\frac{\partial\eta}{\partial x_i} \right) \left(\frac{\partial\eta}{\partial x_i} \right) \frac{1}{(\Delta\eta)^2} \right]^{-1}$$

$$\Delta t_{DF} \leq \left| \frac{3\rho Re}{2\beta_3 - 6} \right| \left[\left(\frac{\partial\xi}{\partial x_i} \right) \left(\frac{\partial\xi}{\partial x_i} \right) \frac{1}{(\Delta\xi)} + \left(\frac{\partial\eta}{\partial x_i} \right) \left(\frac{\partial\eta}{\partial x_i} \right) \frac{1}{(\Delta\eta)^2} \right]^{-1}$$

where β_s is the maximum local normal stress damping value in the three Cartesian coordinate directions.

Mixed Derivative Part

The mixed-derivative part of the governing equations is

$$\frac{\partial U}{\partial t} + D \frac{\partial}{\partial \eta}\left(\frac{\partial U}{\partial \xi} \right) + F \frac{\partial}{\partial \xi}\left(\frac{\partial U}{\partial \eta} \right) = 0$$

By applying the MacCormack scheme to this equation results in the following finite-difference equation:

$$U^{n+1}_{i,j} = U^{n}_{i,j} - \frac{H\Delta t}{4\Delta\eta\Delta\xi} \left[U^{n}_{i+1,j+1} - U^{n}_{i+1,j-1} - U^{n}_{i-1,j+1} - U^{n}_{i-1,j-1} \right]$$

$$+ \frac{1}{2} \left[\frac{H\Delta t}{4\Delta\eta\Delta\xi} \right]^2 \Big[U^{n}_{i+2,j+2} - 2U^{n}_{i+2,j} + U^{n}_{i+2,j-2} - U^{n}_{i,j+2}$$

$$+ 4U^{n}_{i,j} - 2U^{n}_{i,j-2} + U^{n}_{i-2,j+2} - 2U^{n}_{i-2,j} + U^{n}_{i-2,j-2}$$

where

$$H = E + F$$

and where the coefficient matrices E and F are assumed constant.

If we substitute the Fourier term

$$U(\eta,\xi,t) = U_0(t) \exp \left[i(k_1\eta + k_1\xi) \right]$$

into the finite-difference equation, the amplification matrix becomes

$$G = I + \frac{H\Delta t}{4\Delta\eta\Delta\xi} \left[4 \sin\bar{\alpha}\sin\bar{\beta} \right]$$

$$- \left[\frac{H\Delta t}{4\Delta\eta\Delta\xi} \right]^2 \left[\cos 2\bar{\alpha} - \cos 2\bar{\beta} \right]^2$$

where $\bar{\alpha} = k_1 \Delta\eta$, $\bar{\beta} = k_2 \Delta\xi$, and I is the unit matrix. The stability condition for this equation is

$$1 \leq \frac{-4}{h}$$

where h is the eigenvalue of the H matrix. The maximum eigenvalue for the H matrix is found to be

$$h = \frac{-1}{3\rho Re} \left[7 \frac{\partial\eta}{\partial x_i} \frac{\partial\xi}{\partial x_i} + \sqrt{\left(\frac{\partial\eta}{\partial x_i}\right)\left(\frac{\partial\eta}{\partial x_i}\right)\left(\frac{\partial\xi}{\partial x_j}\right)\left(\frac{\partial\xi}{\partial x_j}\right)} \right] \frac{\Delta t}{\Delta\eta\Delta\xi}$$

By inserting this eigenvalue into the stability equation results in the following Δt restriction:

$$\Delta t_{MXD} \leq \frac{12\rho Re\Delta\eta\Delta\xi}{7 \frac{\partial\eta}{\partial x_i} \cdot \frac{\partial\xi}{\partial x_i} + \sqrt{\left(\frac{\partial\eta}{\partial x_i}\right)\left(\frac{\partial\eta}{\partial x_i}\right)\left(\frac{\partial\xi}{\partial x_j}\right)\left(\frac{\partial\xi}{\partial x_j}\right)}}$$

From this analysis, it is estimated that the stability criterion for the full governing equations is

$$\Delta t \leq \frac{c}{\frac{1}{\Delta t_{INV}} + \frac{1}{\Delta t_{DF}} + \frac{1}{\Delta t_{MXD}}}$$

where c is an adjustable constant less than or equal to one. The magnitude of all the damping term constants are set so as to make the damping effective in the inviscid flow region but not to appreciably change the boundary layer behavior or modify the Reynolds number. This linearized stability criterion may not insure numerical stability in all cases (Ref 126), but it should be valid for the experimental cases considered.

APPENDIX D

Elements of the Linearized Matrix Equations

This appendix contains a list of matrix elements used in the linearized governing equations. These matrix elements were used to determine the stability criteria of the numerical integration.

$$A_{11} = A_{22} = A_{33} = A_{44} = A_{55} = u\frac{\partial\eta}{\partial x} + v\frac{\partial\eta}{\partial y} + w\frac{\partial\eta}{\partial z}$$

$$A_{12} = \rho\frac{\partial\eta}{\partial x}$$

$$A_{13} = \rho\frac{\partial\eta}{\partial y}$$

$$A_{14} = \rho\frac{\partial\eta}{\partial z}$$

$$A_{25} = \frac{\varepsilon}{\rho}\frac{\partial\eta}{\partial x}$$

$$A_{35} = \frac{\varepsilon}{\rho}\frac{\partial\eta}{\partial y}$$

$$A_{45} = \frac{\varepsilon}{\rho}\frac{\partial\eta}{\partial z}$$

$$A_{52} = (1+2\gamma\varepsilon)\ p\frac{\partial\eta}{\partial x}$$

$$A_{53} = (1+2\gamma\varepsilon)\ p\frac{\partial\eta}{\partial y}$$

$$A_{54} = (1+2\gamma\varepsilon)\ p\frac{\partial\eta}{\partial z}$$

$$B_{11} = B_{22} = B_{33} = B_{44} = B_{55} = u\frac{\partial\xi}{\partial x} + v\frac{\partial\xi}{\partial y} + w\frac{\partial\xi}{\partial z}$$

$$B_{12} = \rho\frac{\partial\xi}{\partial x}$$

$$B_{13} = \rho\frac{\partial\xi}{\partial y}$$

$$B_{14} = \rho\frac{\partial\xi}{\partial z}$$

$$B_{25} = \frac{\varepsilon}{\rho}\frac{\partial\xi}{\partial x}$$

$$B_{35} = \frac{\varepsilon}{\rho} \frac{\partial \xi}{\partial y}$$

$$B_{45} = \frac{\varepsilon}{\rho} \frac{\partial \xi}{\partial z}$$

$$B_{52} = (1+2\gamma\varepsilon)\ p\frac{\partial \xi}{\partial x}$$

$$B_{53} = (1+2\gamma\varepsilon)\ p\frac{\partial \xi}{\partial y}$$

$$B_{54} = (1+2\gamma\varepsilon)\ p\frac{\partial \xi}{\partial z}$$

$$C_{22} = \frac{-1}{\rho}\left[\frac{4}{3Re}\left(\frac{\partial \eta}{\partial x}\right)^2 + \frac{1}{Re}\left(\frac{\partial \eta}{\partial y}\right)^2 + \frac{1}{Re}\left(\frac{\partial \eta}{\partial z}\right)^2\right]$$

$$C_{23} = \frac{-1}{3\rho Re} \frac{\partial \eta}{\partial x} \frac{\partial \eta}{\partial y}$$

$$C_{24} = \frac{-1}{3\rho Re} \frac{\partial \eta}{\partial x} \frac{\partial \eta}{\partial z}$$

$$C_{32} = \frac{-1}{3\rho Re} \frac{\partial \eta}{\partial x} \frac{\partial \eta}{\partial y}$$

$$C_{33} = \frac{-1}{\rho Re}\left[\frac{4}{3}\left(\frac{\partial \eta}{\partial y}\right)^2 + \left(\frac{\partial \eta}{\partial x}\right)^2 + \left(\frac{\partial \eta}{\partial z}\right)^2\right]$$

$$C_{34} = \frac{-1}{3\rho Re} \frac{\partial \eta}{\partial y} \frac{\partial \eta}{\partial z}$$

$$C_{42} = \frac{-1}{3\rho Re} \frac{\partial \eta}{\partial x} \frac{\partial \eta}{\partial z}$$

$$C_{43} = \frac{-1}{3\rho Re} \frac{\partial \eta}{\partial y} \frac{\partial \eta}{\partial z}$$

$$C_{44} = \frac{-1}{\rho Re}\left[\frac{4}{3}\left(\frac{\partial \eta}{\partial z}\right)^2 + \left(\frac{\partial \eta}{\partial x}\right)^2 + \left(\frac{\partial \eta}{\partial y}\right)^2\right]$$

$$C_{51} = \frac{2\gamma p}{\rho^2 N}\left[\left(\frac{\partial \eta}{\partial x}\right)^2 + \left(\frac{\partial \eta}{\partial y}\right)^2 + \left(\frac{\partial \eta}{\partial z}\right)^2\right]$$

$$C_{55} = \frac{-2\gamma}{\rho N}\left[\left(\frac{\partial \eta}{\partial x}\right)^2 + \left(\frac{\partial \eta}{\partial y}\right)^2 + \left(\frac{\partial \eta}{\partial z}\right)^2\right]$$

$$D_{22} = \frac{-1}{\rho Re}\left[\frac{4}{3}\left(\frac{\partial \xi}{\partial x}\right)^2 + \left(\frac{\partial \xi}{\partial y}\right)^2 + \left(\frac{\partial \xi}{\partial z}\right)^2\right]$$

$$D_{23} = \frac{-1}{3\rho Re} \frac{\partial \xi}{\partial x} \frac{\partial \xi}{\partial y}$$

$$D_{24} = \frac{-1}{3\rho Re} \frac{\partial \xi}{\partial x} \frac{\partial \xi}{\partial z}$$

$$D_{32} = \frac{-1}{3\rho Re} \frac{\partial \xi}{\partial x} \frac{\partial \xi}{\partial y}$$

$$D_{33} = \frac{-1}{\rho Re} \left[\frac{4}{3} \left(\frac{\partial \xi}{\partial y} \right)^2 + \left(\frac{\partial \xi}{\partial x} \right)^2 + \left(\frac{\partial \xi}{\partial z} \right)^2 \right]$$

$$D_{34} = \frac{-1}{3\rho Re} \frac{\partial \xi}{\partial y} \frac{\partial \xi}{\partial z}$$

$$D_{42} = \frac{-1}{3\rho Re} \frac{\partial \xi}{\partial x} \frac{\partial \xi}{\partial z}$$

$$D_{43} = \frac{-1}{3\rho Re} \frac{\partial \xi}{\partial y} \frac{\partial \xi}{\partial z}$$

$$D_{44} = \frac{-1}{\rho Re} \left[\frac{4}{3} \left(\frac{\partial \xi}{\partial z} \right)^2 + \left(\frac{\partial \xi}{\partial x} \right)^2 + \left(\frac{\partial \xi}{\partial y} \right)^2 \right]$$

$$D_{51} = \frac{2\gamma p}{\rho^2 N} \left[\left(\frac{\partial \xi}{\partial x} \right)^2 + \left(\frac{\partial \xi}{\partial y} \right)^2 + \left(\frac{\partial \xi}{\partial z} \right)^2 \right]$$

$$D_{55} = \frac{-2\gamma}{\rho N} \left[\left(\frac{\partial \xi}{\partial x} \right)^2 + \left(\frac{\partial \xi}{\partial y} \right)^2 + \left(\frac{\partial \xi}{\partial z} \right)^2 \right]$$

$$E_{22} = \frac{-1}{\rho Re} \left[\frac{4}{3} \frac{\partial \eta}{\partial x} \frac{\partial \xi}{\partial x} + \frac{\partial \eta}{\partial y} \frac{\partial \xi}{\partial y} + \frac{\partial \eta}{\partial z} \frac{\partial \xi}{\partial z} \right]$$

$$E_{23} = \frac{1}{\rho Re} \left[\frac{2}{3} \frac{\partial \eta}{\partial x} \frac{\partial \xi}{\partial y} - \frac{\partial \eta}{\partial y} \frac{\partial \xi}{\partial x} \right]$$

$$E_{24} = \frac{1}{\rho Re} \left[\frac{2}{3} \frac{\partial \eta}{\partial x} \frac{\partial \xi}{\partial z} - \frac{\partial \eta}{\partial z} \frac{\partial \xi}{\partial x} \right]$$

$$E_{32} = \frac{1}{\rho Re} \left[\frac{2}{3} \frac{\partial \eta}{\partial y} \frac{\partial \xi}{\partial x} - \frac{\partial \eta}{\partial x} \frac{\partial \xi}{\partial y} \right]$$

$$E_{33} = \frac{-1}{\rho Re} \left[\frac{4}{3} \frac{\partial \eta}{\partial y} \frac{\partial \xi}{\partial y} + \frac{\partial \eta}{\partial z} \frac{\partial \xi}{\partial z} + \frac{\partial \eta}{\partial x} \frac{\partial \xi}{\partial x} \right]$$

$$E_{34} = \frac{1}{\rho Re} \left[\frac{2}{3} \frac{\partial \eta}{\partial y} \frac{\partial \xi}{\partial z} - \frac{\partial \eta}{\partial z} \frac{\partial \xi}{\partial y} \right]$$

$$E_{42} = \frac{1}{\rho Re} \left[\frac{2}{3} \frac{\partial \eta}{\partial z} \frac{\partial \xi}{\partial x} - \frac{\partial \eta}{\partial x} \frac{\partial \xi}{\partial z} \right]$$

$$E_{43} = \frac{1}{\rho Re} \left[\frac{2}{3} \frac{\partial \eta}{\partial z} \frac{\partial \xi}{\partial y} - \frac{\partial \eta}{\partial y} \frac{\partial \xi}{\partial z} \right]$$

$$E_{44} = \frac{-1}{\rho Re} \left[\frac{4}{3} \frac{\partial \eta}{\partial z} \frac{\partial \xi}{\partial z} + \frac{\partial \eta}{\partial x} \frac{\partial \xi}{\partial x} + \frac{\partial \eta}{\partial y} \frac{\partial \xi}{\partial y} \right]$$

$$E_{51} = \frac{2\gamma p}{\rho^2 N} \left[\frac{\partial \eta}{\partial x} \frac{\partial \xi}{\partial x} + \frac{\partial \eta}{\partial y} \frac{\partial \xi}{\partial y} + \frac{\partial \eta}{\partial z} \frac{\partial \xi}{\partial z} \right]$$

$$E_{55} = \frac{-2\gamma}{\rho N} \left[\frac{\partial \eta}{\partial x} \frac{\partial \xi}{\partial x} + \frac{\partial \eta}{\partial y} \frac{\partial \xi}{\partial y} + \frac{\partial \eta}{\partial z} \frac{\partial \xi}{\partial z} \right]$$

$$F_{22} = \frac{-1}{\rho Re} \left[\frac{4}{3} \frac{\partial \xi}{\partial x} \frac{\partial \eta}{\partial x} + \frac{\partial \xi}{\partial y} \frac{\partial \eta}{\partial y} + \frac{\partial \xi}{\partial z} \frac{\partial \eta}{\partial z} \right]$$

$$F_{23} = \frac{1}{\rho Re} \left[\frac{2}{3} \frac{\partial \xi}{\partial x} \frac{\partial \eta}{\partial y} - \frac{\partial \xi}{\partial y} \frac{\partial \eta}{\partial x} \right]$$

$$F_{24} = \frac{1}{\rho Re}\left[\frac{2}{3}\ \frac{\partial\xi}{\partial x}\frac{\partial\eta}{\partial z} - \frac{\partial\xi}{\partial z}\frac{\partial\eta}{\partial x}\right]$$

$$F_{32} = \frac{1}{\rho Re}\left[\frac{2}{3}\ \frac{\partial\xi}{\partial y}\frac{\partial\eta}{\partial x} - \frac{\partial\xi}{\partial x}\frac{\partial\eta}{\partial y}\right]$$

$$F_{33} = \frac{-1}{\rho Re}\left[\frac{4}{3}\ \frac{\partial\xi}{\partial y}\frac{\partial\eta}{\partial y} + \frac{\partial\xi}{\partial x}\frac{\partial\eta}{\partial x} + \frac{\partial\xi}{\partial z}\frac{\partial\eta}{\partial z}\right]$$

$$F_{34} = \frac{1}{\rho Re}\left[\frac{2}{3}\ \frac{\partial\xi}{\partial y}\frac{\partial\eta}{\partial z} - \frac{\partial\xi}{\partial z}\frac{\partial\eta}{\partial y}\right]$$

$$F_{42} = \frac{1}{\rho Re}\left[\frac{2}{3}\ \frac{\partial\xi}{\partial z}\frac{\partial\eta}{\partial x} - \frac{\partial\xi}{\partial x}\frac{\partial\eta}{\partial z}\right]$$

$$F_{43} = \frac{1}{\rho Re}\left[\frac{2}{3}\ \frac{\partial\xi}{\partial z}\frac{\partial\eta}{\partial y} - \frac{\partial\xi}{\partial y}\frac{\partial\eta}{\partial z}\right]$$

$$F_{44} = \frac{-1}{\rho Re}\left[\frac{4}{3}\ \frac{\partial\xi}{\partial z}\frac{\partial\eta}{\partial z} + \frac{\partial\xi}{\partial y}\frac{\partial\eta}{\partial y} + \frac{\partial\xi}{\partial x}\frac{\partial\eta}{\partial x}\right]$$

$$F_{51} = \frac{2\gamma p}{\rho^2 N}\left[\frac{\partial\xi}{\partial x}\frac{\partial\eta}{\partial x} + \frac{\partial\xi}{\partial y}\frac{\partial\eta}{\partial y} + \frac{\partial\xi}{\partial z}\frac{\partial\eta}{\partial z}\right]$$

$$F_{55} = \frac{-2\gamma}{\rho N}\left[\frac{\partial\xi}{\partial x}\frac{\partial\eta}{\partial x} + \frac{\partial\xi}{\partial y}\frac{\partial\eta}{\partial y} + \frac{\partial\xi}{\partial z}\frac{\partial\eta}{\partial z}\right]$$

APPENDIX E

Subroutines of the DELTA Code

This appendix provides a description of the important operations performed by each subroutine of the numerical code DELTA. These subroutines are also used in the DELTA1 and CONE programs. The order of the subroutine descriptions follows the same order used to call them in the DELTA program.

COORD

Subroutine COORD calculates the first-order derivatives of the coordinate transformations (as defined in Appendix A). The analytical values of these derivatives are computed for every grid point in the computational domain. These values are stored in common block arrays for easy access during the numerical integration.

PREDICT

The next subroutine used in the DELTA program is PREDICT. This subroutine calculates the predictor term of the MacCormack finite-difference scheme. It uses the BOUND subroutine to compute the boundary conditions on the surface of the body and at the leading edge of the delta wing. A double DO loop is entered wherein the $\overline{U}_{i,j}^{n+1}$ vector is calculated for all computational grid points except the free stream boundary points, the surface grid points, and the grid points opposite the plane of symmetry. Within this DO loop, the subroutines DAMPF, DAMPG, VECTOR, DECODE, and SOLVE are called in sequential order to perform the numerical integration. As a result of this partial integration, the flow quantities are computed for an intermediate time step $t^{\overline{n+1}}$.

BOUND

Subroutine BOUND calculates the pressure and density on the surface of the body and at the leading edge. The velocity at these surface grid points is zero and the surface temperature is provided as part of the input data. The normal momentum equation is used to calculate the surface pressure and then the equation of state is used to determine the density. In the DELTA program, the pressure and density are computed for both the upper and lower wing surfaces, as described in Chapter 3. Second-order accurate, one-sided forward differences are used to model the flow gradients normal to the body surface, while second-order central differences are used for all other gradients.

At the leading edge, the pressure and density are triple valued. The pressure is determined for the upper, side, and lower surfaces of the wing by using the appropriate normal momentum equation. The three values of density are computed from the equation of state. When the numerical integration is applied below the wing, the leading edge is represented by lower surface values of pressure and density. Similarly, when the numerical integration occurs above the wing, the upper surface values model the leading edge on the η-axis. In the DELTA1 program, the leading edge is represented by upper surface values only.

DAMPF and DAMPG

DAMPF and DAMPG subroutines calculate the density damping terms for the η and ξ directions respectively. These terms are added together in the DECODE subroutine to form the fourth-order damping terms $D^{n}_{i,j}$ (predictor step only) and $D^{\overline{n+1}}_{i,j}$ (corrector step only). The damping coefficients, c_i and c_j, are read into the program as part of the input data. The damping terms normal to the free stream boundary surfaces and symmetry plane and within two grid points of these surfaces are zero. The damping at the surface grid points is also zero. All the damping term values are stored in common block arrays for use in the DECODE subroutine.

VECTOR

The next subroutine used in the DELTA program is VECTOR. This subroutine computes the values of the F,G and H matrices as well as the heat flux and shear stress terms in these matrices. The finite-difference quotients used to model τ_{ij} and $\dot{q}$ are described in Chapter 3. The second-order derivatives of the coordinate transformations (used in the H matrix) are calculated by calling subroutine COORDX. The values of these matrices are stored in common block arrays for use in the DECODE subroutine.

Subroutine VECTOR is used in both the predictor and corrector steps. By changing the input parameters when this subroutine is called, the finite-difference quotients can be easily converted for use in either the predictor or corrector step. These input parameters are also used in the DECODE subroutine.

SOLVE

Subroutine SOLVE is used to solve for the flow quantities in the $U_{i,j}^{\overline{n+1}}$ (predictor step only) and $U_{i,j}^{n+1}$ (corrector step only) vectors. The primitive variables u,v,w,ρ, and e are determined by solving the relationships in Eq 70. The flow quantities are then stored in two-dimensional arrays for use in the next integration step.

SYM

Subroutine SYM uses a DO loop to calculate the primitive flow variables on the opposite side of the plane of symmetry. By applying Eqs 79 and 80, the surface boundary conditions and the flow field conditions are determined for the mirror image plane. These flow quantities are then stored in common block arrays for use in the next integration step.

CORRECT

The next subroutine used in the DELTA program is CORRECT. This subroutine calculates the corrector term of the MacCormack finite-difference scheme. It uses the same subroutines as are used in the PREDICT subroutine in the same sequential order. By applying different input parameters, this subroutine is able to calculate the final flow quantities at the new time step t^{n+1}. These newly calculated flow parameters are then stored in the same two-dimensional arrays as the old quantities.

APPENDIX F

Conical Velocity Components and Streamline Plots

This appendix presents a detailed discussion on the conical cross-flow velocity vectors and on the method, used by Ghia (Ref 139) to determine the conical streamline contours in the ξ-η plane. The computer software for the streamline plots was developed by Cooper (Ref 140).

Conical Velocity Vectors

Experimental evidence has shown that the supersonic and hypersonic flow around thin delta wings is nearly conical in the weak interaction region. In delineating the conical aspects of this flow field, the velocity components in the spherical coordinate system are used for flow analysis. The magnitude of the spherical cross-flow velocity vectors is

$$V_c = \sqrt{u_\theta^2 + u_\phi^2} \tag{F1}$$

while the angle of the flow in the ξ-η plane, as determined by Cooper and Hankey (Ref 142), is

$$\tan \gamma_c = \tan (\omega-\phi) = \frac{d\xi}{d\eta} \tag{F2}$$

where

$$\tan \omega = \frac{u_\theta}{u_\phi \cos \theta}$$

When these values are transformed into the conical coordinate system (delta wing), the magnitude and direction of the velocity vectors become

$$V_c = \left[\frac{(v\xi-u\eta)^2+(w-u\xi)^2 + (u\eta-v)^2}{1 + \eta^2 + \xi^2}\right]^{\frac{1}{2}} \qquad \text{(F4)}$$

$$\tan \gamma_c = \left(\frac{u\xi-w}{u\eta-v}\right) \qquad \text{(F5)}$$

The steady state velocity components in the η and ξ directions are

$$V_\eta = V_c \cos \gamma_c \qquad \text{(F6)}$$

$$V_\xi = V_c \sin \gamma_c \qquad \text{(F7)}$$

Conical Streamline Plot

The cross-flow velocity vectors projected on the ξ-η plane trace out "pseudo" conical streamlines. These streamlines represent steady state path lines of incoming fluid particles. These path lines are determined by solving the differential equations

$$\frac{d\eta}{dt} = V_\eta\ (\eta,\xi) \qquad \text{(F8)}$$

$$\frac{d\xi}{dt} = V_\xi\ (\eta,\xi) \qquad \text{(F9)}$$

The modified Euler-Cauchy method (Ref 141) is used to solve Equations F8 and F9 in the form

$$\Delta\eta = \eta^*-\eta_i = \int_t^{t+\Delta t} V_\eta\ (\eta,\xi)dt \qquad \text{(F10)}$$

$$\Delta\xi = \xi^*-\xi_j = \int_t^{t+\Delta t} V_\xi\ (\eta,\xi)dt \qquad \text{(F11)}$$

where η^* and ξ^* are the projected locations of the next point on the streamline curve. Prior to integrating Equations F10 and F11, an incremental time step, Δt, is defined and the initial position of the fluid particles is established at each nodal point on the boundary of the ξ-η plane.

The numerical integration is begun, by initially assuming that V_η and V_ξ at (i,j) are constant over the interval $\eta_i \leq \eta < \eta_{i+1}$ and $\xi_j \leq \xi < \xi_{j+1}$. This results in a preliminary estimate of η^* and ξ^* of

$$\eta^* = \eta_i + V_\eta \Delta t \tag{F12}$$

$$\xi^* = \xi_j + V_\xi \Delta t \tag{F13}$$

The velocity components at (i^*, j^*) are determined by linear interpolation as illustrated in Figure F1.

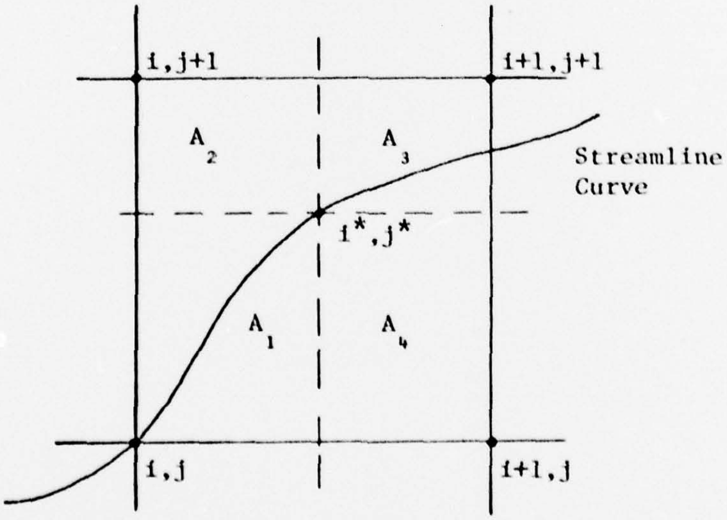

Figure F1

where

$$V_\eta^* = \frac{1}{A}\left(V_{\eta_{i,j}} A_3 + V_{\eta_{i+1,j}} A_2 + V_{\eta_{i+1,j+1}} A_1 + V_{\eta_{i,j+1}} A_4\right) \tag{F14}$$

$$V_\xi^* = \frac{1}{A}\left(V_{\xi_{i,j}} A_3 + V_{\xi_{i+1,j}} A_2 + V_{\xi_{i+1,j+1}} A_1 + V_{\xi_{i,j+1}} A_4\right) \tag{F15}$$

and where

$$\begin{aligned} A_1 &= (\xi^*-\xi_j)\,(\eta^*-\eta_i) \\ A_2 &= (\xi_{j+1}-\xi^*)\,(\eta^*-\eta_i) \\ A_3 &= (\xi_{j+1}-\xi^*)\,(\eta_{i+1}-\eta^*) \\ A_4 &= (\xi^*-\xi_j)\,(\eta_{i+1}-\eta^*) \\ A &= A_1 + A_2 + A_3 + A_4 \end{aligned} \tag{F16}$$

By averaging the appropriate velocity components at (i^*,j^*) with those at (i,j), an improved estimate of η^* and ξ^* is obtained. This improved estimate is

$$\eta^* = \eta_i + \frac{1}{2}\left(V_{\eta_{i,j}} + V_\eta^*\right)\Delta t \tag{F17}$$

$$\xi^* = \xi_j + \frac{1}{2}\left(V_{\xi_{i,j}} + V_\xi^*\right)\Delta t \tag{F18}$$

The velocities at the new (i^*,j^*) are recomputed, by linear interpolation, and then the new location and velocity vector are used as initial conditions for calculating the next point. This integration process is repeated until the maximum number of time steps is reached.

Vita

Guion Stewart Bluford, Jr. was born on 22 November 1942 in Philadelphia, Pennsylvania. He graduated from Overbrook High School in 1960 and attended Penn State University where he received a Bachelor of Science degree in Aerospace Engineering and a commission in the United States Air Force in 1964. After receiving his pilot wings in 1966, he served as an F-4C pilot with the 45th Tactical Fighter Squadron, MacDill Air Force Base, Florida and with the 557th Tactical Fighter Squadron, Republic of Vietnam. In 1967, he was assigned to the 3630th Pilot Training Squadron at Sheppard Air Force Base, Texas where he served as a T-38 flight instructor and assistant flight commander. He was executive support officer to the Deputy Commander of Operations and School Secretary of the 3630th Flying Training Wing prior to entering the Air Force Institute of Technology (AFIT) in 1972. After receiving a Master of Science degree in Aerospace Engineering in March 1974, he entered the doctoral program at AFIT, where he completed the course work in December 1974. He was then assigned to the Air Force Flight Dynamics Laboratory (AFFDL/FXM) as Deputy for Advanced Concepts in the Aeromechanics Division. In April 1977, he became Branch Chief of the Aerodynamics and Airframe Branch in the Air Force Flight Dynamics Laboratory.

Permanent address: 16439 Brookvilla
Houston, Texas 77059

REPORT DOCUMENTATION PAGE		READ INSTRUCTIONS BEFORE COMPLETING FORM
1. REPORT NUMBER AFIT/DS/AA/78S-1	2. GOVT ACCESSION NO.	3. RECIPIENT'S CATALOG NUMBER
4. TITLE (and Subtitle) A NUMERICAL SOLUTION OF SUPERSONIC AND HYPERSONIC VISCOUS FLOW FIELDS AROUND THIN PLANAR·DELTA WINGS		5. TYPE OF REPORT & PERIOD COVERED PhD 6. PERFORMING ORG. REPORT NUMBER
7. AUTHOR(s) Guion S. Bluford Jr. Major		8. CONTRACT OR GRANT NUMBER(s)
9. PERFORMING ORGANIZATION NAME AND ADDRESS Air Force Institute of Technology (AFIT-EN) Wright-Patterson AFB, Ohio 45433		10. PROGRAM ELEMENT, PROJECT, TASK AREA & WORK UNIT NUMBERS 24041002
11. CONTROLLING OFFICE NAME AND ADDRESS Aerodynamics and Airframe Branch Air Force Flight Dynamics Laboratory Wright-Patterson AFB, Ohio 45433		12. REPORT DATE June 1978 13. NUMBER OF PAGES 235
14. MONITORING AGENCY NAME & ADDRESS(if different from Controlling Office)		15. SECURITY CLASS. (of this report) Unclassified 15a. DECLASSIFICATION/DOWNGRADING SCHEDULE

16. DISTRIBUTION STATEMENT (of this Report)

Approved for public release; distribution unlimited

17. DISTRIBUTION STATEMENT (of the abstract entered in Block 20, if different from Report)

18. SUPPLEMENTARY NOTES

Approved for public release; IAW AFR 190-17

JERRAL F. GUESS, Captain, USAF
Director of Information

19. KEY WORDS (Continue on reverse side if necessary and identify by block number)

Delta Wing	Viscous Flows
Supersonic	Conical Flows
Hypersonic	
Numerical	

20. ABSTRACT (Continue on reverse side if necessary and identify by block number)

A numerical technique was used to compute the supersonic and hypersonic, viscous flow fields around thin planar delta wings. These solutions were obtained by solving the Navier-Stokes equations subject to a conical approximation. The integration technique used was the MacCormack finite-difference scheme. Solutions were obtained for the upper-only, lower-only, and total flow fields around delta wings with supersonic leading edges. These solutions span a Mach number range of 2.94 to 10.17, a local Reynolds number range of

Next Page

334500

5,000,000

deg

3.345×10^5 to 5.0×10^6, and various angles of attack from -15° to $+15^\circ$. A stability criteria was developed and used which accounted for both the viscous and inviscid flow regions. Good agreement was obtained between the numerical results and ~~the~~ experimental flow field data. ~~by Cross,~~ Spurlin, and ~~Bannink~~. The shock-induced vortex within the viscous region and the hypersonic viscous "bubble" on top of the boundary layer were computed, for the first time. A unique examination was made of the vortical singularities in the conical cross-flow plane of the delta wing. This investigation demonstrated the feasibility of applying the conical approximation to the Navier-Stokes equations in order to solve flow fields around thin delta wings.